



**HAL**  
open science

## High-gradient S-band electron Linac for ThomX

Luca Garolfi

► **To cite this version:**

Luca Garolfi. High-gradient S-band electron Linac for ThomX. Accelerator Physics [physics.acc-ph]. Université Paris-Saclay, 2018. English. NNT : 2018SACLS007 . tel-01779739

**HAL Id: tel-01779739**

**<https://theses.hal.science/tel-01779739>**

Submitted on 26 Apr 2018

**HAL** is a multi-disciplinary open access archive for the deposit and dissemination of scientific research documents, whether they are published or not. The documents may come from teaching and research institutions in France or abroad, or from public or private research centers.

L'archive ouverte pluridisciplinaire **HAL**, est destinée au dépôt et à la diffusion de documents scientifiques de niveau recherche, publiés ou non, émanant des établissements d'enseignement et de recherche français ou étrangers, des laboratoires publics ou privés.

# Accélérateur linéaire d'électrons à fort gradient en bande S pour ThomX

Thèse de doctorat de l'Université Paris-Saclay  
préparée à l'Université Paris-Sud

École doctorale n°576 Particules Hadrons Energie et Noyau :  
Instrumentation, Image, Cosmos et Simulation (PHENIICS)  
Spécialité de doctorat : Physique des accélérateurs

Thèse présentée et soutenue à Orsay, le 12 janvier 2018, par

**Luca Garolfi**

Composition du Jury :

Achille Stocchi Professeur, Université Paris-Sud – LAL (-UMR 8607)	Président
Philippe Balcou Directeur de Recherche, CELIA – Univ. Bordeaux 1 (-UMR 5107)	Rapporteur
Walter Wuensch Directeur de Recherche, CERN	Rapporteur
Vincent Le Flanchec Chargé de Recherche, CEA – DAM Ile-de-France	Examineur
David Alesini Chargé de Recherche, LNF - INFN	Examineur
Mohamed El Khaldi Ingénieur de Recherche, LAL - CNRS (-UMR 8607)	Directeur de thèse
Christelle Bruni Chercheuse, LAL – CNRS (-UMR 8607)	Encadrante

# Contents

<b>List of Figures</b>	<b>v</b>
<b>List of Tables</b>	<b>x</b>
<b>1 Inverse Compton Scattering X light sources</b>	<b>7</b>
1.1 Physics of Inverse Compton Scattering	7
1.1.1 Kinematics	7
1.1.2 Flux	10
1.1.3 Brightness	12
1.2 The Munich Compact Light Source	14
1.2.1 Layout of the machine	14
1.2.2 X-rays characteristics	15
1.3 ThomX project	16
1.3.1 Layout of the machine	16
1.3.2 Possible applications	17
<b>2 Design of High-Gradient S-band Electron Linac for ThomX</b>	<b>19</b>
2.1 RF cavity fundamentals	20
2.1.1 Electromagnetic modes in RF cavities	20
2.1.2 Particle acceleration in a single RF cell "pill-box cavity"	22
2.1.3 Main characteristics of RF structures	23
2.1.4 Particle acceleration in multi-cell structures	26
2.1.4.1 Travelling wave structures	26
Constant-impedance (CI) structure:	28
Constant-gradient (CG) structure:	29
2.1.4.2 Standing wave structures	30
2.1.4.3 Standing wave versus travelling wave structures	33
2.2 High-Gradient limiting quantities	33
2.3 How to avoid RF breakdowns and damages	35
2.4 ThomX High-Gradient S-band electron Linac design	35
2.4.1 ThomX Linac RF components	36
2.4.2 RF gun	38
2.4.2.1 Electromagnetic analysis	39
2.4.2.2 Thermal analysis	41
2.4.2.3 Structural analysis	42

2.4.3	Design of High-Gradient S-band accelerating section . . . . .	45
2.4.3.1	Resonant frequency determination at normalised conditions . . . . .	46
2.4.3.2	Electromagnetic design of the regular-cells . . . . .	48
2.4.3.3	Coupler design techniques . . . . .	56
2.4.3.4	RF design of the 16-cells copper prototype . . . . .	62
2.4.3.5	Mechanical drawings of the 16-cells copper prototype . . . . .	66
2.4.3.6	RF design of a high-gradient compact S-band accelerating section . . . . .	68
2.4.3.7	Cooling system design and coupled thermal-structural analysis . . . . .	74
2.4.3.8	Dependence on temperature reflection coefficient . . . . .	83
2.4.3.9	Vacuum simulations . . . . .	84
<b>3</b>	<b>Manufacturing process</b> . . . . .	<b>93</b>
3.1	Precision machining . . . . .	94
3.2	Cleaning process . . . . .	96
3.3	High temperature brazing process . . . . .	96
3.4	Development and testing of ThomX RF gun at LAL . . . . .	98
3.4.1	Machining process at LAL . . . . .	98
3.4.2	Cleaning process at LAL . . . . .	99
3.4.3	Tuning process at LAL . . . . .	99
3.4.4	Brazing process at LAL . . . . .	100
3.5	Development and testing of aluminium 7-cells S-band prototypes at PMB-Alcen . . . . .	102
3.5.1	Aluminium 7-cells S-band prototype machining process . . . . .	103
3.5.2	Tuning method under press of regular cells . . . . .	104
3.5.3	Low power test of the aluminium 7-cells prototype . . . . .	108
<b>4</b>	<b>ThomX Linac beam dynamics</b> . . . . .	<b>112</b>
4.1	Some basic principles of beam dynamics . . . . .	113
4.1.1	Phase-space and emittance . . . . .	113
4.1.2	Twiss parameters . . . . .	115
4.1.3	Photo-injector principle: phase of standing wave . . . . .	118
4.1.4	Beam boost by travelling-wave acceleration . . . . .	122
4.1.5	Transverse emittance growth in photo-injectors . . . . .	122
4.2	ThomX RF gun space charge emittance compensation . . . . .	125
4.2.1	Space charge dominated beam . . . . .	125
4.2.2	Principle of space charge compensation . . . . .	126
4.2.3	Magnetic lenses . . . . .	127
4.2.4	Simulation results . . . . .	131
4.3	Beam dynamics with TW accelerating section . . . . .	136
4.3.1	Beam matching to the TW LIL structure . . . . .	138
4.3.2	Beam dynamics for the Linac energy upgrade . . . . .	140
4.3.3	Alternative solenoids configuration . . . . .	141
4.3.3.1	Beam matching to the TW LIL structure . . . . .	142
4.4	Beam dynamics effects on X-rays spectral purity . . . . .	144
<b>5</b>	<b>Conclusions</b> . . . . .	<b>147</b>

---

<b>Bibliography</b>	<b>153</b>
<b>Resumé</b>	<b>161</b>
But du manuscrit de thèse . . . . .	163
Résumé des résultats . . . . .	165

# List of Figures

1	Sketch of an Inverse Compton Scattering machine with storage ring. . . .	3
1.1	An electron is moving with velocity $v$ parallel to the x-axis. It makes an angle $\Phi$ with an incoming photon of frequency $\nu$ (left). In the electron frame, the photon is incoming with a different frequency $\nu'$ making an angle $\Phi'$ with the velocity vector (right). . . . .	8
1.2	In the electron frame of reference, the photon is scattered with an angle $\psi'_1$ according to the conservation of energy and momentum (left). In the frame of reference $K$ the scattering angle is $\psi_1$ (right). . . . .	9
1.3	X-rays energy of scattered photons coming from the interaction of the ideal electron and laser beams (i.e. with no emittance and no energy spread) . . . . .	10
1.4	Photograph of MuCLS [22]. . . . .	14
1.5	Layout of the ThomX machine. . . . .	17
2.1	Electric and magnetic fields of the fundamental mode $TM_{010}$ in a pill-box cavity. . . . .	22
2.2	Accelerating field of the fundamental mode $TM_{010}$ in pill-box cavity. . . .	22
2.3	Sketch of a disk-loaded structure. . . . .	24
2.4	Schematic illustration of a travelling wave structure. . . . .	26
2.5	Dispersion diagram for a disc-loaded travelling wave structure [28]. . . . .	27
2.6	Electric field distribution of the accelerating mode $TM_{010-2\pi/3}$ for an S-band 7-cells TW structure. . . . .	27
2.7	Simple scheme showing how the RF power fills a SWS when it is injected through the input coupler. . . . .	30
2.8	Dispersion diagram for standing wave structure with seven magnetically coupled cells. . . . .	31
2.9	Electric field of the $TM_{010-0}$ mode for standing wave structure with seven electrically coupled cells (half-cell terminated on both sides). . . . .	32
2.10	Electric field of the $TM_{010-\pi}$ mode for standing wave structure with seven electrically coupled cells (half-cell terminated on both sides). . . . .	32
2.11	3D scheme of the ThomX Linac. . . . .	36
2.12	Picture of the LIL accelerating section lent by the SOLEIL laboratory. . .	37
2.13	ANSYS Workbench Analysis Schematic. . . . .	39
2.14	RF gun electric field distribution in vacuum. . . . .	40
2.15	The heat flux for 10 MW peak power at 3 $\mu s$ RF pulse length and 50 Hz repetition rate. . . . .	40
2.16	Cooling system integrated in the gun body. . . . .	42
2.17	Gun body temperature distribution. . . . .	43

2.18	Cooling water temperature distribution along tubes. . . . .	43
2.19	Total deformation of the gun body. . . . .	44
2.20	Gun body equivalent Von-Mises stress for an average dissipated power of 1.5 kW. . . . .	44
2.21	ThomX RF gun. (a) 3D model design, (b) prototype after final brazing. . . . .	45
2.22	Relative efficiency of TW modes in disc-loaded structures. [45] . . . . .	46
2.23	Main geometry parameters of a regular-cell. . . . .	49
2.24	Maximum surface electric field normalised to on-axis accelerating field as a function of the iris ellipticity $r_2/r_1$ for, $a = 9.5$ mm and $t = 5$ mm [51]. . . . .	50
2.25	Normalised on-axis accelerating field as a function of the iris radius and the iris thickness. . . . .	51
2.26	Shunt impedance over Q-factor as a function of the iris radius (a) and the iris thickness (t). . . . .	52
2.27	Group velocity as a function of the iris radius (a) and the iris thickness (t). . . . .	52
2.28	Maximum surface electric field over on-axis electric field as a function of the iris radius (a) and the thickness (t). . . . .	53
2.29	$\mu$ -parameter for a minimum power consumption and minimum risks of BDR as a function of the iris radius (a) and the iris thickness (t). . . . .	54
2.30	Modified Poynting vector over average accelerating field squared as a function of the iris radius (a) and thickness (t). . . . .	54
2.31	2D section and electric field distribution of the half single cell, for $2a = 19$ mm, $t = 5$ mm, $P_{in} = 20$ MW (peak power). . . . .	55
2.32	Distribution of the modified Poynting vector inside in one-quarter regular cell, for $2a = 19$ mm, $t = 5$ mm, $P_{in} = 20$ MW (peak power). . . . .	56
2.33	Geometry parameters of the coupler design. . . . .	57
2.34	CST Studio optimizer tool. . . . .	58
2.35	HFSS model of the three short-circuited structures. . . . .	59
2.36	Reflection $ S_{11} $ and transmission $ S_{12} $ coefficient, as a function of the frequency, for a 7-cells copper prototype ( $ S_{11}  \simeq -40$ dB, $ S_{12}  \simeq -0.5$ dB for the $TM_{010-2\pi/3}$ mode). . . . .	61
2.37	Normalised on-axis electric field amplitude, phase advance per cell along the prototype's axis (7-cells aluminium and copper prototype for the $TM_{010-2\pi/3}$ accelerating mode). . . . .	62
2.38	Reflection $ S_{11} $ and $ S_{21} $ transmission coefficients, as a function of the frequency, for the 16-cells copper prototype (in vacuum at 20 °C). . . . .	62
2.39	Longitudinal electric field distribution of the 16-cells constant impedance copper prototype for 20 MW peak power. . . . .	63
2.40	Longitudinal electric field module and phase advance per cell of the 16-cells constant impedance copper prototype for 20 MW peak power. . . . .	63
2.41	Distribution of the modified Poynting vector in the 16-cells copper prototype. . . . .	64
2.42	Distribution of the surface magnetic field in 16-cells copper prototype. . . . .	65
2.43	3D mechanical drawings of a regular cell. . . . .	67
2.44	3D mechanical drawings of couplers. . . . .	67
2.45	3D mechanical drawings of the 16-cells copper prototype with two couplers and regular accelerating cells. . . . .	68
2.46	Cell diameter (blue line) and resonating frequency of the mode $TM_{010-2\pi/3}$ (orange line) as a function of the iris diameter. . . . .	69

2.47	Scattering parameters $ S_{11} $ (red line), $ S_{21} $ (green line) of the whole accelerating section (in vacuum at 20 °C).	70
2.48	Phase advance along all the whole structure.	70
2.49	Longitudinal electric field module of the $TM_{010-2\pi/3}$ along the whole accelerating structure.	71
2.50	Geometry of the final accelerating section resulting from the CST MWS model.	71
2.51	Group velocity (blue line) and shunt impedance per unit length (orange line) along the structure.	72
2.52	Circulating power (blue line), maximum on-axis electric field (orange line) and effective on-axis electric field (grey line) along the structure.	73
2.53	Energy gain (orange line) and filling time (blue line) along the structure.	74
2.54	Maximum surface electric field and maximum modified Poynting vector over on-axis electric field squared along the structure.	74
2.55	Picture of the the cooling system pipes that are integrated in the 7-cells copper body prototype.	77
2.56	Surface loss density (heat flux) distribution on the cavity walls. The average dissipated power is around 333 W.	78
2.57	HFSS-Fluent coupling scheme.	79
2.58	Temperature distribution of the copper prototype. Input power 20 MW, dissipated power 334 W.	79
2.59	Cooling water temperature distribution tubes.	80
2.60	Pressure drop distribution along the cooling pipes simulated in ANSYS Fluent.	81
2.61	ANSYS Fluent and Structural coupling scheme	82
2.62	Structural deformation of the prototype. Displacement distribution for 334 W dissipated power	83
2.63	Von-Mises structural stress due to an equivalent dissipated power of 333 W.	83
2.64	$ S_{11} $ reflection coefficient as a function of the frequency at 20 °C and 30 °C.	84
2.65	Vacuum pressure simulation in the case of one ionic pump connected to the beam pipe (right side). The plot shows the pressure along the structure (yellow line).	89
2.66	Vacuum pressure simulation in the case of one ionic pump connected to the RF waveguide port (right side). The plot shows the pressure along the structure where the pump is connected to the pipe (yellow line) and to the RF waveguide port (blue line).	89
2.67	Vacuum pressure simulation in the case of one ionic pump connected to both beam pipes (right side). The plot shows the pressure along the structure (blue line).	90
2.68	Vacuum pressure simulation in the case of two ionic pump connected to the RF waveguide ports (right side). The plot shows the pressure along the structure where the pumps are connected to one RF waveguide port (blue line) and to both RF waveguide ports (red line).	91
2.69	Vacuum geometry of the final accelerating section.	91
2.70	Pressure distribution along the length of the final TW CG accelerating structure.	91

3.1	Typical surface finish for classical machining operations [71]. . . . .	95
3.2	LAL furnace for vacuum brazing process of components. . . . .	96
3.3	Multi-tasking precision lathe for machining process at LAL. . . . .	98
3.4	Test bench: low power measurement and tuning procedure of the ThomX RF gun. . . . .	100
3.5	3D mechanical parts of the ThomX RF gun. . . . .	100
3.6	ThomX RF gun in the furnace for the brazing process. . . . .	101
3.7	Turn and mill machine used at PMB-Alcen for regular cells fabrication. . .	102
3.8	View of the inner volume of a regular cell. . . . .	103
3.9	3D mechanical drawing of the power coupler (top) and power coupler parts fabricated by Comeb SrL. (bottom). . . . .	104
3.10	Measurement setting under the press of sample cells at PMB-Alcen. . . .	105
3.11	CST MWS simulation (eigenmode) of the $TM_{010-\pi/2}$ for 2-cells stack. . .	106
3.12	CST MWS simulation (eigenmode) of the $TM_{010-2\pi/3}$ for 3-cells stack. . .	107
3.13	Scheme of regular cells tuning. . . . .	107
3.14	3D mechanical drawing of the 7-cells aluminium prototype. . . . .	108
3.15	7 cells TW CI prototype ready for measurements at PMB-Alcen. . . . .	109
3.16	Principle of the nodal shift technique at PMB-Alcen. . . . .	109
3.17	Measured S-parameters (return loss $S_{11}$ and insertion loss $S_{12}$ ) of the 7 prototype volumes after tuning. . . . .	110
4.1	2D ellipse representation with (x, x') coordinates. . . . .	116
4.2	Normalised electric field profile along the beam axis. . . . .	118
4.3	Electron energy gain as a function of injection phase, taking into account bunch RF phase slippage. . . . .	120
4.4	Energy gain of relativistic electron as a function of phase the $\phi$ . Courtesy of A. Gamelin. . . . .	121
4.5	(Left) Schematic of the gun surrounded by the coils; the focusing coil is equipped with a shielding plate. (Right) 3D OPERA simulation of the two solenoids, the windings (red), the iron yoke (green). . . . .	128
4.6	(Left) Magnetic field strength on the axis for different couples of currents in the two solenoids. (Right) Empirical law of the bucking coil current as a function of the focusing coil current for zeroing the magnetic field at the cathode position. . . . .	129
4.7	Simulated longitudinal magnetic field component on axis for ThomX nom- inal configuration. Comparison between 5 mm shielding plate, without shielding and experimental measurements (left). Comparison between several couples of current supply measured in the coils (right). . . . .	129
4.8	rms normalised transverse emittance x as a function of distance. Total bunch charge 1nC. Laser parameters: rms $\sigma_r = 1\text{mm}$ , rms $\sigma_t = 4\text{ps}$ . Drift space (black line), solenoids without plate (blue line) and solenoids with plate (red line). . . . .	132
4.9	Transverse emittance slope (red line) and transverse emittance value at $z$ $= 1\text{ m}$ (blue line) as a function of magnetic field strength (left). Transverse emittance as a function of the distance for $B = 0.2574\text{ T}$ (right). . . . .	133
4.10	Transverse emittance as a function of the laser spot size. For each value of the spot size, the corresponding value of the magnetic field strength which compensates the emittance growth has been shown. . . . .	134

---

4.11	Total charge per bunch vs RF gun dephasing. . . . .	135
4.12	Nominal ThomX configuration. . . . .	136
4.13	Transverse emittance vs maximum magnetic field strength and RF LIL dephasing. . . . .	137
4.14	$\epsilon_{xy}$ evolution along the RF gun and the drift space. . . . .	138
4.15	$\sigma_{xy}$ evolution along the RF gun and the drift space. . . . .	139
4.16	Transverse emittance evolution for the TW section at $z = 0.57$ m. . . . .	139
4.17	Magnetic field profile along the beam axis. Thomx nominal configuration, focusing solenoid 23 cm away. . . . .	142
4.18	Distribution of energy of the scattering X-rays as a function of their scat- tering angle for an electron bunch normalized emittance of $1 \mu m$ and an electron bunch relative energy spread of 0.1%. . . . .	144
4.19	Distribution of energy of the scattering X-rays as a function of their scat- tering angle for an electron bunch normalized emittance of $1 \mu m$ and an electron bunch relative energy spread of 1%. . . . .	145
4.20	Distribution of energy of the scattering X-rays as a function of their scat- tering angle for an electron bunch normalized emittance of $10 \mu m$ and an electron bunch relative energy spread of 0.1%. . . . .	145

# List of Tables

1	Tasks shared between LAL and PMB-Alcen. . . . .	4
1.1	Typical orders of magnitude of relative energy spreads and divergences of current electron and laser beams and associated broadening of the Compton energy spectrum [20]. . . . .	12
1.2	Table to test captions and labels . . . . .	15
2.1	Basic electromagnetic quantities scaling with the frequency [26]. . . . .	26
2.2	Characteristics of the Linac RF components. . . . .	37
2.3	Main RF parameters of the ThomX gun. . . . .	41
2.4	Frequency sensitivity with respect to the main parameters. . . . .	56
2.5	Main parameters of 16-cells CI TW copper prototype (HFSS and CST results). . . . .	66
2.6	Main parameters of the CG TW structure (HFSS and CST results). . . . .	75
2.7	Cooling system characteristics of the three accelerating structure types. . . . .	82
2.8	Impingement rate for common gas at room temperature [67]. . . . .	86
3.1	Properties of aluminium and copper used for prototyping. . . . .	94
3.2	Measurement of the electric field amplitude and the phase advance per cell by the nodal shift method, before tuning for $TM_{010-2\pi/3}$ at 2996.8 MHz. . . . .	110
3.3	Measurement of the electric field amplitude and the phase advance per cell by the nodal shift method, after tuning for $TM_{010-2\pi/3}$ at 2997.74 MHz. . . . .	110
4.1	Electron bunch parameters settings in ASTRA. . . . .	125
4.2	Nominal Linac beam dynamics parameters. . . . .	131
4.3	Beam parameters. Total bunch charge: 1 nC. Laser parameters: rms $\sigma_r$ = 1mm, rms $\sigma_t$ = 4ps. . . . .	132
4.4	Percentage of the charge lost for different laser transverse spot size. . . . .	134
4.5	Beam parameters at the exit of the gun for different de-phasing values ( $Q$ = 1 nC, $\sigma_{x,y}$ = 0.6 mm, $\sigma_t$ = 2 ps). . . . .	136
4.6	TW accelerating structure (LIL) parameters. . . . .	137
4.7	Beam dynamics parameters for two different de-phasing values ( $Q$ = 1 nC, $\sigma_{x,y}$ = 0.6 mm, $\sigma_t$ = 2 ps). . . . .	137
4.8	ASTRA parameters of the High-Gradient structure. . . . .	140
4.9	Linac beam parameters at $z = 6$ m. Total bunch charge: 1 nC. Laser parameters: rms $\sigma_{x,y}$ = 0.6 mm, rms $\sigma_t$ = 2 ps, peak magnetic field = 0.28 T. . . . .	140

---

4.10	Linac beam parameters at $z = 6$ m. Total bunch charge: 1 nC. Laser parameters: rms $\sigma_{x,y} = 0.6$ mm, rms $\sigma_t = 2$ ps, peak magnetic field = 0.285 T. . . . .	141
4.11	Linac beam parameters at $z = 6$ m. Total bunch charge: 1 nC. Laser parameters: rms $\sigma_{x,y} = 0.6$ mm, rms $\sigma_t = 2$ ps . . . . .	142
4.12	Linac beam parameters at $z = 6$ m. Total bunch charge: 1 nC. Laser parameters: rms $\sigma_{x,y} = 0.5$ mm, rms $\sigma_t = 2$ ps . . . . .	143

# Introduction

Nowadays, it is commonly accepted that in cultural heritage conservation [1], medicine [2–4], nuclear [5] and particle physics [6–8], synchrotron and Free Electron Laser (FELs) light sources are the only machines in term of brightness able to accomplish the most challenging research experiments in the X-ray energy range (from 10 to 100 keV) [9]. However, these kinds of facilities show many constraints. They are expensive machines with a high-cost maintenance and usually the accesses to the experimental areas are not always easy. In the case of art or biology domains, the transport of the samples is not so much practical and the time dedicated to perform experiments is often limited due to plenty of demands.

On the other hand, even though the conventional X-ray tubes technology is still in progress, the most efficient anode tube is able to provide photon fluxes of around  $10^{10}$  ph/s, at limited, fixed and not tunable energy [9]. These limitations do not allow carrying out a broad class of applications where a high flux of X-rays or/and narrow energy bandwidth are required.

Another way to produce high X and  $\gamma$ -ray fluxes is Inverse Compton Scattering (ICS) [10], where electron bunches interact with laser pulses.

The third-generation synchrotron facilities are usually composed of permanent magnets, such as undulators and wigglers. Those light sources then produce X-rays radiation dependent on the characteristics of these magnetic devices [11]. The important parameters are  $\gamma$  (electron Lorentz factor) and  $\lambda_u$  (spatial period of undulator). The wavelength of X-rays emitted from a magnetic undulator is  $\lambda_u/2\gamma^2$  [12]. The parameter  $\lambda_u$  is typically a few centimeters (i.e 2 cm), so  $\gamma$  needs to be of the order of  $10^4$  to achieve a wavelength of the order of the Angstrom ( $\text{\AA} = 10^{-10}$  m). On the contrary, the radiation that is produced by the ICS process has the wavelength of  $\lambda_l/4\gamma^2$  [13]. As the laser has a wavelength of  $\approx 1 \mu\text{m}$ , one only need  $\gamma \approx 50$  (energy beam around 25 MeV) to obtain a wavelength in the angstrom range. For this reason the electron energy is almost two orders of magnitude lower than at large-scale synchrotron facilities. This allows to scale the machine size down to a few tens of meter squares.

Thanks to the relatively low electron beam energy that is needed to produce X-rays with ICS sources (compared to synchrotron machines), these sources can be compact and therefore installed into lab-scale environments. X-rays experiments should be feasible in locations where otherwise those applications would be done only in university or research centres. For instance, such source could be installed in hospitals to realize high quality imaging on patients, in biomedical laboratory to study proteins that are too fragile to be transported, or in museums to analyse precious art objects that cannot be moved. In this sense, such compact sources will be more available and user-friendly than the large machines [14].

The fruitful improvements in both laser technology and high brightness electron beams in the last decades led the scientific community to consider ICS light sources as one of the most promising technique for high energy X-rays production. However, it is important to notice that these radiation sources are not comparable to the current synchrotron machines and FELs in terms of photons flux and brightness but they offer attractive and complementary capabilities in terms of X-rays energy production with respect to the relatively low energy electron beam that is required [14].

The Thomson scattering X-rays source ThomX is a project conceived with different French partners at the Laboratoire de l'Accelérateur Lineaire (LAL), supported by the French "Agence National de la recherche" as a part of the program "investing in the future" under reference ANR-10-EQPX-51 and the grants from the Ile-d-France region.

The sketch of an Inverse Compton Scattering machine with storage ring is shown in Fig.1. Basically, it consists on an electron gun, an accelerating section, a transfer line and a storage ring where, at the interaction point (IP), an intense laser pulse interacts with the injected electron bunch to produce X-rays. The ThomX layout and its components rely on the preeminent expertise that LAL has achieved in the efficiency of laser pulse amplification in optical cavities (see for instance the MightyLaser project [15]). The optical cavity (Fabry-Perrot) is at the state-of-the-art of the technology for this type of devices. Furthermore, the LAL has acquired valuable experience in design, manufacturing and testing of radio-frequency (RF) electron gun for high-brightness (peak brightness of the order of  $10^{12}$  A/m<sup>2</sup>rad<sup>2</sup>) photo-injector. In particular, LAL took advantage to the fabrication of photo-injectors, such as the drive and the probe beam injector RF guns for the Compact Linear Collider (CLIC) Test Facility 3 (CTF3) at CERN [16]. Nowadays, the ThomX accelerator is coming into the installation phase and the commissioning is foreseen in the Orsay scientific campus in 2018 [17].

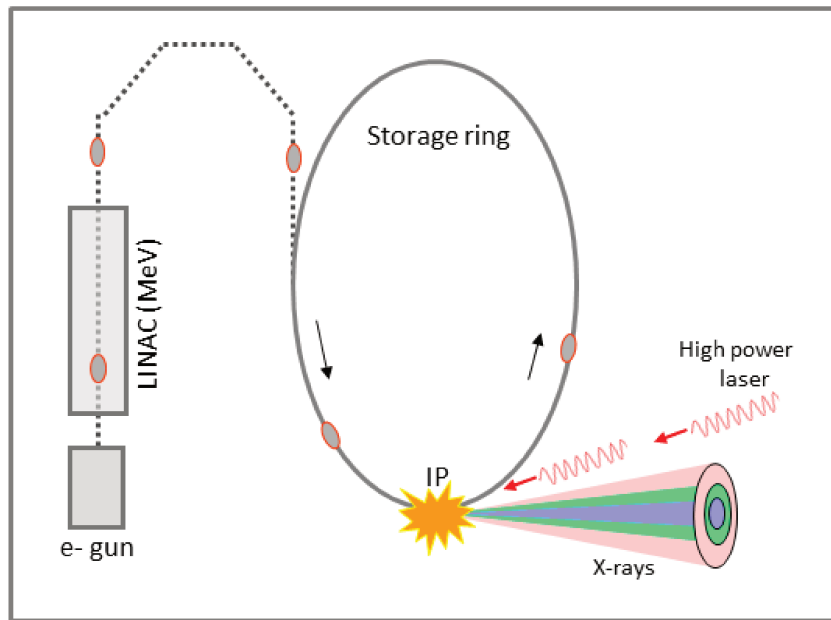


FIGURE 1: Sketch of an Inverse Compton Scattering machine with storage ring.

## Scope of the thesis

This thesis is devoted to the linear accelerator (LINAC) of the ThomX source.

ThomX exhibits several challenges in many aspects especially because the storage ring is not conventional in terms of design and beam dynamics. In fact, the small energy (a few tens of MeV) entails a short "storage time" of the electron bunch circulating in the ring. Then, the time that the electron bunch is stored in the ring the synchrotron damping is negligible. These non-typical characteristics make properties of the electron beam at the exit of the linac crucial for the subsequent performance of the beam at the interaction point. The latter determines the ultimate properties of the X-rays generated by the ICS source. For these reasons, the photo-injector scheme has been thoroughly analysed and different technical solutions for emittance and energy spread minimisation have been considered and proposed with respect to the original scheme.

Another important part is the beam dynamics study of particles that travel along the whole ThomX linac. In particular, the properties of the laser shape that impinges the cathode, the characteristics of the bunch in the photo-injector and its evolution along the travelling wave section with acceleration have been analysed.

One of the most important part is the linear accelerator upgrade to increase energy of the electrons while maintaining the compactness and the beam characteristics at ring

injection. It implies a research and development (R&D) activity at LAL in partnership with a French company (PMB-Alcen) in the High-Gradient (HG) technology of accelerating structures. The LAL - PMB-Alcen collaboration aims at the fabrication of a normal-conducting high-gradient S-band structure by tackling the technological aspects that limit the achievement of high-gradient acceleration mostly due to vacuum RF breakdown and pulsed heating fatigue. Table 1 resumes the different tasks and responsibilities that LAL and PMB-Alcen share in the framework of this collaboration. Basically the electromagnetic and thermal design of the high-gradient S-band accelerating section have been performed at LAL by means of simulation softwares such as, ANSYS HFSS (High-Frequency Electromagnetic Solver), CST MWS (Computer Simulation Technology, Microwave Studio) and ANSYS Computational Fluid Dynamics tool (CFD, Fluent). According to the simulation design performed at LAL, PMB-Alcen made the mechanical drawings of the regular accelerating cells and couplers. The next step was the fabrication of the aluminium S-band prototypes with a reduced number of cells. This step foresees the RF low power tests for checking the geometry and the mechanical tolerances. Once the fabrication process will be validated, copper prototypes with a reduced number of cells will be fabricated. After, these prototypes will be high-power tested for checking the machining precision in term of tolerances and material surface finishing in view of the realisation of the final 3.2-m long High-Gradient copper accelerating section. The collaboration agreement has to last four years (from October, the 1st, 2014 to September, 30th, 2018).

TABLE 1: Tasks shared between LAL and PMB-Alcen.

LAL	PMB - Alcen
Electromagnetic study, thermal analysis.	Mechanical drawings (RF design proposed by LAL).
RF design & mechanical drawings check out.	Fabrication of aluminium prototypes for geometry validation.
Follow up of prototypes & final structure realisation at PMB-Alcen.	Fabrication of copper prototypes for validation of standard & improved manufacturing procedure.
High power RF tests of prototypes.	Low power RF tests of prototypes.
Conditioning process of the final accelerating section.	Final accelerating section fabrication (adjustments, recovery, tests, brazing, surface treatments).
High-gradient structure installation & Commissioning in ThomX.	Checking and testing.

This doctoral dissertation emphasises the technical aspects of the ThomX Linac main components, namely the RF gun, the solenoids and the accelerating section. It is composed of five chapters.

In Chapter 1 an introduction to the Inverse Compton or Thomson light sources is presented. The main factors that made effective the X-rays production by the interaction between electron beam and laser pulses as well as the advantages and drawbacks of the principle are described. Then, the only machine in the World, the MuCLS source, capable providing a flux comparable to that delivered by first generation synchrotron sources is presented. This machine is in operation at the Technical University of Munich. Its layout and X-rays characteristics are reported for sake of comparison with the expected ThomX properties and potentialities. An overview of the ThomX project, including the layout of the accelerator is discussed. Finally, a brief overview of the possible applications is presented.

Chapter 2 focuses on the Linac RF main components. First, some basics of the RF electromagnetic waves in single-cell cavity, the main figures of merit as well as particle acceleration in periodic structures are presented. Second, the limiting quantities to the achievement of an high-gradient acceleration in periodic structures are described. Third, the design of the ThomX linac RF parts are presented. In particular, the thermal-structural analysis of the RF gun, which has been developed at LAL for the ThomX photo-injector, is detailed. Then, the electromagnetic (EM) and mechanical design of the prototypes and the EM design of the final high-gradient accelerating section are reported. Finally, the thermal studies of the cooling system on prototypes and the estimation of the vacuum performance of the prototypes and the final accelerating section have been carried out in order to verify if the structure can sustain the high dissipated power as well as the ultra-high-vacuum regime (UHV) required for this type of application.

Chapter 3 deals with the manufacturing procedure for the ThomX RF gun and the accelerating section prototypes with a reduced number of cells and, in particular, the mechanical solutions for the fabrication of the components. After their fabrication, the components have to be tuned to the right phase advance per cell. Therefore, the tuning procedure and measurement set-up are presented with the low power tests results that have been performed at LAL and PMB-Alcen. Finally, the fabrication issues are mentioned as well.

Chapter 4 deals with the beam dynamics simulations of the electron bunch along the linac beam line. The bunch is generated from the cathode and undergoes electric and magnetic external fields to be matched, at the end of the linac, to the transfer line for the subsequent injection into the ring. To this purpose, different possible operation parameters are proposed to accomplish the ThomX Technical Design Report electron beam specifications at the exit of the Linac. The impact of the electron bunch characteristics on the X-ray beam quality is briefly exposed at the end of this chapter.

Chapter 5 deals with the main achievements that are presented in this dissertation, the conclusions, perspectives and future works concerning all these activities.

# Chapter 1

## Inverse Compton Scattering X light sources

This chapter aims at the physics of the Inverse Compton Scattering interaction between laser pulses and electron beams as well as the definitions of the main quantities that characterise the quality of the X-rays source, such as flux and brightness. Also, the description of the Munich compact light source currently in operation is presented as an example of an ICS source equipped with a storage ring. Finally, the layout of the ThomX machine is described with a brief overview of its possible applications.

### 1.1 Physics of Inverse Compton Scattering

#### 1.1.1 Kinematics

In general, the Compton effect refers to the collision between photons and atomic electrons. This kind of interaction mostly concerns the electrons of the outer shells that are less bounded to the atom. For those electrons we assume that the bonding energy is negligible with respect to the incident photon energy. After collision, the atomic electron is going to be expelled from the atom and the photon is scattered to a different angle with respect to the incident one. The final energy of the photon is less than the initial one because part of that has been transferred to the electron through the collision. If we assume that the electron is at rest while the photon has an initial momentum, in the laboratory frame, after collision both are scattered to precise different angles. Since the energy and the momentum are conserved, the relation between the initial energy ( $\hbar\omega_i$ ),

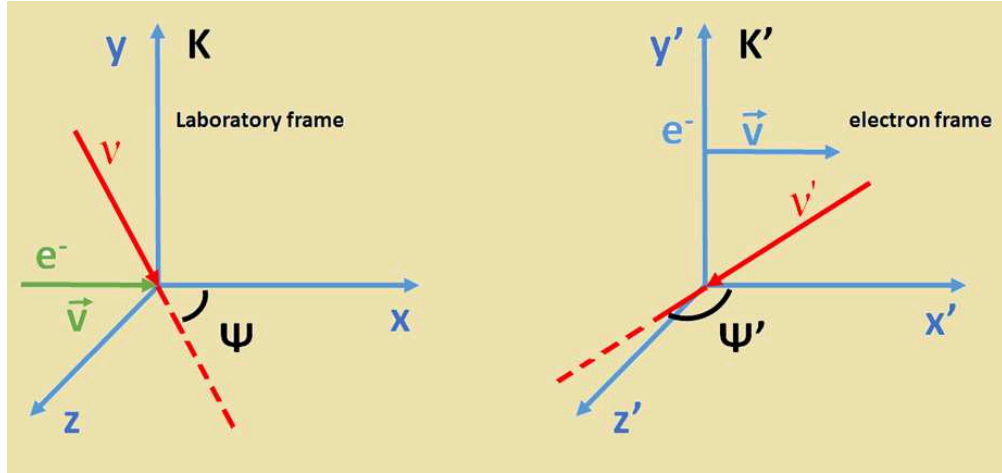


FIGURE 1.1: An electron is moving with velocity  $v$  parallel to the x-axis. It makes an angle  $\Phi$  with an incoming photon of frequency  $\nu$  (left). In the electron frame, the photon is incoming with a different frequency  $\nu'$  making an angle  $\Phi'$  with the velocity vector (right).

the final energy ( $\hbar\omega_f$ ) and the photon scattered angle ( $\varphi$ ) is

$$\hbar\omega_f = \frac{\hbar\omega_i}{1 + \frac{\hbar\omega_i}{m_0c^2}(1 - \cos\varphi)} \quad (1.1)$$

where  $m_0$  is the rest mass of the electron and  $c$  is the speed of light.

Inverse Compton Scattering (ICS) involves the scattering of low energy photons by ultra-relativistic electrons (no longer at rest) so that photons gain and electrons lose energy. The process is called "inverse" because, in this case, electrons lose energy rather than photons resulting in opposite mechanism of the standard Compton scattering.

Figure 1.1 shows a photon with frequency  $\nu_i$  that propagates with an incidence angle  $\psi$  with respect to the x-axis in the laboratory frame of reference,  $K$ . In a frame of reference  $K'$  that moves along the x-axis with velocity  $\vec{\beta}c$ , the frequency and the incidence angle can be calculated according to the relativistic Doppler effect [18]:

$$\omega'_i = \gamma\omega_i(1 - \beta \cos\psi) \quad (1.2)$$

$$k'_x = \frac{\omega'_i}{c} \cos\psi' = \gamma \frac{\omega_i}{c} (\cos\psi - \beta) \quad (1.3)$$

$$k'_y = \frac{\omega'_i}{c} \sin\psi' = \frac{\omega_i}{c} \sin\psi \quad (1.4)$$

The transformation of the formula 1.2 with respect to the photon incidence angle in  $K'$  leads to:

$$\omega'_i = \frac{\omega_i}{\gamma(1 + \beta \cos\psi')} \quad (1.5)$$

Now, let consider  $K'$  a frame of reference co-moving with the electron. The energy of

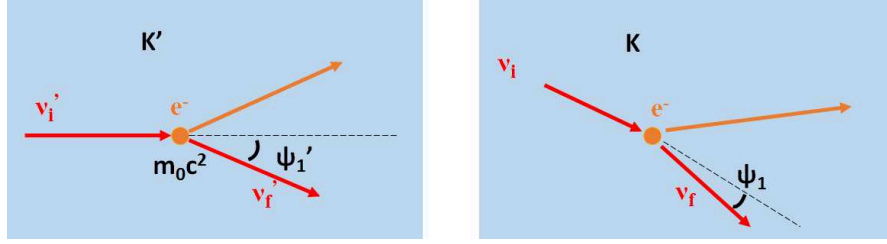


FIGURE 1.2: In the electron frame of reference, the photon is scattered with an angle  $\psi_1'$  according to the conservation of energy and momentum (left). In the frame of reference  $K$  the scattering angle is  $\psi_1$  (right).

the scattered photon is like the formula 1.1. If the photon energy is  $\hbar\omega_i' \ll m_0c^2$ , the scattered energy is conserved after collision, then interaction between the photon and the electron can be considered in the Thomson regime. The scattered photon has the same energy as before the scattering, independent of the scattering angle, namely:

$$\hbar\omega_f' = \hbar\omega_i' \quad (1.6)$$

The photon is scattered at an angle  $\psi_1'$  with respect to the electron velocity. In  $K$  the frequency of the scattered photon becomes (Fig. 1.2):

$$\omega_f = \gamma\omega_f'(1 + \beta \cos \psi_1') \quad (1.7)$$

Rewriting the formula with respect to the photon incidence angle  $\psi$  and the observation angle  $\psi_1$ , eq.1.7 becomes

$$\omega_f = \omega_i \frac{1 - \beta \cos \psi}{1 - \beta \cos \psi_1} \quad (1.8)$$

From the Eq.1.8 it is easy to see that scattered photon energies in the laboratory frame of reference depend on both the incidence angle  $\psi$  and the observation angle  $\psi_1$ . For small observation angles ( $\psi_1 \ll 1$ ) and ultra-relativistic electrons ( $\gamma \gg 1$  and  $\beta \sim 1$ ), the formula becomes:

$$\omega_f = \omega_i \frac{2\gamma^2(1 - \cos \psi)}{1 + \gamma^2\psi_1^2} \quad (1.9)$$

When the photon and the electron interact with  $\psi = \pi$  (head-on collision) the expression becomes:

$$\omega_f = \omega_i \frac{4\gamma^2}{1 + \gamma^2\psi_1^2} \quad (1.10)$$

For example, in the ideal case when an electron with an energy of 50 MeV ( $\gamma \simeq 98$ ) interacts with a photon laser wavelength  $\lambda = 1034$  nm, the scattered X-ray energy as a function of the observation angle is plotted in Fig.1.3.

The maximum energy of scattered photons occurs when  $\psi_1 = 0$  and such photons (called on-axis photons) are scattered along the electron velocity vector. From eq.1.10 we obtain

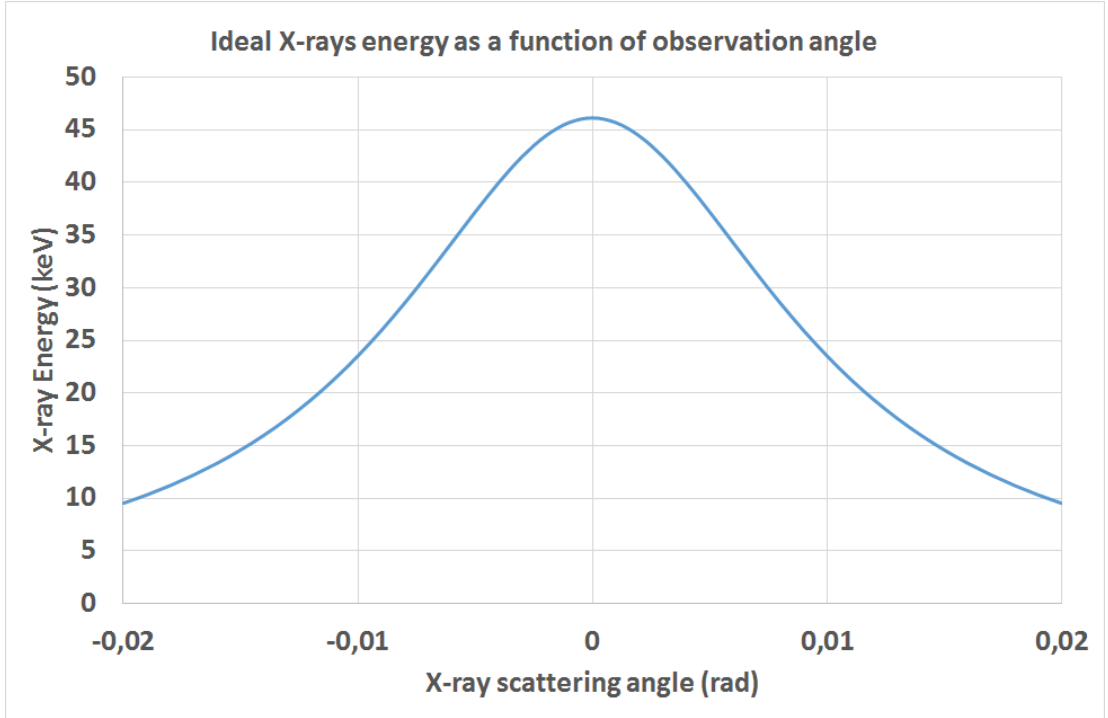


FIGURE 1.3: X-rays energy of scattered photons coming from the interaction of the ideal electron and laser beams (i.e. with no emittance and no energy spread)

the Compton edge energy  $\hbar\omega_f^{max}$  in case of head-on collisions:

$$\hbar\omega_f^{max} = 4\gamma^2\hbar\omega_i \quad (1.11)$$

Equation 1.11 shows that the dependency of the on-axis X-rays energy with the incident photon ( $\hbar\omega_i$ ) and with the electron beam energy ( $\gamma$ ) gives several options for creating an energy tunable source. Indeed, ICS sources allow to vary the produced on-axis X-rays energy over a broad range depending on the electron beam energy. For instance, an accelerator which delivers electrons with an energy between 50 and 70 MeV should cover the Compton edge between 45 and 90 keV, assuming 1030-nm wavelength incoming laser. At higher energy, the European Extreme Light Infrastructure (ELI-NP-GBS) project has been conceived to produce photons in the 1-20 MeV energy range coming out from the interaction between electron bunches with 200-720 MeV energy and laser pulses with 2.4 eV energy (wavelength = 515 nm).

### 1.1.2 Flux

The Compton scattering cross section is given by the Thomson cross section:  $\sigma_{Th} = 6.65 \times 10^{-29} m^2$ . The absolute value of the Thomson cross section can be interpreted as the probability that one photon travelling one meter within a target whose density

is one electron per one cubic meter has to be scattered. That scattering probability is extremely low regarding to the applications which aim at producing high flux light sources (i.e. of the order of magnitude of  $10^{11} - 10^{13}$  ph/s). Compton X-ray sources involve multi-collisions between a laser pulse and an electron bunch. Thus, to establish the total X-ray flux, we need to take into account the laser pulse and the electron bunch characteristics. The number of scattered photons is given by the product of the luminosity of the interaction by the cross section. Assuming that the electron bunch and the laser pulse sizes have Gaussian distributions in the three dimensions and that horizontal and vertical dimensions are equal, for electron-photon collisions taking place with a crossing angle equal to zero, the number of X-rays emitted per second is:

$$N_X = \sigma_{Th} \frac{N_e N_\nu f_{rep}}{2\pi(x_e^2 + x_\nu^2)} \quad (1.12)$$

where  $N_e$  is the number of electrons per bunch,  $N_\nu$  is the number of photons per laser pulse,  $f_{rep}$  is the repetition frequency of the collisions,  $x_e$  and  $x_\nu$  are the rms transverse sizes of the electron bunch and laser pulse at the interaction point.

Because of the low scattering Compton cross section  $\sigma_{Th}$ , a small fraction of electrons and photons interacts, leading to a limited photon flux production. To cope with this limitation, several technological solutions can be considered, such as increase the laser power and the electron current, decrease the electron beam and the laser sizes and increase the electron-laser collision rate.

With the progress of lasers, optical cavities and accelerators, it is now possible to produce X-ray fluxes greater than  $10^{12}$  ph/s, provided that the repetition frequency  $f_{rep}$  is sufficiently high, i.e. in the 10 - 100 MHz range. Let us give orders of magnitude:  $10^{13}$  ph/s are obtained for  $f_{rep} = 20$  MHz, an electron bunch of 1 nC, a photon pulse of 10 mJ and a transverse size of the electron bunch and photon pulse at the interaction point of the order of 40  $\mu\text{m}$ .

To obtain such fluxes, a laser beam with an average power between 100 kW and 1 MW [19] is required. This requirement is still a technology challenge. The most promising results came out from the amplification of laser pulses by an optical cavity, as a Fabry-Perot cavity (FPC) with a very high finesse. In 2011, a FPC equipped with four-mirrors was installed in the ATF storage ring at KEK in Japan and 100 kW laser average power was achieved. These experimental results demonstrated also the capability of a FPC working in an accelerator environment to produce high Compton photon fluxes [19].

To achieve high fluxes, the production of high electron bunch charges is also required and, for this, a good photo-injector and especially good photo-cathode efficiency and

RF gun performances are crucial. Typically, current photo-injectors allow to produce 1 nC charge electron bunches of 50  $\mu\text{m}$  transverse size ( $x_e$ ) and reasonable divergence.

Finally, to achieve a high repetition frequency  $f_{rep}$  there are mainly two different machine schemes: the storage ring scheme and the superconducting linear accelerator scheme. In the latter the electron gun injection frequency is necessarily high ( $\sim 10 - 100$  MHz). In the storage ring scheme, the high repetition frequency of the photon - electron collision is due to the electron bunch revolution frequency in the ring. The ThomX machine is conceived with the latter scheme.

Taking into account the available present technologies, the value of the electron beam intensity necessary to achieve a flux of  $10^{11}$ - $10^{13}$  ph/s imposes the use of a storage ring.

### 1.1.3 Brightness

Equation 1.9 holds to the extent that the X-ray energy spectrum is strictly monochromatic at a given emission angle. It should be the case if the spectrum was produced by electrons and photons whose energies are single-valued. But the energy dispersion and the angular divergence of the stored electrons and photons lead to a significant broadening of the X-ray energy ( $\hbar\omega_f$ ) at a given observation angle ( $\psi_1$ ). The relative rms energy spreads of an electron bunch and a laser pulse are denoted by  $\sigma_e$  and  $\sigma_\nu$  respectively, while their rms angular divergences are denoted by  $\sigma'_e$  and  $\sigma'_\nu$  (with equal horizontal and vertical divergences). By replacing in eq.1.9 the subscriptions  $\gamma$ ,  $\hbar\omega_\nu$ ,  $\psi_1$  and  $\psi$  by  $\gamma(1 + \sigma_e)$ ,  $\hbar\omega_\nu(1 + \sigma_\nu)$ ,  $\sigma'_e$  and  $(\psi + \sigma'_\nu)$  respectively and by performing four first order Taylor expansions in  $\sigma_e$ ,  $\sigma_\nu$ ,  $\sigma'_e$  and  $\sigma'_\nu$  respectively, the order of magnitude of the broadening  $\Delta\hbar\omega_f/\hbar\omega_f$  of the on-axis Compton spectrum due to each one of these four parameters can be estimated [20]. The results are summarised in Tab.1.1.

Variables	Typical current values	$\Delta\hbar\omega_f/\hbar\omega_f$
$\sigma_e$	$10^{-3}$ - $10^{-2}$	$2\sigma_e$
$\sigma_\nu$	$10^{-5}$ - $10^{-3}$	$\sigma_\nu$
$\gamma\sigma'_e$ (rad)	0.01-0.25	$\gamma^2\sigma_e'^2$
$\sigma'_\nu$ (rad)	1-10	$\frac{(\sigma'_\nu \cos \psi)/2 + \sigma'_\nu \sin \psi}{(1 - \cos \psi)}$

TABLE 1.1: Typical orders of magnitude of relative energy spreads and divergences of current electron and laser beams and associated broadening of the Compton energy spectrum [20].

The average brightness is one of the most relevant parameter for a light source since it quantifies the intensity of the beam by taking into account its spectral purity. Brightness is defined as the number of photons emitted per second, per unit of solid angle, per  $mm^2$

of source area, and in 0.1% spectral bandwidth. The units in which it is usually expressed is  $ph/s/mm^2/mrad^2/0.1\%bw$ . At present, the performances of current laser systems and electron accelerators (see Tab.1.1) are such that the main impact on Compton source features comes out from the electron beam angular divergence  $\sigma'_e$ . Taking into account for the spectral bandwidth only the term coming from the electron beam divergence and assuming that the divergence of the Compton beam  $x'_X$  is equal to the divergence of the electron beam (which is a very good approximation), the average on-axis brightness can be written as [21]:

$$\langle Br \rangle = \frac{N_X \cdot 0.1\% F_{tot}}{(2\pi)^2 (x_X^2 x_X'^2)} = \frac{N_X \cdot 0.1\% F_{tot}}{(2\pi)^2} \left( \frac{x_e^2 + x_\nu^2}{x_\nu^2} \right) \left( \frac{\gamma}{\epsilon_n} \right)^2 \quad (1.13)$$

where  $N_X \cdot 0.1\%$  is the fraction of X-rays emitted within 0.1% bandwidth around the on-axis energy,  $\epsilon_n = \gamma x_e \sigma'_e$  is the normalised transverse emittance of the electron beam and  $x_X$  is the transverse size of the source at the interaction point. To obtain the right-hand term in eq.1.13, the transverse size of the source at the interaction point was written as a combination between the laser and the electron beam transverse sizes:  $x_X^2 \sim (x_e x_\nu)^2 / (x_e^2 + x_\nu^2)$ . Therefore, for a given flux, the previous equation shows that small electron beam emittance is an essential condition for having a high brightness.

## 1.2 The Munich Compact Light Source

Nowadays, only one ICS X-ray source is able to produce a total X-ray flux higher than  $\sim 10^{10}$  ph/s. This machine, based on the storage ring scheme, was designed and manufactured by Lyncean Technologies Inc. The latter was founded in 2001 to develop compact light source accelerators based on research performed at the SLAC National Accelerator Laboratory and Stanford University. The Lyncean source, in operation since 2008, was firstly located in Fremont, California [23] and was sold in 2015 at the Technische Universität München, in Germany. At this ICS source, called now The Munich Compact Light Source (MuCLS), the X-ray beam available for experiments is about  $10^9$  ph/s in 3% of energy bandwidth.

### 1.2.1 Layout of the machine

A frequency-quadrupled Nd:YLF laser pulse (wavelength of 262 nm, 25 Hz repetition rate, energy  $\sim 120$   $\mu$ J/pulse) illuminates a copper photo-cathode that emits an electron bunch with a charge of 200 pC. Then, the bunch is accelerated to relativistic energy (range from 25 to 45 MeV) in a linear accelerating section. After, the bunch is injected, by a kicker magnet, into a small storage ring with a circumference of 4.6 m. As we can see from the Fig.1.4, the linear accelerator is followed by a vertical transfer line, hence the storage ring is raised from the ground. After 40 ms (2.6 million turns), the bunch is discarded and a new "fresh" bunch is re-injected in the ring. At the same time, two



FIGURE 1.4: Photograph of MuCLS [22].

Nd:YAG laser pulses (wavelength of 1064 nm) are stored in a high-finesse optical cavity (power  $\sim 70$  kW), since the equivalent optic length is around double of the storage ring ( $\sim 9.2$  m). The electron bunch and the laser pulses are tightly focused at the interaction point and interact in order to produce X-rays at each revolution (64.91 MHz repetition rate). Because of the mechanical structure of the machine, the angular aperture of the Compton cone available for X-ray experiments is 4 mrad [22].

### 1.2.2 X-rays characteristics

A team of researchers from the Technical University Munich reported an independent analysis of the MuCLS performances in September 2016 [22]. The report has benchmarked the operation of the source since April 2015.

The characteristics of the X-rays emission cone has been determined with a detector placed on-axis at 16.61 meters far from the Thomson interaction point. The transverse shape of the emission cone is almost flat and circular in both directions (x and y) in the 4 mrad cone. As it has been mentioned in section 1.1.1, the energy of the emitted photons decreases progressively while increasing the observation angle. The X-ray spectrum has been measured for three different electron energies, leading to on-axis X-ray energies equal to 15 keV, 25 keV and 35 keV, respectively. The corresponding bandwidth has been measured to be  $\sim 3\%$ ,  $3.6\%$  and  $4.3\%$  respectively, while the FWHM are 0.4 keV, 0.9 keV and 1.5 keV respectively. The mean value of the total flux in the 4 mrad cone is around  $1 \times 10^{10}$  ph/s with an r.m.s standard deviation less than 5% (3 hours acquisition time, 1 Hz). The transverse source size measured at the IP is  $42 \mu\text{m}$  in both directions with a standard deviation of 2% maximum. They also observed a movement of the source in both x and y directions, with a standard deviation less than  $4 \mu\text{m}$ . The main characteristics of the measured MuCLS beam are resumed in the following table [22]:

Parameters	Values
Repetition rate	64.91 MHz
Imposed cone angle	4 mrad
Source size	$41.5 \times 42.5 \mu\text{m}^2$
Energy range	15 / 35 keV
Average flux	$0.97 \times 10^{10}$ ph/s
r.m.s flux standard deviation	$< 5 \%$

TABLE 1.2: Table to test captions and labels

The measured performances prove that the MuCLS source is able to produce stable flux over several hours with a small variation in beam position.

## 1.3 ThomX project

ThomX is a compact ICS based X-rays source hosting in the scientific university campus of Paris-Saclay (Orsay, France). The commissioning of the machine is expected to begin in the middle of 2018. First X-ray experiment are expected in 2019. The ThomX project has received funding (10 Meuros) from the French "Agence Nationale de la Recherche" (ANR) as part of the program "investing in the future" under reference ANR-10-EQPX-51 and has also been supported by grants from Ile-de-France region. The goal is to design and build a compact demonstrator able to produce a flux of  $10^{11}$ - $10^{13}$  ph/s in the hard X-ray range (45 - 90 keV).

### 1.3.1 Layout of the machine

The layout of the ThomX machine is shown in Fig.1.5. An electron bunch with an energy of a few eV is first photo-emitted by the impact of a laser pulse on a magnesium cathode. In order to maximize the X-ray flux, the charge of the bunch can reach 1 nC. Then, after a section dedicated to bunch diagnostics (Diag1), the bunch propagates in a linear accelerator which carries its energy at 50-70 MeV. A quadrupole triplet allows for the three-gradients measurement [24] in the straight line that ends up with a diagnostic chamber (Diag2) and a dump. A transfer line ensures the bunch transport from the linac exit to a small storage ring of around 18 m in circumference (corresponding to a revolution frequency of 16.6 MHz). This transfer line consists of four 45 degrees dipoles for steering the beam, four quadrupoles and two chambers for energy spread measurements and beam characterisation (Diag3 and Diag4) before the injection in the ring. A septum and a fast kicker are used to inject the bunch in the ring. The ring optics is designed such as, at the interaction point (IP), the transverse size of the electron bunch is around 50-100  $\mu\text{m}$  and its transverse normalized emittance 5-7  $\mu\text{m}$  rad. The low electron bunch energy leads to gradually increasing the emittance (around 20  $\mu\text{m}$  rad after 20 ms) and the energy spread due to collective effects and Compton back-scattering (CBS) phenomena. Hence, a new bunch is re-injected every 20 ms. Another kicker is inserted to perform a fast bunch extraction. Once extracted, the beam is transported towards a dedicated beam dump.

Concerning the laser system, intense laser pulses are created from a low average power pulsed laser which are firstly amplified by an optical fiber system and then sent at a frequency twice than the storage ring ( $\sim 35.6$  MHz) in a high gain four-mirrors passive Fabry-Perot optical cavity for a second amplification stage. When the system is locked, we expect to stored 0.1-1 MW inside the cavity.

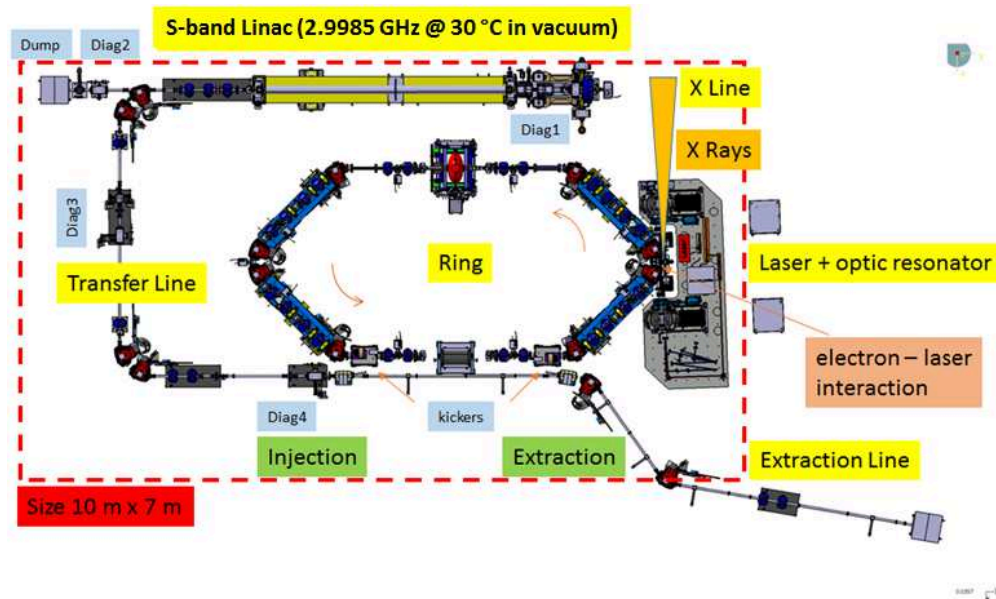


FIGURE 1.5: Layout of the ThomX machine.

In a stable condition, every turn the electron bunch interacts with a laser pulse stored in the optical cavity. The collision angle is two degrees which allows the X-ray photons to be extracted without deteriorating the very high reflectivity of the cavity mirrors. Since the Fabry-Perot cavity operating frequency is an harmonic 2 of that of the storage ring, two-bunches operation mode is even possible [17].

With this design and beam parameters,  $10^{11}$ - $10^{13}$  ph/s of 45 to 90 keV on-axis energy are expected.

### 1.3.2 Possible applications

The ThomX ICS source should provide a sufficient spectral brightness to efficiently perform some diffraction and fluorescence analysis techniques routinely performed by synchrotron facilities using X-rays in the range 45-90 keV. Moreover, the high energy available is a great advantage since the energy of the X-photons can achieve the excitation energy of most chemical elements that are usually used in material science, for instance, the critical K-edge energy excitation of lead (heavy element, 88 keV energy).

In the medical domain, in particular for radiotherapy, the total number of photons available in a given solid angle is the most crucial parameter since there is no need spectral purity in such protocol. Previous clinical trials already realized at ESRF give precious insights and benchmarks for the potential use of ThomX in radiotherapy and show that for some techniques, the ThomX flux should be comparable to that used for medical research and applications at synchrotron sources. For example, considering a 67

---

MeV electron energy beam, the flux available at 80 keV in 10% of energy bandwidth from the ThomX machine should be comparable with that currently used in the Stereotactic Radiation Therapy (SSRT) clinical trials realised at the European synchrotron source (ESRF) [21].

## Chapter 2

# Design of High-Gradient S-band Electron Linac for ThomX

RF linear accelerators usually operate in the frequency range from 100 MHz up to several GHz. They produce intense beams of very good quality and are applied to scientific research (elementary particle physics), as well as industry or medicine. They can be used at low energies as injectors into synchrotrons (typically several tens or hundreds of MeV), or at high energies, e.g. as colliders, accelerating electrons and positrons to 50 GeV, as at the Stanford Linear Accelerator Center (SLAC).

Basically, the linear particle accelerator (linac) is a device where the electric field is used to raise the energy of particles that pass through it along the straight line.

To increase the velocity of the particle the traditional linear accelerators use electrostatic or electromagnetic radio-frequency fields (RF). In the case of electrostatic acceleration, particles increase their energy by the effect of a static high-voltage electric field within a high-vacuum structure. The generation of high voltage is a technical challenge and is restricted by the ability to sustain high electric voltage without electric breakdown in the structure. Usually the maximum voltage this kind of machine can achieve is a few millions of volts.

On the other hand, in radio-frequency fields linear accelerators, electromagnetic waves are established and stored in an array of cavities (or cells). The particles experience the interaction with such a kind of waves and increase their energy as long as the synchronicity condition with the alternating fields is fulfilled.

Using radio-frequency fields, the structure can sustain much higher electric fields without any electric breakdowns compared with static voltage values. RF electric breakdown is probably the most serious physical phenomenon occurring in high-gradient accelerating

structure during operation and is therefore the main limitation to the maximum gradient that can be achieved in the structures. For this reason, high-gradient technology is then essential for either reducing machine dimensions or increase the energy gain of particles. For instance, for achieving 1 TeV electron beam energy with an accelerating gradient equal to the standard 3m-long SLAC structure (20 MV/m, 35 MW input power), one needs at least a linear collider of 50 km. To maintain the length of each linac to reasonable length, namely 5 km, one needs an effective average accelerating gradient 5 times higher, i.e. 100 MV/m. This value is currently considered as one of the main goal for most of the ongoing or future linear collider projects [25]. The performance of the acceleration is evaluated by a common parameter, the breakdown rate (BDR), which is defined as the number of vacuum arcs that occurs over the total number of pulses, per unit length (bpp/m).

The chapter deals with the basic concepts and main parameters of RF linear accelerators, the performance limitations, design and characteristics of the high-gradient S-band accelerating section used for ThomX Linac.

## 2.1 RF cavity fundamentals

The radio frequency (RF) based technology has become an essential part of modern high energy accelerators. An accelerating RF cavity stores electromagnetic energy and delivers it to the charged particles in the form of kick in the direction of motion and hence increase the kinetic energy of particles. This section provides an overview of electromagnetic description of cavity and its performance parameters such as quality factor, accelerating gradient, shunt impedance, etc.

### 2.1.1 Electromagnetic modes in RF cavities

An electromagnetic wave can impart a continuous energy gain to a moving charged particle, if two conditions are satisfied: (1) the wave must have an electric field component along the direction of particle motion, (2) the particle and the wave must have the same velocity to maintain synchronism.

The modes are classified as  $TE_{mnp}$  and  $TM_{mnp}$ : transverse electric modes  $TE_{mnp}$  “ $H_{mnp}$  mode” have no electric field ( $E_z = 0$ ) in the direction of propagation ( $z$  direction: beam axis) and non-vanishing longitudinal magnetic field component ( $H_z \neq 0$ ), while transverse magnetic modes  $TM_{mnp}$  “ $E_{mnp}$  modes” have no magnetic field ( $H_z = 0$ ) in the direction of propagation and non-vanishing longitudinal electric field component

( $E_z \neq 0$ ). In cylindrical coordinates the index  $m$  is the number of full-period variations of field components in the azimuthal direction ( $\varphi$ ),  $n$  is the number of zero-crossings of longitudinal field components in the radial direction ( $r$ ), and  $p$  is the number of half-period variations of field components in the longitudinal direction ( $z$ ). Hence, only  $TM$  modes can be useful for acceleration.

The selection of the appropriate mode gives a more efficient use of the field for acceleration.  $TM_{010}$  mode is the most useful mode for particle acceleration. Its longitudinal electric field is uniform along the propagation direction of the beam and its magnitude is maximum on-axis. The  $TM_{010}$  is the lowest frequency mode, all other modes are "parasitic" as they may cause various unwanted effects. Those modes are referred to as Higher-Order Modes (HOMs).

The simplest case of a resonating cavity is the so-called pill-box cavity, which is nothing else than an empty cylinder with a conducting surface. The simplest mode in this cavity is the so-called  $TM_{010}$  mode. It has a magnetic field  $H_\varphi$  concentrated at the cylindrical wall, responsible for RF losses and a longitudinal electric field  $E_z$  concentrated near the beam axis, responsible for beam acceleration.

The expressions of the field components of the mode  $TM_{010}$  in a pill-box cavity are:

$$E_r = 0 \quad (2.1)$$

$$E_z = E_0 J_0(k_r r) \cos(\omega t) \quad (2.2)$$

$$H_\varphi = -\frac{E_0}{Z_0} J_1(k_r r) \sin(\omega t) \quad (2.3)$$

where  $E_0$  is the amplitude of the electric field,  $J_0$  and  $J_1$  are Bessel functions of the first kind of zeroth and first order,  $\omega = 2\pi f$  is the angular frequency, and  $Z_0$  is the wave-impedance in free space. Since there is no field dependency on  $z$  and  $\varphi$ , the angular frequency of the pill-box cavity is only determined by its radius  $R_{cav}$  and can be written as:

$$\omega_0 = k_r c = \frac{2.405}{R_{cav}} c \quad (2.4)$$

The electric and magnetic field pattern of the  $TM_{010}$  mode can be seen in Fig. 2.1.

In general, a cavity can be constructed as a periodic array of cells by coupling several of these single cells together into a single structure using a single RF feed.

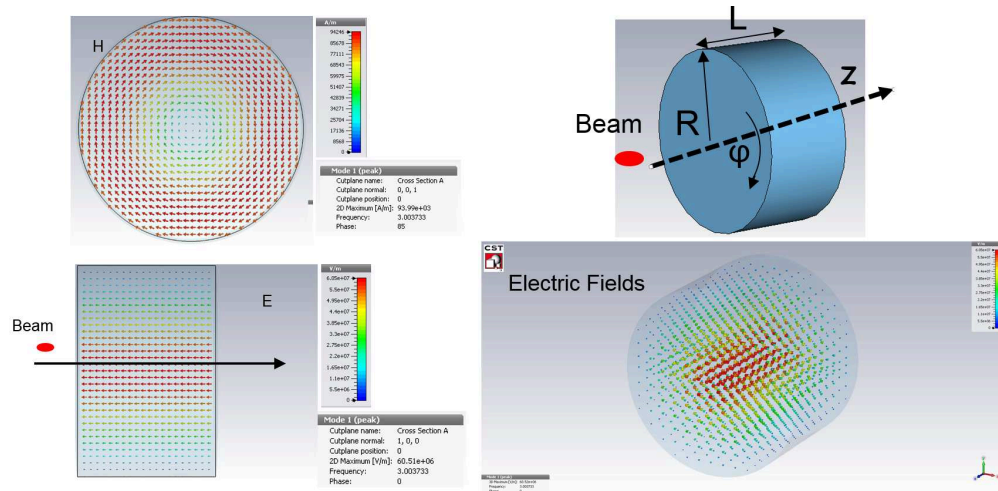


FIGURE 2.1: Electric and magnetic fields of the fundamental mode  $TM_{010}$  in a pill-box cavity.

### 2.1.2 Particle acceleration in a single RF cell "pill-box cavity"

Charged particles that traverse an RF accelerating gap, such as a pill-box cavity in  $TM_{010}$  mode (as shown in Fig.2.2) experience an electric field of the form given by:

$$E_z(z, t) = E_a(z) \cos(\omega t(z) + \phi) \quad (2.5)$$

where  $E_a$  is the accelerating field on-axis,  $\omega$  is the angular frequency and  $\phi$  is the phase of the RF field relative to the particle. If the particle is not at relativistic regime, the longitudinal component of the field varies faster in space and time with respect to the particle path.

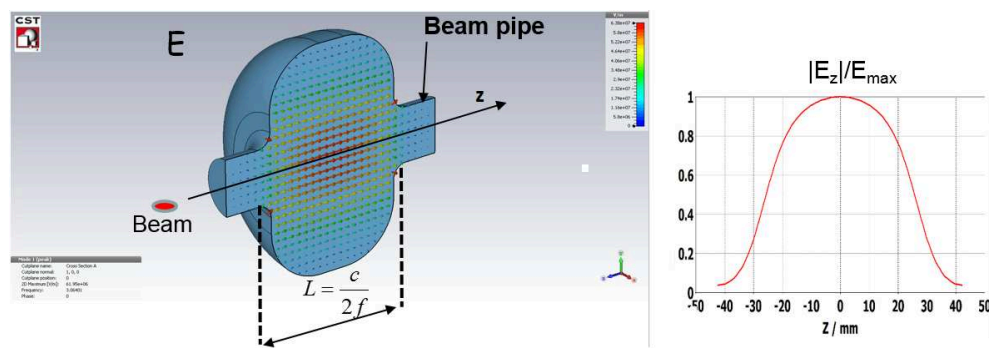


FIGURE 2.2: Accelerating field of the fundamental mode  $TM_{010}$  in pill-box cavity.

For simplicity, if we consider that particle has a constant velocity  $t(z) = z/v$ , we can calculate the energy gain through a cell:

$$\Delta U = e \int_{-L/2}^{L/2} E_z(z) dz = e \int_{-L/2}^{L/2} E_a(z) \cos\left(\frac{\omega z}{v} + \phi\right) dz = \quad (2.6)$$

$$= e \cos(\phi) \int_{-L/2}^{L/2} E_a(z) \cos\left(\frac{\omega z}{v}\right) dz \quad (2.7)$$

where  $e$  is the electron charge. The RF voltage is defined as:

$$V = \int_{-L/2}^{L/2} E_a(z) dz \quad (2.8)$$

Now, we define the transit time factor:

$$T \equiv \frac{\int_{-L/2}^{L/2} E_a(z) \cos\left(\frac{\omega z}{v}\right) dz}{\int_{-L/2}^{L/2} E_a(z) dz} = \frac{\int_{-L/2}^{L/2} E_a(z) \cos\left(\frac{\omega z}{v}\right) dz}{V} \quad (2.9)$$

From Eq.2.8 and Eq.2.9 the energy gain can be written in the form:

$$\Delta U = eVT \cos(\phi) \quad (2.10)$$

Equation 2.10 shows that the energy gain is due to an alternating voltage  $V \cos(\phi)$  traversed at a phase  $\phi$  from the peak, and  $T$  indicates the reduction in the energy gain due to the time that particle pass through a gap. If we consider  $E_a$  as the average longitudinal field on-axis in a cell, we get finally:

$$\Delta U = eE_a L T \cos(\phi) = eE_e L \cos(\phi) \quad (2.11)$$

where  $E_e = E_a T$  is the effective electric field "seen" by the particle that travels across the structure.

### 2.1.3 Main characteristics of RF structures

In electron linear accelerator, particles are quickly accelerated to the ultra-relativistic regime, namely their velocity is close to the speed of light,  $c$ . An uniform waveguide is not suitable for the particle acceleration since any electromagnetic field pattern would always have a phase velocity greater than the speed of light, that means it would never be locked to any particle beam. The reduction of the phase velocity,  $v_p$ , is obtained by introducing some periodic obstacles in the waveguide. In practice, we "load" the waveguide with discs at periodic distance  $d$ . Figure 2.3 shows such a disc-loaded structure. The cells are

electrically coupled via the iris radius ( $a$ ) and this iris area corresponds to the volume where electric field is prevalent.

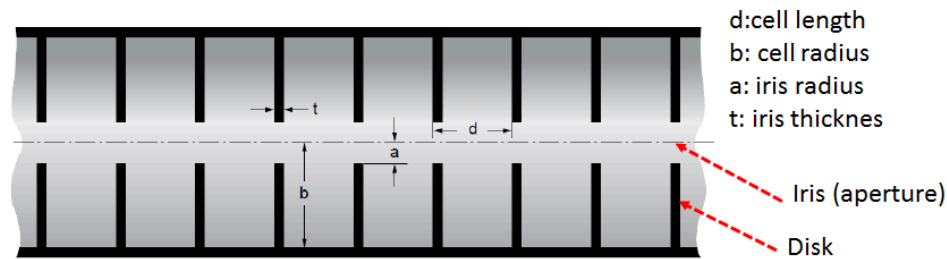


FIGURE 2.3: Sketch of a disk-loaded structure.

The performance of these accelerating structures in terms of gradient and efficiency is determined by the geometry, the material and the working RF frequency  $f$ , and it is described by some parameters summarized in this section.

An important parameter that concerns the power efficiency is the shunt impedance per unit length  $r_s$ , which describes how effective the structure is providing an axial gradient  $E_a$  for a given dissipated power  $-dP_d/dz$  through the walls and can be defined as [25]:

$$r_s(z) = \frac{(dV/dz)^2}{-dP_d/dz} = \frac{E_a^2}{-dP_d/dz} \quad (2.12)$$

$r_s$  is independent of  $E_a$  and the power loss and depends only on the structure itself, i. e. on its configuration, its dimensions, the materials and the operating mode.

From Eq.2.12 we ideally would like to make the shunt impedance as high as possible to reduce the amount of power needed to maintain a constant value of accelerating field. Also, this equation refers to the case of zero beam loading (no beam); this is just the power needed by the structure itself. The effective shunt impedance per unit length is given by:

$$r_s^{eff} = r_s T^2 \quad (2.13)$$

This quantity is commonly used to maximise the energy gain corresponding to the same dissipated power.

The power flow is:

$$P(z) = w_{st} v_g(z) \quad (2.14)$$

where  $w_{st}(z)$  is the electromagnetic (EM) energy stored in the structure per unit length and  $v_g$  is the velocity of the RF energy flow along the structure. By definition of the

attenuation constant,  $\alpha(z)$ , the power attenuation along the structure is:

$$\frac{dP}{dz} = -2\alpha(z)P(z) \quad (2.15)$$

The intrinsic unloaded quality factor is:

$$Q_0 = \omega \frac{W_{st}}{P_d} \quad (2.16)$$

where  $W_{st}$  is the RF stored energy in the cavity and  $P_d$  is the average dissipated power in cavity walls. For an accelerating cavity, the coupling between the cavity and the power transfer line (external load) that feeds it, is described by the external quality factor:

$$Q_{ext} = \omega \frac{W_{st}}{P_{ext}} \quad (2.17)$$

where  $P_{ext}$  is the external power flowing out from the coupling slots. The total power that is dissipated along the structure is  $P_{tot} = P_d + P_{ext}$  which defines then the loaded quality factor  $Q_{load}$ :

$$Q_{load} = \omega \frac{W_{st}}{P_{tot}} = \omega \frac{W_{st}}{(P_d + P_{ext})} \quad (2.18)$$

$Q_{load}$  is related to the unloaded and external quality factor by the expression:

$$\frac{1}{Q_{load}} = \frac{1}{Q_0} + \frac{1}{Q_{ext}} \quad (2.19)$$

The attenuation constant in Nepers per unit length is defined by:

$$\alpha(z) = \frac{\omega}{2Q_{load}v_g(z)} \quad (2.20)$$

Another interesting parameter is the ratio between the shunt impedance per unit length and the quality factor. Basically, it estimates the effectiveness of the interaction between the electromagnetic wave and the beam for acceleration:

$$\frac{r_s}{Q} = \frac{E_a^2}{\omega w_{st}} \quad (2.21)$$

This quantity is independent on the dissipated power, hence depends only on the geometry of the cavity and not on the material or surface properties.

Now Eq.2.12 and Eq.2.15 lead to:

$$E_a^2(z) = -r_s \frac{dP}{dz} = 2\alpha(z)r_s(z)P(z) \quad (2.22)$$

The working frequency is one of the basic parameter of the structure since it affects most of main RF parameters according to the following scale laws summarised in Tab.2.1

Quantities	scaling
Cell radius	$f^{-1}$
Surface area	$f^{-1}$
Volume	$f^{-2}$
Transit-time-factor	1
EM Fields	1
Stored energy	$f^{-2}$
Shunt impedance per unit length	$f^{-1/2}$
Effective shunt impedance per unit length	$f^{-1/2}$
Dissipated power	$f^{-1/2}$
Quality factor	$f^{-1/2}$

TABLE 2.1: Basic electromagnetic quantities scaling with the frequency [26].

### 2.1.4 Particle acceleration in multi-cell structures

Combining a large number of cells into one cavity structure reduces the cost for couplers, RF windows, distributing waveguides, and RF sources. High accelerating voltages can be achieved in multi-cells structures than in a single-cell structure for the same input power. Different classifications of structure designs can be found in [27], but we will focus here on the classification between Traveling Wave (TW) and Standing Wave (SW) structures.

#### 2.1.4.1 Travelling wave structures

The travelling wave structure (TWS) is a waveguide loaded with some iris or discs as shown in Fig.2.4. In the travelling wave structures, power is fed via an input coupler located at one end of the structure, then can flow through the structure exciting an accelerating gradient in the different cells, goes out via an output coupler and finally is absorbed in some power load.

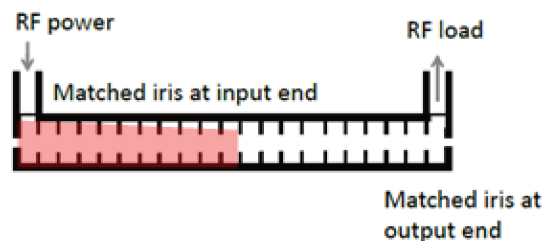


FIGURE 2.4: Schematic illustration of a travelling wave structure.

One can use the dispersion relation for a disc-loaded travelling wave structure [25] with the geometry as in Fig.2.3:

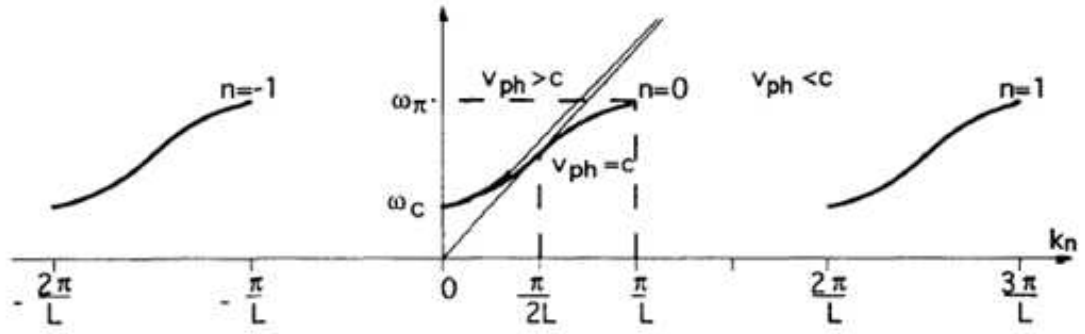


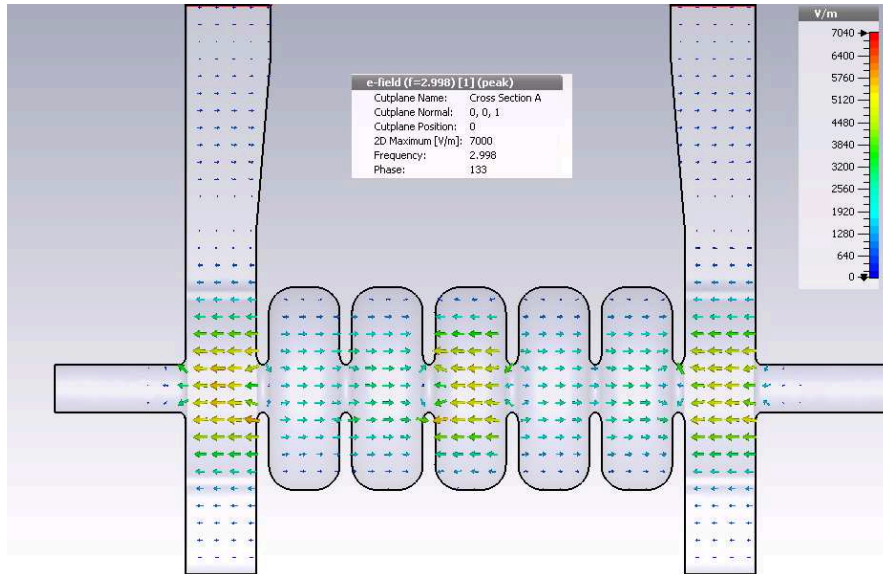
FIGURE 2.5: Dispersion diagram for a disc-loaded travelling wave structure [28].

$$\omega = \frac{2.405c}{b} \sqrt{1 + \kappa[1 - \cos(k_z L)e^{-\alpha t}]} \quad (2.23)$$

where  $L$  is the structure length,  $t$  is the iris thickness,  $k_z$  is the propagation constant,  $\kappa$  is the cell-to-cell coupling and  $\alpha$  is the attenuation constant,

$$\kappa = \frac{4a^3}{3\pi J_1^2(2.405)b^2 L} \ll 1 \text{ and } \alpha \approx \frac{2.405}{a} \quad (2.24)$$

The dispersion relation (Eq.2.23) is plotted in Fig.2.5 and one can see that there are indeed modes with a phase velocity equal to or even lower than the speed of light. It should be noted that for different geometries it is possible to have a different range of modes. When a structure operates in the  $2\pi/3$  mode it means that the RF phase shifts by  $2\pi/3$  per cell, or in other words one RF period stretches over three cells. Particles then move in synchronism with the RF phase from cell-to-cell.

FIGURE 2.6: Electric field distribution of the accelerating mode  $TM_{010-2\pi/3}$  for an S-band 7-cells TW structure.

A TW accelerator operates with the  $n = 0$  space harmonic as the wave amplitude is largest in this case. The structure is usually designed so that the dispersion curve crosses the  $v_{ph} = c$  line, for a phase advance per period from  $\pi/2$  to  $2\pi/3$ , approximately in the middle of the pass-band. The mode  $TM_{010-2\pi/3}$  is the most useful for particle acceleration in travelling wave disc-loaded structures. Figure 2.6 shows the electric field distribution of the fundamental mode  $TM_{010-2\pi/3}$  for an S-band 7-cells travelling wave structure. Furthermore, the field builds up in space. The filling time is the time needed to fill the whole section and is given by:

$$t_f(z) = \int_0^L \frac{dz}{v_g(z)} \quad (2.25)$$

where  $L$  is the length of the structure.

These structures can be built either with constant-impedance or constant-gradient.

**Constant-impedance (CI) structure:** A constant-impedance (CI) structure has a uniform cell geometry independent on the propagation direction  $z$ , and identical parameters for each cell including  $Q$ ,  $v_g$ ,  $r_s$  and  $\alpha$ . The attenuation per unit length is constant so from Eq.2.15 the power flow decays exponentially along the structure as:

$$P(z) = P_{in}e^{-2\alpha z} \quad (2.26)$$

where  $P_{in}$  is the input power. Any remaining power at the end is dissipated in the load leading to a gradient which decreases along the structure as:

$$E_a(z) = \sqrt{2\alpha r_s P_{in}} e^{-\alpha z} = E_a(0)e^{-\alpha z} \quad (2.27)$$

Now, let us list some relations dealing with RF energy and power. The energy gain of a synchronous particle riding at a phase  $\phi$  relative to the crest of the wave is written as:

$$\Delta U = e(2\tau)^{\frac{1}{2}} [(1 - e^{-\tau})/\tau] (P_{in} r_s L)^{\frac{1}{2}} \cos(\phi) \quad (2.28)$$

where  $\tau$  is the attenuation factor along the structure

$$\tau = \int_0^L \alpha(z) dz = \frac{\omega L}{2Q_{load} v_g} \quad (2.29)$$

The structure efficiency  $\eta$  is defined as the ratio of the stored energy to the energy supplied by the source:

$$\eta = \frac{W_{st}}{P_{in} t_f} = \frac{1 - e^{-2\tau}}{2\tau} \quad (2.30)$$

where  $t_f = 2\tau Q_{load}/\omega$ .

**Constant-gradient (CG) structure:** In the constant impedance (CI) structure with uniform cell geometry and uniform parameters, we found that the RF power and electrical field decay exponentially as the wave propagates away from the input. This raises the question of whether we could do better by varying the transverse geometry cells to keep the accelerating field constant along the structure. This design approach is called the constant-gradient structure. The group velocity ( $v_g$ ) and the attenuation per unit length ( $\alpha$ ) are sensitive to the iris aperture ( $2a$ ).

The iris diameter in a constant-gradient (CG) structure is decreased from cell-to-cell in order to slow down the power flow of the incoming RF pulse by reducing the group velocity for achieving:

$$\frac{dP(z)}{dz} = const = \frac{d}{dz} \left( P_{in} + \frac{P(L) - P_{in}}{L} z \right) = -2\alpha(z)P(z) \quad (2.31)$$

This leads to the expression of the output power at the end of the structure:

$$P_{out} = P_{in} e^{-2\tau} \quad (2.32)$$

The linear power flow is:

$$P(z) = P_{in} \left[ 1 - \frac{z}{L} (1 - e^{-2\tau}) \right] \quad (2.33)$$

The attenuation constant is given by:

$$\alpha = \frac{1}{2L} \frac{1 - e^{-2\tau}}{1 - \frac{z}{L}(1 - e^{-2\tau})} \quad (2.34)$$

The group velocity decreases linearly as a function of the power flow:

$$v_g(z) = \frac{\omega}{2Q_{load}\alpha(z)} = \frac{\omega L}{Q_{load}} \frac{1 - (z/L)(1 - e^{-2\tau})}{1 - e^{-2\tau}} \quad (2.35)$$

The time needed for the EM energy to fill the structure is:

$$t_f = \int_0^L \frac{dz}{v_g(z)} = \tau \frac{2Q_{load}}{\omega} \quad (2.36)$$

The energy gain of a charged particle is given by:

$$\Delta U = e(1 - e^{-2\tau})^{\frac{1}{2}} (P_{in} r_s L)^{\frac{1}{2}} = (P_d r_s L)^{\frac{1}{2}} \cos(\phi) \quad (2.37)$$

where  $P_d = P_{in} - P_{out} = (1 - e^{-2\tau})P_{in}$ , is the power dissipated in the section.

The CG structure has several advantages over the CI structure in term of performances [29]:

- the reduced ratio of maximum to average field strengths,
- the power dissipated per unit length in the CG structure is constant over its entire length. In contrast, the ratio of power loss at the input end to that at the output end of a CI structure may be high.
- the CG structure gives a slightly higher no-load beam energy than the CI structure and somewhat lower load beam derivative ( $-dV/dI$ ). Thus, the CG structure has greater relative energy advantage in the loaded case than in the unloaded case.
- the CG structure has a higher maximum conversion efficiency (ratio of maximum electron beam power to input RF power) and a higher corresponding maximum peak beam current than the CI structure.

The constant impedance structure may be simple and easy to fabricate but may not be the best for long accelerating sections.

#### 2.1.4.2 Standing wave structures

In the case of standing wave structures (SWS), single coupler is used to feed a certain number of cells as represented in Fig.2.7. RF power propagates in both upstream and downstream directions. The standing wave field pattern can be thought as the combination of two waves with the same frequency travelling at the same velocity in opposite directions along the same medium. It is characterized by the existence of node locations with zero displacement and anti-node locations with a maximum displacement distant from each other by  $d = \pi/2k$ , where  $k = \omega/v_p$  and where  $v_p$  is the phase velocity. The pattern does not travel at any direction but simply oscillates, hence there is not net power flow in the structure.

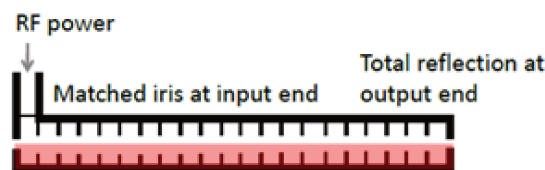


FIGURE 2.7: Simple scheme showing how the RF power fills a SWS when it is injected through the input coupler.

The corresponding dispersion relation for standing wave cavities [25] for a half-cell terminated standing wave structure, which practically represents the behaviour of an infinite

chain of  $N+1$  magnetically coupled resonators is given by:

$$\omega_n = \frac{\omega_0}{\sqrt{1 - k \cos(n\pi/N)}}, \quad n = 0, 1, \dots, N \quad (2.38)$$

Assuming an uneven number of cells,  $\omega_0$  is the angular frequency of the  $\pi/2$  mode. A more general definition is to say that  $\omega_0$  is the angular frequency of the uncoupled single cells.  $k$  is the cell-to-cell coupling constant, and  $n\pi/N$  the phase shift from cell-to-cell. For  $k \ll 1$ , which is usually fulfilled, the coupling constant is given by:

$$k = \frac{\omega_{\pi\text{-mode}} - \omega_{0\text{-mode}}}{\omega_0} \quad (2.39)$$

Figure 2.8 depicts the dispersion curve for seven-cell (half-cell terminated) magnetically coupled structure according to Eq.2.38.

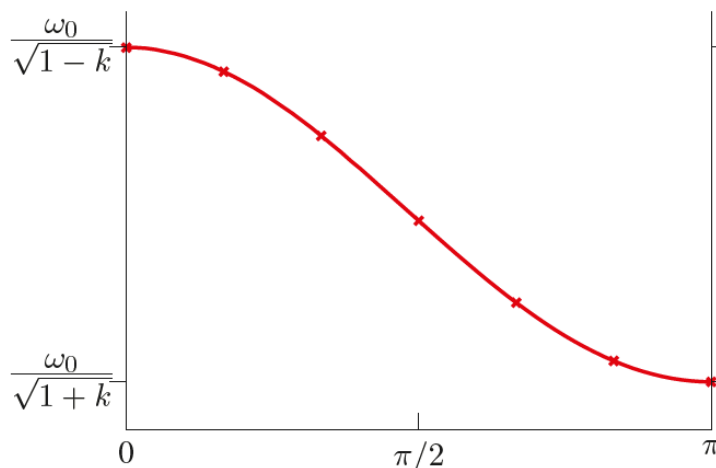


FIGURE 2.8: Dispersion diagram for standing wave structure with seven magnetically coupled cells.

For magnetic coupling, the 0-mode has the highest frequency and the  $\pi$ -mode has the lowest frequency. This means that standing-wave linear accelerators operate either at the lowest or at the highest frequency of the pass band. Standing wave structures use both direct and reflected wave to accelerate particles. At the point where direct and reflected waves join, they have the same phase velocity and if they are synchronous to the particle velocity both waves contribute to the acceleration. According to the Fig.2.8 these points correspond either to the lowest ( $k = \pi$ , magnetic coupling) or the highest ( $k = 0$ , magnetic coupling) frequency of the pass-band. In the case of electric coupling this behaviour is reversed. For 0-mode the electric fields in all the cells are in phase (as you can see in Fig.2.9), for  $\pi$ -mode the electric fields in adjacent cells are in phase opposition (as shown in Fig.2.10). The  $TM_{010-0}$  and  $TM_{010-\pi}$  modes are specially

interesting for optimal acceleration, for which the effective shunt impedance per unit length is maximized.

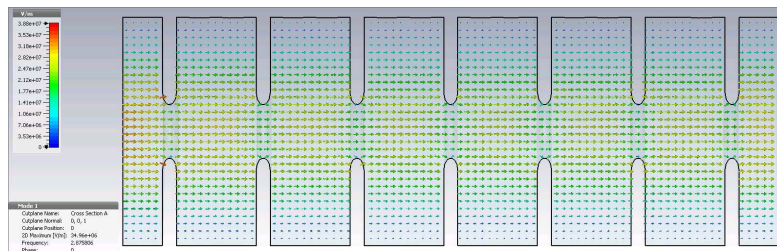


FIGURE 2.9: Electric field of the  $TM_{010-0}$  mode for standing wave structure with seven electrically coupled cells (half-cell terminated on both sides).

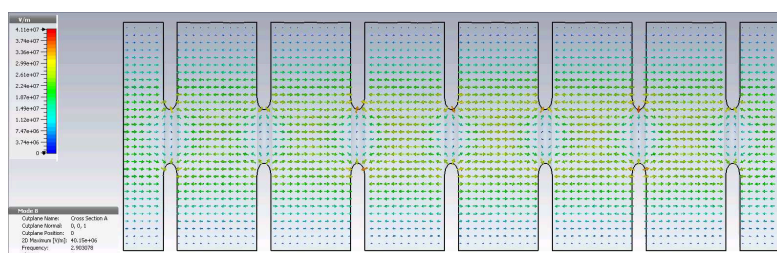


FIGURE 2.10: Electric field of the  $TM_{010-\pi}$  mode for standing wave structure with seven electrically coupled cells (half-cell terminated on both sides).

The filling time  $t_f$  is defined as the time needed to build up the field to  $(1-1/e) = 0.632$  times the steady-state field:

$$t_f = \frac{2Q_{load}}{\omega} = \frac{2Q_0}{(1 + \beta_c)\omega} \quad (2.40)$$

where  $\beta_c$  is the coupling coefficient of the section to the input RF network.

The energy gain of the charged particle is given by:

$$\Delta U = e(1 - e^{-t/t_f})(P_d r_s L)^{\frac{1}{2}} \quad (2.41)$$

The structure efficiency is given by:

$$\eta = \frac{W_{st}}{P_{in} t_p} = \frac{1}{1.228} \left( \frac{1}{1 + \frac{1}{\beta_c}} \right) \quad (2.42)$$

where  $t_p$  is the end of the pulse length,  $t_p = 1.257t_f$ . The structure efficiency can be expressed as:

$$\eta = \frac{W_{st}}{P_{in} t_f} = \frac{1 - e^{-2\tau}}{2\tau} \quad (2.43)$$

### 2.1.4.3 Standing wave versus travelling wave structures

There is a difference between the filling time of standing wave structures and travelling wave structures. Whereas the filling time of the TWS is the time required for the RF power to travel from the input to the output coupler, the filling time of the SWS corresponds to the time to build up the fields in the structure. In other words, in TWS, fields build up in space from cell-to-cell along the structure, while in SWS fields build up in time. A typical example of SW short structure is the RF gun which has a reduced filling time compared with its RF pulse and can be used for ultra-relativistic particles generation and acceleration. Also, SWS are usually used in synchrotrons and storage rings for beam acceleration, energy compensation or synchrotron radiation energy loss. In case of high power pulsed RF sources, a travelling wave accelerating structure is usually used when dealing with a short pulsed beam and when particle velocities approach the velocity of light as it is the case of electrons.

## 2.2 High-Gradient limiting quantities

In normal-conducting temperature accelerating structures, the achievable on-axis electric field is mostly limited by two main effects: the RF breakdown and the fatigue cracking due to the pulsed heating [30]. One of the most important aspects of the operating conditions is that the breakdown probability of the individual accelerating structures must be of the order of  $10^{-6}$  to  $10^{-7}$  bpp/m [30]. The BDR has shown a strong dependence on accelerating gradient and RF pulse duration [31–34] and an empirical scaling law that correlates the three quantities has been defined as:

$$\frac{E_a^{30} t_p^5}{BDR} = const \quad (2.44)$$

From Eq.2.44 an important criterion for the high-gradient structure optimisation can be deduced. In fact, for a fixed BDR, a trade-off between the RF pulse duration and the maximum on-axis electric field has to be taken into account.

Since the surface electric field is considered to be strongly connected to the field emission of electrons from the cavity surface, it was thought to be one of main quantity limiting the accelerating gradient. Historically, an empirical law determining a threshold between no-vacuum discharge and possible vacuum discharge regimes was established by Kilpatrick [35]. The threshold between the two regimes depends only on the operation frequency and does not take into account the BDR and RF pulse duration. For 3 GHz, the maximum surface electric field predicted by the Kilpatrick's law is around 47 MV/m. However, in the last years, new improvements in the structure fabrication and cleaning

techniques have demonstrated the reliable operation of cavities at surface electric field level double than Kilpatrick's threshold [36]. For this reason the maximum surface electric field could not be considered as the only constraint in the RF design because of its large variation in different structures.

In the framework of the high-gradient technology collaboration between different laboratories around the world, a huge amount of experimental measurements on different type of copper-made TW structures and the operation frequencies (3 - 30 GHz) has been collected and carefully analysed. In general, it was observed that breakdown occurrence depends on many parameters, such as the RF pulse duration, the power flow [31]. The most interesting point is the following relation between some relevant quantities that determine a breakdown scaling empirical law:

$$\frac{P \cdot t_p^{1/3}}{C} = const \quad (2.45)$$

where  $P$  is the power flow through the structure,  $t_p$  is the RF pulse duration and  $C$  is the minimum inner cavity circumference that is usually determined by the iris aperture. However, this empirical law holds for only travelling wave structure because in the case of standing wave there is not power flow circulating into the structure.

A new model which takes into account the effect of field emitters generated by the defects of the surface has been proposed [34]. This model proposes the modified Poynting vector,  $S_c$ , as the new quantity that predict the limit given by the breakdown:

$$S_c = |\Re(\vec{S})| + 1/6|\Im(\vec{S})| \quad (2.46)$$

where  $\vec{S} = \vec{E} \wedge \vec{H}$  is the Poynting vector. The real part  $\Re(\vec{S})$  corresponds to the power flux that passes through the TW structure while the imaginary part  $\Im(\vec{S})$  corresponds to the electromagnetic energy that is periodically transferred from the electric contribution to the magnetic one and vice-versa. The modified Poynting vector has been derived from a specific breakdown model, which allows to deduce other dependencies related to the physical mechanism that triggers breakdown, such as pulse shape and material [34]. Moreover it takes into account the frequency scaling that has been experimentally observed and the performance of SW cavities (imaginary part of Eq.2.46) [34]. Also, this is a local quantity that can be easily defined in electromagnetic simulation solvers (HFSS and CST MWS) as a geometry design parameter. According to Eq.2.44, the scaling law becomes:

$$\frac{S_c^{15} t_p^5}{BDR} = const \quad (2.47)$$

## 2.3 How to avoid RF breakdowns and damages

At present there seems to be three main ways to avoid breakdown damages. First, the optimisation of the RF structure geometry entails the minimization of parameters like the maximum surface electric and magnetic fields and modified Poynting vector  $S_c$  [37]. Second, new techniques in surface machining, cleaning and high RF power conditioning leading to achieve much more high gradient than Kilpatrick's prediction. Third, the use of new materials other than copper in the critical area (iris region) such as tungsten (W) and molybdenum (Mo) [38] for increasing damage resistance. In particular, a DC breakdown study is still underway at CERN in order to investigate the material capability to sustain high electric field with a low breakdown rate and low damages [39]. The measurement of accelerating gradient limits and conditioning speeds have been performed on several materials and alloys. Results indicate that the limitation to the accelerating gradient given by breakdown is strongly dependent on the material and the chemical composition of the film on their surface.

## 2.4 ThomX High-Gradient S-band electron Linac design

This paragraph discusses the characteristics of the RF gun and the accelerating section that constitute the ThomX Linac. First, a brief overview of the main RF Linac components is presented. Second, I briefly describe the main RF gun electromagnetic characteristics. Third, a thermal-structural coupled analysis aiming at the validation of the gun cooling system for operation requirements is presented. This study has been performed by means of 3D Multiphysics simulation solver like ANSYS. The other paragraphs describe the S-band accelerating section design. This consists in the choice of the operation frequency, the regular cell geometry optimisation, the couplers design of 7-cells aluminium and copper constant-impedance prototypes with a reduced number of cells. Moreover, the RF design of a 16-cells copper prototype and the main aspects that limit its performance in term of high-gradient acceleration achievement as well as the mechanical drawings are presented. Furthermore, the RF design and the main features of the final 97-cells (95 regular cells + 2 coupling cells) high-gradient compact S-band accelerating section are proposed. All these analyses have been carried out with two 3D electromagnetic simulation solvers: ANSYS Electromagnetic (HFSS) [40], which is based on Finite Element Method (FEM) and CST MWS [41], which is based on Finite Integration technique (FIT). In addition, the thermal-structural coupled analysis has been performed on the 7-cells copper prototype for the cooling system validation. The impact of the temperature variations on the resonating frequency has been also

estimated. The paragraph ends with the vacuum simulations on the 16-cells copper prototype and the final 97-cells accelerating structure in order to predict practical pumping solutions during the operation of the linac.

### 2.4.1 ThomX Linac RF components

Basically, the ThomX linear accelerator is composed of two main warm RF components: the RF gun and the accelerating section that boosts the electron beam to the final energy for the ring injection. Figure 2.11 shows the 3D scheme of the linear accelerator components composed of the two solenoids that surround the RF gun, the diagnostic line and the accelerating section.

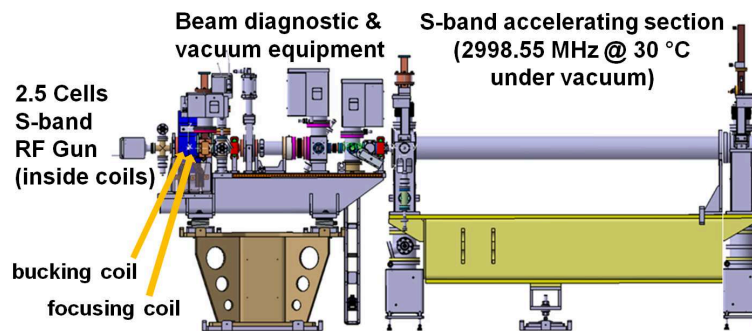


FIGURE 2.11: 3D scheme of the ThomX Linac.

The LAL gathered long and fruitful experience in RF gun designs and manufacturing from the "probe beam gun" CLIC "Test Facility 3" (CTF3) at CERN. This gun has successfully been in operation for four years. So, it is not surprising that ThomX RF gun has mainly the same design and the same mechanical concept as the CTF3 model. It is a 2.5-cells SW copper cavity with a resonating frequency of 2998.55 MHz (at 30°C, in vacuum).

In addition, we took advantage from all technical drawings which already existed and all the fabrication procedure that has been mastered by the LAL, such as machining, brazing and tuning procedure and cleaning.

The French National Synchrotron Facility (SOLEIL), as a partner of the project, is willing to lend a standard S-band accelerating structure that owns as a spare of its accelerator injector. This section has been manufactured at LAL for the pre-injector of the Large Electron-Positron collider (LEP) at CERN (Fig.2.12). The LEP Injector Linac (LIL) structure is an S-band travelling wave quasi-constant gradient section composed of 135 cells, with  $2\pi/3$  phase advance per cell at 2998.55 MHz (30 °C in vacuum). The section length is about 4.5 m. To achieve a final energy of 50 MeV, the energy gain in the

section must be 45 MeV. The latter value implies a peak accelerating field of 14 MV/m and an RF power of about 10 MW. However, the accelerator should achieve higher energies in order to produce X-rays beyond 45 keV. Toshiba E37310, S-band (2998.5



FIGURE 2.12: Picture of the LIL accelerating section lent by the SOLEIL laboratory.

TABLE 2.2: Characteristics of the Linac RF components.

Parameters	RF gun	LIL section	HG section
Charge per bunch	1 nC	1 nC	1 nC
Repetition rate	50 Hz	50 Hz	50 Hz
RF frequency	2998.55 MHz	2998.55 MHz	2998.55 MHz
Number of cells	2.5	135	97
Length	0.125 m	4.5 m	3.5 m
Beam Energy	5 MeV	45 MeV	65 MeV
Shunt impedance	49 M $\Omega$ /m	63-74 M $\Omega$ /m	71-85 M $\Omega$ /m
Quality factor	15000	15000	15000
Input power	6 MW	10 MW	24 MW
$E_a$ on-axis	80 MV/m	14.5 MV/m	25 MV/m
Filling time	0.7 $\mu$ s	1.35 $\mu$ s	0.9 $\mu$ s

MHz) high power amplifier klystron compatible with the ScandiNova modulator (k2-3) will be used as linac RF power source. The E37310 delivers 35-37 MW peak output power with a variable RF flat top pulse width of 0-4.5  $\mu$ s and a variable repetition rate of 0-100 Hz. The high-power RF, which is provided by a 35 MW peak power klystron, is divided into the RF standing wave RF gun (10 MW) and the traveling wave accelerating section (25 MW) .

Since X-rays production has a maximum target of 90 keV, the standard LIL section will be replaced by a high-gradient S-band TW structure. This structure is designed by the LAL and will be fabricated by PMB-Alcen in the framework of the collaboration

research. The structure should provide 70 MeV electron beam energy at the exit of the Linac.

Table 2.2 summarises the main characteristics of the ThomX linear accelerator RF components, such as gun, LIL accelerating structure and high-gradient accelerating cavity.

### 2.4.2 RF gun

Photo-cathode RF guns are used in the first stage of the electron beam generation and acceleration in particle accelerators. They are copper structures with different internal shapes fed by RF klystrons. They can work at different frequencies (from few hundred of MHz up to several GHz) depending on the different applications. RF photo-injectors are the ultimate choice to generate electron pulses of high bunch charges with low transverse emittance.

The proposed 2.5-cell RF SW gun for ThomX operates with a nominal body temperature of 30 °C in the  $\pi$ -mode at the S-band frequency of 2998.55 MHz under vacuum. The electrons are emitted on the cathode through a laser that hits the surface and are then accelerated by an axial longitudinal electric field component. The beam energy at the exit of the RF Gun is about 5 MeV for an input peak RF power of 6 MW.

A thermally stable operation of the gun cavity is mandatory to prevent from parasitic RF amplitude and phase jitters which are in turn converted into beam energy and timing jitters of the electron beam. In these injectors the photocathode is exposed to electric field in the range of several ten MV/m to quickly accelerate the beam and minimise the effect of space charge force. Operating at high repetition rates, such high field levels requires average power levels of several kW that are dissipated in cavity walls. Hence the cooling system of the gun has to be well designed to take under control the deformation of the structure by providing a temperature increase as small and uniform as possible. For this purpose, a complete simulation has been performed [42] with the multi-physics package of the finite element analysis code ANSYS [40].

The commercial finite element analysis (FEA) code ANSYS provides the ability to link electromagnetic to thermal and structural analyses as shown in Fig.2.13. ANSYS provides the high frequency (HF) analysis module and associate elements. This module has been applied to evaluate the RF loss and the consequent temperature distribution in the gun body. A coupled field analysis by a unique code is more efficient than the use of different specialized softwares. In fact, the exchange of information between electromagnetic field simulators and structural/thermal simulators can be difficult and can

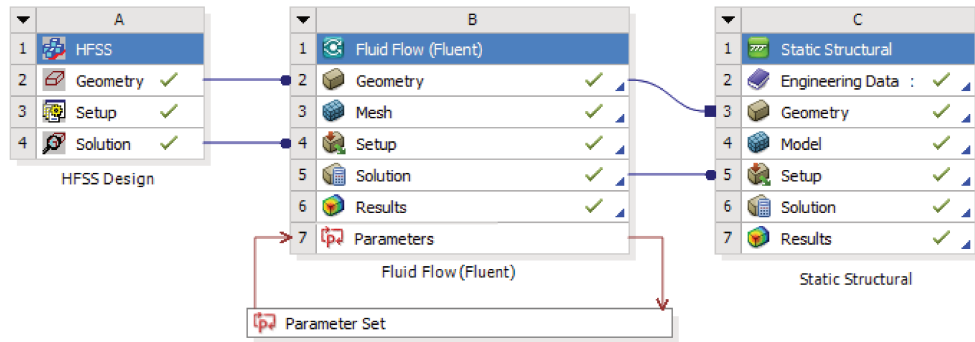


FIGURE 2.13: ANSYS Workbench Analysis Schematic.

lead to errors. In the multi-physics code like ANSYS, this exchange of information between different modules is a built-in feature of the software. The model can be therefore established by one single software and related data can be transferred more efficiently and easily in between solvers.

#### 2.4.2.1 Electromagnetic analysis

The RF gun of THOMX is a 2.5-cell standing wave copper cavity with a resonance frequency of 2998.55 MHz at 30 °C under vacuum, operating on the  $TM_{010}$ -like accelerating mode and field phase advance per cell is  $\pi$ . The THOMX RF gun geometry design comes from the geometry improvement of the probe beam photo-injector (PBPI) of CTF3 [43] that was already designed and constructed by LAL. RF power is fed through one waveguide coupler only, the waveguide is located 180 degrees opposite the input one and its main purpose is to cancel the field dipole component. The RF cavity shape, was optimised with several innovative electromagnetic features, including an enhanced cell-to-cell coupling to produce a higher mode separation, elliptical irises to reduce the surface electric field and symmetric couplers for the dipole mode minimization. It is externally fed only by one side for avoiding the need of power splitter and making the whole assembly much more compact, easier to handle and cost efficient.

The electromagnetic analysis is performed using the ANSYS Electromagnetic (HFSS), which determines resonant mode frequencies and the electromagnetic field distribution. The accelerating electric field on the cathode for the THOMX gun is 100 MV/m for an input RF power of 10 MW at 3  $\mu$ s RF pulse length and 50 Hz repetition rate as shown in Fig.2.14. Also from the picture of the electric field amplitude inside the structure and on the cell surface (Fig.2.14), we can see that the peak value on the iris area is about 110 MV/m.

The analysis of heating is important for determining the behaviour of the material in various applications. Specifically, one worries about damage induced in the material by

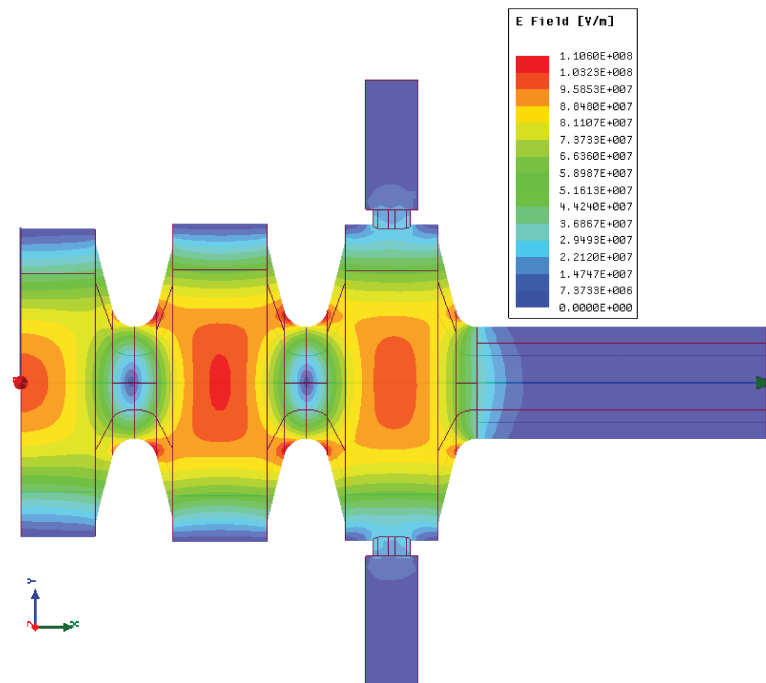


FIGURE 2.14: RF gun electric field distribution in vacuum.

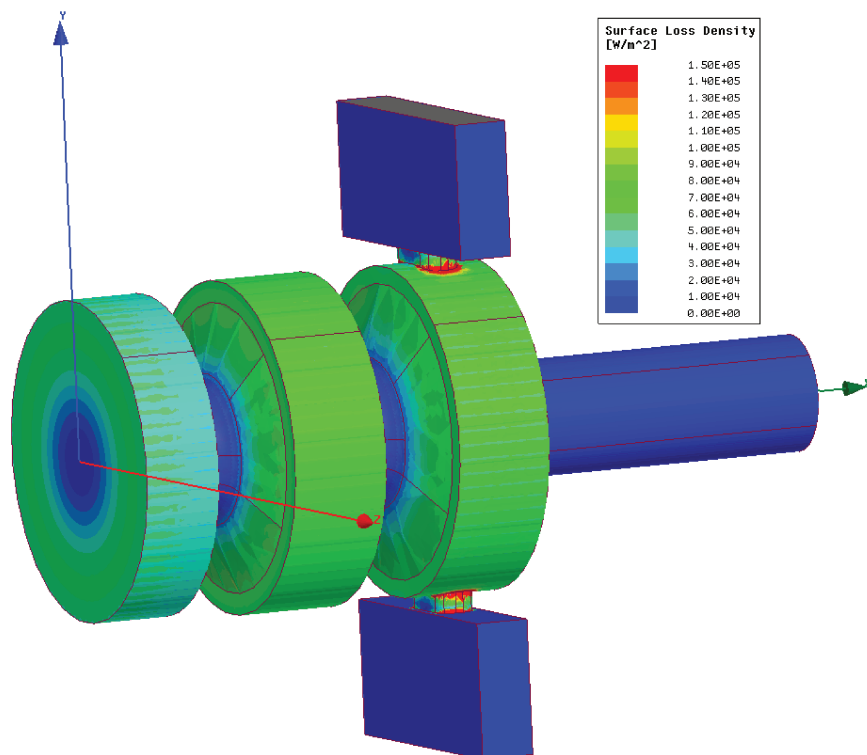
FIGURE 2.15: The heat flux for 10 MW peak power at 3  $\mu$ s RF pulse length and 50 Hz repetition rate.

TABLE 2.3: Main RF parameters of the ThomX gun.

Parameters	Simulated values
$\pi$ -mode frequency	2998.55 MHz
Quality factor	15000
Shunt impedance	49 M $\Omega$ /m
Peak accelerating field	100 MV/m @ 10 MW
Filling time	0.7 $\mu$ s
Repetition Rate	50 Hz
RF pulse, input RF power	3 $\mu$ s, $\leq$ 10 MW
$E_{smax}/E_a$	1.07
Average dissipated power	1.5 kW

thermal loads that make the materials useless. Usually an induced stress below the yield strength is considered as a criterion.

EM simulations show that the maximum magnetic field is equal to  $H_{max} = 4 \times 10^5$  A/m for an input RF power of 10 MW. This field value causes a temperature rise of about 60 °C for an RF flat top pulse length of 3  $\mu$ s, which is below the damage threshold of 110 °C, for fully annealed OFE copper. As general experimental rule, if this pulsed heating exceeds  $\sim$ 110 °C, a serious damage to the coupler region has a high probability of occurrence. The average heat flux (power loss density) obtained for 3  $\mu$ s RF pulse length and 50 Hz repetition is shown in Fig.2.15, the maximum heat flux at the coupling slot area is 150 kW/ $m^2$ . The average dissipated power on the internal cavity surfaces is 1.5 kW. The main gun parameters are given in Tab.2.3.

#### 2.4.2.2 Thermal analysis

The heat source for the thermal simulation is the power loss of the accelerating mode on the cavity walls. This RF heating, if not properly dissipated, may result in an excessive structural stress, deformations, and an accelerating frequency shift. The computed power loss is then imported and applied as a heat flux load (W/ $m^2$ ) to the surface of the metal body of the gun. The metal part is composed of two different materials, copper and stainless steel. The cooling system is directly made in the copper gun body. It is composed by one feeding pipe and runs through the gun body with two parallel small pipes (Fig.2.16).

In the thermal analysis performed with ANSYS Fluent, we assume an overall 50 Hz repetition rate, with 3  $\mu$ s RF pulse length. Thus, with 10 MW peak power, that means an average dissipated power of 1.5 kW. Water inlet velocity (diameter of 8 mm) is set to 2.5 m/s. This value derived from considerations about channel pressure and corrosion problems. Higher values of fluid velocity, until 3 m/s, could be in case adopted. The inlet

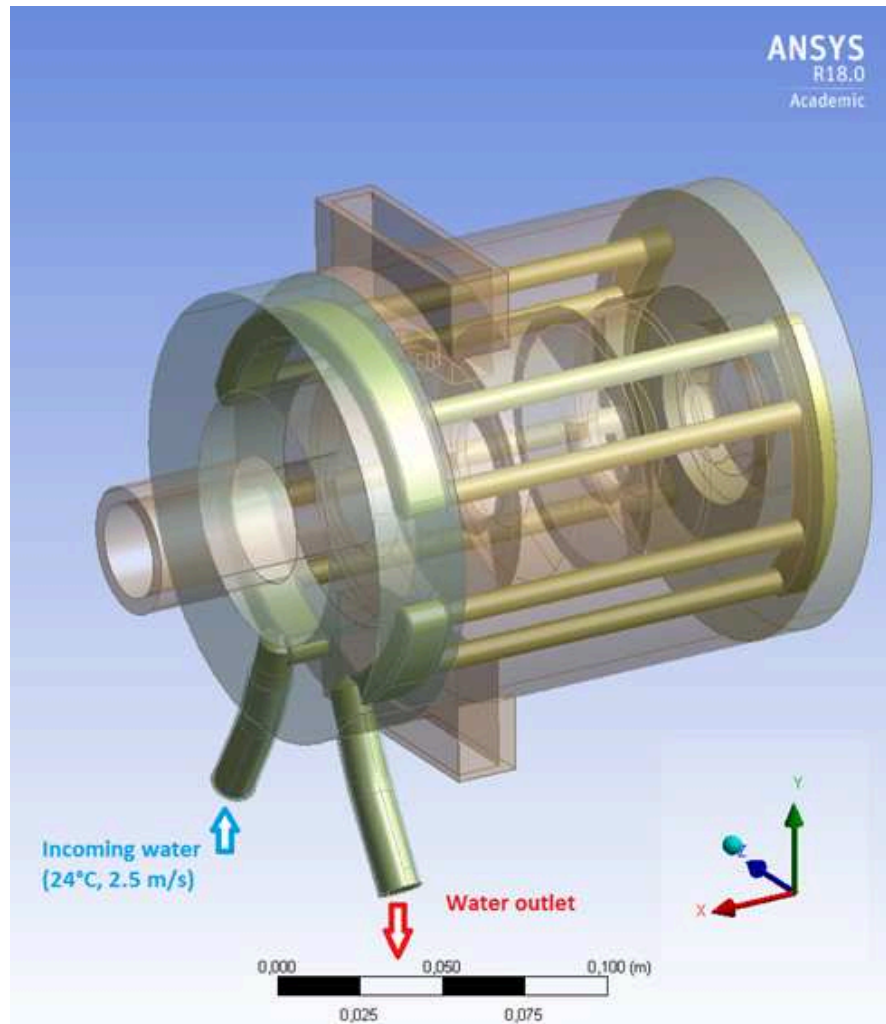


FIGURE 2.16: Cooling system integrated in the gun body.

water temperature is 24 °C and the ambient temperature is 22 °C. Natural convection with air on the external surface is taken into account as boundary conditions.

The temperature distribution calculated in the gun body is represented in Fig.2.17. The temperature distribution is uniform throughout the whole gun body with an average value of about 29.6 °C and a peak value of 33 °C at the photocathode area. The temperature on the internal cavity walls, which has the larger impact on the gun resonant frequency, is between 29 °C and 31 °C.

The related cooling water temperature distribution inside tubes is depicted in Fig.2.18. The maximum temperature rise is about 1.4 °C and the pressure drop is around 0.5 bar for 2.5 m/s water flow rate.

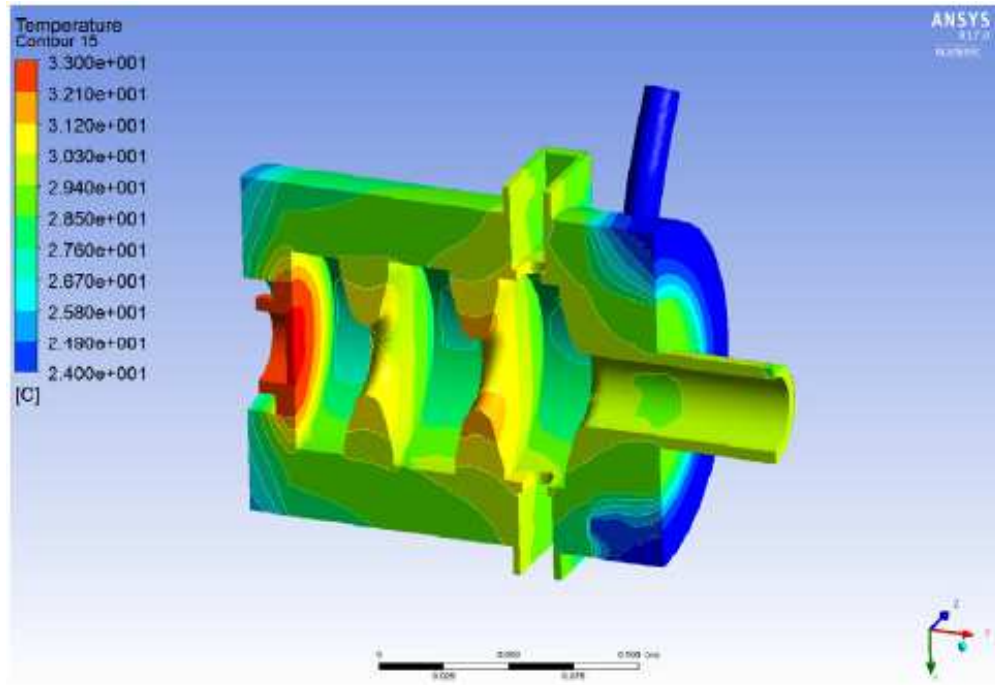


FIGURE 2.17: Gun body temperature distribution.

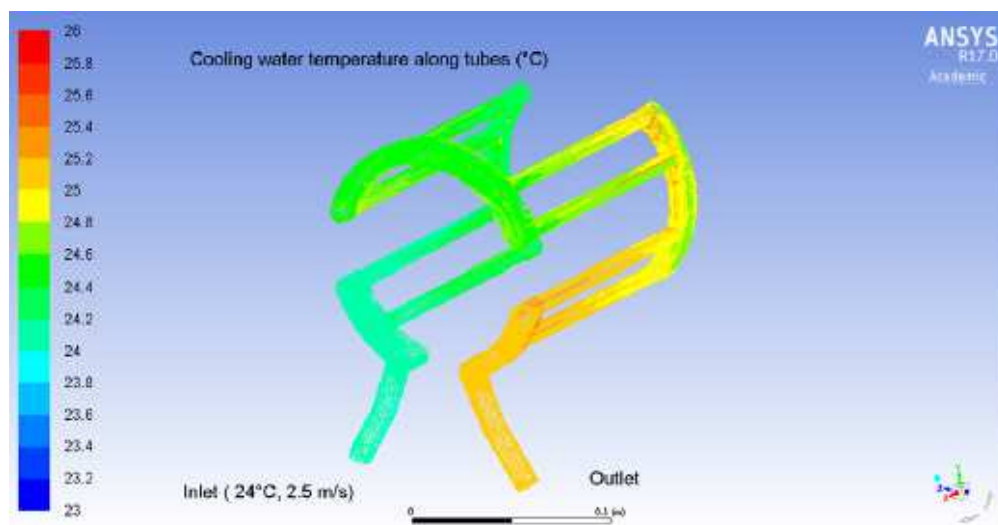


FIGURE 2.18: Cooling water temperature distribution along tubes.

### 2.4.2.3 Structural analysis

After obtaining the thermal solutions, the structural solution may be calculated by applying the thermal analysis results as a load in the model. The goal of the model is to evaluate the deformation due to the thermal load acting on the gun. The total deformation (displacement) is displayed in Fig.2.19. The maximum deformation is about of 25  $\mu\text{m}$ . The deformation calculated at the inner surfaces, in radial direction, is below 20  $\mu\text{m}$ . The local stress caused by the RF heating should be controlled below the yield

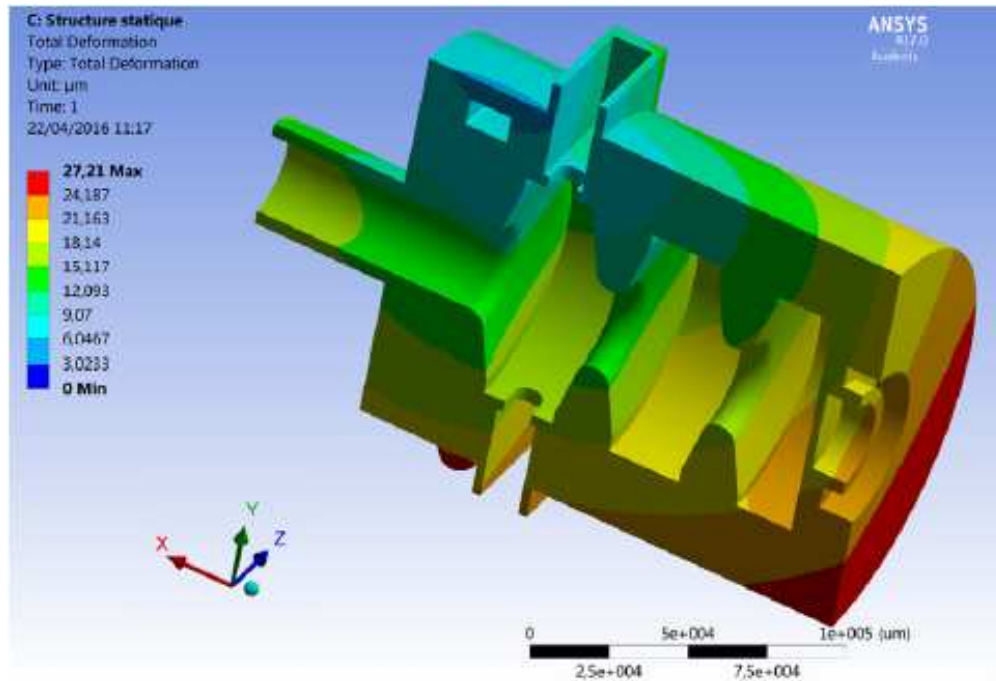


FIGURE 2.19: Total deformation of the gun body.

stress of the annealed oxygen free copper, 62 MPa [44]. At the slot coupling area the peak Von Mises stress is 18 MPa (Fig.2.20), which is near the tolerance threshold but still in the safe region.

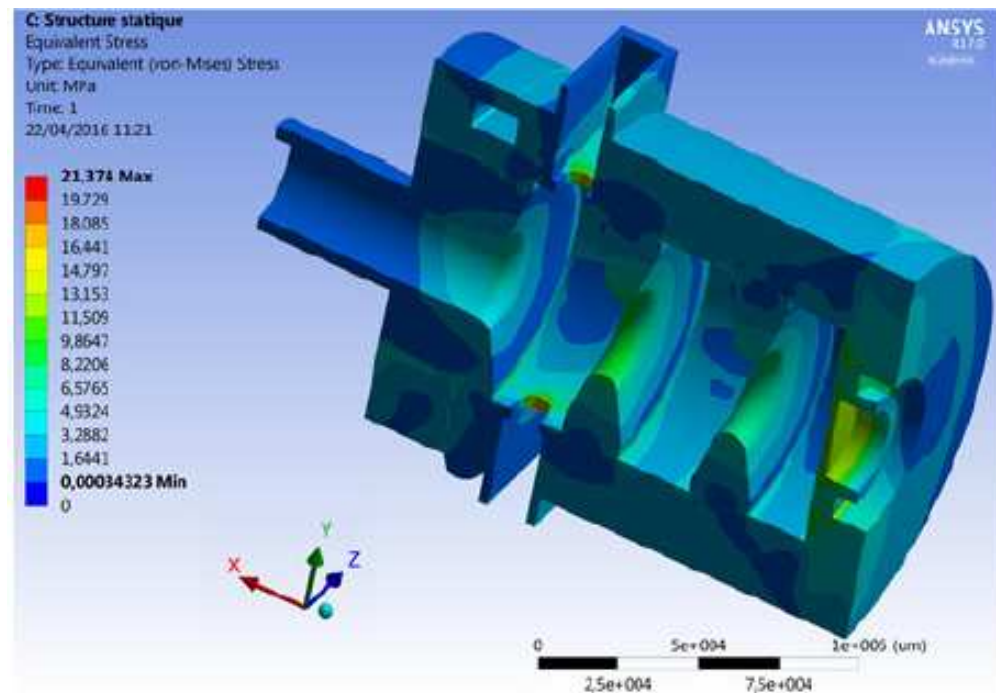


FIGURE 2.20: Gun body equivalent Von-Mises stress for an average dissipated power of 1.5 kW.

The present coolant channel design in 2.5 cells photocathode gun seems adequate for 50 Hz operation at 100 MV/m peak gradient and 3  $\mu$ s RF pulse length with 2.5 m/s water flow rate. The RF gun was designed, machined and brazed in-house, followed by final tuning. RF gun will be RF conditioned up to full power in the casemate "shielded room" of the new IGLEX research platform located at the Orsay university campus. The gun after the final brazing step is shown in Fig.2.21.

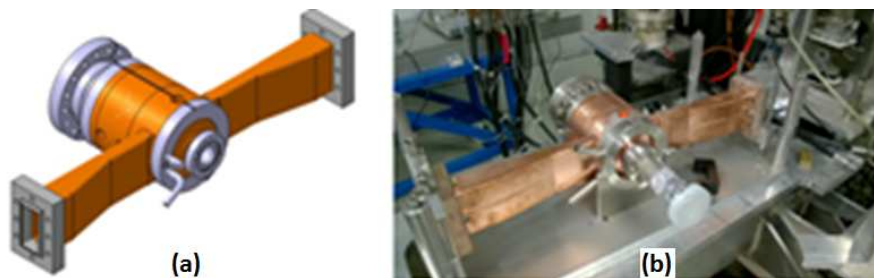


FIGURE 2.21: ThomX RF gun. (a) 3D model design, (b) prototype after final brazing.

### 2.4.3 Design of High-Gradient S-band accelerating section

For short pulse application, as in the ThomX case, travelling-wave structures may give greater efficiency, in terms of dissipated power, than standing wave structures because the filling time is smaller. Usually the beam is injected only after the structure has achieved steady state. Hence the RF power dissipated in the cavity before reaching steady state represents wasted energy. Since for short-pulse applications, the filling time represents a large fraction of the power loss per pulse, travelling-wave results in more efficiency.

The efficiency of the TW structure as an accelerator of electrons is measured by a quantity called the shunt impedance per unit length. This quantity, which has already been introduced earlier and designated by the symbol  $r_s$ , is defined as the square of the energy gained (in electron volts) by an electron per unit length of accelerator structure for unit RF power dissipation in this same length. The fundamental electric field mode  $TM_{010}$  with a phase advance per cell of  $2\pi/3$  is used in most linacs for particle acceleration thanks to its high efficiency. Figure 2.22 shows the relative efficiency defined by the ratio between the shunt impedance for a number of travelling wave modes and the shunt impedance of the  $\pi$ -mode.

The constant impedance structure may be simple and easy to fabricate but may not be the final choice for accelerator applications [46]. The constant gradient structure has higher shunt impedance and more uniform power dissipation and is less sensitive to

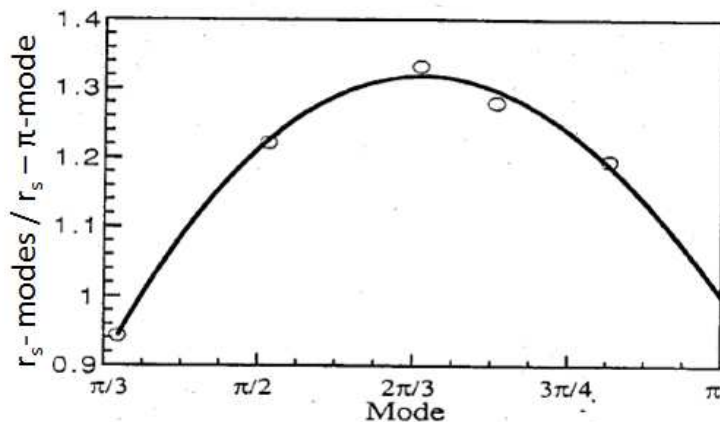


FIGURE 2.22: Relative efficiency of TW modes in disc-loaded structures. [45]

the frequency deviations and beam break-up when compared to the constant impedance structure [47].

The prototypes of high-gradient S-band section with reduced number of cells are based on constant impedance structure in order to validate the geometry, manufacturing process and all technical choices. The final high-gradient TW accelerating section is based on constant gradient structure.

The design of HG S-band structure can be summarised in several main steps: the choice of the operating frequency, the RF design of the regular cells, the input and output coupler design, the electromagnetic simulation of prototypes and the final configuration of the section, the thermal and structural analysis and vacuum simulations.

#### 2.4.3.1 Resonant frequency determination at normalised conditions

The operating frequency  $f_0$  is one of the basic parameters of the structure since it affects most of its RF parameters (shunt impedance, energy stored, quality factor, filling time, etc). So the final choice  $f_0$  is usually made by adjusting all of the above factors and by considering the available RF source (S-band klystron) as well. Most electron linac in Europe work at a frequency of 2998.55 MHz.

Accelerating sections operate in high-vacuum ( $\approx 10^{-9}$  mbar) at temperature of the order of 30 °C. Usually, it is difficult to perform experimental measurements in these conditions. So, starting from experimental measurements at the laboratory conditions, we have to be able to estimate values at the normalised and real operation conditions. The accelerating section operating frequency, in vacuum at 30 °C, has been determined to be

$$f_0 = 2998.550 \text{ MHz} \quad (2.48)$$

Low power measurements are carried out in the air, we need to calculate the frequency value  $f_N$  for normalised conditions (in air at room temperature, 20 °C). Considering that dielectric constant in air as a function of the temperature is in the form:

$$(\epsilon - 1) \times 10^6 = \frac{1}{T} \left[ 210p_s + 180 \left( 1 + \frac{5580}{T} \right) p_w \right] \quad (2.49)$$

where  $p_s$  and  $p_w$  are partial pressure of dry air and vapour water, respectively. For temperature = 20 °C, pressure = 760 Torr and 60 % relative humidity, Eq.2.49 becomes:

$$(\epsilon - 1) = 666.5 \times 10^{-6} \quad (2.50)$$

From the following relation between resonating frequency variation  $f$  and dielectric constant  $\epsilon$ :

$$\frac{\Delta f}{f} = -\frac{1}{2} \frac{\Delta \epsilon}{\epsilon} \quad (2.51)$$

We obtain:

$$\Delta f_{vacuum-air} = -\frac{2.998550 [MHz]}{2} (-666.5 \times 10^{-6}) = 999.27 \text{ kHz} \quad (2.52)$$

We practically consider:

$$\Delta f_{vacuum-air} \simeq 1 \text{ MHz} \quad (2.53)$$

Taking into account that a small systematic frequency error on the accelerating cavity is easily compensated for temperature regulation, the temperature correction leads to the following frequency shift:

$$\Delta f_T [\text{kHz}] = -50 \cdot (T - 20) \text{ °C} \quad (2.54)$$

$$\Delta f_{30-20^\circ C} = -50 \cdot 10 \text{ kHz} = -500 \text{ kHz} \quad (2.55)$$

Resonating frequency at normalised conditions is the sum of previous corrections:

$$f_N = (2998.55 - 1 + 0.5) \text{ MHz} = 2998.05 \text{ MHz} \quad (2.56)$$

Also, close to the following laboratory conditions, we took for reference:

$$\text{Atmospheric pressure} = 760 \text{ Torr}, \quad (2.57)$$

$$\text{Temperature} = 20 \text{ °C} \quad (2.58)$$

$$\text{relative humidity (rh)} = 60 \% \quad (2.59)$$

The frequency shift as a function of the pressure and the relative humidity respects the following relations:

$$\Delta f_p \text{ [kHz]} = -\Delta p = -(p - 760) \text{ [Torr]} \quad (2.60)$$

$$\Delta f_{rh} \text{ [kHz]} = -3 \cdot \Delta rh = -3 \cdot (rh - 60) \text{ [%]} \quad (2.61)$$

### 2.4.3.2 Electromagnetic design of the regular-cells

To evaluate the effectiveness of a regular-cell geometry with regard to the acceleration, there exist some RF quantities able to drive the optimisation of the geometry parameters. These quantities have to be defined in a 3D simulation solver, for instance CST MWS and then analysed in its template based post-processing. The main figures of merit for a regular-cell are given below:

$$E_z \text{ is the complex on-axis accelerating field} \quad (2.62)$$

$$Z_s = \frac{E_e^2}{P_{in}} \text{ is the series impedance} \quad (2.63)$$

$$\alpha = \frac{p_d}{2P_{in}} \text{ is the field attenuation factor} \quad (2.64)$$

$$v_g = \frac{P_{in}}{w_{st}} \text{ is the group velocity} \quad (2.65)$$

$$r_s = \frac{E_a^2}{p_d} = \frac{R}{d} \text{ is the shunt impedance per unit length} \quad (2.66)$$

$$S_c = \Re(\vec{S}) + 1/6\Im(\vec{S}) \text{ is the modified Poynting vector} \quad (2.67)$$

where

$$eV_z = e \left| \int_0^d E_z e^{j\omega \frac{z}{c}} dz \right| \text{ is the regular cell energy gain} \quad (2.68)$$

$$E_e = \frac{V}{d} = \frac{\left| \int_0^d E_z e^{j\omega \frac{z}{c}} dz \right|}{d} \text{ is the effective gradient in the cell (mean value)} \quad (2.69)$$

$$P_{in} = \int_S \frac{1}{2} \Re(\vec{E} \times \vec{H}^*) \cdot \hat{z} dS \text{ is the average input power} \quad (2.70)$$

$$P_d = \frac{1}{2} R_s \int_{S_{ext}} |\vec{H}_{tan}|^2 dS_{ext} \text{ is the average dissipated power in cell} \quad (2.71)$$

$$p_d = \frac{P_d}{d} \text{ is the average dissipated power per unit length} \quad (2.72)$$

$$W_{st} = \frac{1}{4} \mu_0 \int_V \vec{H} \cdot \vec{H}^* dV + \frac{1}{4} \epsilon_0 \int_V \vec{E} \cdot \vec{E}^* dV \text{ is the stored energy in cell} \quad (2.73)$$

$$w_{st} = \frac{W_{st}}{d} \text{ is the average stored energy per unit length} \quad (2.74)$$

$$\vec{S} = \vec{E} \times \vec{H} \text{ is the Poynting vector} \quad (2.75)$$

$$d = \lambda/3 \text{ is the length of cell} \quad (2.76)$$

The 3D electromagnetic codes HFSS and CST MWS allow to simulate periodic structures by using only one period and applying proper boundary conditions. The conditions "master and slave" for HFSS and "periodic" for CST MWS enable to impose a phase shift of 120 degrees between the two outer faces of the regular cell. Then, a simulation with the eigenmode solver finds the frequency at which the electromagnetic field satisfies the desired phase shift. Exploiting the symmetry in the field only a portion of the whole cell can be used for simulations and a condition of perfect magnetic boundary, called "perfect H", is applied.

Starting from the well known S-band accelerating cells design developed by the LAL and the Stanford Linear Accelerator Center (SLAC) for linear accelerators; it is possible to improve the main RF parameters, such as quality the factor, the shunt impedance, the enhancement factor and the group velocity by choosing a suitable shape of the inner surface [48].

The 2D profile of a regular cell with its main geometric dimensions is given in Fig.2.23. The cell period  $\lambda/3$  is set by the mode phase advance,  $2\pi/3$ . The iris is characterized by an elliptical shape with minor and major axes  $2r_1$  and  $2r_2$ , respectively. The cell radius  $b$  is a derived number given by setting the cell resonant frequency,  $f_{RF}$ .

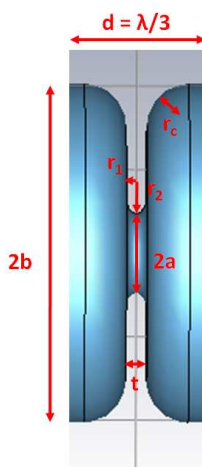


FIGURE 2.23: Main geometry parameters of a regular-cell.

The final shape should be the best solution in geometrical space parameters using several criteria: the optimization of  $r_s/Q$ , the minimization of the ratio between the maximum surface electric field  $E_{smax}$  and the accelerating field on-axis  $E_a$ , which is called electric field enhancement factor [49], the minimization of the modified Poynting vector  $S_c$  as a quantity correlated to the breakdown rate, BDR (Eq.2.47)

A brief description of the main RF parameters depending on the geometry is now presented. The cavity radius,  $b$ , is very sensitive to the frequency of the fundamental mode.

Hence, the tuning of the cell can be easily performed by varying  $b$  without changing any other independent geometric parameters, such as  $a$ ,  $r_1$ ,  $r_2$ . By means of the simulations, the relation between the cavity diameter ( $2b$ ) and the iris diameter ( $2a$ ) has been found. To do this, the value of the ellipticity ratio  $r_2/r_1$ , the iris thickness,  $t$ , and the rounded edge of the cell,  $r_c$ , were fixed in order to maintain a constant resonating frequency.

For the resonant cell, a round inner edge  $r_c$ , gives higher  $Q$  value. Thus, the corresponding quality factor for different values of  $r_c$  has been calculated while the inner radius  $b$  was adjusted to maintain a constant frequency. It has to be noticed that the use of a rounded cell edge  $r_c = 10$  mm leads to increased values in the  $Q$ -factor more than 10%.

The accelerating gradient in normal-conducting structures is limited by RF breakdowns. In order to mitigate possible breakdowns, a thorough study of the cell shape and the corresponding EM field distribution has been carried out. For instance, the iris shape ( $r_1$ ,  $r_2$ ) strongly influences the electric field distribution [50]. The choice of the iris shape derives from an optimization process aiming at minimising the surface electric field at high accelerating gradients (low field enhancement factor). Such a gradient value can be achieved using a shape-optimized elliptical iris. Figure 2.24 shows the ratio  $E_{smax}/E_a$  as a function of the iris ellipticity for fixed values of the iris radius ( $a = 9.5$  mm), the iris thickness ( $2r_1 = 5$  mm) and the rounded edge cell ( $r_c = 10$  mm). The plot shows that for a certain iris aperture there is an optimum elliptical profile of the iris itself that minimizes the surface field. The maximum reduction of the surface field is around 14% with respect to the circular profile [51].

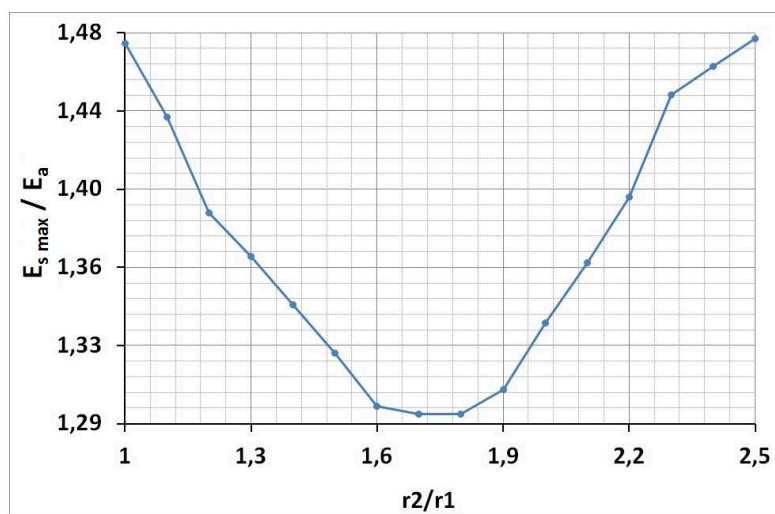


FIGURE 2.24: Maximum surface electric field normalised to on-axis accelerating field as a function of the iris ellipticity  $r_2/r_1$  for,  $a = 9.5$  mm and  $t = 5$  mm [51].

During the design stage, a scan over the iris radius,  $a$ , and the thickness,  $t$ , has been performed in order to find the best couple of these geometry parameters in terms of high

gradient operation performance and reduced power consumption.

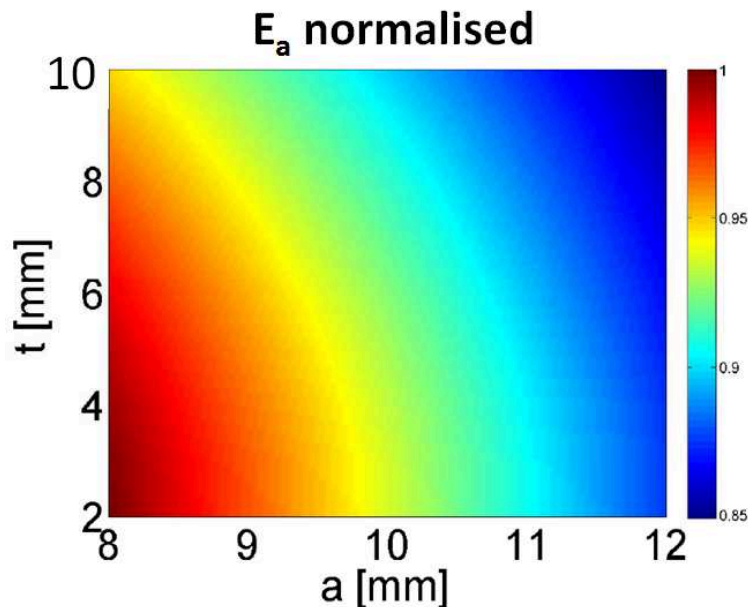


FIGURE 2.25: Normalised on-axis accelerating field as a function of the iris radius and the iris thickness.

Figures 2.25, 2.26 and 2.27 represent the trend of normalised accelerating gradient,  $r_s/Q$  and  $v_g/c$ . The radius and the thickness of the iris are both very important parameters which influence several RF features. For a fixed iris thickness, the on-axis electric field is more important for smaller iris radius as we can see from Fig.2.25.

Hence  $r_s/Q$  is higher for smaller  $a$ . However, a structure consisting of purely small-aperture cells would not be practical as the group velocity in these cells is very small and leads to high filling time. Therefore, normal conducting accelerating structures should be built with smaller iris radii for obtaining higher  $r_s/Q$ , which results in reduction of power dissipation on the walls. In addition, lower enhancement factor leads to increase the accelerating gradient. Moreover, a large iris aperture ( $2a$ ) reduces the filling time of the structure itself and leads to shorter required input pulse length. Usually, shorter pulses are preferred as the RF breakdown probability increases with pulse length. It is easy to see from Fig.2.26 and 2.27 that the suitable iris radius must be chosen to obtain an high  $r_s/Q$  value for a reasonable value of  $v_g/c$ . That means a filling time lower than the pulse length of the RF power source.

Figure 2.28 shows the ratio between the maximum surface electric field and the accelerating gradient (field enhancement factor). We can see that the field enhancement factor decreases when the iris radius is decreasing. Also, this quantity become smaller when the iris thickness is increasing.

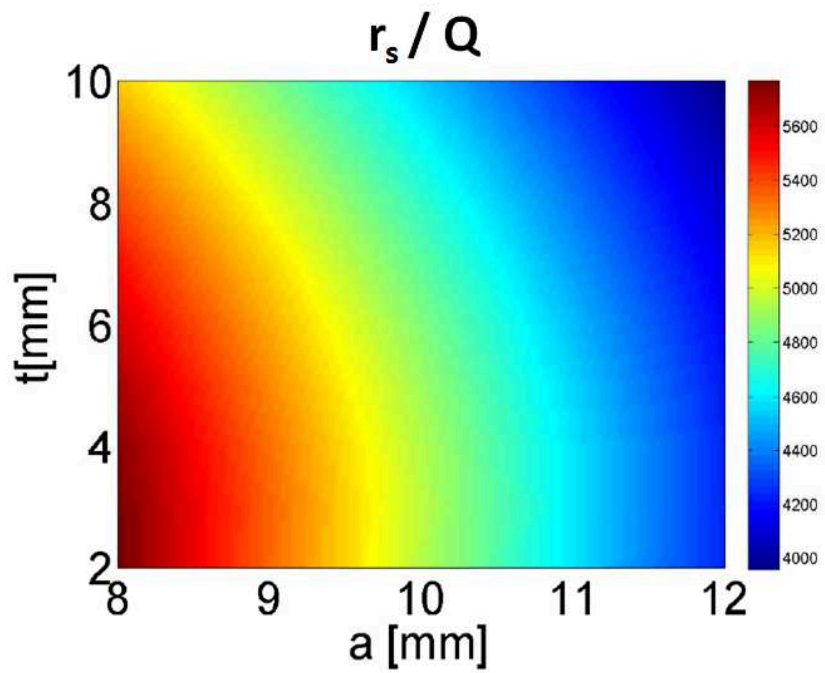


FIGURE 2.26: Shunt impedance over Q-factor as a function of the iris radius ( $a$ ) and the iris thickness ( $t$ ).

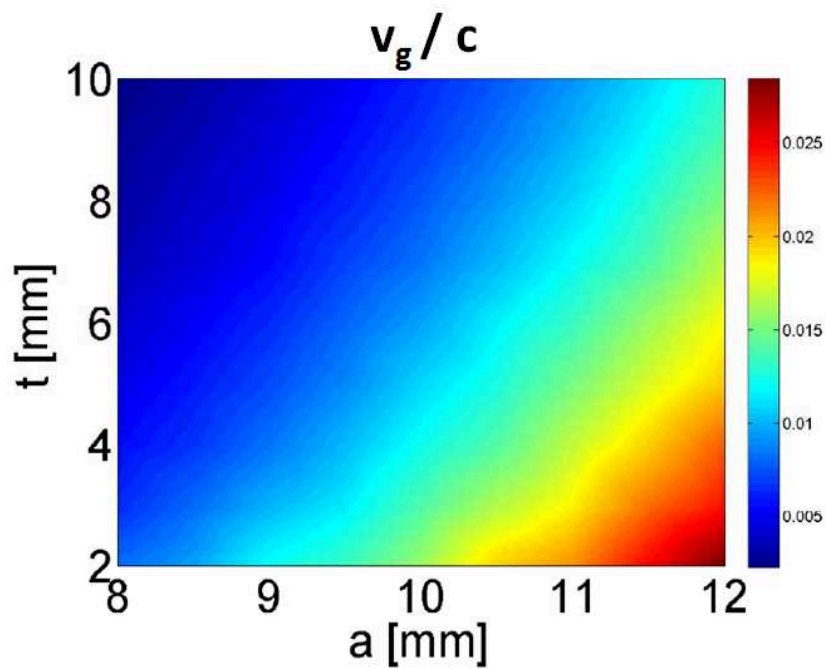


FIGURE 2.27: Group velocity as a function of the iris radius ( $a$ ) and the iris thickness ( $t$ ).

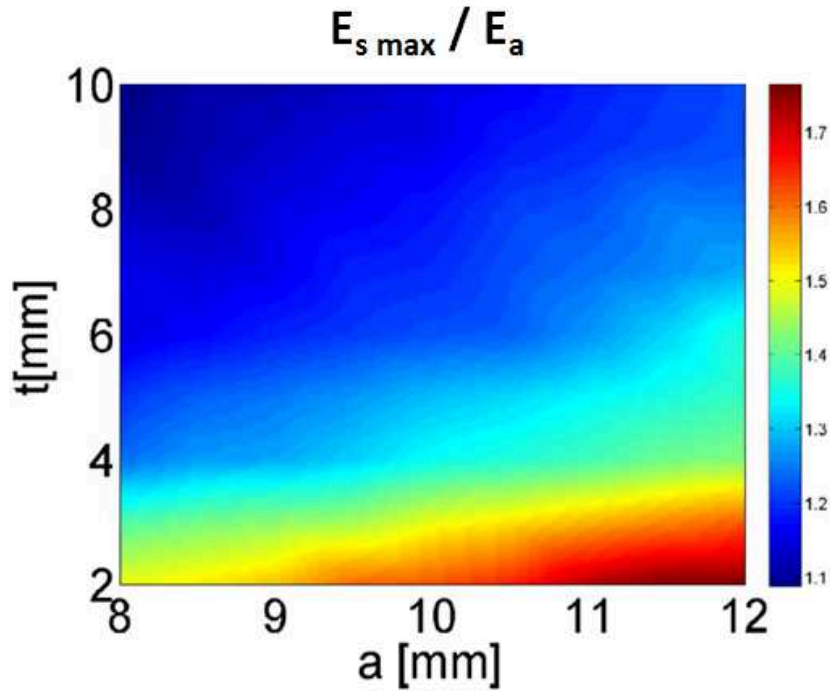


FIGURE 2.28: Maximum surface electric field over on-axis electric field as a function of the iris radius ( $a$ ) and the thickness ( $t$ ).

Since  $S_c$  is available from numerical RF simulator for every point of the structure, this local quantity can be considered as a new constraint to explain the limited high-gradient structure performance due to a vacuum RF breakdown [52]. It has to be noticed that the iris aperture range has to be reasonably large in order to guarantee a high acceleration efficiency and, at the same time, a low power dissipation on the cavity wall, short filling time and a good pumping speed. The short filling time,  $t_f = L/v_g$ , allows using short RF pulses, thus reducing the BDR. In order to have a quantitative approach, it has been decided to find the cell geometry which minimises the quantity  $\mu$  [53], [54]:

$$\mu = \frac{P_{in} S_c}{E_a^2 E_a^2} = \frac{v_g S_c / E_a^2}{\omega r_s / Q} \quad (2.77)$$

where  $\omega$  is the angular frequency. This corresponds to have simultaneously the minimum power consumption and the minimum risk of breakdown (based on the  $S_s$  model) for a given accelerating gradient (Fig.2.29). In addition, the quantity  $S_{cmax}/E_a^2$  that is independent of the power consumption has been plotted in Fig.2.30. Once again we can see that the small value of  $\mu$  and  $S_{cmax}/E_a^2$  occur for small iris radii and high thickness.

We can deduce from above that all geometrical dimensions of the regular-cell have direct impacts on the RF performances. Therefore the design of the cell geometry is a difficult process because an improvement in one RF parameter usually results in a degradation in

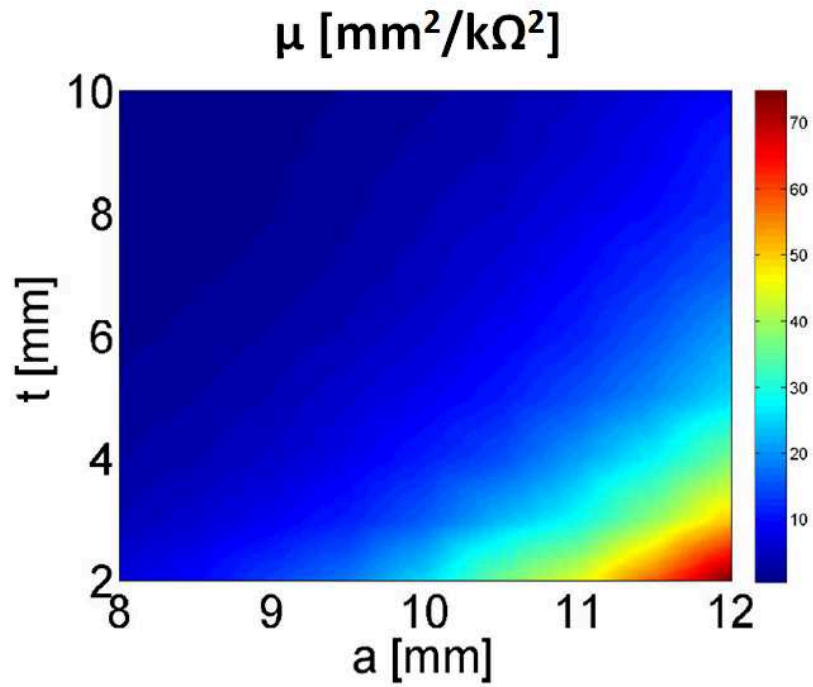


FIGURE 2.29:  $\mu$ -parameter for a minimum power consumption and minimum risks of BDR as a function of the iris radius ( $a$ ) and the iris thickness ( $t$ ).

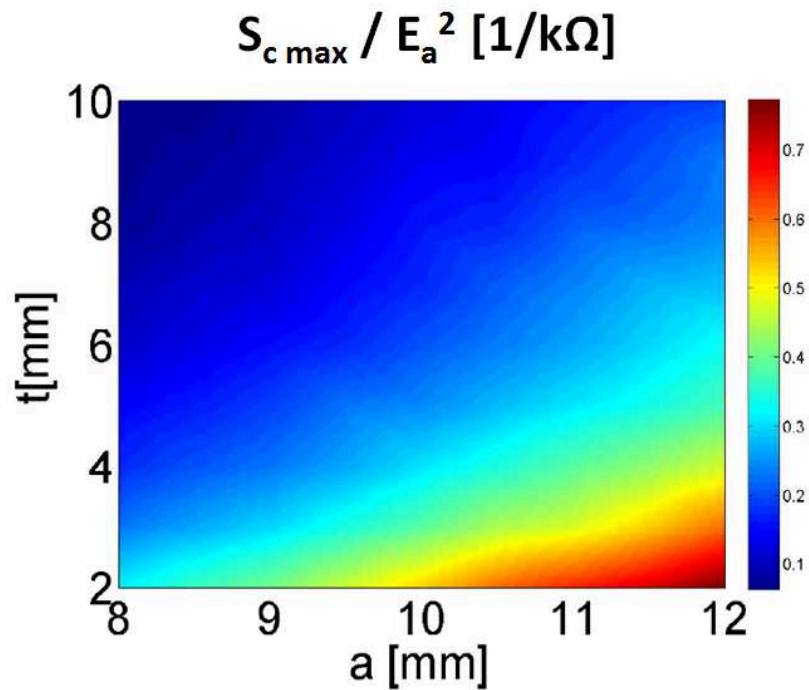


FIGURE 2.30: Modified Poynting vector over average accelerating field squared as a function of the iris radius ( $a$ ) and thickness ( $t$ ).

another one. That is why, the optimum design of the cell is the consequence of a series of trade-off between different cavity parameters aiming at accomplish all operational requirements with respect to the structure machining.

The final dimensions and the shape of the regular cell has been optimized to obtain a minimum modified Poynting vector and a low maximum surface electric field in the iris regions, an average accelerating gradient able to provide the desired energy gain with respect to the available input power and a relatively high group velocity. The cell-to-cell iris thickness,  $t$ , has been chosen in order to get an acceptable compromise between the desired effective shunt impedance, the acceptable filling time and the mechanical rigidity. It is fixed at 5 mm along the structure. These irises have an elliptical cross-section to reduce the surface electric field. The rounding of the cell edge ( $r_c = 10$  mm) noticeably improves the quality factor by more than 10% and reduces the wall power consumption. The optimized cell shape is the result of a trade-off between RF efficiency, accelerating gradient, optimal filling time and breakdown limitations.

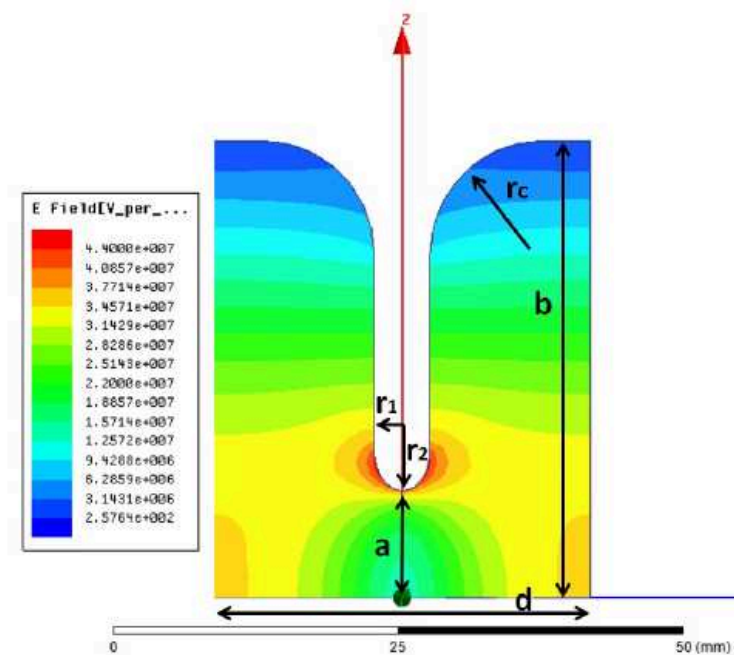


FIGURE 2.31: 2D section and electric field distribution of the half single cell, for  $2a = 19$  mm,  $t = 5$  mm,  $P_{in} = 20$  MW (peak power).

As an example, for the previous set of geometry parameters, the electric field and the modified Poynting vector  $S_c$  distributions for one quarter of the full cell are shown in Fig.2.31 and Fig.2.32. It is easy to see that the maximum values of the surface electric field and the modified Poynting vector occur around the iris region. Because of this, operating at high-gradient requires a special attention to minimize these quantities in that region [55].

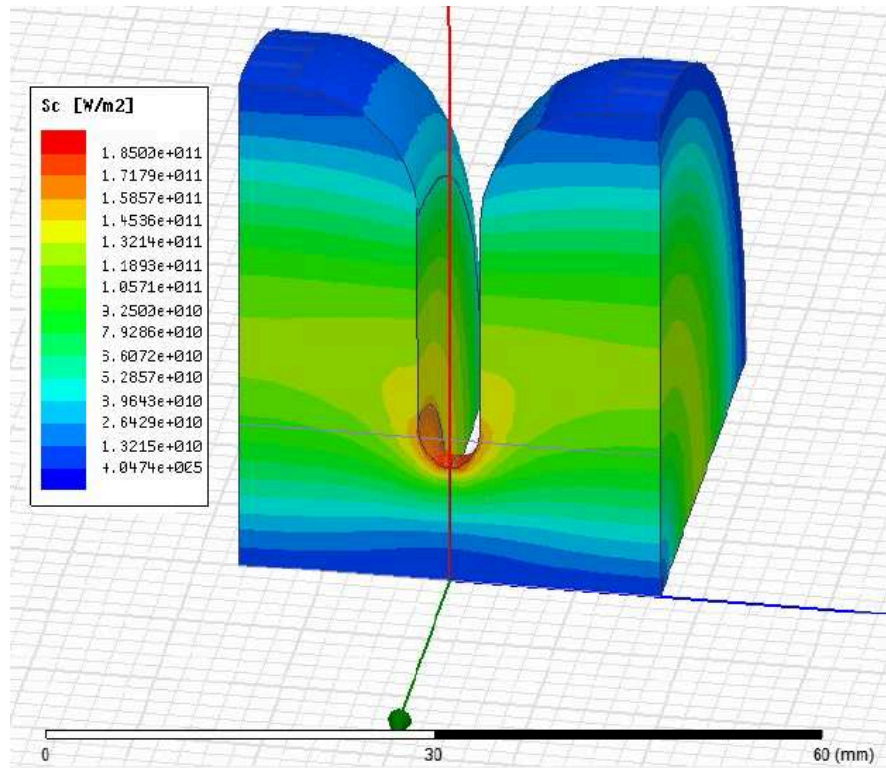


FIGURE 2.32: Distribution of the modified Poynting vector inside in one-quarter regular cell, for  $2a = 19$  mm,  $t = 5$  mm,  $P_{in} = 20$  MW (peak power).

Taking into account all the previous aspects, one can deduce that the best compromise for the design optimisation is to consider a reasonable iris aperture range in order to guarantee a high-accelerating efficiency with the minimum risks of breakdown, and at the same time, short filling time compared to the RF pulse and a good pumping speed. These aspects lead to consider the iris radius,  $a$ , for the final high-gradient accelerating section configuration in the range between 11.5 and 8.5 mm.

The simulated frequency sensitivity for different geometrical parameters of the regular cell are reported in the Tab.2.4. From these quantities one can extrapolate the maximum tolerances of manufacturing and how to correct errors with a proper cell tuning.

TABLE 2.4: Frequency sensitivity with respect to the main parameters.

Parameter	Frequency sensitivity
Cell radius ( $b$ )	-75 kHz/ $\mu\text{m}$
Iris half aperture ( $a$ )	15 kHz/ $\mu\text{m}$
Iris thickness ( $t$ )	5 kHz/ $\mu\text{m}$
Cell length ( $d$ )	-5 kHz/ $\mu\text{m}$

### 2.4.3.3 Coupler design techniques

A TW accelerating section boosts the particle beam by means of high level EM fields. The input power at the entrance of the section may be of the order of MW. Usually this RF power is provided by klystrons. The EM wave generated by the klystron is transmitted to the cavity by a rectangular waveguide operating at  $TE_{10}$ -mode. In order to impart the maximum energy to the beam while protecting the power supply circuit, a good coupling between the waveguide and the accelerating structure is required. The coupling consists in reducing as much as possible power reflections at the entrance of the section.

In our case, the coupling system is illustrated in Fig.2.33. The waveguide is connected to the periodic structure through an aperture in a cavity which is usually called coupler. For travelling wave sections, another coupler is connected to the output waveguide at the end of the structure. This coupler is identical to the input one, for CI structures. Single

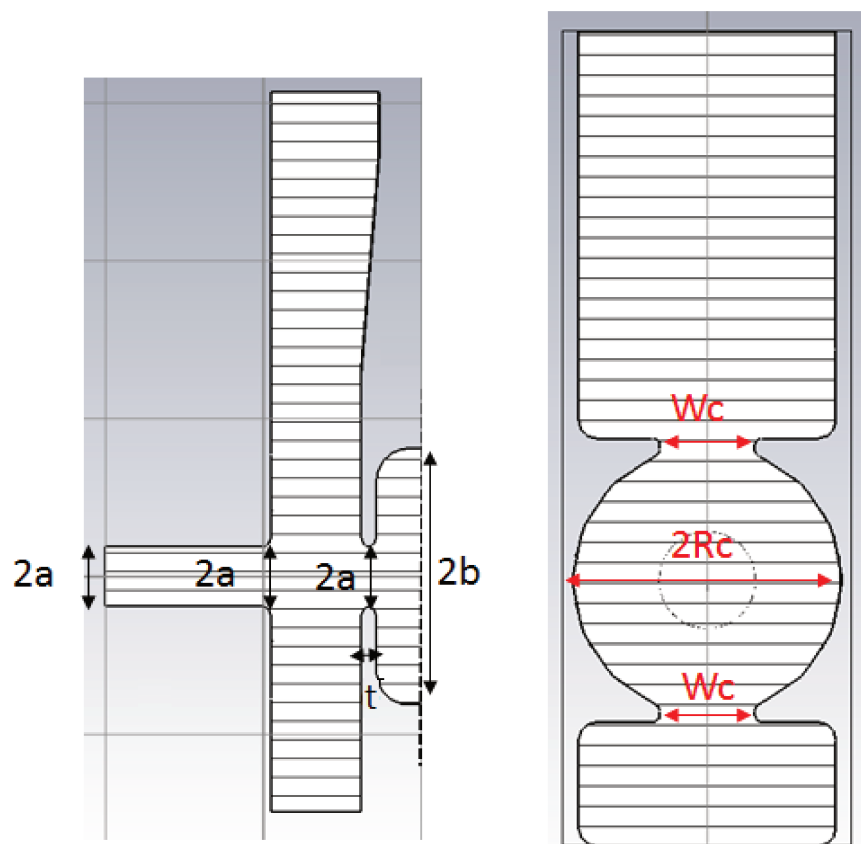


FIGURE 2.33: Geometry parameters of the coupler design.

coupling slots introduce a distortion in the field distribution and multi-pole components can appear and affect the beam dynamics. The simple way to compensate the dipole field is to introduce a symmetric compensating slot opposite to the RF input. The

opposite slot is not feed by RF power and can be used, for instance, for pumping the structure.

The coupling aperture consists in a rounded slot opened between the coupling cell and the waveguide. Its dimensions have been optimized to match the waveguide mode  $TE_{10}$  to the accelerating mode  $TM_{010}$ -like [56]. The surfaces of that slot have been strongly rounded to reduce the pulsed heating.

A TWS equipped with couplers and waveguides has been simulated with the EM solvers such as CST MWS and HFSS. The main goal of the coupler tuning is to minimize the reflected power at the input/output coupling port but also to verify two conditions: the phase advance per cell of the TW structure must be equal to the nominal value ( $2\pi/3$  in our case), the axial electric field amplitude must be flat if the structure is considered without losses (perfect conductor). The geometrical parameters used for the tuning depend in our case on the slot width ( $W_c$ ) and the radius of the coupling cell ( $R_c$ ), as illustrated in the Fig.2.33. This can be done using different techniques.

First, the optimisation technique in CST Studio and HFSS allow the user to check how a device behaviour is affected as its properties change and to find the parameters which maximise and minimise a given effect or fulfill a certain goal. This can optimise any property of the model that can be parameterized, such as dimensions, material properties, etc. This optimizer tool allows optimization tasks to run automatically. For very complex systems such as long accelerating structure or with large number of variables high-performance computing techniques are available to speed up simulations and optimization, but this requires a faster and more powerful computer. For example CST

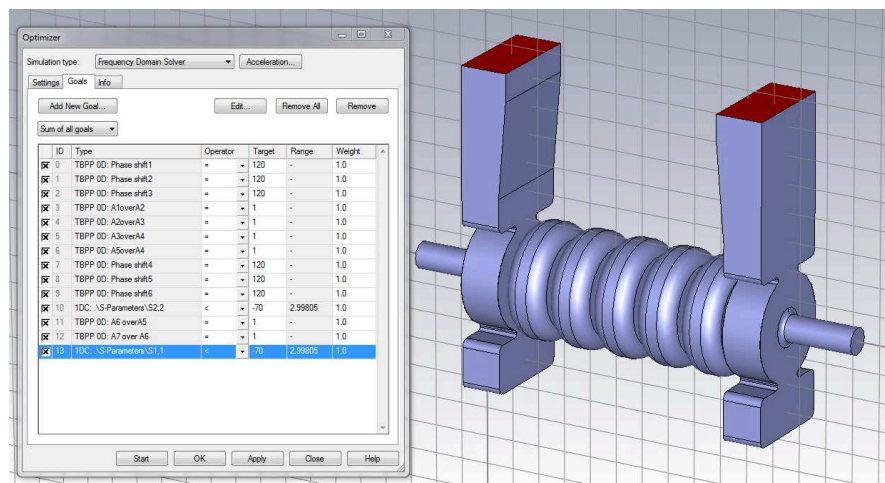


FIGURE 2.34: CST Studio optimizer tool.

optimizer allows us to define different goals for the case of 7-cells constant-impedance prototypes, such as the minimization of input and output reflection coefficients, the phase advance per cell and the flatness of axial electric field along the structure (see

Fig.2.34). The latter is defined as the ratio between the amplitudes of two adjacent cells  $A_{i+1}/A_i=1$ . To achieve the goals, we defined a range for the variables  $W_c$  and  $R_c$  where the optimizer tool provides the optimum values.

Second, the choice of  $W_c$  and  $R_c$  is determined by applying the "method of the shorts" [57]. We apply this method to the geometry designed in Fig.2.35 (right side) using HFSS solver. We set a phase advance per cell of  $2\pi/3$  of the periodic structure at a frequency of 2998.05 MHz in air at 20 °C. The geometry in Fig.2.35 represents the input waveguide that is connected to the coupling cavity plus a half-cell considered as a part of the coupler. The half-cell is closed with a perfect electric field plane that is automatically considered as a boundary condition in HFSS ("Perfect-E"). If we define a port at the entrance of the waveguide  $\Gamma$ , the simulation can provide the reflection coefficient with an unit module and a certain phase  $\Gamma_s(0)$ . It has been demonstrated that, for good coupling, the reflection coefficient ( $S_{11}$ ) of the scattering matrix has to be equal to zero [58]. The latter condition is fulfilled as long as the following conditions are satisfied:

- by adding a cell (middle of Fig.2.35) and performing the simulation we obtain  $\Gamma_s(1)$  with a phase shift of -240 degrees with respect to the  $\Gamma_s(0)$ ,
- by adding another cell (left side of Fig.2.35) and performing the simulation we obtain  $\Gamma_s(2)$  with a phase shift of -240 degrees with respect to the  $\Gamma_s(1)$

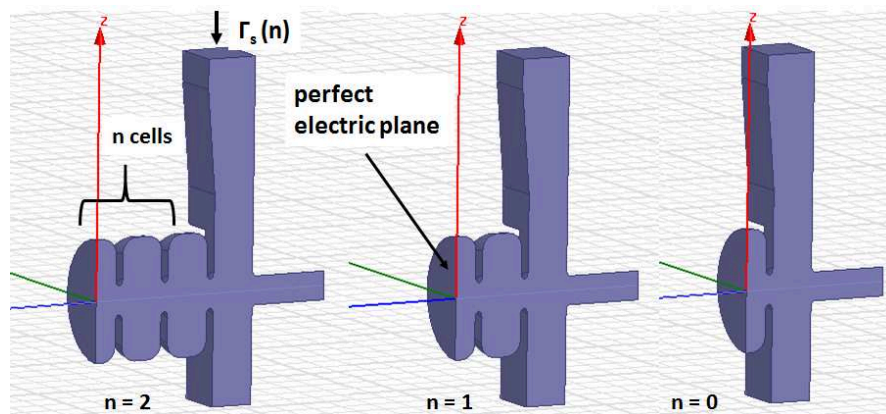


FIGURE 2.35: HFSS model of the three short-circuited structures.

If  $S_{11} = 0$ , the reflection coefficients previously calculated lay on the complex plane and constitute an equilateral triangle inscribed in a circumference with radius equal to one [58]. The mathematical condition are expressed by

$$S_{11} = 0 \longleftrightarrow \frac{\Gamma_s(n+2)}{\Gamma_s(n+1)} = \frac{\Gamma_s(n+1)}{\Gamma_s(n)} = e^{-j2\phi} \quad (2.78)$$

with  $|\Gamma_s(n)| = 1$ . The previous conditions result in:

$$\angle\Gamma_s(2) - \angle\Gamma_s(1) = -240^\circ \quad (2.79)$$

$$\angle\Gamma_s(1) - \angle\Gamma_s(0) = -240^\circ \quad (2.80)$$

It has been demonstrated [57], for small  $|S_{11}|$ , that:

$$|S_{11}| \simeq \frac{1}{2 \sin^2 \phi} \sqrt{\frac{(\theta_{21} + \theta_{10})^2}{4 \cos^2 \phi} + \theta_{10}^2 - \theta_{10}(\theta_{21} + \theta_{10})} \quad (2.81)$$

where  $\theta_{10}$  and  $\theta_{21}$  are the phase distortions at the waveguide input due to a non-ideal coupler and written as:

$$\theta_{10} = \frac{\angle[\Gamma_s(1)/\Gamma_s(0)]}{2} + \phi \quad (2.82)$$

$$\theta_{21} = \frac{\angle[\Gamma_s(2)/\Gamma_s(1)]}{2} + \phi \quad (2.83)$$

$$(2.84)$$

By using HFSS as EM simulator and an algorithm developed with MATLAB for achieving the goals, an iterative process allows to find the right values of  $W_c$  and  $R_c$  by solving the following system of partial differential linear equations:

$$\Delta\varphi_{21} = \left. \frac{d\varphi_{21}}{dR_c} \right|_{dW_c=0} \Delta R_c + \left. \frac{d\varphi_{21}}{dW_c} \right|_{dR_c=0} \Delta W_c \quad (2.85)$$

$$\Delta\varphi_{10} = \left. \frac{d\varphi_{10}}{dR_c} \right|_{dW_c=0} \Delta R_c + \left. \frac{d\varphi_{10}}{dW_c} \right|_{dR_c=0} \Delta W_c \quad (2.86)$$

where  $\varphi_{21} = \angle\Gamma(2) - \angle\Gamma(1)$ ,  $\varphi_{10} = \angle\Gamma(1) - \angle\Gamma(0)$  and where the partial derivatives represent the sensitivity of the parameters  $\varphi_{21}$  and  $\varphi_{10}$  with respect to  $R_c$  and  $W_c$ , respectively. The quantities  $\Delta\varphi_{21}$  and  $\Delta\varphi_{10}$  are the differences between the values obtained at each iteration with respect to the goal value:

$$\Delta\varphi_{21} = -240 - \varphi_{21} \quad (2.87)$$

$$\Delta\varphi_{10} = -240 - \varphi_{10} \quad (2.88)$$

Let us consider the system of linear Eq. 2.85 and 2.86 under the following matrix form:

$$\begin{pmatrix} \Delta\varphi_{21} \\ \Delta\varphi_{10} \end{pmatrix} = \begin{pmatrix} \left. \frac{d\varphi_{21}}{dR_c} \right|_{dW_c=0} & \left. \frac{d\varphi_{21}}{dW_c} \right|_{dR_c=0} \\ \left. \frac{d\varphi_{10}}{dR_c} \right|_{dW_c=0} & \left. \frac{d\varphi_{10}}{dW_c} \right|_{dR_c=0} \end{pmatrix} \begin{pmatrix} \Delta R_c \\ \Delta W_c \end{pmatrix} = M \begin{pmatrix} \Delta R_c \\ \Delta W_c \end{pmatrix}$$

Inverting the matrix  $M$ , the variations  $\Delta R_c$  and  $\Delta W_c$  to add to the starting values  $R_c$  and  $W_c$  can be obtained:

$$\begin{pmatrix} \Delta R_c \\ \Delta W_c \end{pmatrix} = M^{-1} \begin{pmatrix} \Delta \varphi_{21} \\ \Delta \varphi_{10} \end{pmatrix}$$

This procedure has to be iteratively applied until the conditions 2.79 and 2.80 are satisfied within a reasonable error, namely 1 degree.

The CST Studio optimizer tool and the "method of the shorts" by HFSS have been applied to the EM design for different constant-impedance accelerating structure prototypes. Optimum values  $R_c = 37.71$  mm and  $W_c = 26.49$  mm have been obtained for given regular cell dimensions ( $2b = 81.11$  mm,  $2a = 19$  mm,  $t = 5$  mm,  $r_c = 10$  mm and  $r_2/r_1 = 1.7$ ) have been found.

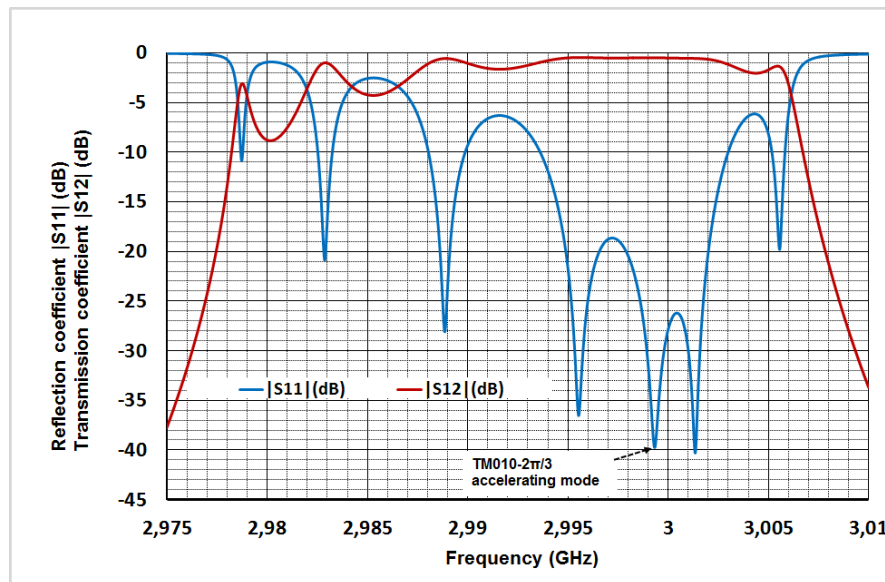


FIGURE 2.36: Reflection  $|S_{11}|$  and transmission  $|S_{12}|$  coefficient, as a function of the frequency, for a 7-cells copper prototype ( $|S_{11}| \simeq -40$  dB,  $|S_{12}| \simeq -0.5$  dB for the  $TM_{010-2\pi/3}$  mode).

Figure 2.36 shows the final reflection coefficient ( $S_{11}$ ) and insertion loss ( $S_{12}$ ) at the structure input port for a 7-cells S-band constant-impedance copper prototype. The coupler in this example has been tuned at 2998.05 MHz (in air at 20 °C). The minima ( $TM_{010-\varphi_k}$ , where  $\varphi_k = k\pi/(N-1)$ , with  $0 \leq N \leq 7$ ,  $N$  is the number of cells) are located in the pass band of the TW periodic structure and their number is equal to the number of cells. By increasing the number of cells we progressively increase the number of minima in the pass band.

Figure 2.37 shows the amplitude and the phase distribution of the longitudinal electric field along the structure. The simulated phase advance per cell is equal to  $120^\circ \pm 0.5$ .

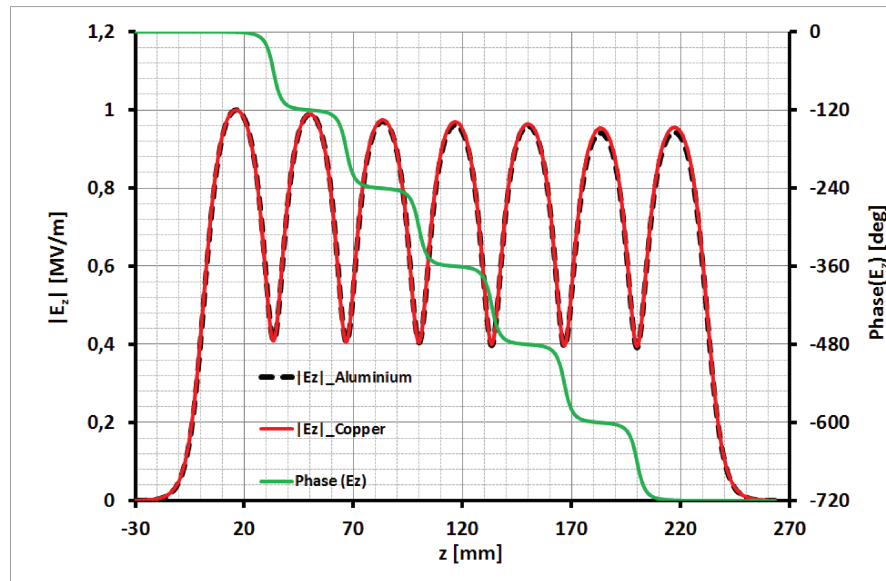


FIGURE 2.37: Normalised on-axis electric field amplitude, phase advance per cell along the prototype's axis (7-cells aluminium and copper prototype for the  $TM_{010-2\pi/3}$  accelerating mode).

#### 2.4.3.4 RF design of the 16-cells copper prototype

The 16-cells copper prototype is a TW constant-impedance section working on the  $2\pi/3$  mode at 2.9991 GHz in vacuum at 20 °C (2998.55 MHz at 30 °C). The design of this structure has been performed using the previous techniques. The goals of this prototype are the test of the geometry design, the manufacturing procedure and the check of the validity of all technical choices.

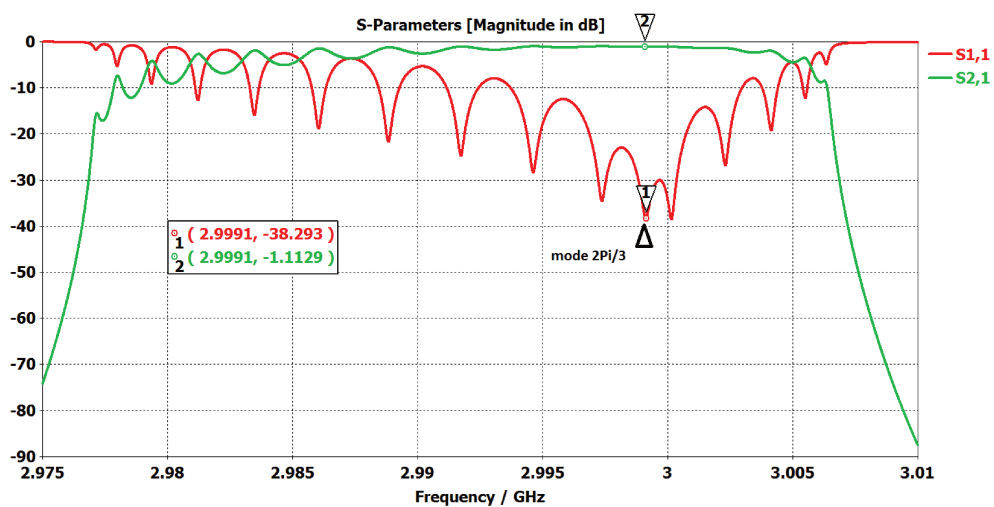


FIGURE 2.38: Reflection  $|S_{11}|$  and  $|S_{21}|$  transmission coefficients, as a function of the frequency, for the 16-cells copper prototype (in vacuum at 20 °C).

The reflection coefficient ( $S_{11}$ ) at the structure input port and the insertion loss ( $S_{21}$ )



The simulated amplitude and phase advance per cell of the accelerating on-axis electric field  $TM_{010-2\pi/3}$  mode are reported in Fig.2.40. The simulated phase advance per cell is equal to  $120^\circ \pm 0.5^\circ$ . The simulated electric field module decreases along the length of the CI structure as the transmitted power drops due to the finite resistivity of the copper.

After the EM design, the performance of this prototype have been studied from the point of view of the high-gradient limiting factors, such as the breakdown probability and pulsed heating. As we have already mentioned, the RF breakdown is one of the major factors determining the performance of the high-gradient accelerating section.

As design guideline for a new RF structures,  $S_c$  should not exceed  $4 \text{ MW/mm}^2$  if the structure is supposed to operate at a breakdown rate smaller than  $10^{-6}$  bpp/m and pulse length of 200 ns [33, 34].

By re-scaling these data to the pulse length of the Thomx linac, i.e.  $3 \mu\text{s}$  flat top, the maximum threshold in this case should not exceed  $S_{cmax} = 1.6 \text{ MW/mm}^2$  if the structure is supposed to operate at BDR smaller than  $10^{-6}$  bpp/m, which corresponds to the acceptable breakdown rate for a medical accelerator. For an input power of 20 MW the simulated maximum modified Poynting vector  $S_{cmax}$  is  $0.19 \text{ MW/mm}^2$ , as shown in Fig.2.41. It is far below the limit of  $1.6 \text{ MW/mm}^2$  for a BDR of  $10^{-6}$  bpp/m. This limit is derived for structure which were constructed on the base on the high gradient assembly procedure. This procedure includes keeping everything rather clean and having high-temperature bonding or brazing cycle in hydrogen or in vacuum.

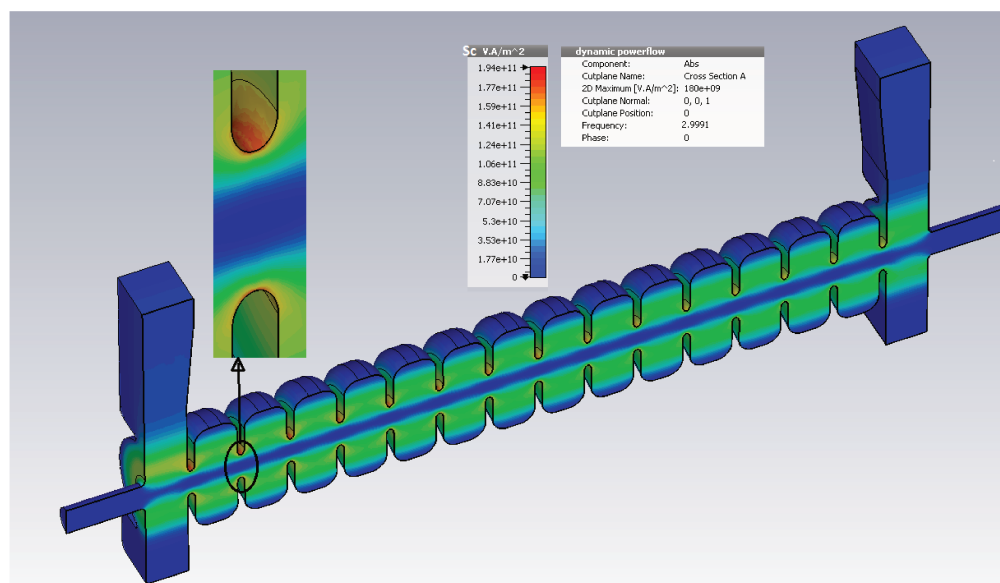


FIGURE 2.41: Distribution of the modified Poynting vector in the 16-cells copper prototype.

In fact, RF power enters the structure through the slot where the surface currents flowing along the edges can achieve very high densities. These high currents can give localized losses and create hot spots leading to dangerous breakdown effects. The cause of this phenomena is known as pulsed heating and has to be carefully evaluated and monitored in each place of the designed structure where there are high surface currents (i.e. high magnetic field). RF pulsed heating causes a temperature rise  $\Delta T$  on the metal at each RF pulse.  $\Delta T$  is written as:

$$\Delta T [^{\circ}\text{C}] = 127 |H_{\parallel} [\text{MA}/\text{m}]|^2 \sqrt{f_{\text{RF}} [\text{GHz}]} \sqrt{t_p [\mu\text{s}]} \quad (2.89)$$

The subsequent cooling between pulses causes some surface fatigue, namely cyclic stress. Cycling stress can give rise to micro-cracks that may decrease the heat conductivity and in some conditions cause RF breakdowns. Usually the crucial areas is the waveguide-to-coupling cells.

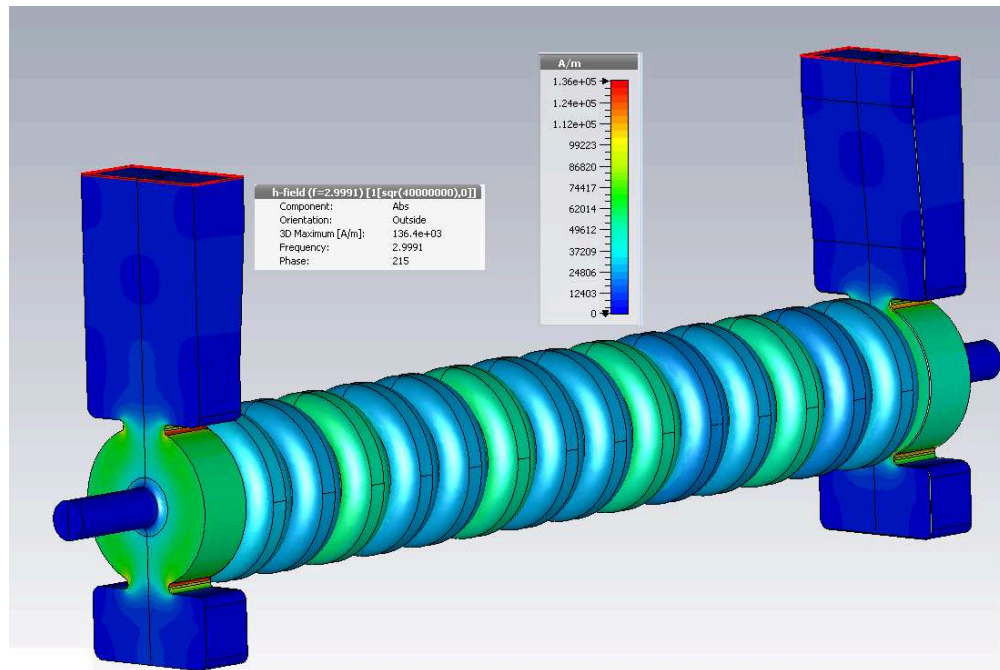


FIGURE 2.42: Distribution of the surface magnetic field in 16-cells copper prototype.

There exists practical safe limit in case of S-band copper structures:

1. if  $\Delta T < 50$  °C, couplers damage are practically avoided,
2. if  $50$  °C  $\leq \Delta T \leq 110$  °C, there is some probability of couplers damage,
3. if  $\Delta T \geq 110$  °C, damage to the coupler regime has a high probability of occurrence.

In our design, the coupling hole has been rounded to reduce the pulsed heating. A fillet of 2 mm has been applied to the coupling slot. The surface magnetic field on the

coupler has been calculated using CST MWS as it is reported in Fig.2.42. For an input power  $P_{in} = 20$  MW and an RF flat top pulse length  $t_p = 3 \mu s$ , we have obtained a peak surface magnetic field  $H_{||}$  equal to  $1.36 \times 10^5$  A/m. We have estimated that the temperature increase due to the pulsed heating on the coupler was less than  $8^\circ\text{C}$ , below the "safe limit".

Table 2.5 reports the main parameters that are the basis for the structure design.

TABLE 2.5: Main parameters of 16-cells CI TW copper prototype (HFSS and CST results).

Parameters	values	unit
Structure type	constant impedance (CI)	
Working mode	$TM_{010}$ -like	
Repetition rate	50	Hz
RF pulse	3	$\mu s$
Frequency design	2999.1 ( in vacuum)	MHz
Temperature design	20	$^\circ\text{C}$
$v_g/c$	0.00913	
Cell phase advance	$2\pi/3$	
Number of cells	14 + 2 coupling cells	cell
Structure length	0.628 (with beam pipes)	m
Iris radius	9.5	mm
Quality factor (unloaded)	15154	
Shunt impedance	81.4	$M\Omega/m$
Series impedance ( $Z_c$ )	37	$M\Omega/m^2$
Attenuation factor	0.226	Neper/m
Filling time	194	ns
Input power	20	MW
Output power	$0.8 \cdot P_{in}$	MW
$E_e$ in/out	28 - 25	MV/m
$\langle E_e \rangle$	26	MV/m
$E_a$ in/out	35 - 31	MV/m
$\langle E_a \rangle$	33	MV/m
$E_{smax}$	42	MV/m
Energy gain	13.3	MeV
Max Modified Poynting vector ( $S_{cmax}$ )	$0.194 \times 10^{12}$ at 20 MW	$W/m^2$
$E_{smax}/\langle E_a \rangle$	1.27	
$E_{smax}/\langle E_e \rangle$	1.62	
$S_{cmax}/\langle E_a \rangle^2$	0.0002	A/V
$H_{smax}$ at 20 MW	136	kA/m
$H_{smax}/\langle E_a \rangle$	4.12	kA/MV
Pulsed heating $\Delta T$	$\sim 8$	$^\circ\text{C}$

### 2.4.3.5 Mechanical drawings of the 16-cells copper prototype

The mechanical design of the 16-cells CI copper prototype has been carried out with CATIA [59], a 3D modeling software for mechanical 3D CAD drawings. Figure 2.43 shows the details of a regular cell. All the cells are identically machined disc-loaded cell with elliptical iris shape. The cells present a step on the outer edge for cell assembly

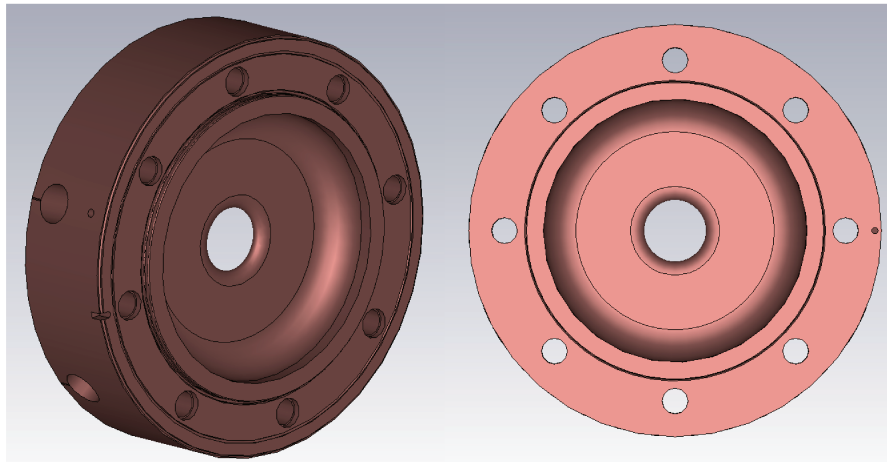


FIGURE 2.43: 3D mechanical drawings of a regular cell.

and alignment. Each regular cell and coupling cell present four tuning holes. The tuners have a diameter of 14 mm and wall thickness of 2 mm. This last parameter has to allow enough deformation of the outer cavity walls to produce a tuning effect but without rupture (see Fig.2.43, left side). In addition, in each cell eight cooling channels are directly drilled in the copper body as shown in the cross view of the cell (Fig.2.43, right side).

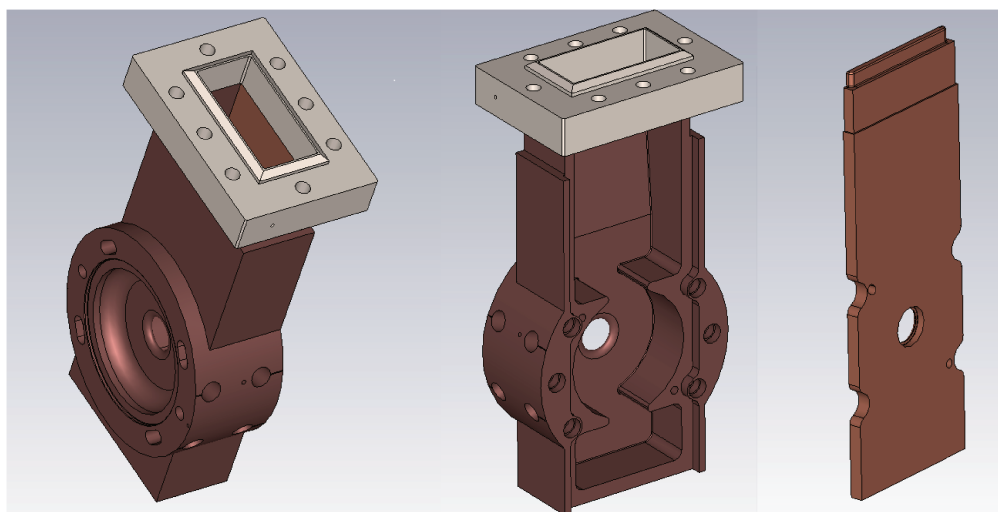


FIGURE 2.44: 3D mechanical drawings of couplers.

Figure 2.44 illustrates the input and output copper couplers. Basically the couplers are composed of two different parts: the body and the cover. These mechanical parts are separately machined. A coupler body consists in the coupling cell with the waveguide and the stub as shown in the middle of the Fig.2.44 and in one-half regular cell which its volume is shown in the left side of Fig.2.44.

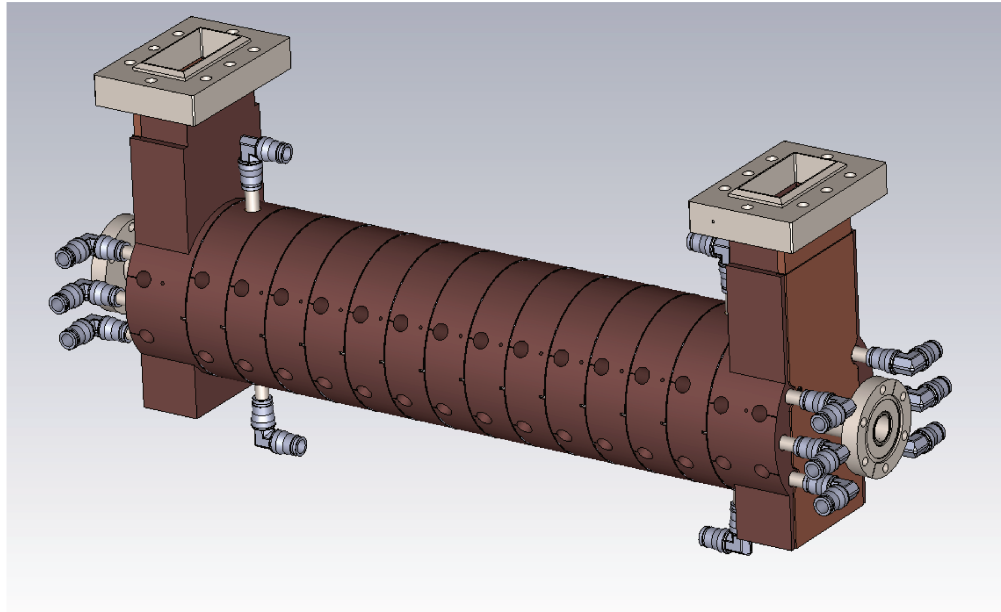


FIGURE 2.45: 3D mechanical drawings of the 16-cells copper prototype with two couplers and regular accelerating cells.

The screw holes have been distributed around the coupler profile and the cover is screwed to the coupler body. At the end, a stainless steel flange is connected to the RF window.

The prototype is made up of two couplers and thirteen regular cells, as it is illustrated in Fig.2.45. The cooling system is integrated in the body. Once all the mechanical parts are fabricated, the assembly phase will start from the input coupler, then all the regular cells will be stacked together and finally the output coupler will be connected to the structure.

#### 2.4.3.6 RF design of a high-gradient compact S-band accelerating section

We present in this section the design of a high-gradient compact S-band accelerating section. It is a travelling wave constant-gradient type with 95 regular cells and 2 coupling cells, resonating at a frequency of 2998.5 MHz at 30 °C at the  $TM_{010-2\pi/3}$ -mode.

The constant gradient design was chosen over the constant impedance design for ThomX Linac for reasons which include the uniformity of the power dissipation, and lower value

for the peak surface electric field and the modified Poynting vector for the same energy gain.

A constant accelerating gradient along the structure is maintained by suitable shaping the iris aperture of each cell. The iris radius is then decreasing along the structure in order to have a flatness of the accelerating field amplitude through the whole section and to maintain a uniform cell to cell phase advance of 120 degrees in the accelerating mode.

The design of a linear tapered structure can be performed by obtaining at first a set of the main RF figure of merits of regular cells with different iris radius. The cell diameter ( $2b$ ) has been set to maintain the required phase advance at the design frequency according to a precise law. The semi-empirical relation between the cell diameter and the iris aperture is a polynomial expression in the form:

$$2b \text{ [mm]} = 79,844 - 0,0542 \cdot (2a) + 0,0056 \cdot (2a)^2 + 0,00004 \cdot (2a)^3 \text{ [mm]} \quad (2.90)$$

To achieve the constant-gradient design, the iris radius ( $a$ ) was tapered from 11.5 mm to 8.68 mm. This range of iris radius was chosen as a compromise between maximizing the energy gain and minimizing the filling time.

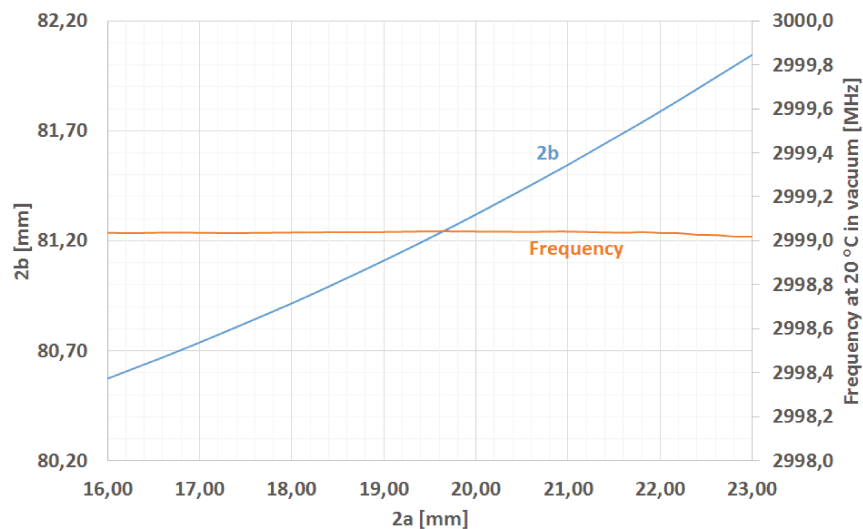


FIGURE 2.46: Cell diameter (blue line) and resonating frequency of the mode  $TM_{010-2\pi/3}$  (orange line) as a function of the iris diameter.

The coefficients of Eq.2.90 have been determined with CST MWS where the regular cell has been simulated using periodic conditions. As shown in Fig.2.46, the resonating frequency keeps constant and equal to the frequency design (2999.05 MHz in vacuum at 20 °C) and not depend from the variation of the iris ( $2a$ ) and cell diameters ( $2b$ ).

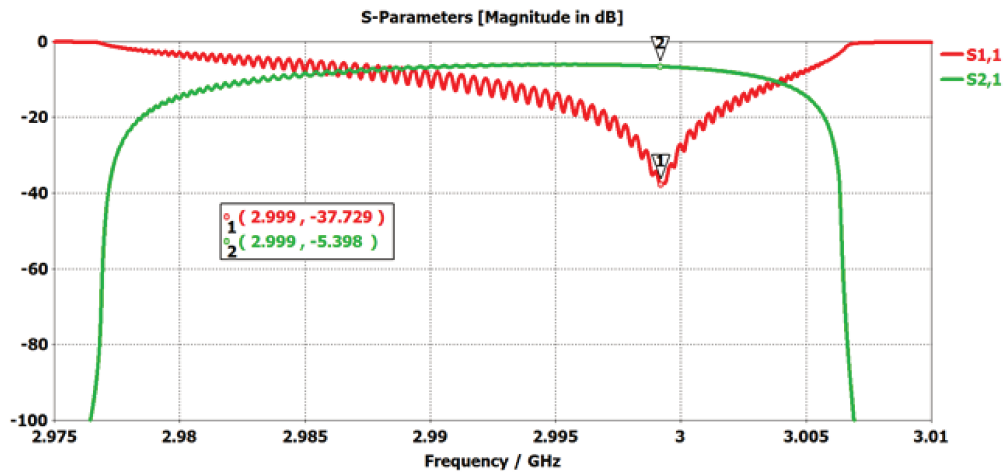


FIGURE 2.47: Scattering parameters  $|S_{11}|$  (red line),  $|S_{21}|$  (green line) of the whole accelerating section (in vacuum at 20 °C).

Figure 2.47 shows the reflection coefficient  $|S_{11}|$  at the structure input port and the insertion loss  $|S_{21}|$  for the whole structure. The  $TM_{010-2\pi/3}$  mode corresponds to a resonating frequency of 2.999 GHz, with a reflection coefficient equal to -37 dB, which means a good transmission capability of the structure to the RF signal for acceleration.

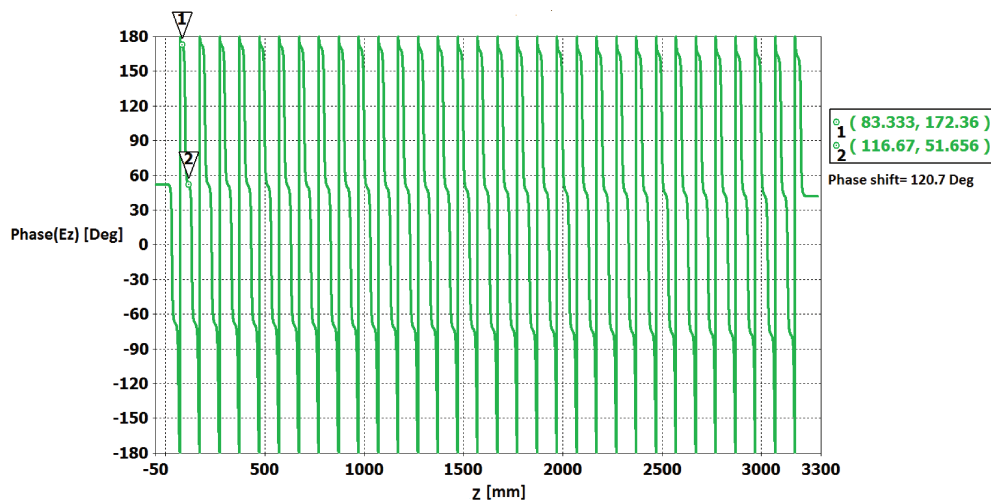


FIGURE 2.48: Phase advance along all the whole structure.

The simulated phase shift of the longitudinal electric field between two adjacent cells is reported in Fig.2.48. The phase shift is equal to  $120^\circ \pm 0.7^\circ$ .

The resulting longitudinal electric field amplitude along the structure has been determined as shown in the Fig.2.49. We can see that the longitudinal electric field amplitude is almost constant along the total length of the section. A zoom of the flatness of the

field amplitude both at the start and the end of the section is also displayed in Fig.2.49.

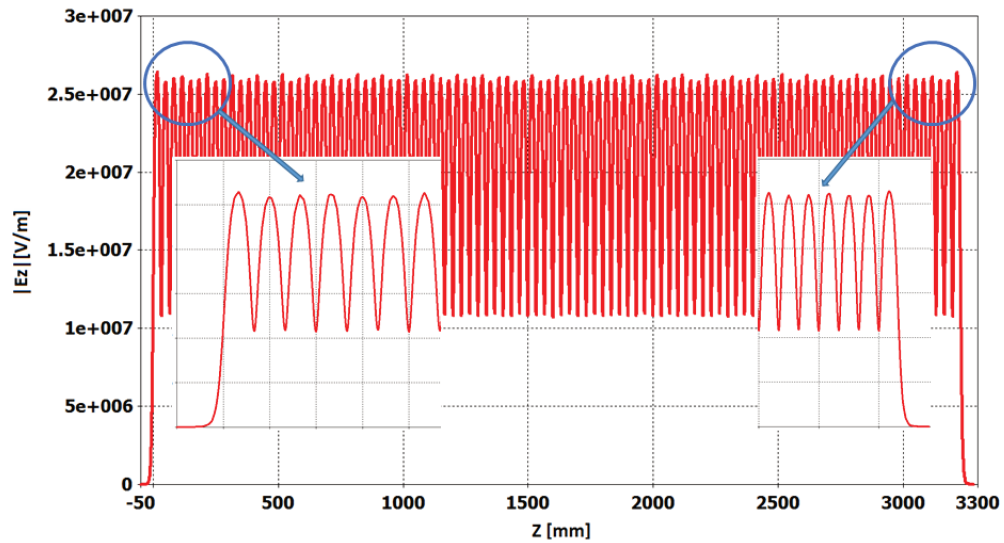


FIGURE 2.49: Longitudinal electric field module of the  $TM_{010-2\pi/3}$  along the whole accelerating structure.

The accelerating structure is equipped with two quasi-symmetrical-type single feed couplers which have a guide of  $\lambda/4$  length at the coupling slot opposite site in order to compensate the asymmetry of the electromagnetic field in the coupling cell. A CST Studio model geometry of the final high-gradient section is illustrated in Fig.2.50.

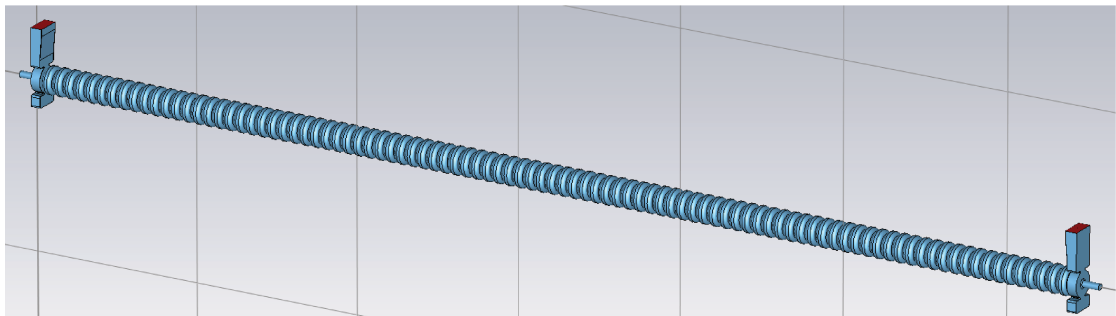


FIGURE 2.50: Geometry of the final accelerating section resulting from the CST MWS model.

By means of electromagnetic solvers we can obtain for each cell the value of the main important RF parameters, such as the filling time, the group velocity, shunt impedance, the circulating power, the energy gain as well as the surface electric field, and the high accelerating gradients. Moreover, we have calculated the ratio between the modified Poynting vector and the square of on-axis electric field. This ratio is an important quantity to prevent a high probability of RF breakdowns. All these quantities have been obtained considering a range of variation of the iris diameter ( $2a$ ) that takes into

account the compromises in their optimisation that have been already analysed in the regular cell design.

Some quantities have been directly simulated for each iris radius variation, such as group velocity and shunt impedance. Other quantities like power flow has been calculated by a simplified differential equation formula of Eq.2.33. The energy gain has been calculated according to the Eq.2.37 for on-crest acceleration ( $\phi = 0$ ). The surface electric field and high accelerating gradient have been calculated by means of the constants in Eq.2.91 and Eq.2.92 for each iris radius.

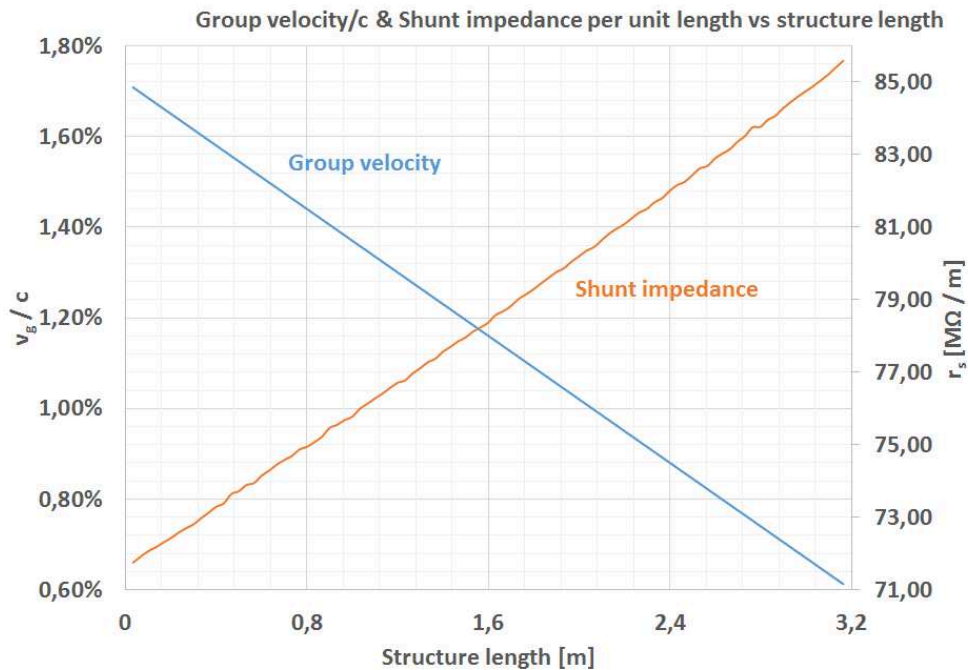


FIGURE 2.51: Group velocity (blue line) and shunt impedance per unit length (orange line) along the structure.

Figure 2.51 shows the group velocity and the shunt impedance along the structure. As we have already seen in the EM design optimisation of the regular cell, the optimum value of the iris diameter entails a high shunt impedance value for the acceleration efficiency with a reasonable group velocity in order to limit the filling time of the EM wave in the structure.

The maximum available power at input accelerating section is 24 MW for the ThomX linac. Then, the circulating power is decreasing according to the constant gradient structure law. The maximum and effective accelerating gradients are related to the

input power by the following expressions:

$$E_a = 5.1\sqrt{P_{in}} \quad (2.91)$$

$$E_e = 4.2\sqrt{P_{in}} \quad (2.92)$$

Figure 2.52 shows the circulating power along the structure. At the end of the section the remaining power is around 7 MW, which means that the dissipated power in the walls of the cavity is around 17 MW (2.55 kW average power). Also, the distribution of the maximum and effective accelerating fields are represented. The effective accelerating

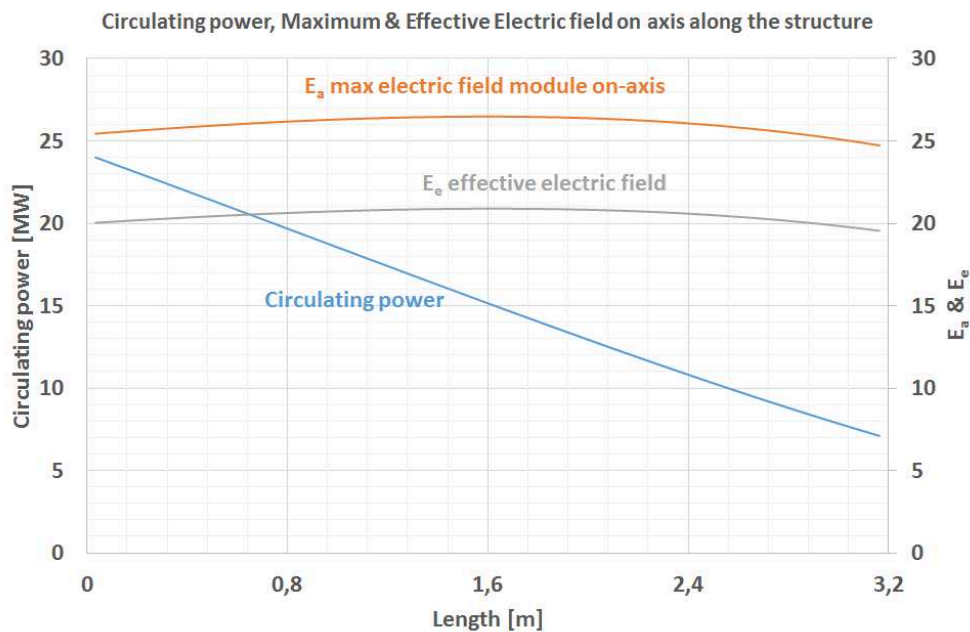


FIGURE 2.52: Circulating power (blue line), maximum on-axis electric field (orange line) and effective on-axis electric field (grey line) along the structure.

field is around 20 MV/m, at the beginning of the structure. It slightly increases along the structure up to 21 MV/m over a distance of 2-meters, then it slightly decreases up to the end of the structure where the final value is 18 MV/m. The maximum on-axis electric gradient shows almost the same trend: it starts at around 25 MV/m and at the half of the structure it begins to decrease until 24.5 MV/m at 3.2-meters. Figure 2.53 shows the filling time and the energy gain along the whole structure.

Taking into account an energy of around 5 MeV provided by the RF gun, the energy gain of the accelerating section is around 65 MeV. It should be enough to accomplish the final goal of 70 MeV for the upgrade phase of the linac. The filling time is less than 1  $\mu$ s. This value should be reasonable to prevent breakdown phenomena in the structure during operation.

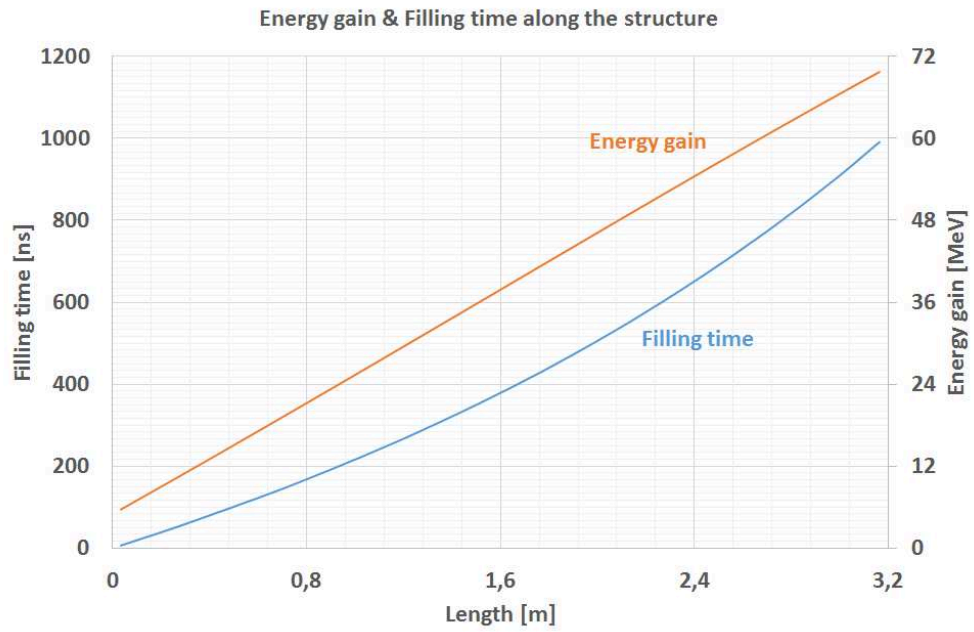


FIGURE 2.53: Energy gain (orange line) and filling time (blue line) along the structure.

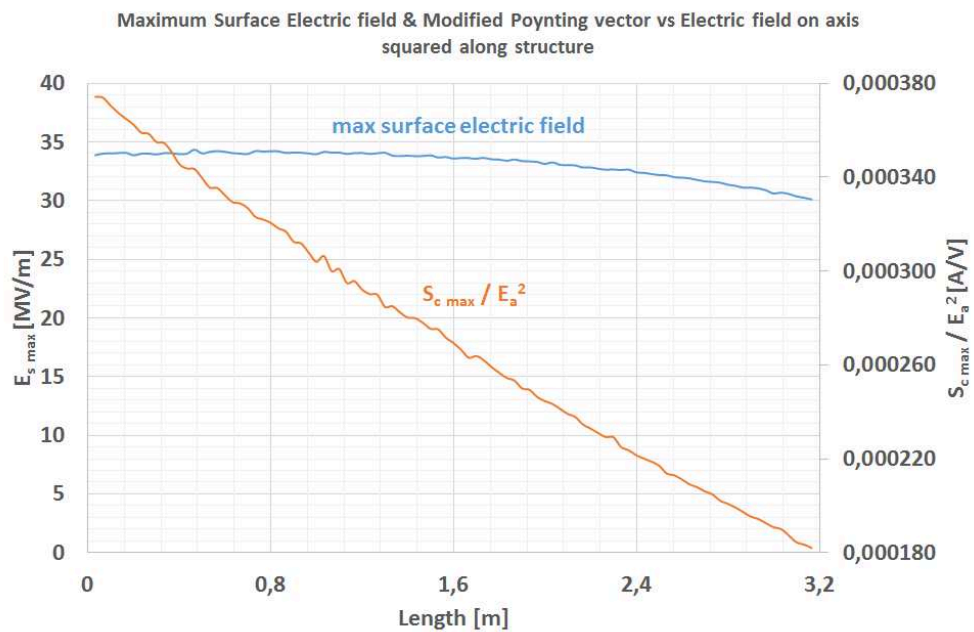


FIGURE 2.54: Maximum surface electric field and maximum modified Poynting vector over on-axis electric field squared along the structure.

As shown in Fig.2.54, the maximum surface electric field keeps constant to the value of 34 MV/m up to 1.2-meters. Then it starts to decrease along the structure achieving 29 MV/m. These values are well below the breakdown threshold of 47 MV/m according to the Kilpatrick's criterion.  $S_{cmax}/E_a^2$  is represented in Fig.2.54. For an input power of 24 MW, the maximum simulated value of  $S_c$  along the structure is  $S_{cmax} = 0.25$  MW/mm<sup>2</sup> which is far below the limit of 1.6 MW/mm<sup>2</sup> for a BDR of 10<sup>-6</sup> bpp/m calculated before.

All the main RF characteristics based on the design are summarised in Tab.2.6:

TABLE 2.6: Main parameters of the CG TW structure (HFSS and CST results).

Parameters	values	unit
Structure type	constant gradient (CG)	
Mode	$TM_{010-2\pi/3}$	
Repetition rate	50	Hz
RF pulse length	3	$\mu s$
Frequency design in vacuum	2999	MHz
Temperature design	20	$^{\circ}C$
group velocity $v_g/c$	1.71% - 0.67%	
Cell phase advance	$2\pi/3$	
Number of cells	95 regulars + 2 coupling cells	cell
Structure length	3.2635	m
Iris aperture (2s)	23 - 17.36	mm
Average Quality factor (unloaded)	15175	
Average Shunt impedance	73	M $\Omega$ /m
Average Series impedance ( $Z_c$ )	35	M $\Omega/m^2$
Average Attenuation factor	0.21	Neper/m
Filling time	991	ns
Input peak power	24	MW
Output power	$0.29 \cdot P_{in}$	MW
$\langle E_e \rangle \simeq E_e$	20.5	MV/m
$\langle E_a \rangle \simeq E_a$	25	MV/m
$E_{smax}$	34	MV/m
Energy gain	65	MeV
Max Modified Poynting vector ( $S_{cmax}$ )	$0.193 \times 10^{12}$ at 24 MW	W/m <sup>2</sup>
$E_{smax} / \langle E_a \rangle$	1.36	
$E_{smax} / \langle E_e \rangle$	1.66	
$S_{cmax} / \langle E_a \rangle^2$	0.0004	A/V
$H_{smax}$	$1.1 \times 10^5$	A/m
Pulsed heating $\Delta T$	6.5	$^{\circ}C$

### 2.4.3.7 Cooling system design and coupled thermal-structural analysis

This section is dedicated to the thermo-mechanical study of ThomX accelerating section prototypes with a reduced number of cells and also to the final high-gradient structure. The development of copper prototypes allow to verify the geometry, validate the fabrication procedure and check if the normal operation conditions are fulfilled. One of the main goal is the validation of the water cooling system devoted to extract the heat generated by the dissipated power on the walls of the structure and guarantee that the temperature distribution is uniform along the accelerating section.

The analysis of the cooling system is based on the heat transfer theory. Heat transfer mechanisms are simply ways by which thermal energy can be transferred between objects, and they all rely on the basic principle that kinetic energy or heat wants to be at equilibrium or at equal energy state. There are three different ways for heat transfer to occur: conduction, convection and radiation. Each of these heat transfer processes obeys its laws:

- Heat conduction is the process of molecular heat transfer by micro-particle (molecules, atoms, ions, etc) in medium with a non-uniform temperature distribution,
- Convection is the process of heat transfer by displacing the macroscopic element of a medium (molar volumes),
- Radiation is the process of heat transfer from one body to another by EM waves.

The heat transfer between our structure and the water circulating in the cooling system is equivalent to a forced convection exchange inside water pipes. Fig.2.55 shows the 3D model of the 7-cells prototype where the cooling system is directly integrated in the copper body. Water inside the cooling system is circulating in opposite senses in adjacent tubes leading to a better temperature stabilization along the structure.

In order to complete the set up for thermal analysis we need to model the convection phenomena. The heat source for the thermal simulation is the power loss of accelerating mode on the structure walls. The dissipated power on the cavity walls is calculated as:

$$P_d = \frac{R_s}{2} \int_{\Sigma} H^2 dA \quad (2.93)$$

where  $H$  is the surface magnetic field,  $R_s$  is the surface resistance and  $A$  is the surface boundary between the vacuum and the metal regions.

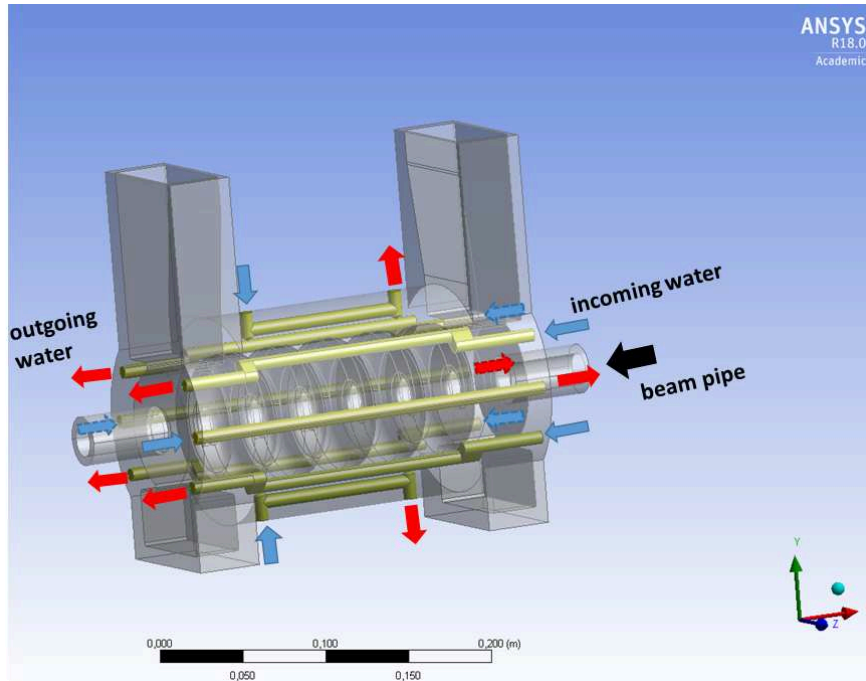


FIGURE 2.55: Picture of the the cooling system pipes that are integrated in the 7-cells copper body prototype.

Let us calculate the heat transfer coefficient  $h$ . Starting from the data we have, we can evaluate  $h$  as:

$$h = \frac{Nu \cdot \lambda}{L} \quad (2.94)$$

where  $Nu$  is the Nusselt number,  $\lambda$  is the thermal conductivity and  $L$  is the characteristic length of the water pipes.

In our case,  $Nu$  has the following expression:

$$Nu = 0.023Re^{0.8}Pr^{0.333} \quad (2.95)$$

The Reynold number is given by:

$$Re = \frac{\rho v D}{\mu} \quad (2.96)$$

where  $\rho$  is the water density,  $v$  is the water velocity,  $D$  is the pipes diameter and  $\mu$  is the dynamic water viscosity.

The Prandtl number is given by:

$$Pr = \frac{c_p \mu}{\lambda} \quad (2.97)$$

where  $c_p$  is the specific heat.

Considering the diameter of the pipe of  $D = 8$  mm and the inlet water velocity of  $v = 2.5$  m/s we obtain the heat transfer coefficient  $h = 10180$  W/(m<sup>2</sup>K).

Let us now calculate the difference between the inlet water temperature and the average temperature of the structure using the following expression:

$$\Delta T = T_{structure} - T_{inwater} = \frac{P_d}{h\pi DL} \quad (2.98)$$

The simulated dissipated power on the 7-cells prototype walls using HFSS is around 333 W for an input peak power of 20 MW (RF pulse length of 3  $\mu$ s and repetition rate of 50 Hz). The  $\Delta T_{structure} = 0.7$  °C.

We can estimate the increase of the water temperature using this formula:

$$\Delta T_{water} = T_{out} - T_{in} = \frac{P_d}{\dot{m}c_p} \quad (2.99)$$

where  $\dot{m}$  is the mass flow rate. The  $\Delta T_{water} = 0.08$  °C.

To setup the thermal analysis, the RF dissipated power simulated with HFSS (Fig.2.56) is applied as a heat flux load on the copper surface of the accelerating section in ANSYS Fluent solver. The HFSS-ANSYS Fluent scheme is illustrated in Fig.2.57.

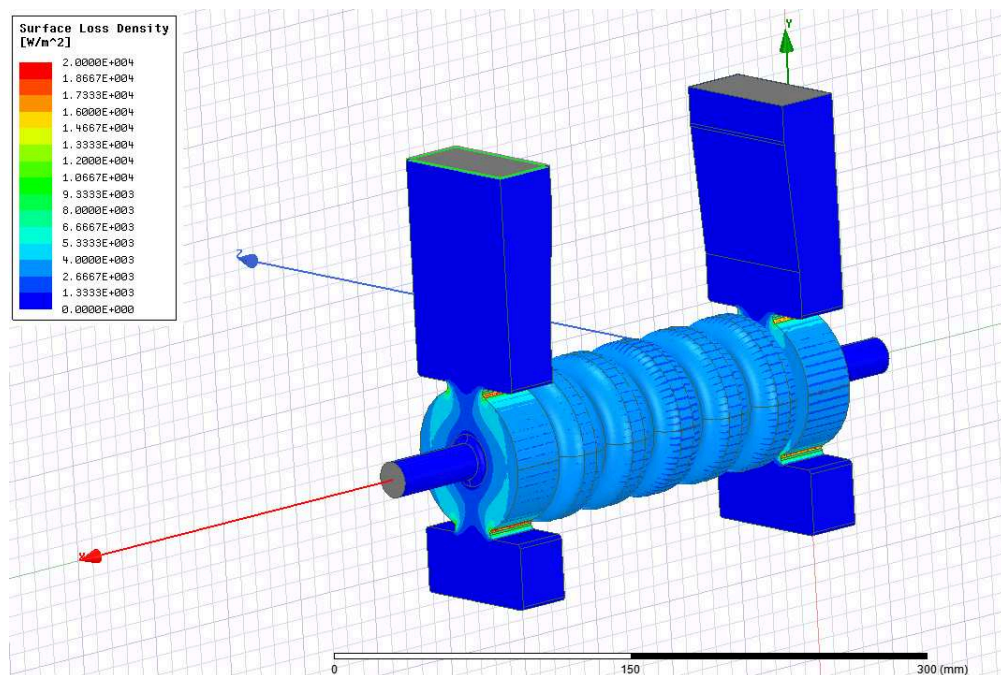


FIGURE 2.56: Surface loss density (heat flux) distribution on the cavity walls. The average dissipated power is around 333 W.

Furthermore, cooling system parameters (the inlet water temperature of 24 °C, the inlet pressure of 6 bars and the inlet water velocity of 2.5 m/s) are applied to the Fluent model as thermal loads.

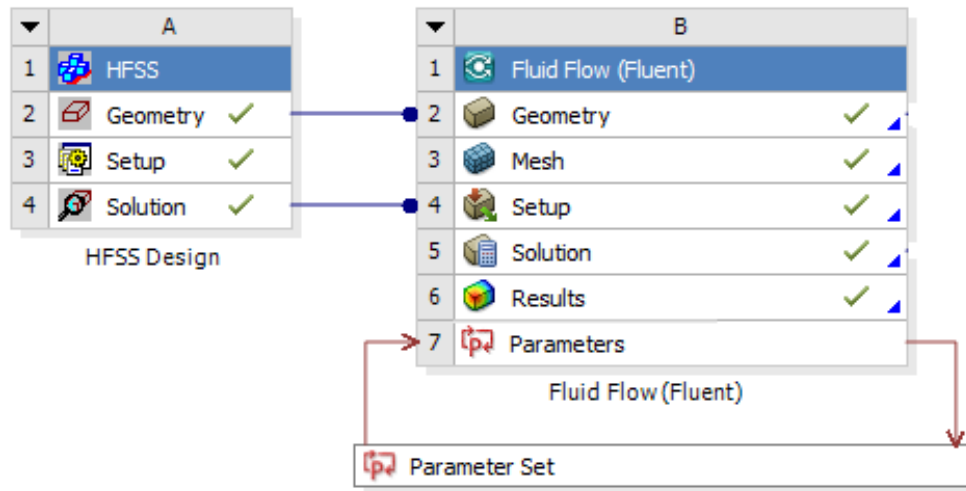


FIGURE 2.57: HFSS-Fluent coupling scheme.

The ambient temperature of 22 °C and natural convection with air on the external surface of the whole structure ( $h_{nc1} = 5.9 \text{ W/m}^2\text{K}$  for beam pipes and  $h_{nc2} = 3.8 \text{ W/m}^2\text{K}$  for the cavity body) are taken into account as boundary conditions.

The temperature distribution simulated inside the structure is represented in Fig. 2.58. The temperature is uniform throughout the whole structure body with an average value of about 24.8 °C that it closes the analytical one. The temperature of the cells, which has the largest impact on the structure resonant frequency is about 26 °C.

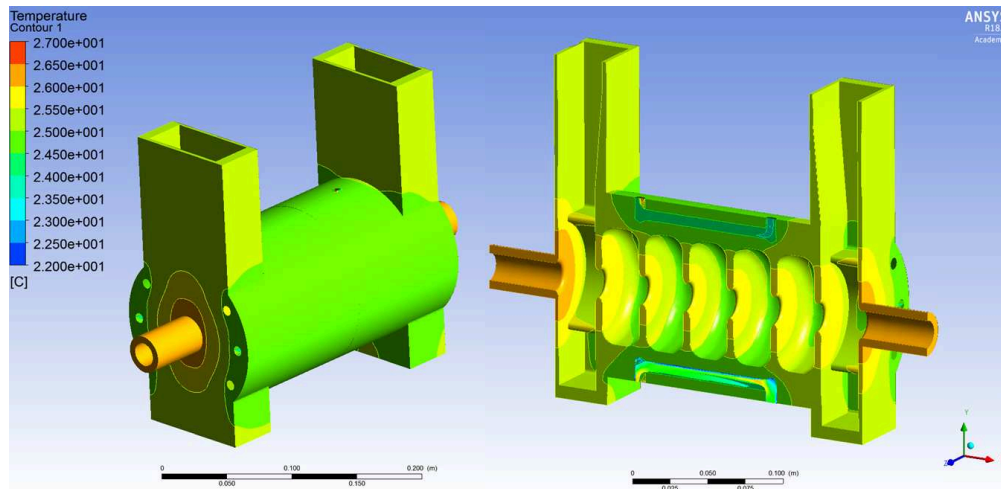


FIGURE 2.58: Temperature distribution of the copper prototype. Input power 20 MW, dissipated power 334 W.

The related water cooling temperature distribution inside tubes is depicted in Fig. 2.59. The maximum temperature rise is around 0.08 °C. We obtain a good agreement with analytical results.

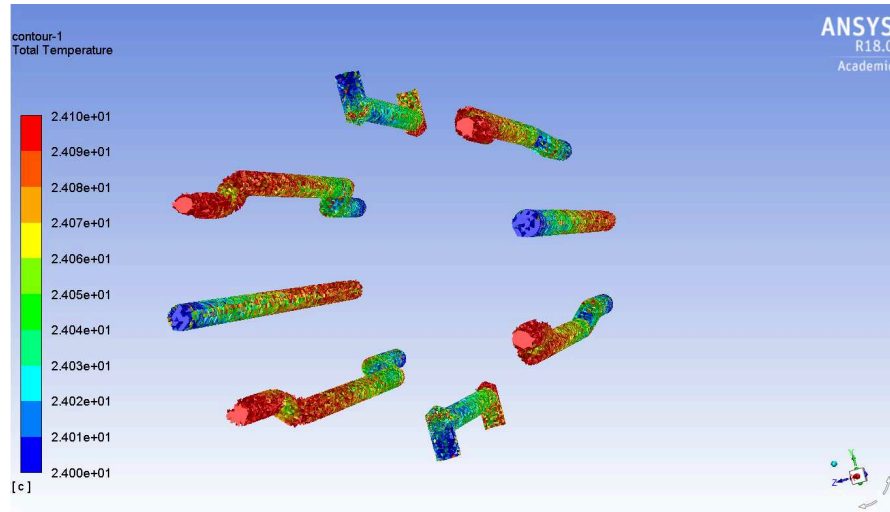


FIGURE 2.59: Cooling water temperature distribution tubes.

In fluid dynamics, the pressure drop corresponds to the dissipation of the mechanics energy due to the friction of the fluid when it moves. This energy dissipation happens as a pressure variation,  $\Delta P$  and appears also in the Bernoulli's equation. For instance, to keep a fluid on moving through a pipe, one need to provide the amount of energy necessary to compensate the one dissipated by friction.

When we deal with friction, the Bernoulli's theorem does not longer hold. In case of incompressible fluids, we consider the general formula:

$$\frac{1}{2}\rho \cdot v_1^2 + p_1 + \rho \cdot g \cdot z_1 = \frac{1}{2}\rho \cdot v_2^2 + p_2 + \rho \cdot g \cdot z_2 \quad (2.100)$$

where  $v_1$ ,  $v_2$ ,  $p_1$ ,  $p_2$  are the velocity and the pressure at the entrance and the exit of the tube, respectively. If the pipe cross section is constant, the velocity is constant ( $v_1 = v_2$ ) and the dissipation of energy is equivalent to the pressure drop. The Eq.2.100 can then be written in the form:

$$\Delta P = (p_1 - p_2) = \rho \cdot g \cdot (z_2 - z_1) = \rho \cdot g \cdot \Delta h \quad (2.101)$$

$\Delta h$  is calculated by the Darcy-Weisbach's equation:

$$\Delta h_L = \Lambda_L \frac{L v^2}{D 2g} \quad (2.102)$$

where  $\Lambda_L$  is a friction coefficient,  $v$  is the average velocity of the water in the pipe,  $L$  is the length of the pipe,  $D$  is the hydraulic diameter and  $g$  is the gravity acceleration (9.81 m/s). It has to be noticed that Eq.2.102 holds only for horizontal pipes. Therefore, pressure drop is in the form:

$$\Delta P_L = \Lambda_L \frac{L \rho \cdot v^2}{D 2} \quad (2.103)$$

If the Reynolds's number is between 4000 and 100000 (turbulent regime), one can use the Blasius correlation to determine the friction coefficient as follow:

$$\Lambda_L = 0.3164Re^{-0.25} \simeq 0.03 \quad (2.104)$$

Then, from Eq.2.103, the pressure drop is:

$$\Delta P_L = \Lambda_L \frac{L \cdot \rho \cdot v^2}{2D} \simeq 2245 \text{ Pa} \simeq 0.02 \text{ bar} \quad (2.105)$$

In our case, the friction coefficient for the non-linear segments like the elbows of the

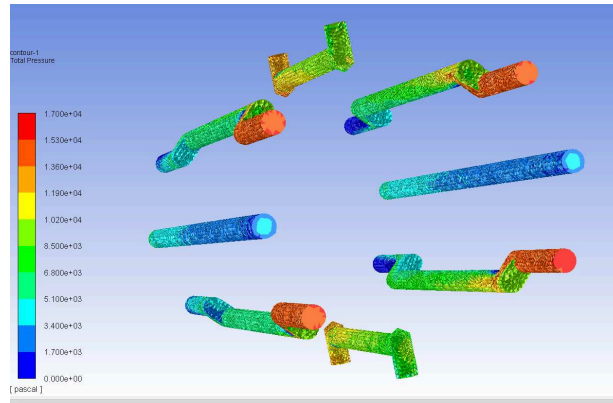


FIGURE 2.60: Pressure drop distribution along the cooling pipes simulated in ANSYS Fluent.

cooling channels is around:

$$\Lambda_{NL} = 1.2 \quad (2.106)$$

Then, the pressure drop due to the elbows is:

$$\Delta P_{NL} = 4\Lambda_{NL} \frac{v^2}{2g} = 14934 \text{ Pa} \simeq 0.15 \text{ bar} \quad (2.107)$$

The maximum pressure drop is:

$$\Delta P_{max} = \Delta P_L + \Delta P_{NL} \simeq 0.17 \text{ bar} \quad (2.108)$$

The simulated pressure drop distribution of the water along pipes is represented in Fig.2.60. The maximum pressure drop is around 0.17 bar showing the good agreement with analytic results.

The eight pipes of the TW structure cooling system are connected in parallel, the incoming total flow rate  $Q$  is the sum of the flow rates in each individual pipe  $Q_i$ . Taking into account the use of flexible tubes and piping fittings, the calculated pressure drop

TABLE 2.7: Cooling system characteristics of the three accelerating structure types.

	7 cells CI TW prototype	16 cells CI TW prototype	Final CG TW accelerating section
Incoming water flow rate $Q$ (l/min)	60	60	72
Number of pipes	8	8	8
Pipe diameter (mm)	8	8	8
Pipe length (m)	0.23	0.53	3.2
Water flow rate in pipe $Q_i$ (l/min)	7.5	7.5	9
Water speed in pipe (m/s)	2.5	2.5	3
Heat transfer coefficient ( $W/m^2K$ )	10186	10186	11788
Input peak power (MW)	20	20	24
Average dissipated power (W)	330	600	2500
$T_{avg\ structure} - T_{in\ water}$ ( $^{\circ}C$ )	0.69	0.55	0.33
$T_{out\ water} - T_{in\ water}$ ( $^{\circ}C$ )	0.08	0.14	0.5
Maximum pressure drop $\Delta p$ (bar)	0.29	0.32	0.82

values are reported in Tab.2.7. These analytical results are overestimated compared to the simulated ones.

Starting from the thermal analysis, we are able to evaluate the deformation of the structure due to RF heating's using the ANSYS Fluent and structural coupling scheme illustrated in Fig.2.61. The simulated total deformation (displacement) is depicted in Fig.2.62.

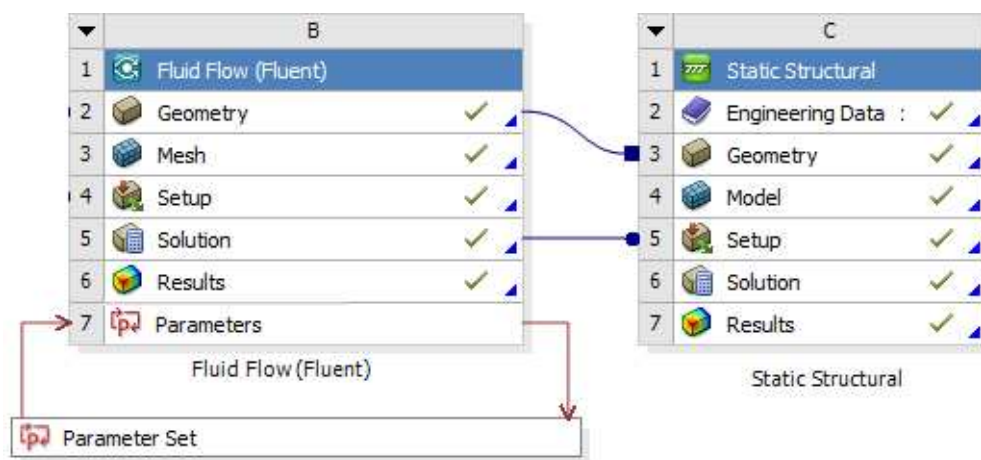


FIGURE 2.61: ANSYS Fluent and Structural coupling scheme

The maximum deformation is around  $12\ \mu m$  as it is shown in Fig.2.62. The deformation calculated on the inner surfaces in the radial direction is below  $20\ \mu m$ . The local stress

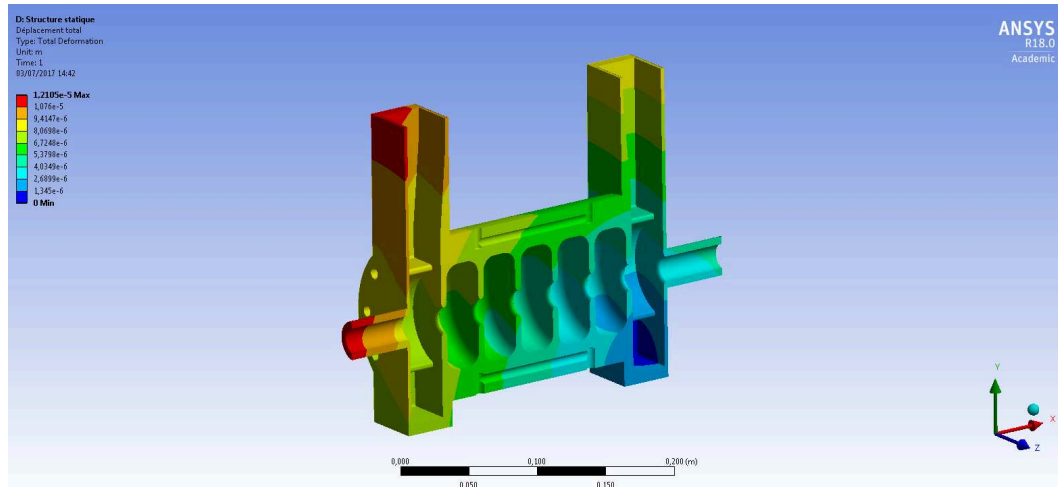


FIGURE 2.62: Structural deformation of the prototype. Displacement distribution for 334 W dissipated power

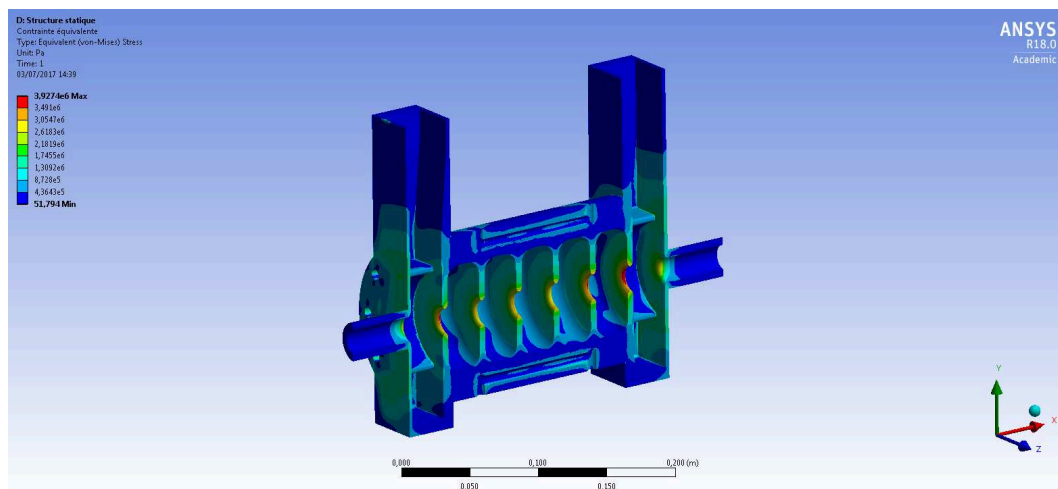


FIGURE 2.63: Von-Mises structural stress due to an equivalent dissipated power of 333 W.

caused by the RF heating should be controlled below the yield stress of the annealed oxygen free copper equal to 62 MPa. At the slot coupling area the maximum Von-Mises stress is around 1 MPa (Fig.2.63).

The thermal behaviour of the ThomX accelerating structure has been analysed. A structural analysis of the 7-cells CI prototype has been carried out. The designed cooling system seems also adequate for the 16-cells CI prototype and for the final CG TW section. This cooling system allows to take under control the deformations of the structure and to keep a temperature increase as small and uniform as possible.

### 2.4.3.8 Dependence on temperature reflection coefficient

The cavity volume expands as the temperature increases, leading to a decrease of resonating frequency.

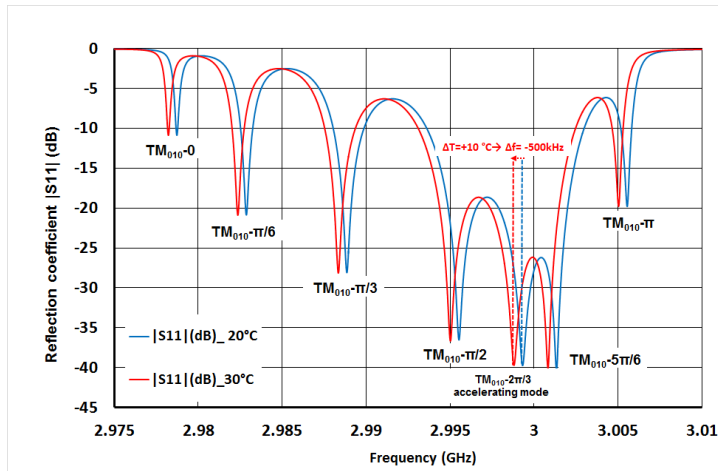


FIGURE 2.64:  $|S_{11}|$  reflection coefficient as a function of the frequency at 20 °C and 30 °C.

Thermo-mechanical simulations performed for the copper 7-cells CI structure with ANSYS predict that the frequency shift  $\Delta f$  with temperature  $T$  would be:

$$\Delta f [MHz] = -0.05 \Delta T [^{\circ}C] \quad (2.109)$$

Figure 2.64 shows the reflection coefficient of the prototype at two different temperatures: 20 °C and 30 °C.

### 2.4.3.9 Vacuum simulations

For the ThomX Linac upgrade, the linear accelerator will benefit of a new shorter S-band accelerating structure (3 m-long) with respect to the standard LIL-type section (4.5 m-long). In general, accelerating structures should be as long as possible for RF power efficiency and cost reduction optimisation. The major concern for the vacuum of the accelerator chamber is whether the limited conductance will lead to too high pressure in the center of the chamber. Vacuum calculations are thus required. However, the effect of the RF fields and conditioning on dynamic vacuum conditions are difficult to perform requiring more sophisticated and powerful tools. These aspects are usually treated experimentally and are beyond the scope of this thesis. The aim of our simulations is to determine the better pumping configuration for the best static vacuum.

We have simulated vacuum performance of the accelerating structure prototype, for three main purposes:

- to avoid multipacting events and prevent inner surface damages,
- to ensure fast RF conditioning of the cavity,
- to protect the RF ceramic window.

Even if the value of the conductance would be lower in case of the final 3 m-long high-gradient structure with respect to the prototype with a reduced length, the vacuum performances of the 0.533 meters long prototype has been checked to prevent high probabilities of RF breakdowns, short beam lifetime and emittance blow-up. For vacuum calculations, there are several available methods: analytical resolution of the gas flow equation [60], the finite element method (FEM) [61], the equivalent circuit analysis [62], Monte Carlo [63] and commercial codes [64]. We have adopted Molflow developed by R. Kersevan from CERN [65], a test-particle Monte-Carlo simulator for ultrahigh vacuum systems.

Although Molflow contains basic tools for drawing geometry, a CATIA program is used to construct the inner vacuum volume of the prototype which is imported in the simulation software. Once the geometry has been imported, the software automatically creates the suitable mesh of the vacuum surface to enable calculations. After, for each facet that constitutes the mesh, a "sticking" coefficient has to be defined. The latter can be defined as the ratio between the adsorbed molecules (or "stick") to the surface and the total number of molecules that impinge the surface. Also, the out-gassing rate, the type of gas molecules and the type of diffused reflection of the molecules have to be defined.

We calculate some basic typical quantities for vacuum system estimations. From the ideal gas law, the number of molecules is defined as:

$$N = \frac{pV}{k_B T} \quad (2.110)$$

where  $p$  is the pressure,  $V$  the volume,  $k_B$  is the Boltzmann's constant and  $T$  the temperature. Equation 2.110 can be expressed also in term of molecule flux:

$$\frac{dN}{dt} = \frac{p}{k_B T} \frac{dV}{dt} \quad (2.111)$$

We refer to the kinetic theory of gas that describes the particle impact to the surrounding walls, in terms of temperature, pressure and volume properties. Maxwell-Boltzmann law, provides the probabilistic distribution of the molecular speed magnitude, then, the

Gas	Pressure [mbar]	$\phi$ $\left[\frac{\text{molecules}}{\text{cm}^2 \cdot \text{s}}\right]$
$N_2$	$10^{-3}$	$2.9 \times 10^{17}$
	$10^{-8}$	$2.9 \times 10^{12}$
$H_2$	$10^{-3}$	$1.1 \times 10^{18}$
	$10^{-8}$	$1.1 \times 10^{13}$
	$10^{-14}$	$1.1 \times 10^7$
$H_2O$	$10^{-3}$	$3.6 \times 10^{17}$
	$10^{-8}$	$3.6 \times 10^{12}$

TABLE 2.8: Impingement rate for common gas at room temperature [67].

average molecular velocity of nitrogen molecules ( $N_2$ ) can be calculated as follow [66]:

$$v_{avg} = \left(\frac{8RT}{\pi m}\right)^{1/2} = 145.5 \left(\frac{T}{M}\right)^{1/2} = 470 \frac{m}{s} \quad (2.112)$$

where  $R = 8.314 \text{ J}/(\text{mol} \cdot \text{K})$ ,  $T = 293 \text{ K}$  is the temperature,  $m = 28 \times 10^{-3} \text{ Kg/mol}$ , and  $M = 28 \text{ u.m.a}$  is the nitrogen molar mass. We can consider the molecular impingement rate  $\phi$  at which the molecules collide with a unit surface area:

$$\phi = \frac{n \cdot v_{avg}}{4} \left[\frac{\text{molecules}}{\text{cm}^2 \cdot \text{s}}\right] \quad (2.113)$$

where  $n$  is the gas particle density [ $\text{molecules}/\text{cm}^{-3}$ ]. Table 2.8 resumes the numerical values of the molecular impingement coefficient for different gases:

In the molecular flow regime, the gas flow rate is defined as:

$$Q = p \frac{dV}{dt} = C(p_1 - p_2) \quad (2.114)$$

where  $C$  is called the conductance. In free molecular regime, the conductance does not depend on the pressure but only on the geometry of the system and on the molecular speed inside it. Since  $Q$  is expressed in [ $\text{mbar} \cdot \text{l/s}$ ], the conductance takes the form of a volume flow rate [ $\text{l/s}$ ].

We can now find the relation between the conductance and the impingement rate for a special case where the diameter of the pipe is comparable to its length. We consider a vacuum chamber which is divided into two volumes connected by an thin orifice with a cross section  $A$ . The vacuum volume is in isotherm condition. Only the molecules that face on the orifice can pass through it. Thus, nearby the orifice one has double flux of molecules. The net flux of molecules is:

$$\frac{dN}{dt} = \frac{1}{4} v_{avg} A (n_1 - n_2) \quad (2.115)$$

where  $n_1$  and  $n_2$  are the molecules density of the volume 1 and volume 2, respectively. Eq. 2.116 becomes:

$$\frac{dN}{dt} = \frac{1}{4} \frac{v_{avg}}{k_B T} A (p_1 - p_2) \quad (2.116)$$

Considering Eq. 2.111 in analogy to formula 2.114 the conductance assumes the form:

$$C = \frac{1}{4} v_{avg} A \quad (2.117)$$

Equation 2.117 is called the Graham law. The conductance is therefore inversely proportional to the square root of the molecular mass of the species passing through the pipe. For example, the conductance per unit area of nitrogen ( $N_2$ ) with temperature  $T = 293$  K is calculated as:

$$C = \frac{v_{avg}}{4} = \frac{470 \times 10^3}{4 \times 10^4} \left[ \frac{l}{cm^2 \cdot s} \right] = 11.75 \frac{l}{cm^2 \cdot s} \quad (2.118)$$

Another important parameter of the vacuum technology is the pumping speed,  $S$ , which is namely defined as the ratio between the gas flow entering the pump  $Q$  and the inlet pressure  $p$ :

$$S = \frac{Q}{p} = \frac{dV}{dt} \quad (2.119)$$

The sticking coefficient is the probability that a molecule hitting a facet will be permanently pumped. In a Monte Carlo simulation, a model representing the structure of a pipe is first built. Next, molecules are generated from the entrance facet in the model using a random number generator and bounced off the walls until they leave the duct or return to the entrance facet. By comparing how many molecules have hit the exit facet to the total number generated, one obtains the probability factor of transmission:

$$C = \frac{v_{avg}}{4} \cdot A \cdot P_{j \rightarrow i} \quad (2.120)$$

where  $P_{j \rightarrow i}$  is the transmission probability coefficient, namely the portion of molecules that reach the "exit"  $j$  of the tube once they are injected through its "entrance"  $i$  (whether or not  $i$  and  $j$  are the real entrance and exit of the tube) and  $A$  is the "entry" surface of the conductance. The relationship between the sticking coefficient  $\sigma$  and the pumping speed  $S$  of a facet is given by [68]:

$$S = \frac{v_{avg}}{4} \cdot A \cdot \sigma \quad (2.121)$$

where  $\sigma$  is the sticking coefficient. Equation 2.121, as we will see, is not only valid for the speed  $S$  referring to pumps but also for surfaces which act as pumps. Anyway, the values  $S_0$  of pumping speed given by the pump suppliers become merely theoretical,

because they refer only to the inlet of the pump. In practice, what we have is  $S_{eff}$ , an effective pumping speed which is acting directly in the vacuum vessel of interest. The effective pumping speed, which is lower than the nominal one, is calculated considering the gas flow from the vessel to the pump. In the end, we end up to the practical formula:

$$\frac{1}{S_{eff}} = \frac{1}{S_0} + \frac{1}{C} \quad (2.122)$$

Once we have defined the basic quantities of interest, we describe the practical operation we have performed for simulations. The inner surface of the accelerating prototype is divided into a number of elements and its pressure distribution is obtained by solving a matrix equation. The conductance, the volume, the thermal out-gassing, the photo-stimulated out-gassing and the pumping speed for each element are calculated individually and used for matrix calculations. The influence of the pressure difference upon neighboring elements is included in the throughput as a product of the conductance and the pressure difference. The respective conductance between neighboring elements is calculated from the individual conductances using the formula of conductances in series. We defined the following parameters:

- the temperature of the inner surface equal to around 293 K,
- the out-gassing rate, identical for all the facets, is equal to  $2 \times 10^{-11}$  (mbar · l)/(s · cm<sup>2</sup>) for copper OFHC with no thermal treatment after 100 hours pumping (equivalent  $N_2$ ) at 20 °C,
- an effective pumping speed,  $S_{eff} = 5$  l/s ( $N_2$  at 20°C) set on the ending facet. According to the Eq.2.121, the sticking coefficient is:

$$\sigma = \frac{4S_{eff}}{v_{avg}A} = 0.154 \quad (2.123)$$

where  $A = 2.76$  cm<sup>2</sup> is the cross section.

Four pumping configurations are studied:

- pumping through one beam pipe of the prototype: the diameter of the tube connected to the pumping system is 19 mm;
- pumping through one RF waveguide port of the prototype;
- pumping through both beam pipes of the prototype;
- pumping through both RF waveguide ports of the prototype.

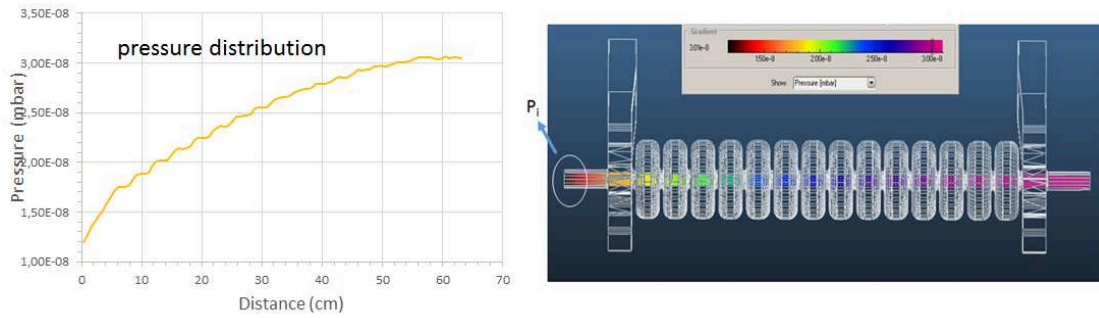


FIGURE 2.65: Vacuum pressure simulation in the case of one ionic pump connected to the beam pipe (right side). The plot shows the pressure along the structure (yellow line).

Figure 2.65 shows the pressure along the accelerating prototype in the case of the pump connected to one side of the beam pipe. The number of molecules that are degassed is 68200. The maximum pressure value is  $3.1 \times 10^{-8}$  mbar while the average value of the pressure is  $2.5 \times 10^{-8}$  mbar.

We consider the case where the pump is connected to one RF waveguide port of the coupling cell. In this case, the effective pumping speed is  $S_{eff} = 36$  l/s and the cross section is  $A = 24.547 \text{ cm}^2$ . According to Eq. 2.121, the sticking coefficient is:

$$\sigma = \frac{4S_{eff}}{v_{avg}A} = 0.125 \quad (2.124)$$

Fig.2.66 shows the pressure along the accelerating prototype in case where the pump

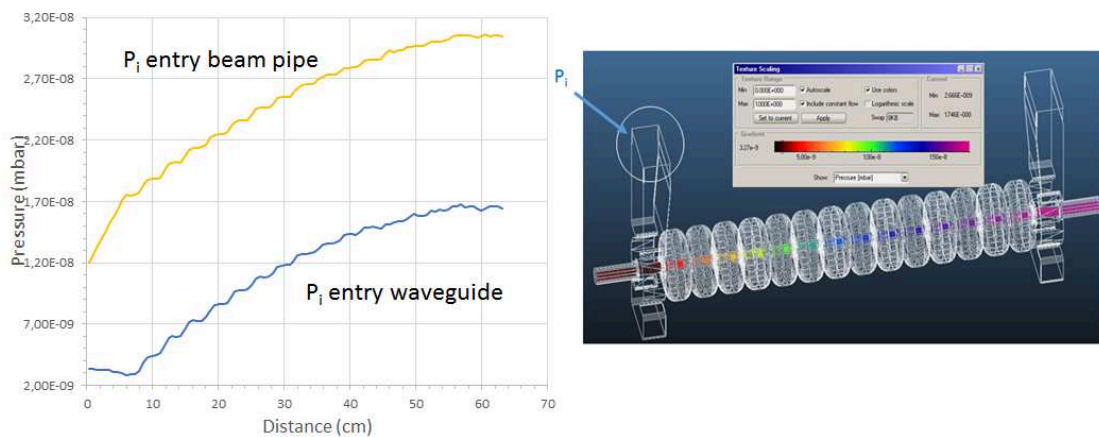


FIGURE 2.66: Vacuum pressure simulation in the case of one ionic pump connected to the RF waveguide port (right side). The plot shows the pressure along the structure where the pump is connected to the pipe (yellow line) and to the RF waveguide port (blue line).

is connected to one RF waveguide port. The number of molecules that are degassed is 9100. The plot shows that the maximum pressure value is  $1.7 \times 10^{-8}$  mbar while the average value of the pressure is  $1.1 \times 10^{-8}$  mbar. We can easily see that this configuration

allows to decrease by a factor 2 the maximum and the average pressure values along the structure.

We consider the case where the pump is connected to both side of beam pipes. In this case, the effective pumping speed is  $S_{eff} = 5$  l/s and the cross section is,  $A = 2.76$  cm<sup>2</sup>. According to Eq.2.121, the sticking coefficient is the same as the one of Eq. 2.123.

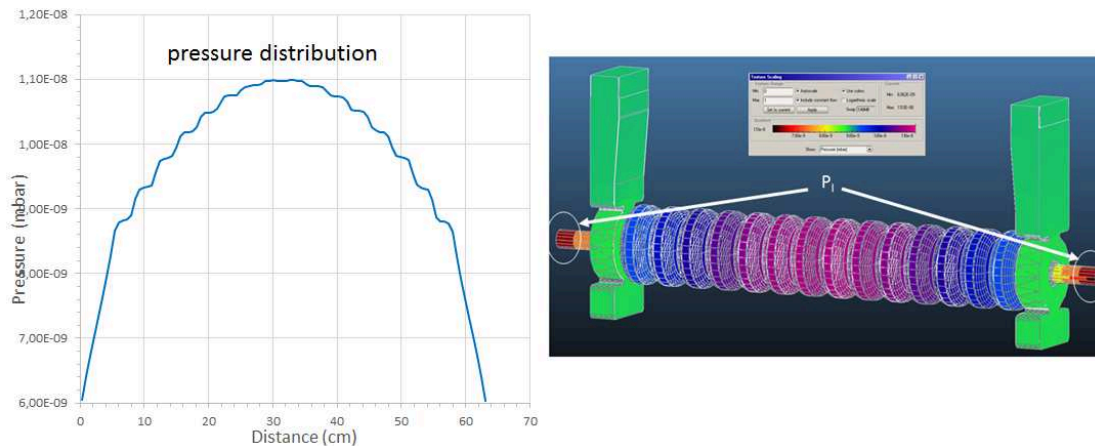


FIGURE 2.67: Vacuum pressure simulation in the case of one ionic pump connected to both beam pipes (right side). The plot shows the pressure along the structure (blue line).

Figure 2.68 shows the pressure along the accelerating prototype in case of where both beam pipes are connected to the pumps. The number of molecules that are degassed is 938200. The limited conductance of the chamber will build up a higher pressure at the center cells than at the end cells. From the plot, the maximum pressure value is  $1.1 \times 10^{-8}$  mbar, while the average value of the pressure is  $9.6 \times 10^{-9}$  mbar. We can easily see that this configuration allows to decrease by a factor 3 the maximum and the average pressure values along the structure in comparison with the case of a single ionic pump.

As the last configuration, we consider the case where the pump is connected to both RF waveguide ports. In this case, the effective pumping speed is  $S_{eff} = 36$  l/s and the cross section is,  $A = 24.547$  cm<sup>2</sup>. According to Eq. 2.121, the sticking coefficient is the same one as of Eq.2.124. Figure 2.68 shows the pressure along the accelerating prototype in the case of both RF waveguides ports connected to the pumps. The number of molecules that are degassed is 67700. From the plot, the maximum pressure value is  $3.7 \times 10^{-9}$  mbar, while the average value of pressure is  $2.6 \times 10^{-9}$  mbar. We can easily see that this configuration allows to decrease of a factor 3 the maximum and the average pressure values along the structure in comparison with the case of a single ionic pump connected to the waveguide port.

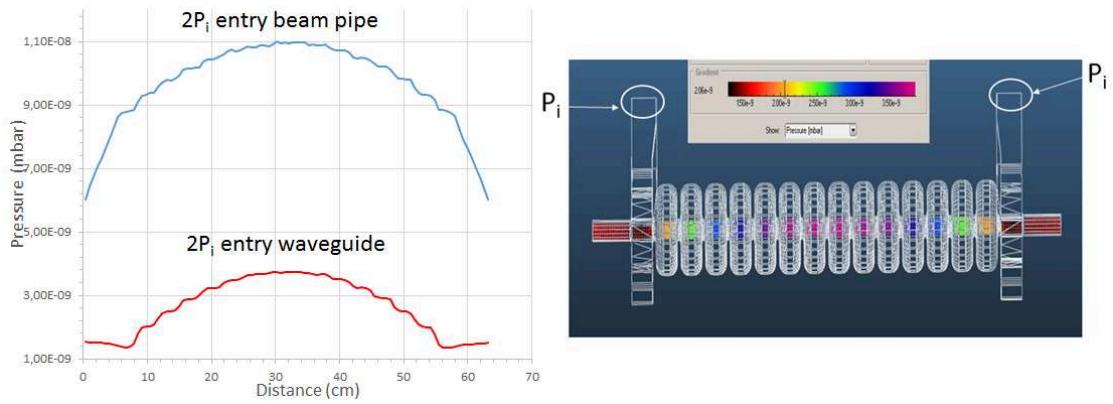


FIGURE 2.68: Vacuum pressure simulation in the case of two ionic pump connected to the RF waveguide ports (right side). The plot shows the pressure along the structure where the pumps are connected to one RF waveguide port (blue line) and to both RF waveguide ports (red line).

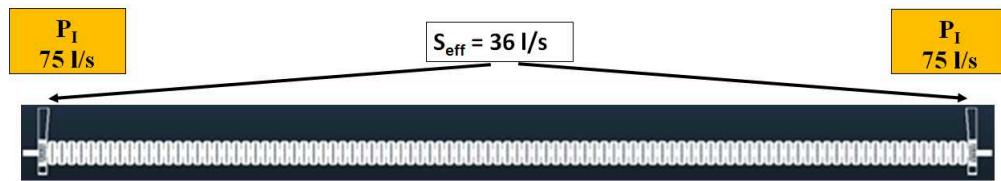


FIGURE 2.69: Vacuum geometry of the final accelerating section.

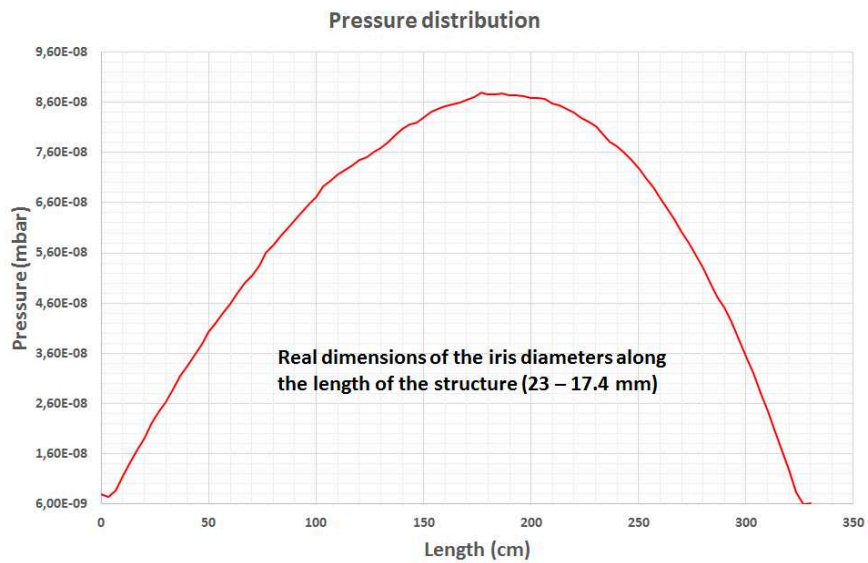


FIGURE 2.70: Pressure distribution along the length of the final TW CG accelerating structure.

Finally, the vacuum simulation of the 3.5-m long final accelerating section has been performed. We have supposed that all the facets on the external surface of the vacuum geometry are degassing except the outer surfaces that compose the beam pipes and at the entry of the waveguide ports. As for the previous case, the out-gassing rate of copper has been considered without bake-out and after 100 hours pumping at  $2 \times 10^{-11}$  (mbar/cm<sup>2</sup> s) that is equivalent to nitrogen at 20 °C. We have considered the following conditions (Fig.2.69): there is no out-gassing from the RF waveguide ports, the ionic pump has a nominal pumping speed of  $S = 75$  l/s ( $N_2$ ), flange CF100-type (for pressure equal to  $10^{-9}$  mbar,  $S_0 = 38$  l/s), the effective pumping speed is  $S_{eff} = 36$  l/s.

Figure 2.70 shows the pressure inside the vacuum geometry of the final constant-gradient accelerating structure along its length. As we should expect, the pressure is increasing along the section (because the iris diameters are progressively decreasing) until achieving its minimum value equal to  $5.97 \times 10^{-9}$  mbar. The average pressure value is  $5.83 \times 10^{-8}$  mbar and the maximum is  $8.78 \times 10^{-8}$  mbar.

In summary, the calculation of the pressure along the structure of several pumping configurations were performed using a Monte-Carlo program. We have considered a uniform out-gassing rate which is sufficient to compare the different pumping configurations. In the case of 16-cells section prototype, when two vacuum pumps are connected to the two waveguides, the maximum pressure at the center of the structure is around  $4 \times 10^{-9}$  mbar without bake-out treatment. In the case of the final accelerating section configuration, the maximum vacuum pressure is  $8.78 \times 10^{-8}$  mbar without bake-out treatment. These values are below or comparable to  $8 \times 10^{-8}$  mbar [69], that is enough for high-gradient operation [70]. Also, with bake-out treatment the simulated vacuum pressure would be divided by a factor 10 - 100. The good news is that according to our conservative calculations, the vacuum pumping for the prototype under present design should be adequate. the final 3.5-m long High-Gradient accelerating section we need to increase the vacuum inside the structure at least of factor 10 (better 100). We believe that pumping through the waveguide and performing back-out process to the section after installation will play a key role to the achievement of this goal.

## Chapter 3

# Manufacturing process

This chapter aims at briefly reviewing materials, fabrication methods and metal-joining techniques generally used in radio-frequency structure manufacturing, as accelerators. The fabrication of the ThomX gun and aluminium 7-cells CI prototypes are presented. Also, the experimental measurement of the RF low power test on aluminium prototypes are detailed.

There exist several forming techniques for cavity fabrication, such as machining, rolling, forging, spinning, pressing and deep drawing, hydro-forming, electroplating, electro-forming, sputtering and explosion forming [71]. For disk-loaded copper structures, the usual fabrication technique is the high-precision machining. Accelerator components are manufactured by turning different mechanical pieces through high precision lathes and/or milling tools. Then, they are joined together by brazing. The main steps of both RF gun and multi-cell periodic accelerating structure manufacturing procedure are:

- mechanical component machining,
- tuning process according to RF low power tests,
- re-machining of mechanical pieces to get the attended RF performances,
- structure assembling and brazing,
- vacuum test and leak detection,
- backing of the whole component (at least 150 °C), if necessary,
- installation and high power tests.

### 3.1 Precision machining

Copper is the favoured material for room temperature RF accelerating structures. In the framework of the collaboration agreement between the LAL and PMB-Alcen for the fabrication of a high-gradient S-band accelerating cavity, aluminium has also been used for prototyping. However, aluminium is not well suited for high-vacuum application because it tends to suffer from multipacting problems [71]. So, a prototype with a reduced number of cells has been fabricated only to validate the geometry.

Accelerators are made up of materials that have to exhibit some specific properties. A list of such characteristics is presented below [71]:

- electrical conductivity, which determines the maximum quality factor,
- thermal conductivity, which determines the operation temperature taking into account the dissipated power on the cavity walls,
- mechanical stiffness, which determines the elastic deformation of the cells and, therefore, the resonating frequency shift and thickness of the components for preventing collapses,
- vacuum out-gassing rate, which determines the static pressure in the volume for a given pumping speed,
- the secondary emission coefficient of the surface, which determines the multipacting rate,
- machinability, brazability or weldability,
- market costs.

The electrical and thermal conductivity, the mechanical stiffness and out-gassing rate for aluminium and copper are resumed in Tab.3.1 [71].

TABLE 3.1: Properties of aluminium and copper used for prototyping.

Materials	Electrical conductivity [1/( $\Omega$ m)]	Thermal conductivity [W/(cm K)]	Mechanical Stiffness [Pa]	out-gassing rate [(mbar l)/(cm <sup>2</sup> s)]
OFHC copper	$5.8 \times 10^7$	4	$120 \times 10^9$	$2 \times 10^{-11}$ (unbaked)
Aluminium	$3.7 \times 10^7$	2.2	$72 \times 10^9$	$2 \times 10^{-11}$ (unbaked)

Figure 3.1 gives tolerances and surface finishes that are normally achieved in several classical machining processes. For applications requiring the best dimensional accuracy

SURFACE FINISH	N8	N7	N6	N5	N4	N3	N2	N1
Ra (μm)	3.2	1.6	0.8	0.4	0.2	0.1	0.05	0.025
PLANING	████████████████████							
DRILLING	████████████████							
TURNING	██							
DIAMOND TURNING					██			
MILLING	██							
LAPPING					██			
POLISHING				██				
Roughness obtained with usual workshop practice								████████████████
Roughness obtained with special care								████████████

FIGURE 3.1: Typical surface finish for classical machining operations [71].

and surface finish, the fabrication is usually performed with single-crystal diamond-cutting tools.

The diamond-turning process produces high-quality surface finishes by accurately cutting away thin layers of the surface. It is generally applicable to ductile materials that machine well. In diamond-turning, the surface finish is largely determined by the machine tool and the cutting process. However, material characteristics such as grain size, inclusion size, etc., limit the ultimate achievable surface finish. The tool has to be very accurately moved with respect to the element to generate a good optical surface and the edge of the diamond tool has to be free of defects.

Diamond tools have been used for some time in the fabrication of cavities. Using a standard lathe with careful tool adjustment, 10 μm machining precision and N3 level ( $R_a < 0.1 \mu\text{m}$ , see Fig.3.1) of surface finish can be obtained in OFHC copper [72].  $R_a$  is the average roughness, namely the average of the absolute values of the surface height variations,  $z_i$ , measured from the mean surface level [73]:

$$R_a = \frac{1}{N} \sum_{i=1}^N |z_i| \quad (3.1)$$

Nowadays, RF cavities can be fabricated to much tighter tolerances and with a greatly improved surface finish. This is possible on specialised sub-micron precision lathes using single point cutting with natural-diamond tools. The combination leads to an improvement over a “classical” diamond turning: for instance, for a soft material as copper, one gains an order of magnitude in tolerance to achieve  $\pm 1 \mu\text{m}$  and an order of magnitude in surface finish quality to achieve a level better than N1 ( $R_a < 25 \text{ nm}$ ) [72].

These advantages are particularly important for high-frequency accelerator applications where the structure dimensions are small and the mechanical tolerances are critical to guarantee the expected performance of the RF components.

## 3.2 Cleaning process

The primary purpose of cleaning is to assure a uniform brazing diffusion of the materials during the brazing process. The cleaning procedure starts from the removal of gross contaminants and moves to progressively remove finer contaminants leading to a finer surface. How far the cleaning should be carried out depends on the required total pressure of the system, the required limits on surface reactions and pumping speed [74].

## 3.3 High temperature brazing process

Brazing is one of the most common ways for assembling cavities. Brazing is a joining technique where a filler metal or alloy having a lower melting point than the base materials is heated to a certain temperature (typically above 800 - 900 °C). The filler melts, wets and flows by capillary action through a defined gap and solidifies on cooling. The size of the gap is typically a few hundredths of mm. The brazing process is usually carried out under vacuum. In this condition, surface contaminants are removed (at least at elevated temperatures) and the hydrogen content of the base materials and their subsequent out-gassing rate are significantly reduced. This process increases the



FIGURE 3.2: LAL furnace for vacuum brazing process of components.

copper ductility reducing its hardness (copper annealing) and, during each brazing step,

the parts undergo high mechanical and thermal stresses (more than 800 °C) due to the high temperature [56]. In general the brazing process presents several drawbacks:

- the risk of failure of the brazing is not negligible (vacuum leaks, damages, etc.);
- it requires a large vacuum furnace not always easy to get,
- in general, it is expensive,
- at the end of the process, the copper is “soft” since it has lost its mechanical hardness.

PMB-Alcen is able to perform brazing process under vacuum ( $10^{-3}$  -  $10^{-6}$  mbar) of hi-tech products for medical diagnosis, scientific researches, defence & security, space technologies and nuclear power. The high-temperature brazing vacuum furnace at PMB-Alcen is able to host mechanical components with length up to 0.9 m. Figure 3.2 shows the high-temperature furnace available at LAL where vacuum brazing processes are performed. With this furnace, the LAL has brazes the CTF3 gun, the PHIL gun (Photo-injector Facility at LAL) and the ThomX guns. The maximum temperature attainable is 1300 °C, the diameter is 380 mm and the length is 660 mm.

### 3.4 Development and testing of ThomX RF gun at LAL

This paragraph describes the main steps performed during the ThomX RF gun fabrication. Basically, the procedure consists in the machining, tuning, brazing and cleaning processes that were carried out at LAL.

#### 3.4.1 Machining process at LAL

The pieces are machined with a precision lathe (Fig.3.3). The cell diameter is around 0.5 mm smaller with respect to the design dimension that is calculated by EM simulations. The coupling hole, at this stage, is very small with respect to what is set by EM simulations. All mechanical components are realised without joint parts designated for brazing. After the first machining process, the dimensional control of each mechanical component is performed. Then, RF low power measurements are carried out in order to estimate how far the mechanical dimensions are from the design geometry. Before re-machining the cells, the flatness of each cell plane is checked on a traditional lathe. Also, this operation is usually repeated after re-machining is finalised. During re-machining process, alcohol is used as oil. The re-machining process is iterated with RF low power measurements until the RF performances are fulfilled.



FIGURE 3.3: Multi-tasking precision lathe for machining process at LAL.

When the final re-machining process is finalised, the pieces are machined with the joint parts designated for brazing. Finally, each cell will be wrapped up in clean tissues and stored in a shockproof box. Often, the LAL uses to fabricate a second RF gun as a “spare” of the first one. The “spare” gun is machined following the same procedure than the first gun.

### 3.4.2 Cleaning process at LAL

All pieces are cleaned according to the following procedure:

- ultrasonic cleaning,
- hot acid-bath (temperature around 20 °C),
- demineralized-water rinsing,
- alcohol rinsing,
- steaming in a specific furnace.

### 3.4.3 Tuning process at LAL

The experimental workbench is settled to perform RF measurements in air at controlled temperature conditions (20 °C). The tuning procedure is performed taking into account the transmission coefficient. First, the resonating frequency and unloaded quality factor with a low coupling factor are measured and compared with the simulations. Second, the coupling hole is progressively enlarged to achieve around -3 dB transmission coefficient between the two coupling ports (Fig.3.4).

Electromagnetic simulations gave the sensitivity of the resonating frequency due to variation of each individual cell diameter. Then, the cells are individually re-tuned in order to improve the electric field balance and approach the designed resonating frequency. The Slater’s perturbation method allows to estimate the electric field balance from cell-to-cell by means of frequency shift measurements (bead-pull method). Finally, the position of the short-circuit is defined for keeping the frequency design value and coupling adaptation with respect to the reflection coefficient. In particular, for the third ThomX RF gun, thirty iterations have been performed for six months.

Once tuning process is validated, a new cleaning procedure is carried out before brazing.



FIGURE 3.4: Test bench: low power measurement and tuning procedure of the ThomX RF gun.

#### 3.4.4 Brazing process at LAL

The ThomX gun has to sustain an ultra-high-vacuum level of operation (UHV,  $< 10^{-9}$  mbar). It has to be hermetic for several years and sustain thermal treatments (e.g steaming in-situ), if necessary, for promoting the surface degassing and decreasing the static vacuum without intervention (the residual pressure becomes an important criterion in order to preserve the cathode lifetime, especially with thin layers).

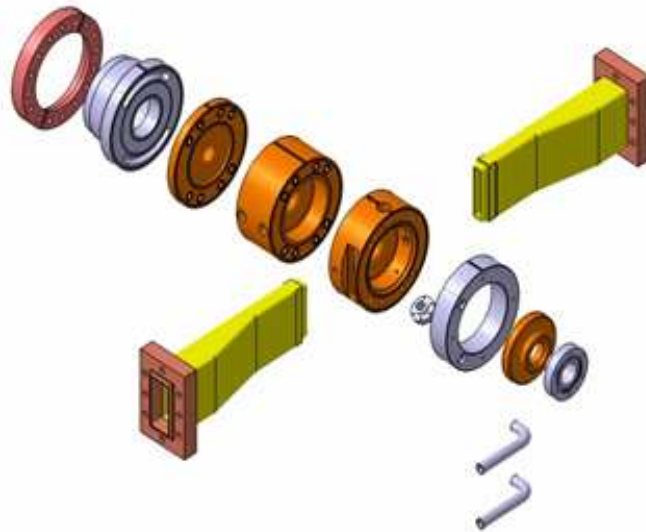


FIGURE 3.5: 3D mechanical parts of the ThomX RF gun.

Figure 3.5 shows the 3D mechanical components of the gun. For assembling all the pieces, twelve brazing planes, thirty joint brazing point and seven different brazing cycles are

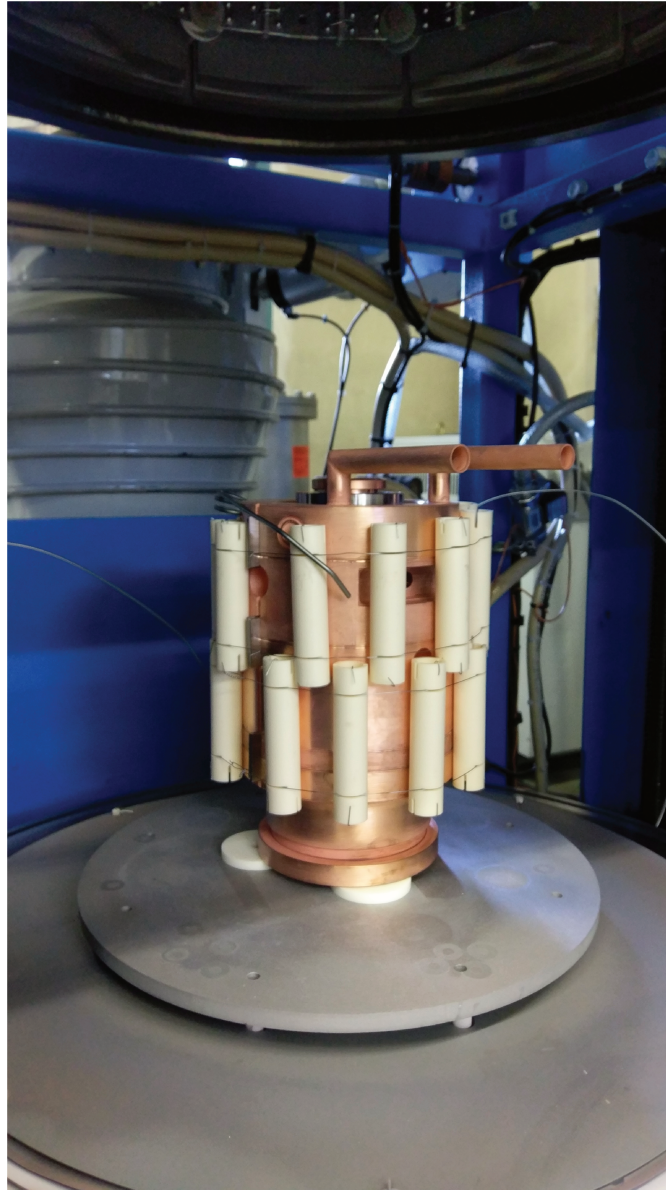


FIGURE 3.6: ThomX RF gun in the furnace for the brazing process.

required. The ThomX RF gun will be installed at the accelerator site and then high power tested in-situ before starting the commissioning phase of the linear accelerator.

Figure 3.6 shows the picture of the copper gun placed in the high-temperature vacuum furnace. Ceramic cylinders are installed around the copper body for the mechanical alignment between the different parts. Also, a good alignment has to be assured at high-temperature so the ceramic cylinders are tightened to exert a pressure nearby brazing points.

### 3.5 Development and testing of aluminium 7-cells S-band prototypes at PMB-Alcen

The design of a constant-impedance TW structure with a reduced number of cells has been carried out with CST MWS and HFSS. The details are presented in Chapter 2. After the mechanical drawings validation, PMB-Alcen started to fabricate many identical regular accelerating cells while two couplers were fabricated by a subcontractor. In our design, the machining of the power couplers is one of the most critical part of the RF structure fabrication. The fabrication of two 7-cells aluminium prototypes lasted two years. Concerning the first prototype, the subcontractor performed a standard fabrication procedure and power couplers presented manufacturing defects. After a dimensional control and an inner surface inspection, we found missing parts at coupling apertures. Regarding geometrical and dimensional tolerances the requirements have not been respected. A picture of the turn and mill machine that has been used for regular cells fabrication at PMB-Alcen is displayed in Fig.3.7. Because of the difficulties and complexity of the couplers geometry, PMB-Alcen decided, with the agreement of the LAL, to commission these parts to Comeb SrL. Two aluminium RF couplers have been fabricated with ultra-precision machining tools, whereas for the second prototype, regular cells were fabricated with standard tools by PMB-Alcen.

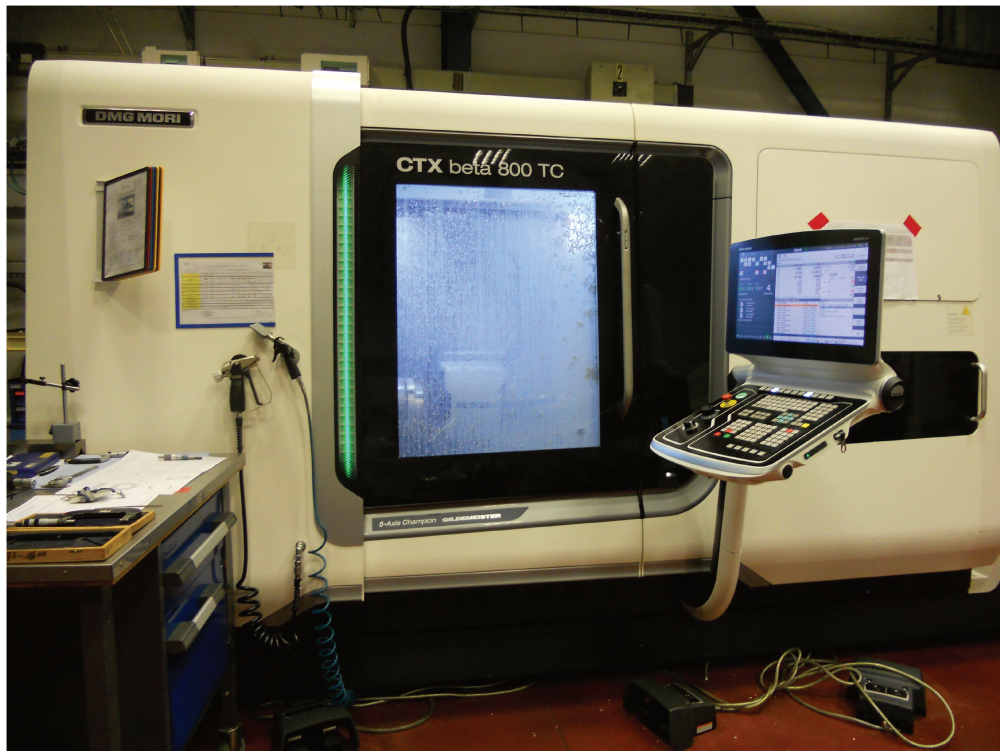


FIGURE 3.7: Turn and mill machine used at PMB-Alcen for regular cells fabrication.

### 3.5.1 Aluminium 7-cells S-band prototype machining process

The turning process performed at PMB-Alcen for regular cells machining can be resumed as follows:

- preparing the blank (in this case it is cylindrical) with an extra thickness of material on the surface to be turned,
- mounting the blank in an appropriate fixture or chuck on the turning machine,
- selecting the appropriate tool according to the material and shape of components,
- machining (1st step) the component to around 1 mm of final dimensions,
- machining (2nd step) the component to around 50  $\mu\text{m}$  of final dimensions,
- machining (3rd step) the component to around 10  $\mu\text{m}$  of final dimensions,
- cleaning the surface to remove cutting oils or solvents,
- dimensional precision controls.

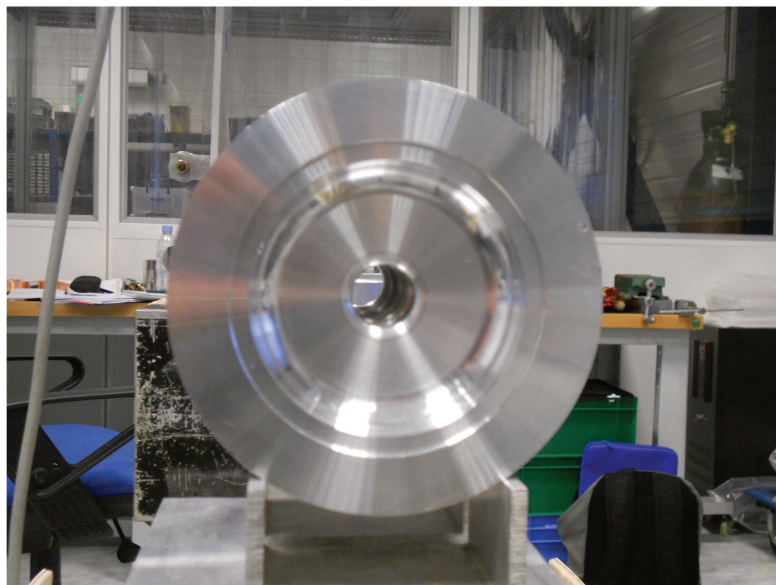


FIGURE 3.8: View of the inner volume of a regular cell.

Machining errors of regular cells fabricated by PMB-Alcen (Fig.3.8) are greater than 10  $\mu\text{m}$  with respect to the nominal design. Working at 2998 MHz (in air at 21 °C,  $2\pi/3$  TW structure), errors of 20  $\mu\text{m}$  in the single regular cell radius causes a frequency shift of 1.5 MHz leading to a phase advance per cell error more than  $3^\circ$ . If these discrepancies are not compensated, it will lead to the degradation of the prototype performance.

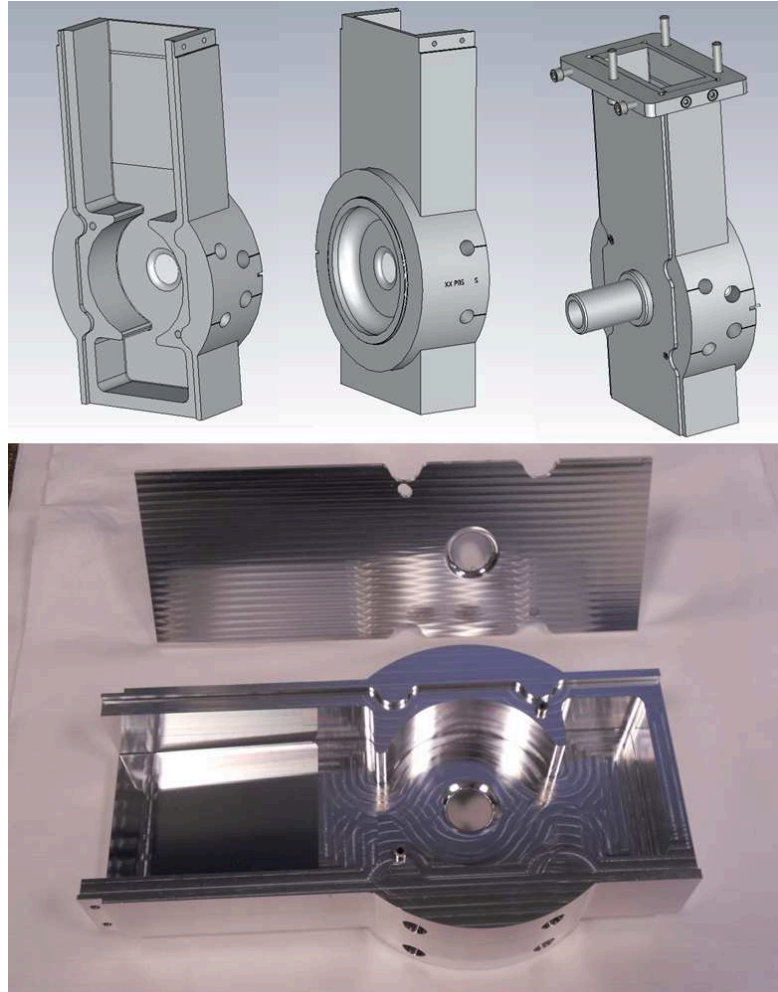


FIGURE 3.9: 3D mechanical drawing of the power coupler (top) and power coupler parts fabricated by Comeb SrL. (bottom).

The fabrication of the two aluminium power couplers has been carried out at Comeb SrL (Fig.3.9). The latter are composed of two parts: the body and the cover. They are not brazed but screw threaded because they do not have to sustain vacuum application.

They were realised by a mono-crystalline single-diamond tool turning in order to achieve tolerances up to  $2 \mu\text{m}$  causing a frequency shift of 100 kHz and a surface finish up to 25-30 nm.

### 3.5.2 Tuning method under press of regular cells

The tuning of regular cells at the desired resonance frequency requires two different steps: the tuning of sample cells and the tuning of regular cells (which compose the prototype assembly) by means of sample cells. Sample cells are tuned by the insertion of conducting rods as illustrated in Fig.3.10.

In general, the tuning of cells at  $2\pi/3$ -mode must be performed by placing metallic plates located in planes of symmetry in such a way that the standing wave “trapped” between them is an exact representation of the instantaneous travelling wave propagating along the structure. We have metallic plates under press at both ends of the cell stack. The frequency control of the TW cells is performed in a standing wave mode (eigenmode).

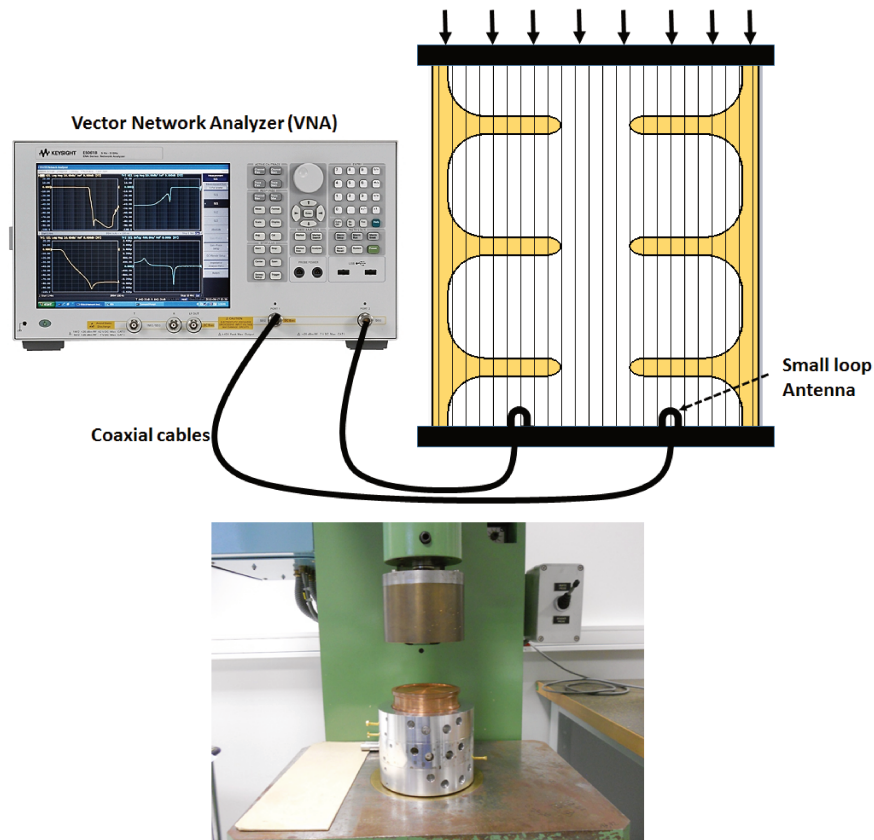


FIGURE 3.10: Measurement setting under the press of sample cells at PMB-Alcen.

Figure 3.10 shows the measurement setting for the frequency control under press together with the equipment that are required for the measurement. The aim of the tuning procedure on sample or regular cells for  $TM_{010-2\pi/3}$  mode is to reduce the contribution of the “mixed” electric field pattern leading to a possible tuning of the different cells individually. We first consider the tuning under press of two sample cells. In this case, propagating modes ( $TM_{010-\varphi_k}$ ,  $\varphi_k = k\pi/(N-1)$ ,  $0 \leq k \leq N-1$ , where  $N = 3$  is the number of volumes) are  $0$ ,  $\pi/2$  and  $\pi$ , respectively. We tune the outer volumes of the sample cells at the  $\pi/2$ -mode because the central volume has no field, as shown in Fig. 3.11. So we can eliminate the contribution of the “mixed cells” field pattern and tune the cavity volumes one by one.

After, we add one sample cell in the middle. Now, we have three sample cells under press corresponding to one RF wavelength for the mode  $2\pi/3$ . The propagating modes

( $TM_{010-k\pi/3}$  where  $0 \leq k \leq 3$ ) for these four volumes can only be  $0, \pi/3, 2\pi/3$  and  $\pi$ , respectively. We tune the 3-cells stack at the  $2\pi/3$  mode by comparing the third peak of the reflection coefficient ( $S_{11}$  parameter) to the resonating frequency obtained from the EM design simulations. Figure 3.12 shows the geometry for tuning together with the electric field vector and its profile on-axis. As we can see from the plot, for this propagating mode the electric field is present in all volumes. In this propagating mode, we cannot eliminate the contribution of “mixed cells” and we must tune the cell volumes by permuting the position of each cell.

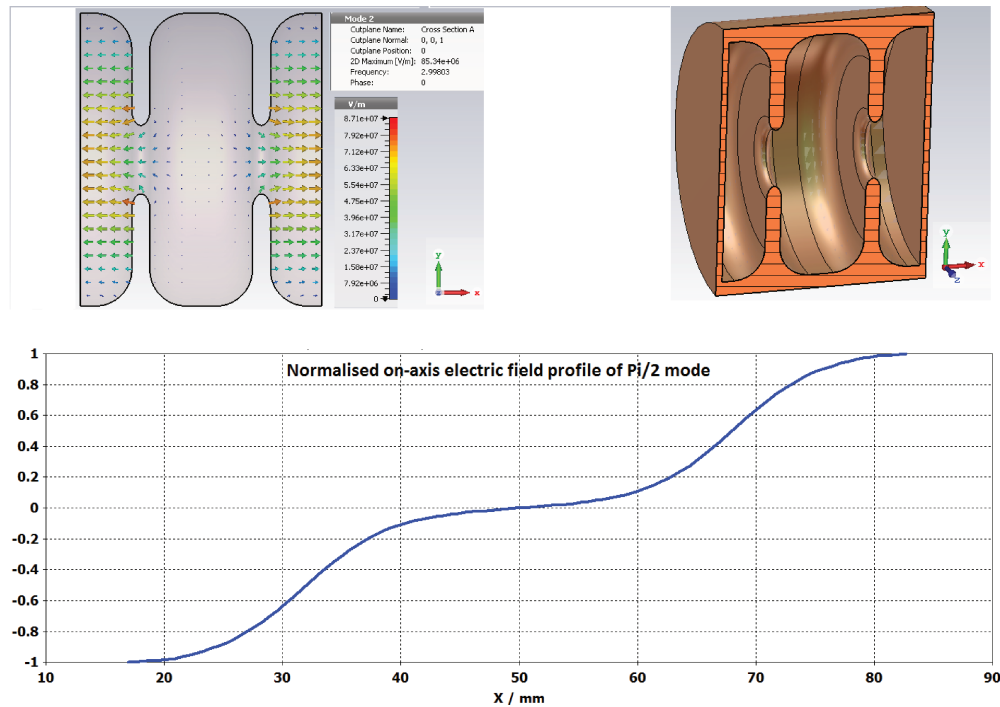


FIGURE 3.11: CST MWS simulation (eigenmode) of the  $TM_{010-\pi/2}$  for 2-cells stack.

Once we have tuned a sample 3-cells stack, we can perform the tuning of regular cells by the wall deformation (4 tuners for each cell). We are able to tune three by three regular cells at  $2\pi/3$  mode by inserting them in the sample 3-cells stack previously tuned.

In this step, each regular cell can be tuned at  $2\pi/3$  mode by permuting its position within the regular cell stack (Fig.3.13).

At the end, regular cells should be tuned at the  $2\pi/3$ -mode with a resonating frequency of 2998 MHz at room temperature  $21^\circ\text{C}$  in air at PMB-Alcen. Usually, these cells are used to compose the regular cells stack of the prototype structure.

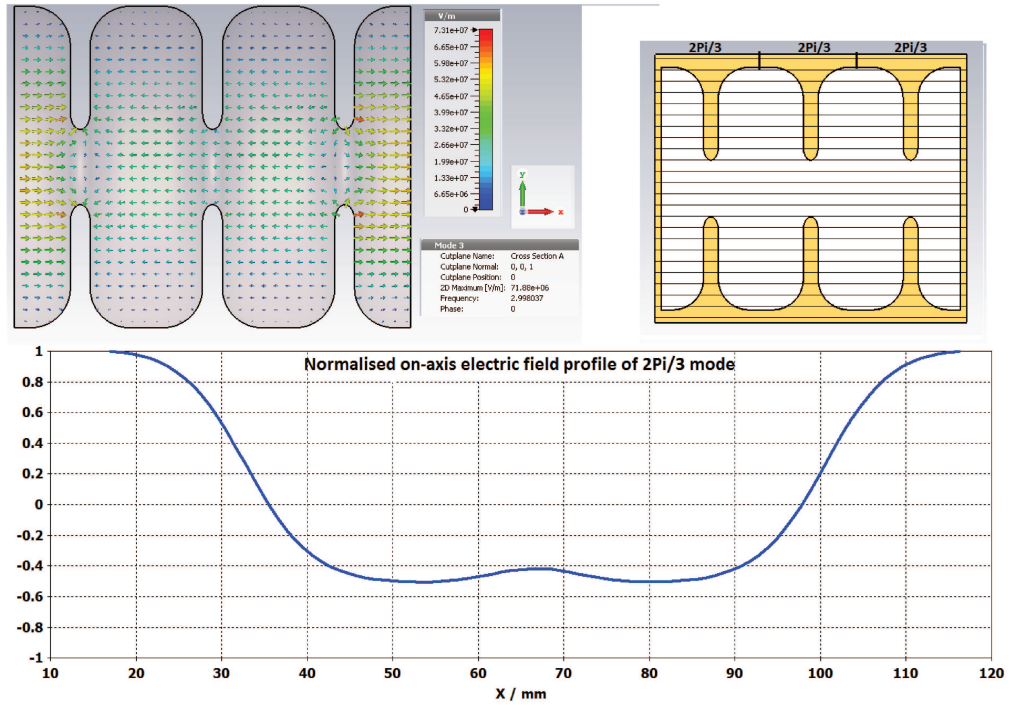


FIGURE 3.12: CST MWS simulation (eigenmode) of the  $TM_{010-2\pi/3}$  for 3-cells stack.

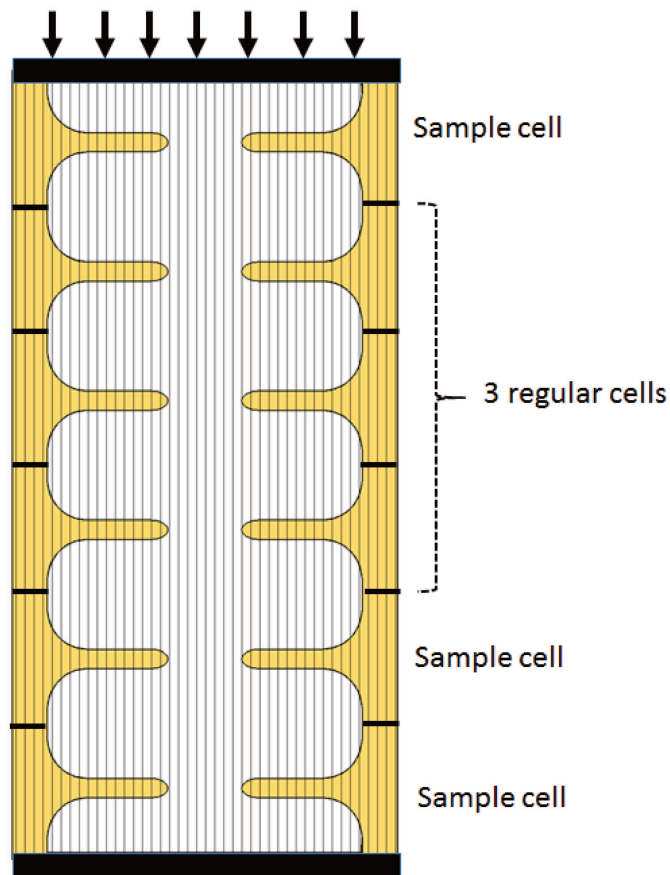


FIGURE 3.13: Scheme of regular cells tuning.

### 3.5.3 Low power test of the aluminium 7-cells prototype

An RF low power test of the 7-cells aluminium prototype is performed in order to validate the 3D geometry design and the machining process. Those last steps are very important to tackle mechanical problems and technological constraints for the future copper prototype.

Figure 3.14 and Fig. 3.15 show the 3D mechanical design and the prototype assembly ready for measurement. The RF measurement was performed by the nodal shift method

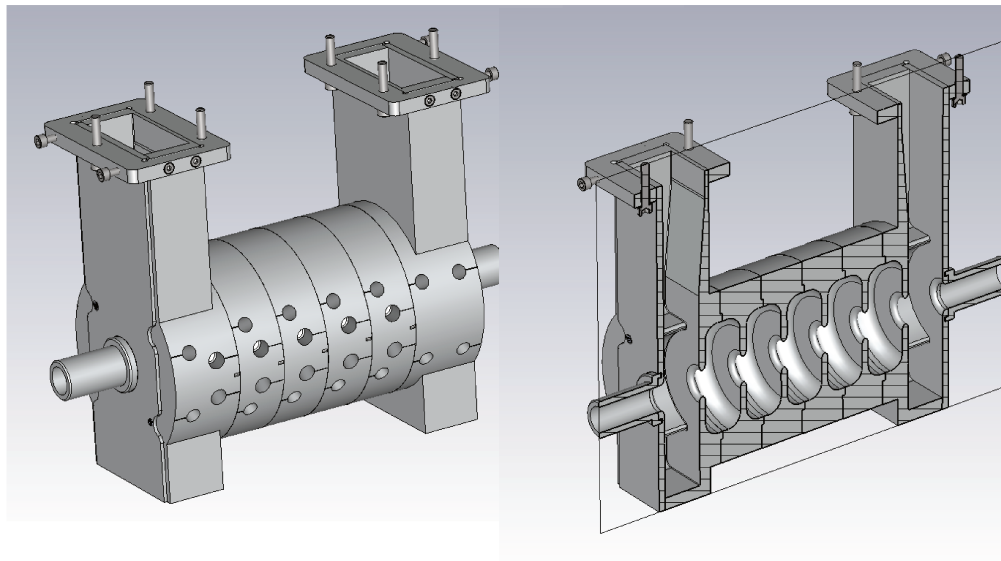


FIGURE 3.14: 3D mechanical drawing of the 7-cells aluminium prototype.

using Vector Network Analyser (VNA). Figure 3.16 illustrates the principle of the nodal shift technique [75, 76] that was used for amplitude and phase measurements of the longitudinal electric field of the fundamental mode  $TM_{010-2\pi/3}$ . A copper plunger, starting from the center of the input coupling cell, is progressively pulled through the structure. It de-tunes successive cells and thereby causes the standing wave pattern to shift. As the measurement of the reflection coefficient  $S_{11}$  is performed through a coupler, each point represents the reflection coefficient,  $S_{11}$ , of the travelling wave reflected back at each cell. One can therefore deduce the amplitude of the electric field and the phase advance per cell from the S-parameter ( $S_{11}$ ) data saved in a text file.

Before tuning, the analysis of the measured results indicate that the cell-to-cell phase advance error is around  $10^\circ$  and the resonant frequency is shifted down by 1.3 MHz with respect to the design frequency as shown in Tab.3.2. So the tuning procedure is necessary to have a phase advance per cell equal to the nominal value of  $120^\circ$  and also minimise the reflection from the tuned cell. This allows to avoid the standing wave in the structure which introduces a local field enhancement and may limit the overall accelerating gradient.

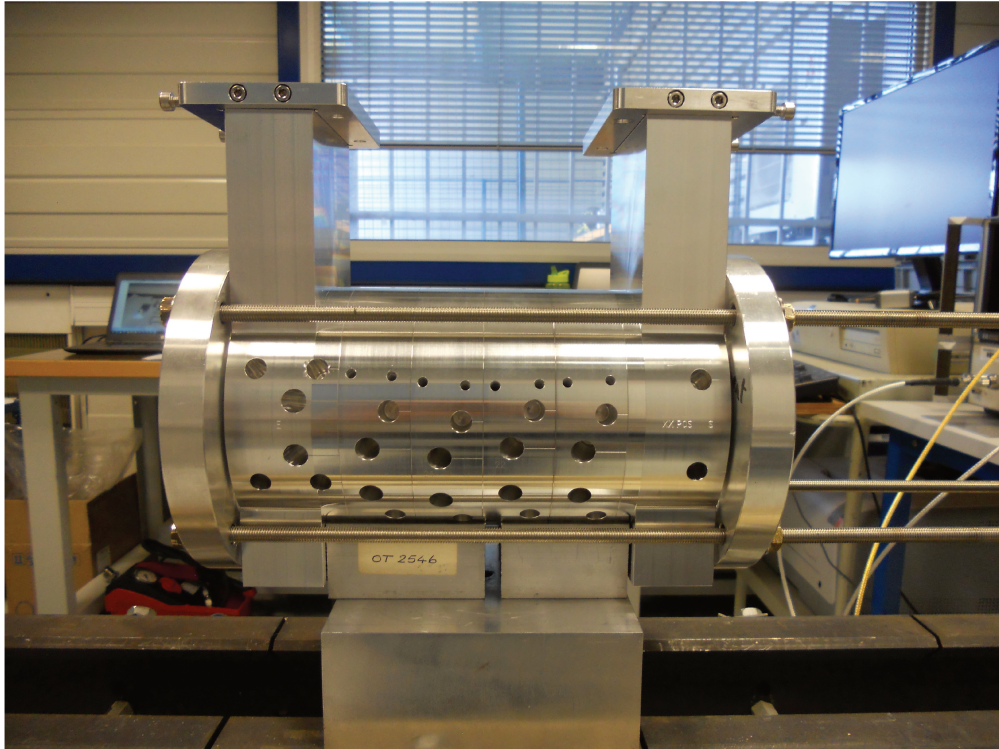


FIGURE 3.15: 7 cells TW CI prototype ready for measurements at PMB-Alcen.

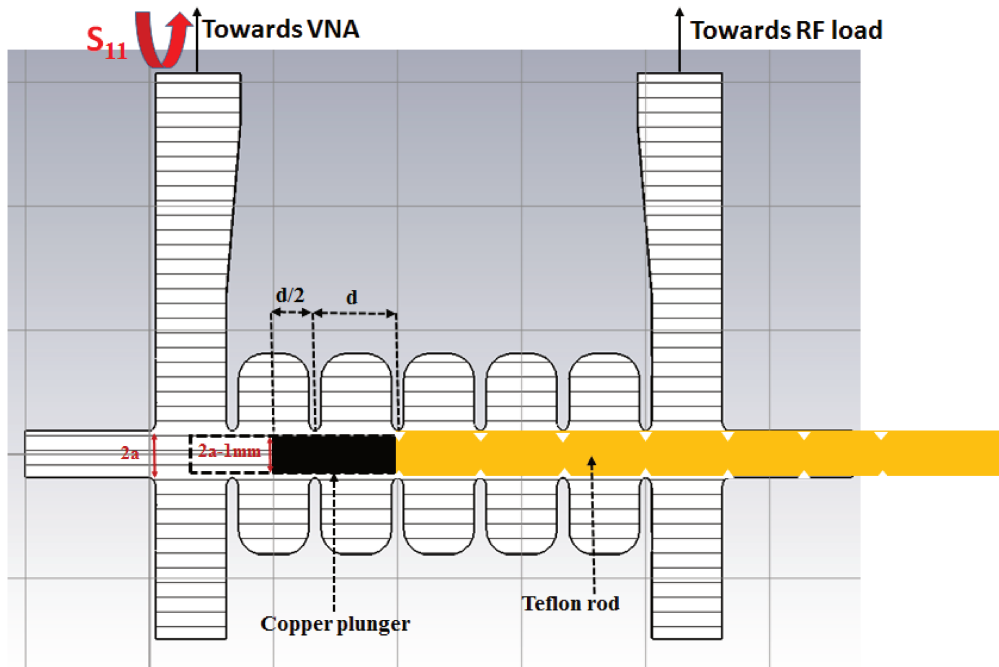


FIGURE 3.16: Principle of the nodal shift technique at PMB-Alcen.

The tuning of regular cells is first made by tuning holes (four tuners per cell) and consists in the introduction of a deformation on the cell wall in order to correct the cell-to-cell phase advance and minimise the input reflection coefficient ( $S_{11}$  and  $S_{22}$ ). This wall deformation is obtained by applying a force with special tools on the outer walls of the

TABLE 3.2: Measurement of the electric field amplitude and the phase advance per cell by the nodal shift method, before tuning for  $TM_{010-2\pi/3}$  at 2996.8 MHz.

	Normalised field amplitude	$\Delta Phase$ [deg]
input coupling cell	1	
1st cell	0.868	118
2nd cell	0.863	110
3rd cell	0.926	119.5
4th cell	0.769	117.5
5th cell	0.816	110.5
output coupling cell	0.833	118.5

cell (by pair tuners). This one directional tuner allows to apply this force in order to

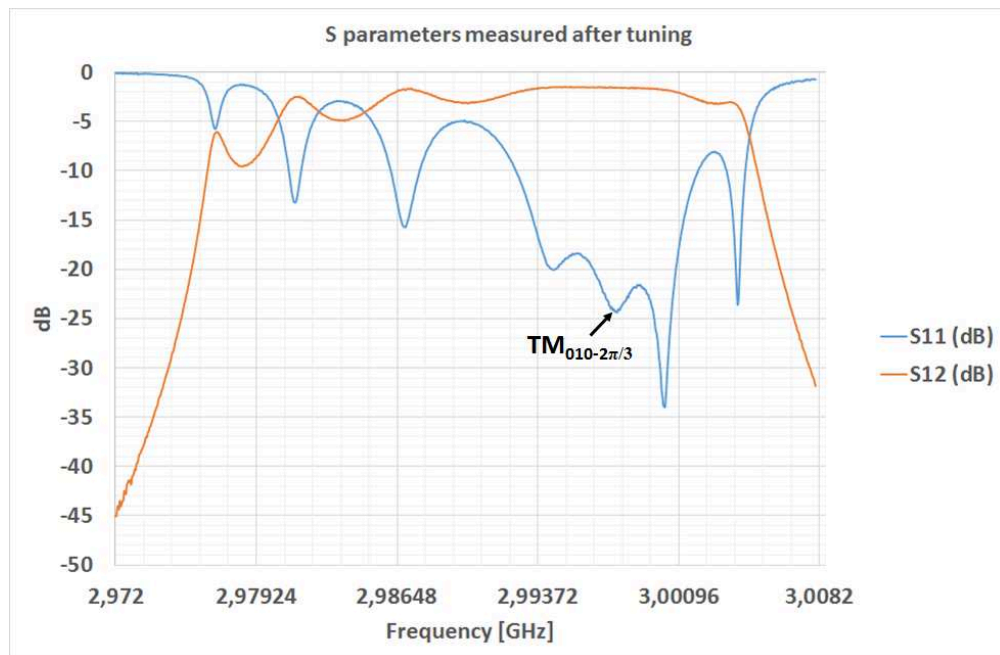


FIGURE 3.17: Measured S-parameters (return loss  $S_{11}$  and insertion loss  $S_{12}$ ) of the 7 prototype volumes after tuning.

TABLE 3.3: Measurement of the electric field amplitude and the phase advance per cell by the nodal shift method, after tuning for  $TM_{010-2\pi/3}$  at 2997.74 MHz.

	Normalised field amplitude	$\Delta Phase$ [deg]
input coupling cell	1	
1rst cell	0.836	118
2nd cell	0.820	119.5
3rd cell	0.911	120.5
4th cell	0.753	119
5th cell	0.744	121
output coupling cell	0.823	120.5

decrease the internal volume of the cell. In fact, aluminium is a hard material so the RF tuning sensitivity due to the wall deformation is weak. Instead of using high-precision

machining for regular cells fabrication with minimum errors, PMB-Alcen decided to use the tuning rods (Fig.3.10) as an alternative solution for cells having additional holes for the insertion of rods, as shown in Fig.3.15. The tuning rods method is not appropriate for high performance structures since rods behave as coaxial conductors and may induce multipacting between the tuner and the cell walls spoiling the cavity performance.

After tuning, the phase advance per cell was within  $\leq 2^\circ$  with respect to the nominal one (see Tab.3.3). As shown in Fig.3.17, the measurement of the input reflection coefficient  $S_{11}$  of the tuned structure is about -25 dB for the accelerating mode  $TM_{010-2\pi/3}$  at frequency 2997.74 MHz in air at room temperature (21 °C). The measured insertion loss  $S_{12} \sim -1.5$  dB is higher than the simulated one  $S_{12} \sim -0.5$  dB.

Future work will focus on the fabrication of the 16-cells copper CI prototype for the validation of the manufacturing process, the RF conditioning and high power tests. After, a 3-m long high-gradient S-band accelerating section for the ThomX linac energy upgrade will be fabricated.

## Chapter 4

# ThomX Linac beam dynamics

The kinematics and the main quantities that evaluate the quality of the X-rays produced by the ThomX ICS source have been presented in Chapter 1 and the requirement for an electron beam with small energy spread as well as transverse emittance has been highlighted.

Since each single electron bunch is injected in the ring every 20 ms, the beam dynamics happens on relatively short timescales. In this case radiation damping, which is usually the dominant effect in the storage ring, is of the order of seconds. In addition, the relatively low energy beam makes others single-bunch collective effects responsible of beam losses or emittance degradation. Since the quality of the X-ray production is mostly determined by the electron beam characteristics, the lack of radiation damping in the ring makes an high quality electron beam essential at the exit of the linac. In fact, the electron beam properties at the exit of the transfer line strongly dominate the subsequent particle dynamics in the ring and the ultimate machine performances at the interaction point. So, a dedicated tuning of the linac is necessary.

At present, the technology capable to produce an electron beam with high-brightness, small emittance and energy spread is the photo-injector. The scheme of a traditional photo-injector usually consider a photo-cathode gun, solenoids for space charge emittance growth compensation and beam matching with one or several accelerating sections. Since a thermo-ionic gun would entail a beam pre-buncher and buncher scheme leading to more longer and complex linac, the photo-injector scheme has been considered as the best technical choice for the ThomX accelerator.

This chapter concerns the electron beam dynamics of the ThomX linac. The properties of the electron bunch are presented from the early stage of its production to the exit of the accelerating section. First, some beam dynamics basic principles, such as the phase

space and the matrix formalism which allow describing the characteristics of the beam in this space are introduced. Also, the principle of electron acceleration by standing wave, travelling wave and the importance of the particle phase relative to the oscillation in time of the longitudinal on-axis electromagnetic field component are presented.

Second, an overview of the X-rays spectral flux as a function of the observation angle is proposed. In particular, the characteristics of the X-rays with respect to two different beam transverse emittance and energy spread values at the interaction point are presented. Third, the emittance compensation scheme is detailed. The 3D model of the solenoids concerning the ThomX Technical Design Report configuration (ThomX TDR) [17] is described. In fact, the electron beam quality strongly depends on the particular solenoid compensation scheme that is chosen. The main effect of the longitudinal on-axis magnetic field component on the electron bunch dynamics is detailed in section 4.2.3. In order to improve the beam properties at the linac exit, a new solenoid configuration has also been considered taking into account the mechanical constraints.

Finally, the comparison between the ThomX TDR and the new solenoids configurations is proposed in terms of the beam characteristics requirements at the exit of the linac. As it has been mentioned before, these specifications have to be fulfilled for the matching with the transfer line.

## 4.1 Some basic principles of beam dynamics

The Hamiltonian formalism in the phase space is the common tool for describing the particle dynamics in accelerators.

### 4.1.1 Phase-space and emittance

The phase space is a 2n-dimensional space that is represented by canonical coordinates  $(q_i, p_i)$ , where  $i = 1, 2, 3, \dots, n$ . Considering canonical coordinates, the equation of motion is described by the Hamilton's function,  $H(q,p,t)$ , with the following equations:

$$\dot{q}_i = \frac{\partial H}{\partial p_i} \quad (4.1)$$

$$\dot{p}_i = -\frac{\partial H}{\partial q_i} \quad (4.2)$$

$$\frac{dH}{dt} = \frac{\partial H}{\partial t} \quad (4.3)$$

The motion of a single particle in the phase space can be described with a trajectory that is function of time. Instead, considering  $N$  non-interacting particles, at any time

$t$  there are  $N$  points in the phase space which are enclosed in the hyper-volume that describes the bunch.

The Hamiltonian formalism in the phase space of canonical coordinates uses the Liouville's theorem [77]. According to the latter, the hyper-volume defining the bunch of non-interacting particles is constant with respect to time. The Hamiltonian description of beam dynamics is not really compatible with mutual interaction of the particles due to space charge effects, interaction of the particles with the vacuum chamber (wakefield) and synchrotron radiation. However, the formalism is well suited for describing the motion of non-interacting particles under external fields.

Let consider for the phase space the three dimensional position coordinates  $(x, y, z)$  with the three dimensional momentum coordinates  $(p_x, p_y, p_z)$ . The Hamilton's function is therefore:

$$H = H(x, p_x, y, p_y, z, p_z, t) \quad (4.4)$$

The beam is represented by an invariant (hyper-volume) in the phase space in the form:

$$\int \int dx dp_x \int \int dy dp_y \int \int dz dp_z = constant \quad (4.5)$$

If the Hamilton's function is separable, the sub-spaces are decoupled and we have:

$$H = H_x(x, p_x) + H_y(y, p_y) + H_z(z, p_z) \quad (4.6)$$

in each subspace, the hyper-volume has an area:

$$\int \int dx dp_x = constant \quad (4.7)$$

$$\int \int dy dp_y = constant \quad (4.8)$$

$$\int \int dz dp_z = constant \quad (4.9)$$

The area of each subspace, when the equations of motion are decoupled, defines the horizontal, vertical and longitudinal emittances, respectively.

In the transverse plane (with respect to the bunch motion), the coordinates  $(x, x')$  and  $(y, y')$  are usually considered, where the variable:

$$x' = \frac{dx}{dz} \quad (4.10)$$

$$y' = \frac{dy}{dz} \quad (4.11)$$

$$(4.12)$$

are usually called divergences and are measured in radiant. We rewrite Eq.4.10 as:

$$x' = \frac{dx}{dz} \simeq \frac{p_x}{p_0} \quad (4.13)$$

with  $p_0$  the momentum of the reference particle and considering at first order  $p_z \simeq p_0$ . If  $p_0$  is constant then the transverse geometric emittance is constant:

$$\epsilon_x = \int \int dx dx' = \frac{1}{p_0} \int \int dx dp_x = \frac{\text{constant}}{p_0} \quad (4.14)$$

The geometric emittance,  $\epsilon_x$  is not actually invariant because it varies with the momentum of the reference particle ( $p_0$ ). So, the geometric emittance is always referred to some specific energy or momentum of the reference particle. From Eq.4.14 one can define the normalised emittance:

$$\epsilon_{n,x} = \beta\gamma\epsilon_x \quad (4.15)$$

The normalised emittance is invariant with energy and allows to compare different beam with different energy as long as the nature of the particle is the same (electrons or protons) and if there are no mutual interaction between them.

### 4.1.2 Twiss parameters

In the  $n$ -dimensional phase space the beam is therefore described as an hyper-volume enclosed in a surface. In a 6D phase-space, the beam is an hyper-ellipsoid and any projection on any subspace is still an ellipsoid and does not change applying a linear transformation (transfer matrix).

In 2D the ellipsoid becomes an ellipse and can be described through a 2x2 matrix that is called “beam matrix”,  $\sigma$ , considering there is no coupling between axes. The ellipse profile that encloses the beam can be obtained from:

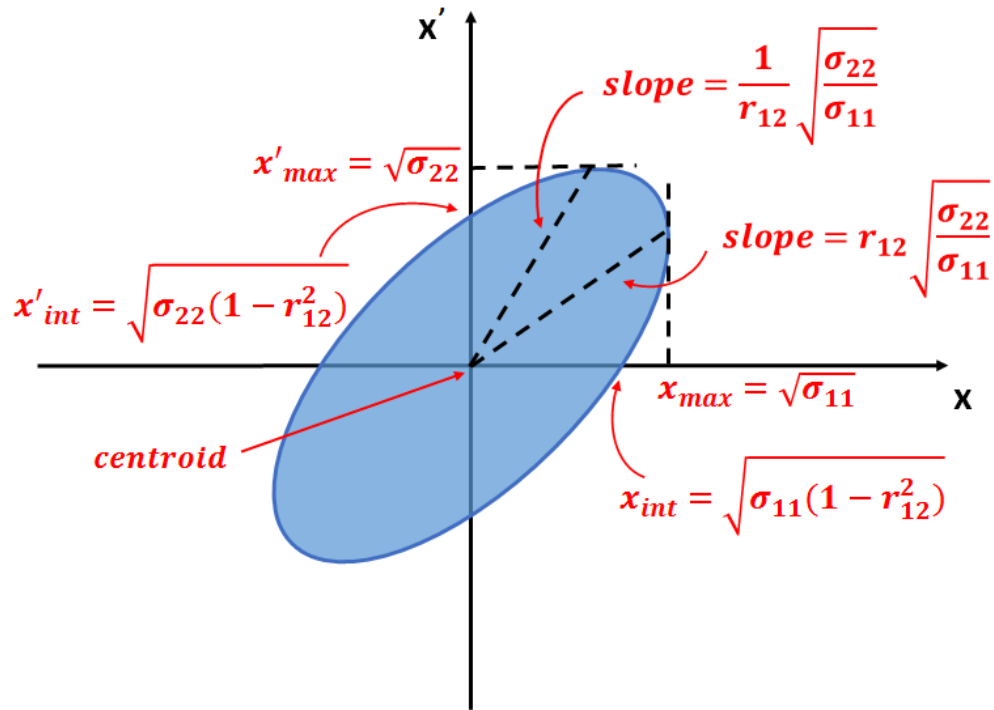
$$X^T \sigma^{-1} X = 1 \quad (4.16)$$

where the beam matrix is written as:

$$\sigma = \begin{pmatrix} \sigma_{11} & \sigma_{12} \\ \sigma_{21} & \sigma_{22} \end{pmatrix} \quad (4.17)$$

The inverse matrix is then written as:

$$\sigma^{-1} = \frac{1}{\det\sigma} \begin{pmatrix} \sigma_{22} & -\sigma_{12} \\ -\sigma_{21} & \sigma_{11} \end{pmatrix}$$

FIGURE 4.1: 2D ellipse representation with  $(x, x')$  coordinates.

Using the coordinate vector:

$$X = \begin{pmatrix} x \\ x' \end{pmatrix}$$

and assuming  $\sigma_{12} = \sigma_{21}$ , Eq.4.16 becomes:

$$\frac{(\sigma_{22}x^2 - 2\sigma_{12}xx' + \sigma_{11}x'^2)}{\det\sigma} = \frac{(\sigma_{22}x^2 - 2\sigma_{12}xx' + \sigma_{11}x'^2)}{(\sigma_{11}\sigma_{22} - \sigma_{12}^2)} = 1 \quad (4.18)$$

Equation 4.18 has a direct interpretation in terms of the ellipse parameters and highlights the physical meaning of the beam matrix elements (Fig.4.1):

1.  $\sigma_{11}$  is related to the maximum dimension of the beam ( $x_{max}$ ) by:  $x_{max} = \sqrt{\sigma_{11}}$ ,
2.  $\sigma_{12}$ ,  $\sigma_{11}$  and  $\sigma_{22}$  are related to the correlation term  $r_{12}$  ( $-1 < r_{12} < 1$ ) by:  $r_{12} = r_{21} = \sigma_{12}/\sqrt{\sigma_{11}\sigma_{22}}$ ,
3. the intersection of the ellipse with the x axis:  $x_{int} = \sqrt{\sigma_{11}(1 - r_{12}^2)}$ ,
4.  $\sigma_{22}$  is related to the maximum divergence of the beam ( $x'_{max}$ ) by:  $x'_{max} = \sqrt{\sigma_{22}}$ ,
5. the intersection of the ellipse with the x' axis:  $x'_{int} = \sqrt{\sigma_{22}(1 - r_{12}^2)}$ .

Let consider the following particular expression of the beam matrix:

$$\sigma = \frac{1}{\epsilon} \begin{pmatrix} \beta & -\alpha \\ -\alpha & \gamma \end{pmatrix} \quad (4.19)$$

with:

$$\gamma = \frac{1 + \alpha^2}{\beta} \quad (4.20)$$

$\alpha$ ,  $\beta$  and  $\gamma$  are usually called optic functions. Then, Eq.4.18 can be written in the form:

$$\gamma x^2 + 2\alpha x x'^2 + \beta x'^2 = \epsilon \quad (4.21)$$

and the corresponding area can be calculated as:

$$Area = \frac{\pi\epsilon}{\sqrt{\gamma\beta - \alpha^2}} = \pi\epsilon \quad (4.22)$$

Comparing with the formula 4.18, the corresponding ellipse area is:

$$Area = \frac{\pi det\sigma}{\sqrt{\sigma_{11}\sigma_{22} - \sigma_{12}^2}} = \frac{\pi det\sigma}{\sqrt{\sigma_{11}\sigma_{22}(1 - r_{12}^2)}} = \pi\sqrt{det\sigma} = \pi\sqrt{\sigma_{11}\sigma_{22}(1 - r_{12}^2)} \quad (4.23)$$

The coefficient  $r_{12}$  represents the slope of the ellipse. Indeed, if  $r_{12}$  is positive the ellipse is tilted to the right while  $r_{12}$  is negative, the ellipse is tilted to the left. Also, we can deduce the meanings of the optic functions: the maximum transverse size of the beam  $x_{max} = \sqrt{\epsilon\beta} = \sqrt{\sigma_{11}}$  and the maximum divergence of the beam  $x'_{max} = \sqrt{\epsilon\gamma} = \sqrt{\sigma_{22}}$ .

However, in the computational or simulation case, beam dynamics includes, for instance non-linear effects, couplings of the sub-spaces (correlation) and space charge effects. Therefore, a common definition of emittance allowing to compare results obtained with different set of parameters becomes useful. Usually, the initial bunch in the phase space is generated with uniform or Gaussian distribution and its evolution is analysed along the beam line. The parameter that is usually considered to quantify the beam quality is the rms emittance (root mean square). For example, in a tracking simulation, all coordinates for each individual macro-particles are considered:  $x$ ,  $x'$ ,  $y$ ,  $y'$ ,  $\Delta z$ ,  $\Delta p_z$ ,  $t$ , where  $\Delta z$  is the bunch length and  $\Delta p_z$  is the energy spread. Then, by means of these coordinates, the statistical rms emittance can be estimated.

To simplify the formalism, let consider the case where  $\langle x \rangle = \langle x' \rangle = 0$ . Then the rms transverse size and divergence are defined as follow:

$$x_{rms} = \sqrt{\frac{1}{N} \sum x^2} \quad (4.24)$$

$$x'_{rms} = \sqrt{\frac{1}{N} \sum x'^2} \quad (4.25)$$

Now, from Eq.4.24 and Eq.4.25, with Eq.4.22 and Eq.4.23, the rms geometric emittance is defined as:

$$\epsilon_{rms} = \sqrt{\langle x^2 \rangle \langle x'^2 \rangle - \langle xx' \rangle^2} \quad (4.26)$$

By means of the beam dynamics simulation tools, we can obtain the rms emittance, the transverse size and the divergence values of the beam. Therefore, we can calculate the optic functions that allow to characterise the transfer line and the magnetic lattice of the ThomX accelerator.

### 4.1.3 Photo-injector principle: phase of standing wave

The RF gun is the first accelerating cavity in the ThomX linear accelerator. A photocathode is installed inside the gun and emits electrons after being illuminated by laser pulses. The transverse sizes in both directions (x and y) and the longitudinal duration of the emitted electron bunch have the same values as those of the laser pulse at the cathode.

A standing electromagnetic wave is established in the gun cells. This wave oscillates at discrete frequency functions (eigen-functions) according to the geometry dimensions of the cell. As it has already been mentioned in Chapter 2, the only mode able to accelerate the electrons in the RF gun is the  $TM_{010}$ -mode where the electric field is oriented along the longitudinal axis. Fig.4.2 shows the normalized profile of the ThomX RF gun electric field along the longitudinal axis at the center of the cells for the  $TM_{010-\pi}$ -mode. This profile has been obtained by Superfish simulations [78].

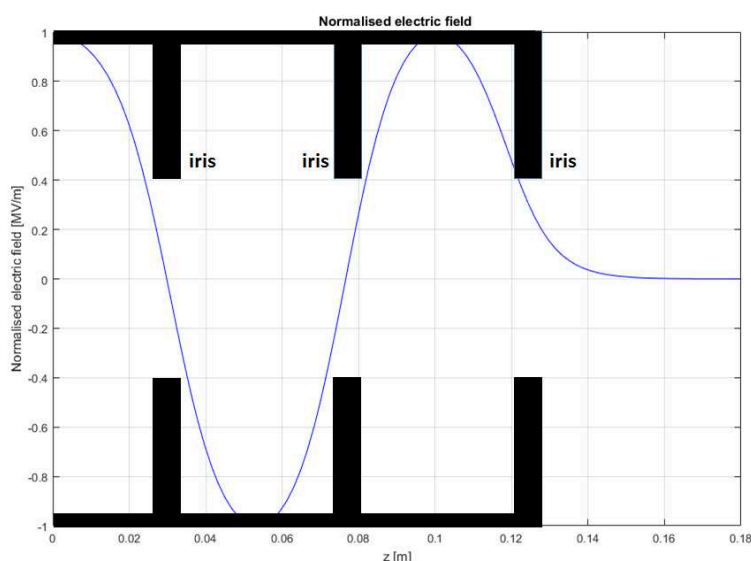


FIGURE 4.2: Normalised electric field profile along the beam axis.

We can see from Fig.4.2 that, in the  $TM_{010-\pi}$ -mode, the wave has two “nodes” at the iris aperture positions where the electric field amplitude is constantly equal to zero in space and time. Also, the field amplitude is  $\pi$ -phase shifted, so at any time its sign is reversed every half period between two adjacent cells. To ensure that the particles are exclusively exposed to accelerating RF phases and not to decelerating ones, the motion of the particles through the accelerator must be synchronized with the RF field frequency  $f = \omega/2\pi = 1/T$ , where  $T$  is the RF period. Hence, a particle must run from an accelerating cell to the next one during the time  $T/2$  that takes the field to reverse sign. For the maximum electron energy gain along the RF gun, the electric field has to change sign at the time the electron beam changes cell. In general, for preserving the synchronicity condition, the length of the cell is determined by the phase advance of the RF field in each cell.

Since the rest mass energy ( $m_e c^2$ ) of the electrons is small compared with energy provided by the electric field, about 2 MeV in the first cell, electrons are quickly accelerated close to the speed of light in vacuum. This allows considering that all along their motion after the first cell they have an almost constant velocity equal to  $c$ . This fixes the length of the cells other than the first that for an S-band gun operating in  $TM_{010-\pi}$  mode should be:

$$L = \frac{c}{2f} \quad (4.27)$$

so that the field changes sign when the bunch is moving from one cell to the next.

The first cell has to be shorter than the others because otherwise the maximum accelerating field  $E_a$  would be at any time zero at the photocathode position. It would be then impossible to accelerate the emitted electrons. Usually, it is a half cell or 0.6 cell.

The phase  $\phi$  between the RF signal and the laser pulse that illuminates the cathode must therefore be adjusted such that the electrons undergo an accelerating field all along the first cell and leave it just when the field changes sign. Under these conditions the energy of the electrons is maximum at the exit of the gun.

When electrons are emitted from the cathode, their velocity is very low compared with the speed of light. On the contrary the phase velocity of the RF wave is equal to the speed of light. This difference in velocities leads to the bunch phase slippage with respect to the RF field phase. This effect is significant in term of final energy gain with respect to the bunch injection phase. Figure 4.3 shows the energy gain as a function of the bunch injection phase, taking into account the bunch RF phase slippage.

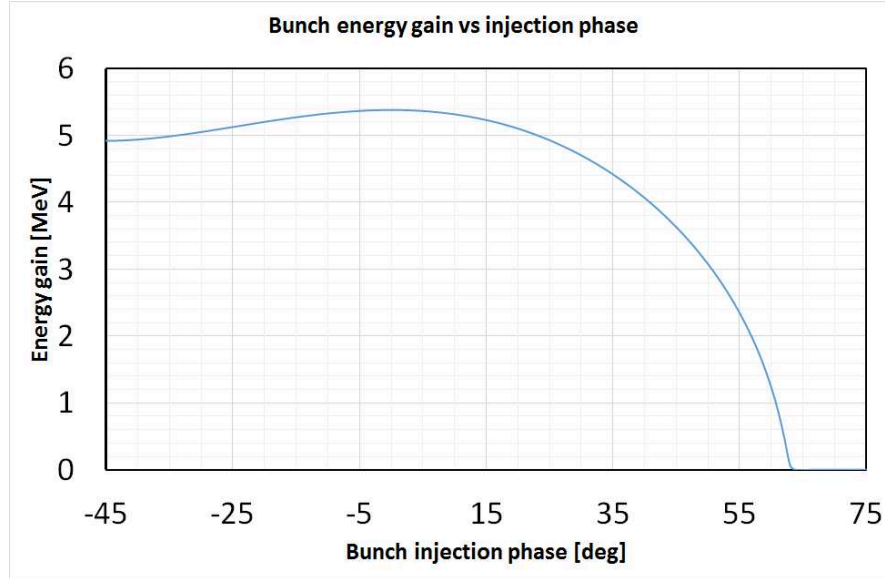


FIGURE 4.3: Electron energy gain as a function of injection phase, taking into account bunch RF phase slippage.

To simply express in an analytic manner the energy spread over the RF field phase, let us assume that the electrons already have relativistic velocity in the first cell of the gun, the energy gain per cell is therefore calculated by:

$$U_f - U_i = e \int_0^L E_a(z, t) dz \quad (4.28)$$

where  $U_f$  and  $U_i$  are the final and the initial energy of the relativistic particle, respectively. In order to retrieve a simple analytic expression, the standing wave amplitude along the longitudinal axis at the center of the cells can be approximated by a purely sinusoidal TM010-mode on-axis accelerating field profile :

$$E_a(z, t) = E_a \cos(kz) \sin(\omega t + \phi) \quad (4.29)$$

where  $E_a$  is the maximum electric field,  $\omega$  is the mode angular velocity,  $t$  the time and  $\phi$  the particle phase relative to the standing wave time oscillation.

This analytic expression is an approximation compared with the real profile established inside the gun in which the on-axis maximum electric field and field profile are not exactly the same in each cells and the fringe field at the gun exit deform the profile with respect to a perfect sinusoid. Although all these effects are ignored in the analytic expression, the latter describes the main features of the fields, and allows to simply understand the basis of the beam dynamics through the gun. Now, if we consider that  $E_z(z, t)$  has the form 4.29, the energy gain per cell varies as a function of the phase  $\phi$

according to the expression:

$$U_f - U_i = eE_a \left[ \cos(\phi) \frac{\sin^2(kL)}{2k} + \sin(\phi) \left( \frac{\cos(kL) \sin(kL)}{2k} + \frac{L}{2} \right) \right] \quad (4.30)$$

we obtain the energy gain per cell of a relativistic electron as a function of phase  $\phi$ , at the exit of the S-band 2.5-cells RF gun. Figure 4.4 shows the energy gain per cell as a function of the phase  $\phi$ . If we consider the length of the cell  $L = \lambda/2$ , Eq.4.30 allows to

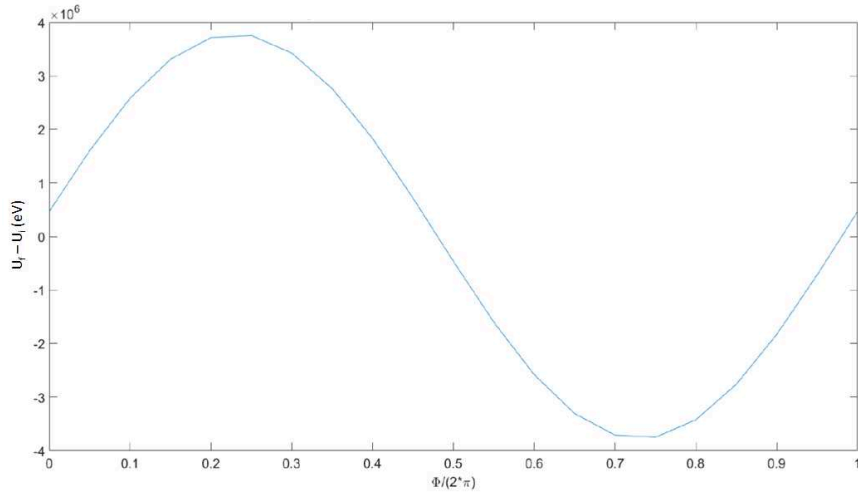


FIGURE 4.4: Energy gain of relativistic electron as a function of phase the  $\phi$ . Courtesy of A. Gamelin.

obtain the energy gain per cell as a function of the phase:

$$U_f - U_i = eE_a \frac{\lambda}{4} \sin(\phi) \quad (4.31)$$

Equation 4.31 shows that for  $\phi = \pi/2$  the energy gain per cell is maximum and equal to  $(U_f - U_i)_{max} = eE_a\lambda/4$ . Hence the effective gradient is  $\Delta V/(\lambda/2) = E_a/2$ , or half the maximum accelerating field. The ThomX gun can achieve up to 80 MV/m which should mitigate the space-charge forces by rapidly accelerating the photo-electrons to relativistic energies. Then the energy gain at the RF gun exit is around 5 MeV.

Now, if we consider  $\Delta U$  and  $\Delta t$  as the energy and time differences of any electron with respect to the time and energy mean values of the bunch distribution (which correspond to the reference particle), we can calculate the energy spread of each electron as a function of  $\Delta U$ ,  $\Delta t$  and  $\phi$  by the derivative of Eq.4.30:

$$\Delta U_f = \Delta U_i + \pi f e E_a \left[ -\frac{\sin^2(kL)}{k} \sin \phi + \left( \frac{\cos(kL) \sin(kL)}{k} + L \right) \cos(\phi) \right] \Delta t_i \quad (4.32)$$

where the phase difference  $\Delta\phi = 2\pi f \Delta t$ .

#### 4.1.4 Beam boost by travelling-wave acceleration

In the TW mode, the electromagnetic wave travels along the disks-loaded structure. The longitudinal field along the z-axis of the accelerating section is:

$$E_a(z, t) = E_a \cos(kz - \omega t + \phi) \quad (4.33)$$

Considering that the phase velocity ( $v_p = \omega/k$ ) is equal to the speed of the particles, then the particles maintain a constant phase relation as they pass through the structure. Eq.4.33 then becomes:

$$E_a(\phi) = E_a \cos \phi \quad (4.34)$$

In the same way as the case of standing wave, we can estimate the energy spread due to the energy and time differences of any electron with respect to the time and energy mean values of the bunch distribution (reference particle):

$$\Delta U_f = \Delta U_i + 2\pi f e E_a L \sin(\phi) \Delta t_i \quad (4.35)$$

#### 4.1.5 Transverse emittance growth in photo-injectors

The first description of the beam dynamics in a photo-injector was proposed by K. J. Kim [79]. The Kim model considers just the fundamental harmonic of the electromagnetic field components that constitutes one of the main limitations to this description. Kim's model indicates two contributions to the transverse emittance growth: the dependence of the RF longitudinal on-axis electric field component  $E_z$  (cylindrical symmetric RF cavity) with the longitudinal position  $z$  and time, namely  $\epsilon_{RF}$ , and the space charge effect  $\epsilon_{sc}$ . That implies the radial electric and azimuth magnetic fields components are proportional to the z- and t-derivatives, respectively of the longitudinal component  $E_z$ :

$$E_r = -\frac{r}{2} \frac{\partial}{\partial z} E_z \quad (4.36)$$

$$cB_\theta = \frac{r}{2c} \frac{\partial}{\partial t} E_z \quad (4.37)$$

Therefore, the radial force is:

$$F_r = e(E_r - \beta c B_\theta) \quad (4.38)$$

The radial momentum kick is then calculated:

$$\Delta p_r = \frac{1}{m_0 c^2} \int_0^{z_f} F_r \frac{dz}{\beta} = \frac{e E_a r}{2c} \sin(\phi_e) \quad (4.39)$$

where the electric field strength  $E(z)$  is constant inside the gun and sharply decrease to zero at the gun exit, according to the function  $E(z) = E_a \delta(z_f - z)$ ,  $z_f$  the position of the gun exit.  $\phi_e$  is the electron phase at the gun exit. From Eq.4.39 one can deduce that each electron at different longitudinal position along the bunch length, corresponding to different phase  $\phi_e$  at the gun exit, will experience kicks with different strength. This causes transverse projected emittance growth because each slice of the bunch has a different slope in the trace space  $(x, x')$ . The minimum emittance contribution occurs when the radial momentum kick is independent from the electron phase  $d\Delta p_r/d\phi_e = 0$ , hence  $\phi_e = \pi/2$ . Considering a Gaussian electron bunch distribution, the Kim's model estimates the emittance growth as:

$$\epsilon_{RF} = \frac{eE_a k^2 \sigma_x^2 \sigma_z^2}{2m_0 c^2 \sqrt{2}} \quad (4.40)$$

The strong defocusing produced by the radial force acting on the particles requires an adequate compensation, which is usually provided by the longitudinal magnetic field produced by a solenoid. The latter plays a double roles: not only compensates the defocusing effect of the RF field contribution but also aligns the bunch slices in the trace space thus reducing the transverse projected emittance.

Kim's model estimates also the contribution of the space charge to the emittance growth. Considering an axi-symmetric bunch charge distribution, where  $Q$  is the total charge that is uniformly distributed over a radius  $a$  and  $I$  is the current. Also, the bunch length  $L$  is larger than the radius  $a$  ( $L \gg a$ ) and it is travelling with a constant velocity along the longitudinal direction. Then, this charge distribution gives rise to a radial electric field as well as an azimuth magnetic field components inside and outside the bunch:

$$E_r = \frac{I}{2\pi\epsilon_0 a^2 v}, \quad r \leq a \quad (4.41)$$

$$cB_\theta = \mu_0 \frac{Ir}{2\pi a^2}, \quad r \leq a \quad (4.42)$$

The radial force is:

$$F_r = e(E_r - \beta cB_\theta) = \frac{eIr}{2\pi\epsilon_0 \gamma^2 \beta c a^2} \quad (4.43)$$

The contribution to the transverse momentum due to the space charge force is given by:

$$p_r = \frac{1}{m_0 c^2} \int F_r dt \quad (4.44)$$

After the integration, the transverse momentum acting on the particles is:

$$p_r = \frac{1}{E_a \sin \phi_e} \frac{\pi}{2} E_r^{sc} \quad (4.45)$$

where  $E_r^{sc}$  is the radial electrostatic field component of the charge distribution at rest in the laboratory frame.

Once again, Kim's model provides the normalised transverse emittance due to space charge effect in the case of longitudinal and transverse Gaussian particle distribution:

$$\epsilon_{sc} = \frac{c^2}{8\sqrt{2\pi}\alpha f \sin(\phi_e)} \frac{Q}{I_A} \frac{1}{(3\sigma_x + 5c\sigma_t)} \quad (4.46)$$

where the definition of peak current as  $I = Q/\sqrt{2\pi}\sigma_t$  has been used. Also,  $I_A = 4\pi\epsilon_0 m_0 c^2/e = 17$  kA is known as the Alfvén current.

In addition to the RF field defocusing and space charge effects, there is another contribution to the emittance growth due to the electron photo-emission process that depends on the temperature of the cathode surface, namely the thermal emittance. When the electrons are emitted from the cathode in an isotropic way within a half-sphere, the emittance contribution is [80]:

$$\epsilon_{th} = \frac{\gamma\sigma_x}{2} \sqrt{\frac{k_B T [eV]}{m_0 c^2}} \sqrt{\frac{2 + \cos^3(\phi_{max}) - 3\cos(\phi_{max})}{2[1 - \cos(\phi_{max})]}} \quad (4.47)$$

where  $\phi_{max}$  is the electron emission angle with respect to the cathode surface normal vector. The  $\sigma_x$  is the laser spot that illuminates the cathode surface. From Eq.4.47 we deduce that the thermal emittance depends on the emission area on the cathode surface and the angular distribution of the emitted electrons. If we consider  $\phi_{max} = \pi/2$ , Eq.4.47 becomes:

$$\epsilon_{th} = \frac{\gamma\sigma_x}{2} \sqrt{\frac{k_B T}{m_0 c^2}} \quad (4.48)$$

From Eq.4.48 the temperature of the cathode is considered equal to that of the corresponding laser energy that impinges the surface.

After having described the main contributions that increase the projected transverse emittance in the trace space, in the case where these contributions are uncorrelated, the total transverse normalised emittance can be calculated by quadratically adding these terms:

$$\epsilon_{n,x,y,tot} = \sqrt{\epsilon_{RF}^2 + \epsilon_{sc}^2 + \epsilon_{th}^2} \quad (4.49)$$

In the ThomX case, we will see that the space charge contribution dominates.

## 4.2 ThomX RF gun space charge emittance compensation

### 4.2.1 Space charge dominated beam

The estimation of the emittance growth in the ThomX photo-cathode gun is done using a combined analytic and numerical analysis approach for estimating the various contributions to the total emittance budget. Particle tracking simulations have been performed with ASTRA taking into account the longitudinal on-axis component of the electric (courtesy of P. Lepercq), magnetic fields (courtesy of C. Vallerand) and the space charge force.

Henceforth, in all the simulations we suppose that the laser that produces the electrons from the cathode has a Gaussian distribution in the transverse and longitudinal planes with a fixed sigma ( $\sigma_x = \sigma_y$ ) and time duration ( $\sigma_t$ ). The initial parameters that have been set for the beam dynamics simulation are listed in Tab.4.1.

TABLE 4.1: Electron bunch parameters settings in ASTRA.

Parameters	values
Number of particles	10000
Total charge per bunch	1 nC
Initial kinetic energy (ref. particle)	0 MeV
rms energy spread	0 keV
Type particle distribution	Gaussian
rms transverse size, $\sigma_x$	1 mm
rms transverse size, $\sigma_y$	1 mm
rms longitudinal size	4 ps

We explore and estimate the impact of each contribution to the transverse emittance growth. Equation 4.40 can be rewritten in more practical units:

$$\epsilon_{RF} = 2.73 \times 10^{-11} E_a f^2 \sigma_x^2 \sigma_z^2 = 0.25 \text{ mm mrad} \quad (4.50)$$

where  $E_a$  is the maximum RF gradient [MV/m],  $f$  is the resonating frequency [MHz],  $\sigma_x$  is the transverse rms beam size [mm] and  $\sigma_t$  is the bunch length [ps]. In this case, the nominal peak accelerating field was set to 80 MV/m, the frequency is 2998.5 MHz, the rms beam size is 1 mm and the bunch length 3.6 ps.

Considering 1 mm laser spot size, we can predict that the contribution of the thermal emittance is around 0.4 mm mrad [80].

Equation 4.46 can be expressed in more practical units:

$$\epsilon_{sc} = 3.76 \times 10^3 \frac{Q}{E_0(2\sigma_x + \sigma_z)} = 8.4 \text{ mm mrad} \quad (4.51)$$

where  $Q$  is equal to 1 nC. The Kim's model overestimates this contribution and a proper matching done by the invariant envelop equation [81] can improve this contribution at the linac output. The individual contributions from the above mentioned effects are quadratically added to the total normalised beam dynamics emittance. The general formula is:

$$\epsilon_{n,x,y,tot} = \sqrt{\epsilon_{RF}^2 + \epsilon_{sc}^2 + \epsilon_{th}^2} = 8.4 \text{ mm mrad} \quad (4.52)$$

According to the model, the space charge effect near the cathode is the dominant contribution to the emittance growth while the RF field and thermal effects are almost negligible in the RF gun. In the next paragraph a method to partially mitigate the contribution of the linear space charge effect to the emittance growth is presented.

## 4.2.2 Principle of space charge compensation

Kim's model considers only the sinusoidal components of the electromagnetic fields that are established in the RF gun. To deal with this limitation, Serafini et al., [81] has developed a different model for the description of the beam dynamics in a photo-injector, where also the high-order space harmonics are taken into account.

We do not go into details of the Serafini's model, we just mention the fundamental result that came out from this model that is, the beam transverse emittance produced in a photo-injector is degraded by four mechanisms: the linear and non-linear z- and t-dependence of the longitudinal component of the RF field and the linear and non-linear space charge effect.

Several techniques have been applied for decreasing the projected emittance blow up under the effect of the RF electric field and space charge. These methods are usually called "transverse emittance compensation" and basically consist in applying a transverse force on the beam that compensates the defocusing effect acting on it. We focus on the technique that has been proposed by Carlsten [82] as it has been used for the ThomX photo-injector transverse emittance compensation.

The transverse emittance compensation technique developed by Carlsten uses a magnetic linear lens for compensating the effects of the linear space charge effect. It is worthy to notice that this method does not compensate the linear and non-linear effect of the RF field as well as the non-linear effect of the space charge.

Basically, Carlsten considers a beam line composed of a drift space, a linear magnetic lens and a drift space. The bunch is cylindrical with a uniform charge density at the beginning of the first drift space. The representation of the beam in the trace space  $(x, x')$  at this position is a horizontal line with the hypothesis that the bunch has no-divergence ( $x' = 0$ ). The projected emittance is zero. Every position inside the bunch is described by two internal coordinates  $(\rho, \xi)$  so that it can be divided in slices along the longitudinal coordinate  $(\xi)$ . The only effect acting on the bunch is the linear space charge. The important assumption is that every slice undergoes a different space charge effect so that the radial velocity is different from the central slice to the head or tail of the bunch. After the evolution along the first drift space, the bunch is represented as a fan shape in the trace space. The area on the trace space is augmented therefore the projected emittance is increased. When the bunch passes through the linear magnetic lens, the rotation of the fan shape representation of the electron distribution on the trace space occurs. During rotation the area on the trace space is conserved and therefore the emittance remains constant. Once again, the evolution of every slice in the second drift space is not uniform, the emittance compensation is achieved in a particular condition when each slice is aligned in the trace space, thus minimising the area and therefore the projected emittance in the trace space. It succeeds for a given focusing strength of the lens and at a given distance from the photocathode.

### 4.2.3 Magnetic lenses

Once the beam is produced and accelerated from the cathode, the electrons interact with themselves by the space charge force and undergo external RF electromagnetic fields that contribute to its emittance growth. There are four mechanisms in the injector that contribute to emittance growth: linear space charge, non-linear space charge, non-linear time independent RF gradient and linear time-dependent RF gradient [82].

Solenoids are used to apply a transverse focusing force to the electrons while they are accelerated. These magnets are able to focus the beam at the minimum transverse size (bunch waist) at or near the accelerating section entrance. The transverse focusing is needed for two reasons: balance the radial de-focusing space charge forces inside the electron bunch and counter-act the radial component when the electrons leave the last cell of the gun [83]. In addition, the solenoids are able to “match” the emittance of the beam into the first accelerating cavity [81].

However, as the photo-emission mechanism makes particles extraction from the cathode at a very low velocity to near relativistic one in few centimeters, a local description of the magnetic field with a transfer matrix would not be so accurate for describing its

contribution on the electron beam dynamics. A more precise description of the magnetic field effects produced by the solenoids is provided by considering the distribution of the magnetic field profile along the longitudinal axis. The latter allows to deduce the radial component of the magnetic field determining the effectiveness of the focusing on the particles.

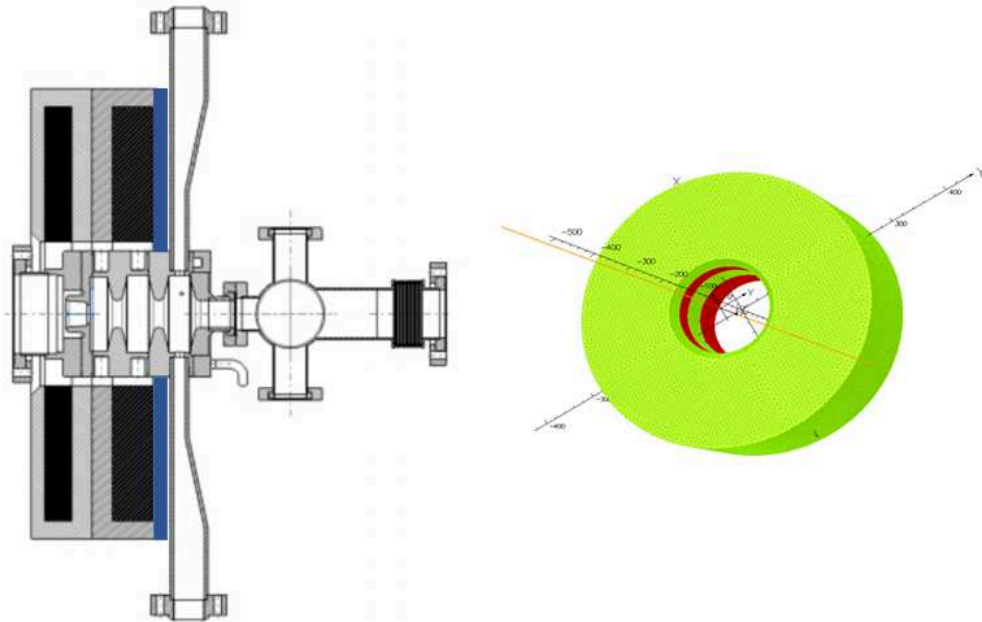


FIGURE 4.5: (Left) Schematic of the gun surrounded by the coils; the focusing coil is equipped with a shielding plate. (Right) 3D OPERA simulation of the two solenoids, the windings (red), the iron yoke (green).

According to the ThomX Technical Design Report (ThomX TDR) the focusing and the bucking coils are side by side and surround the gun. The focusing coil produces the focusing force to mitigate the transverse emittance growth. Figure 4.5 (left side) shows the ThomX nominal photo-injector scheme. The RF gun, which is mounted inside the bore of two solenoid magnets, is equipped with two wave-guides. The bucking coil surrounds the photo-cathode vacuum chamber whereas the focusing coil surrounds the gun. A metal shielding shaping the magnetic field profile along the longitudinal axis has also been installed between the focusing coil and the wave-guides (blue elements in the figure). The effect of both bucking and focusing solenoids has been simulated by the 3D OPERA solver for determining the magnetic field profile along the beam axis (Fig. 4.5, right side).

If at the cathode, the magnetic field is not zero, the electrons acquire an additional canonical angular momentum and thus experience an additional contribution to the total emittance budget [84]. Then, the right current values of the coils are set in order to cancel the magnetic field ( $B_z(0, z) = 0$  T) at the photo-cathode location. This demonstrates

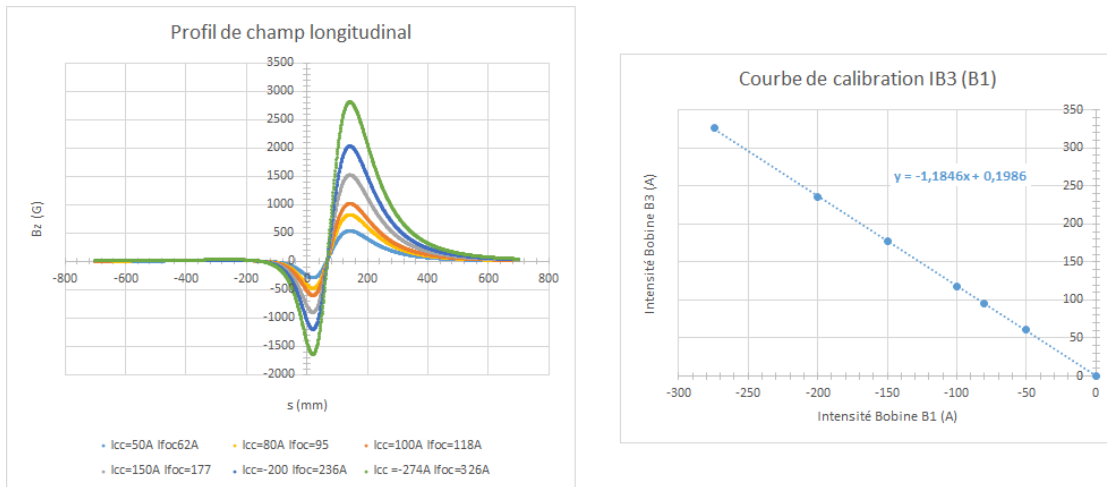


FIGURE 4.6: (Left) Magnetic field strength on the axis for different couples of currents in the two solenoids. (Right) Empirical law of the bucking coil current as a function of the focusing coil current for zeroing the magnetic field at the cathode position.

the importance of having an accurate model of the solenoids to optimise the beam dynamics. Figure 4.6 shows the simulated on-axis magnetic field profile for different values of the circulating current in the coils. The maximum field is around 0.28 T for 326 A excitation current in the focusing coil and -274 A in the bucking coil. Also, the empirical law without shielding for obtaining the correct balancing of the field, at a certain location, is shown on the right. The comparison between the simulations and experimental measurements have confirmed that the maximum value of the magnetic field profiles along the beam axis increases linearly with the current, for that range of couples of current values, without any deviation due to the saturation in the iron yoke.

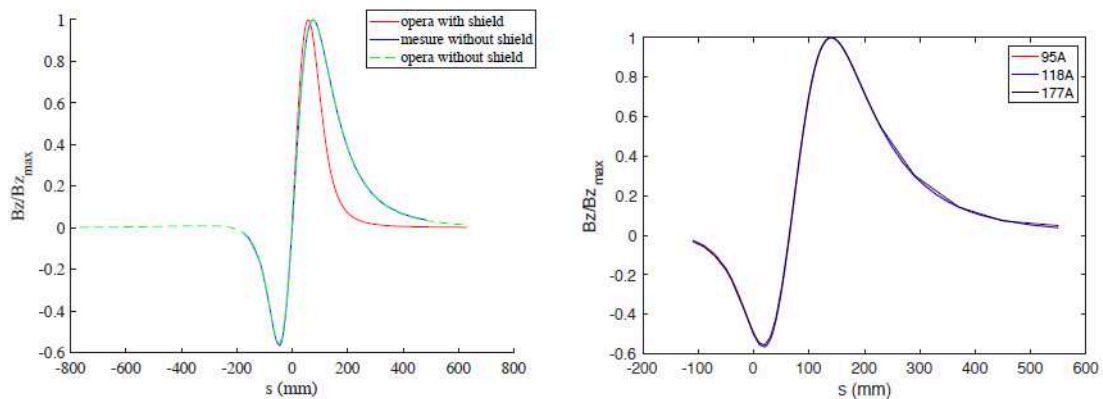


FIGURE 4.7: Simulated longitudinal magnetic field component on axis for ThomX nominal configuration. Comparison between 5 mm shielding plate, without shielding and experimental measurements (left). Comparison between several couples of current supply measured in the coils (right).

The on-axis magnetic field profile has also been obtained by adding the shielding to the focusing coil, as it is shown on the left side of Fig.4.7. We can observe that the

slope of the magnetic field is large in the first half-cell. The maximum value is at 6.5 cm from the beginning of the first cell. The remarkable difference between the two profiles is the behaviour of the fringe field. Without shielding plate, the magnetic field strength slowly decreases along the axis. A comparison between different couples of current feeding the coils has been carried out (Fig.4.7, right side) showing that even though the current values are different, the magnetic field is the same, validating the empirical law previously mentioned (Fig.4.6, right side). The measurement of the on-axis magnetic field allows simulations of the beam dynamics to be as close as possible to the experimental conditions.

The particle tracking code ASTRA needs the longitudinal on-axis component of the electric and magnetic fields. Considering the cylindrical symmetry, the radial and azimuthal components are deduced from the longitudinal on-axis component by derivative. So, it is important to obtain the on-axis magnetic field profile over a long distance. This allows to be sure that profile smoothly decreases to zero without any discontinuity avoiding errors due to the artifacts in the derivative.

In Fig.4.7 the position of the photo-cathode is considered at the position on the beam axis where the magnetic field is cancelled by the contribution of the two coils. In practice, the electrons start at a position where a small solenoid magnetic field is already present. The result is that the azimuth momentum compensation is not complete. Because the electrons are created inside the solenoid they do not travel through the complete entrance fringe field and thus gain more azimuth momentum in the exit fringe field than needed to compensate for the gain in azimuth momentum in the entrance fringe field. The difference can be calculated by the Busch's theorem, which relates the momentum difference to the difference in magnetic field [85]:

$$\Delta p_\theta = \frac{e}{2\gamma m_0} (B_{z_0} - B_z) \quad (4.53)$$

where  $m_0$  is the rest mass,  $B_{z_0}$  is the cathode magnetic field,  $B_z$  is the longitudinal magnetic field downstream of the cathode at a position  $z$ . Integrating the Eq.4.53 along the longitudinal component, one can demonstrate that the final contribution, to the rms normalised emittance is:

$$\epsilon_{n,rms} = \beta\gamma\sqrt{\langle x^2 \rangle \langle x'^2 \rangle} = \frac{eR_0^2|B_{z_0}|}{8m_0c} \quad (4.54)$$

where  $R_0$  is the radius of the transverse size. For a typical beam radius of  $\sigma_x = 1$  mm, this contribution is equal to 37 mm mrad/T. For a small emittance contribution compared with the thermal contribution the residual magnetic field on the cathode should thus be lower than  $2 \times 10^{-3}$  T.

#### 4.2.4 Simulation results

In a photo-injector, the longitudinal shape of the electron bunch that is extracted from the cathode resembles the laser longitudinal shape that impinges on the cathode. In the same way, the transverse shape of the bunch also depends on the transverse shape of the laser, so that the longitudinal properties and transverse spot size of the laser can be manipulated to obtain minimum emittance growth. In our case, the laser pulse duration that impinges on the cathode is of the order of picoseconds. Therefore the generated electron bunch length has the same order of magnitude. Then, a combined effect of electric and magnetic fields in the RF gun drives the electron bunch. After a drift space, the electron bunch is boosted up to the ring injection energy by means of an accelerating section. The transfer line ensures the bunch transport from the linac exit to the storage ring. In the commissioning phase, the machine should produce X-rays of 45 keV. This goal requires strict specifications for the linac, which are summarised in Tab.4.2:

TABLE 4.2: Nominal Linac beam dynamics parameters.

Parameters	values
Energy	50 MeV
Total charge per bunch	1 nC
Repetition rate	50 Hz
Average current	50 nA
Number of bunches per RF pulse	1
Normalised rms emittance	$< 5 \pi$ mm mrad
Energy spread rms	$< 0.3$ %
Bunch length rms	$< 5$ ps

Beam dynamics of the ThomX nominal TDR configuration solenoids has been studied in three different cases, without solenoids, with solenoids without shielding plate and with shielding plate, respectively. In Fig.4.8 we can see that in the drift space the emittance growth induced by space charge is linear with the distance. The transverse emittance after 1 m is around  $14 \pi$  mm mrad (black line) while it is around  $11 \pi$  mm mrad (red and blue lines) in the case of the solenoid focusing effect.

Results with and without plate are resumed in Tab. 4.3.

In general, the effect of the shielding plate is not very much important over several beam parameters, such as emittance, bunch length, energy spread, but it has more much impact on the transverse beam size because of smaller integral magnetic length contribution due to the rapidly decreasing of the fringe field profile.

A criterion to determine the best magnetic field strength that compensates the transverse emittance in the drift space after the gun has been considered (see Fig. 4.9). In

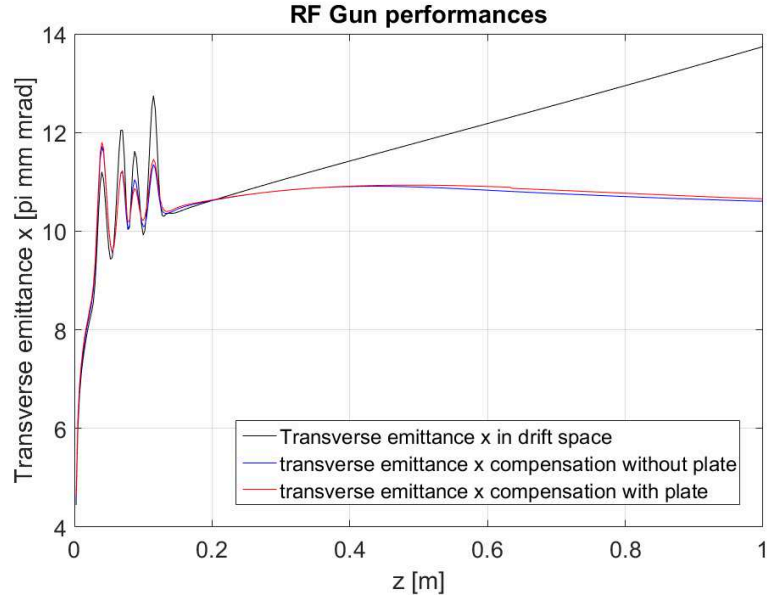


FIGURE 4.8: rms normalised transverse emittance  $x$  as a function of distance. Total bunch charge 1nC. Laser parameters: rms  $\sigma_r = 1\text{mm}$ , rms  $\sigma_t = 4\text{ps}$ . Drift space (black line), solenoids without plate (blue line) and solenoids with plate (red line).

TABLE 4.3: Beam parameters. Total bunch charge: 1 nC. Laser parameters: rms  $\sigma_r = 1\text{mm}$ , rms  $\sigma_t = 4\text{ps}$ .

without solenoids, $z = 1\text{ m}$	
E [MeV]	5.4
$\epsilon_{x,y}$ [pi mm mrad]	13.7
$\sigma_{x,y}$ [mm]	9.7
$\sigma_z$ [ps]	3.8
$\Delta E / E$ [%]	0.7
with solenoids without shielding, $z = 1\text{ m}$	
E [MeV]	5.4
$\epsilon_{x,y}$ [pi mm mrad]	10.6
$\sigma_{x,y}$ [mm]	$\sim 2$
$\sigma_z$ [ps]	3.8
$\Delta E / E$ [%]	0.87
with solenoids with shielding, $z = 1\text{ m}$	
E [MeV]	5.4
$\epsilon_{x,y}$ [pi mm mrad]	10.6
$\sigma_{x,y}$ [mm]	$\sim 3$
$\sigma_z$ [ps]	3.8
$\Delta E / E$ [%]	0.84

particular, for fixed bunch charge the slope of the emittance variation is calculated as a function of the last 30 cm, for different maximum solenoid strength. The intersection between the slope and the zero cross line defines the right magnetic strength value while the blue line gives the corresponding normalised emittance. The reached value of the emittance is here  $4\pi$  mm mrad, but we will explain in the following that it is at the

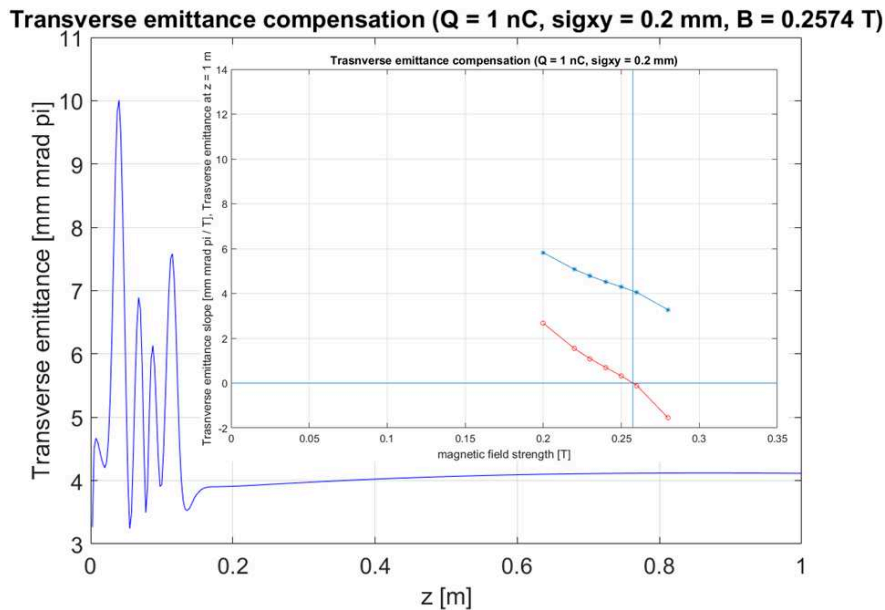


FIGURE 4.9: Transverse emittance slope (red line) and transverse emittance value at  $z = 1$  m (blue line) as a function of magnetic field strength (left). Transverse emittance as a function of the distance for  $B = 0.2574$  T (right).

expense of charge losses.

We examine the influence of the different beam dynamics parameters on the energy spread, transverse emittance and transverse size at  $z = 1$  m from the cathode, which are interesting for achieving the ThomX TDR specifications.

The characteristics of the beam mainly rely on the choice of the laser parameters. Indeed, the laser transverse sizes and profile can have a strong impact on the beam emittance. A scan across different laser spot sizes has been performed and the corresponding normalised emittance values for the suitable magnetic field strength that compensates the emittance growth after the gun has been estimated. In general when the bunch transverse size increases the radial force due to the space charge effect decreases resulting in reduction of the emittance growth, but meanwhile for larger transverse spot sizes the radial kick that is generated by the  $z$ - and  $t$ -derivatives of the RF longitudinal electric field is increasing. Taking into account these effects, the suitable laser spot size is chosen as the best compromise between the RF field and space charge contributions to the total transverse emittance. Figure 4.10 shows that a transverse emittance value of around 4 mm mrad is achieved for a laser spot size of 0.2 mm. This value accomplishes the ThomX TDR requirement.

However, when the laser spot size is decreasing, the electron extraction from the cathode is much more affected by self-fields produced by the electron bunch itself [86]. Even at the first stage of the photo-emission at the cathode surface, the electrons undergo their

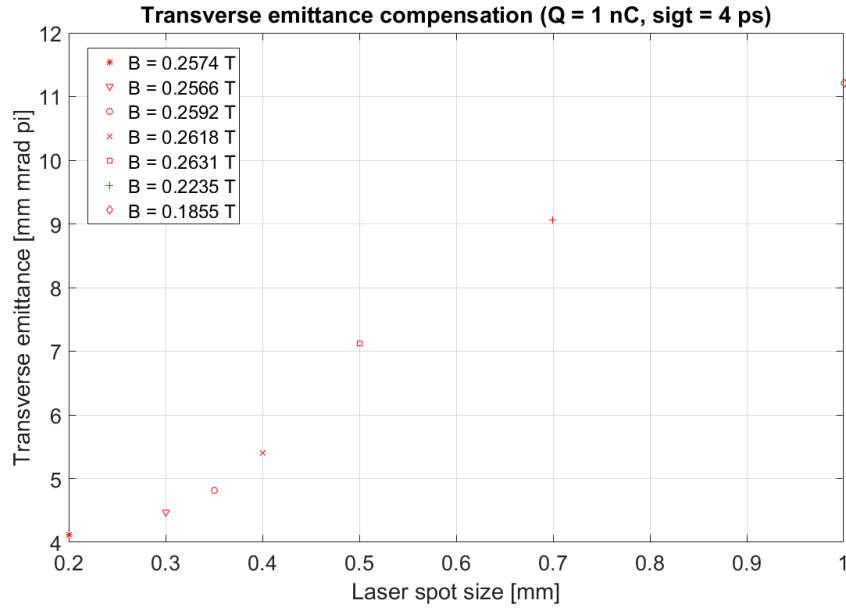


FIGURE 4.10: Transverse emittance as a function of the laser spot size. For each value of the spot size, the corresponding value of the magnetic field strength which compensates the emittance growth has been shown.

own image charge which produces an electric field that opposes the accelerating RF one. When the mirror charge field becomes as much strong as the external RF field, electron emission saturates (space charge limit) [87], i.e the extracted charge is limited even if the number of electrons (laser intensity) is increased at the cathode (charge saturation). This phenomenon has practically been observed in the simulations at zero RF gun de-phasing, where more than 40% (see Fig.4.11) of the particles were lost even at the photo-cathode position due to the de-celerating field created by the mirror charge distribution. This phenomenon is sensitive to the laser spot size ( $\sigma_x$ ,  $\sigma_y$ ) as it is represented in Tab.4.4, which corresponds to Fig.4.10.

TABLE 4.4: Percentage of the charge lost for different laser transverse spot size.

Laser spot size [mm]	Charge lost
$\sigma_{x,y} = 0.2$	40%
$\sigma_{x,y} = 0.3$	15%
$\sigma_{x,y} = 0.35$	7%
$\sigma_{x,y} = 0.4$	2%
$\sigma_{x,y} = 0.5$	0%
$\sigma_{x,y} = 0.7$	0%
$\sigma_{x,y} = 1$	0%

Table 4.4 shows that for a laser spot size larger than  $\sigma_x = \sigma_y = 0.4$  mm, the number of lost particles at the photocathode is less than 2% proving the importance of the transverse size of the laser at the cathode.

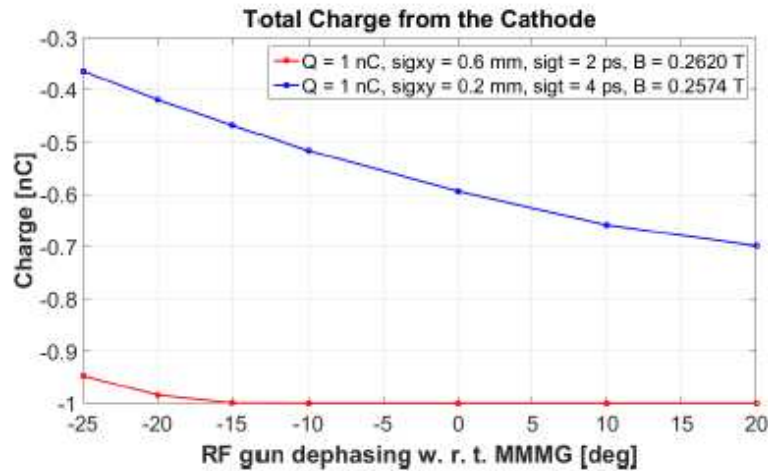


FIGURE 4.11: Total charge per bunch vs RF gun dephasing.

The extracted charge also depends on the difference in phase between the laser and the RF field at the cathode. Figure 4.11 shows the simulations of the bunch charge extracted from the cathode as a function of the relative phase between the RF field and the laser at the cathode. Hereinafter, the zero phase corresponds to the Maximum Mean Momentum Gain (MMMGM) [88].

In order to increase the laser spot size while mitigating the effects on the energy spread, we have decided to reduce the longitudinal bunch time duration. In the case of 0.2 mm transverse spot size, at least 30% of electrons are lost at the cathode, whereas the number of particles which are lost is roughly 5% for 0.6 mm laser spot size. However, the increase of the laser spot size is also limited by the thermal emittance contribution to the total transverse emittance, which linearly increases with the laser transverse size. In the 0.6 mm case, one can observe that in the dephasing range from  $20^\circ$  to  $-10^\circ$ , the total charge of 1 nC per bunch is extracted from the cathode. Also, we observe that losses start when the de-phasing is equal to  $-15^\circ$ , when the mirror charge field balances the RF field at the cathode. In Tab.4.5, the main beam properties at the exit of the RF gun ( $z = 1$  m) are summarised as a function of the de-phasing. As we can see from the data, the transverse emittance varies from  $8.5$  to  $7.6 \pi$  mm mrad, the bunch length remains approximately constant to 3 ps, while the energy spread varies significantly across the de-phasing values due to the different accelerating field amplitude seen by the head and the tail of the electron bunch travelling along the RF field (see Eq.4.32). Also, a de-phasing of  $-15$  degrees improves significantly the energy spread at the gun exit.

TABLE 4.5: Beam parameters at the exit of the gun for different de-phasing values ( $Q = 1$  nC,  $\sigma_{x,y} = 0.6$  mm,  $\sigma_t = 2$  ps).

Parameters	de-phasing [deg]			
	-15	-10	0	10
$\epsilon_{xy}$ [mm mrad $\pi$ ]	7.6	8	8.4	8.5
$\Delta E/E$ [%]	0.37	0.6	1.3	2.2
$\sigma_z$ [ps]	3.1	3	3.1	3.4

### 4.3 Beam dynamics with TW accelerating section

In order to minimise the energy spread at the end of the whole linac while maintaining reasonable values of transverse emittance and longitudinal bunch length, we have considered the following RF gun and laser simulation parameters: de-phasing value of  $-15^\circ$ , laser spot size of  $\sigma_x = \sigma_y = 0.6$  mm and pulse duration of  $\sigma_t = 2$  ps.

The beam dynamics along the linac has been studied by adding the effect of the travelling wave acceleration to the beam line. Simulations have been performed in order to demonstrate the capability of the linear accelerator to meet the requirements for the high spectral flux electron beam using the nominal photo-injector configuration. Different working points that minimise the transverse emittance and energy spread at the end of the linac (i.e. at  $z = 6$  m, Fig.4.12) have been analysed.

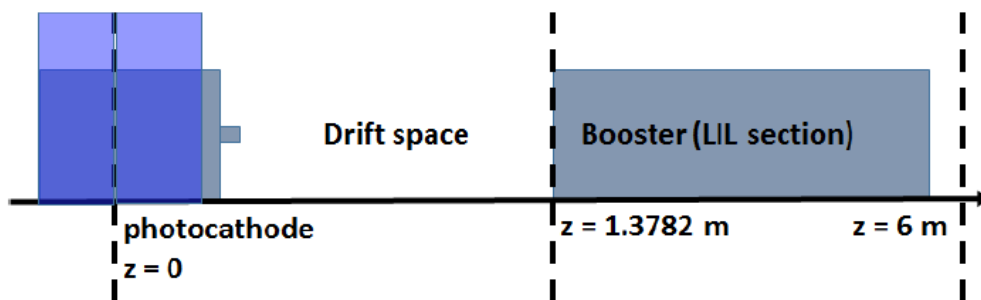


FIGURE 4.12: Nominal ThomX configuration.

In order to reproduce a travelling wave acceleration in ASTRA, boundary conditions require that the field profile in the input and output half cells of the RF period oscillates with standing wave pattern and is smoothly matched to the travelling wave profile of the inner cells [89]. The parameters that have been set in ASTRA for the travelling wave acceleration are resumed in Tab.4.6.

Table 4.7 shows a beam parameters comparison between the case where the RF gun and the accelerating section present the MMMG condition ( $\phi_{RFgun} = 0^\circ, \phi_{LIL} = 0^\circ$ ) and the case where the de-phasing of the gun is equal to  $-15^\circ$  ( $\phi_{RFgun} = -15^\circ, \phi_{LIL} = 0^\circ$ ).

TABLE 4.6: TW accelerating structure (LIL) parameters.

Parameters	values
Frequency	2998.5 MHz
Peak electric field	14 MV/m
Phase advance per cell	120 deg
Starting position	1.3782 m
Number of cells	132

TABLE 4.7: Beam dynamics parameters for two different de-phasing values ( $Q = 1$  nC,  $\sigma_{x,y} = 0.6$  mm,  $\sigma_t = 2$  ps).

Parameters	$\Delta\phi_{RF\ gun} = 0^\circ$	$\Delta\phi_{RF\ gun} = -15^\circ$
Normalised transverse emittance [ $\pi$ mm mrad]	8.2	7.3
Transverse size [mm]	3.5	3.5
Energy spread [%]	0.45	0.36
Longitudinal size [ps]	3.4	3.2

In the drift space, just after the gun exit, in the case of  $-15^\circ$  de-phasing the emittance is still linearly increasing while in the case of  $0^\circ$  de-phasing, the emittance is well compensated by the magnetic field strength. Furthermore, the energy spread is rapidly decreasing along the section.

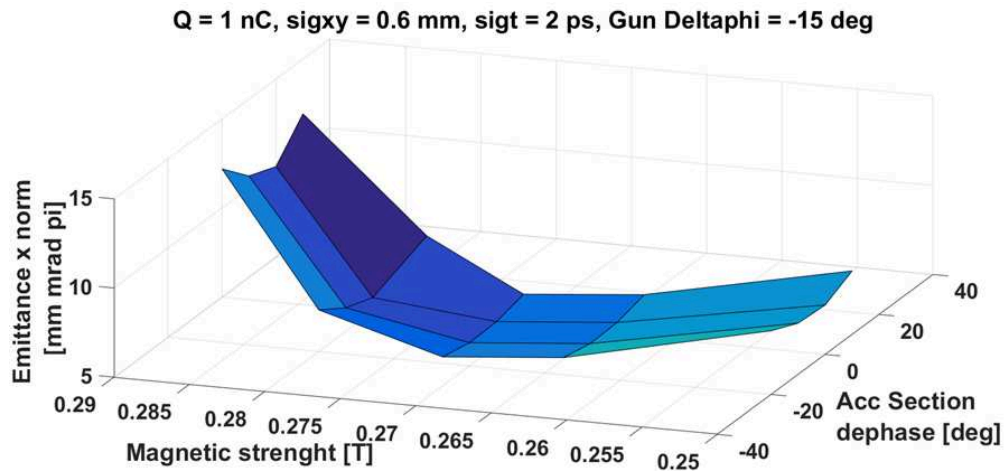


FIGURE 4.13: Transverse emittance vs maximum magnetic field strength and RF LIL dephasing.

A cross scan over the maximum magnetic field  $B_z^{max}$  as well as the TW section de-phasing with respect to laser pulses  $\phi_{LIL}$  has been performed. Figure 4.13 shows the transverse emittance as a function of the maximum magnetic field strength and the accelerating cavity de-phasing. The plot has a minimum for  $B_z^{max} = 0.28$  T (shielding plate with 5 mm thickness) and  $\phi_{LIL} = 0^\circ$ . The increasing of the maximum magnetic field strength allows decreasing the transverse emittance to 5.7 mm mrad. The de-phasing of the RF gun allows reducing the bunch length and therefore reducing the energy spread value

up to  $\Delta E/E \sim 0.36\%$  while maintaining the transverse beam size and bunch length unchanged.

The normalised transverse emittance that has been obtained with this set of parameters considering the ThomX TDR configuration is higher than that expected from specification. A proper electron beam matching with the travelling wave accelerating section has been performed to improve the normalised transverse emittance up to the specification. This new injector configuration will be presented in the next section.

### 4.3.1 Beam matching to the TW LIL structure

The theory of linear emittance compensation in a high brightness RF photo-injector is well established [81].

As we have already mentioned, the transverse emittance growth compensation induced by space charge is usually performed by locating different solenoids around or at the exit of the gun. Then, in the drift space the accelerating section has to be properly matched to the beam, according to the so called "invariant envelope" condition [89]. The principle [90] has been simulated.

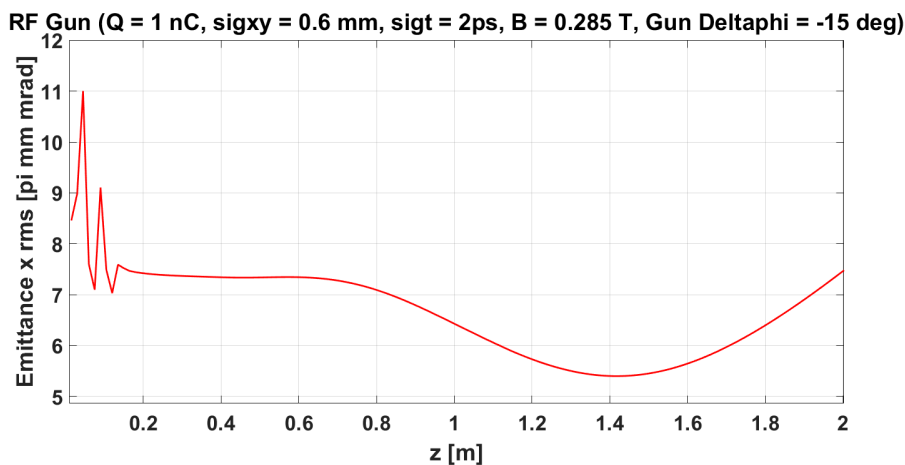
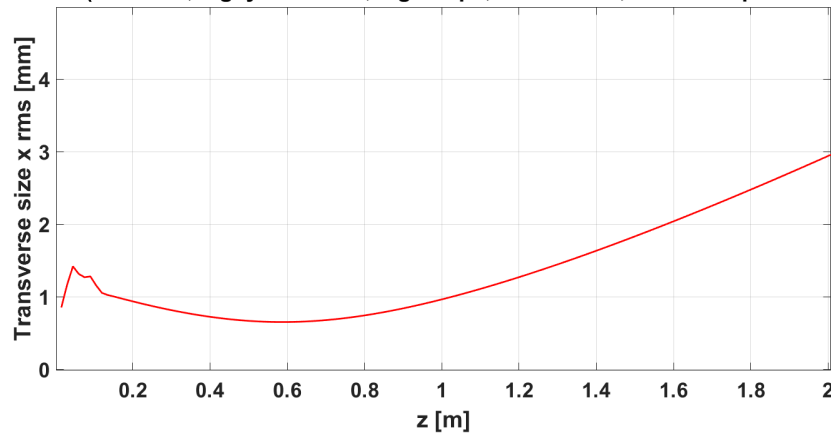


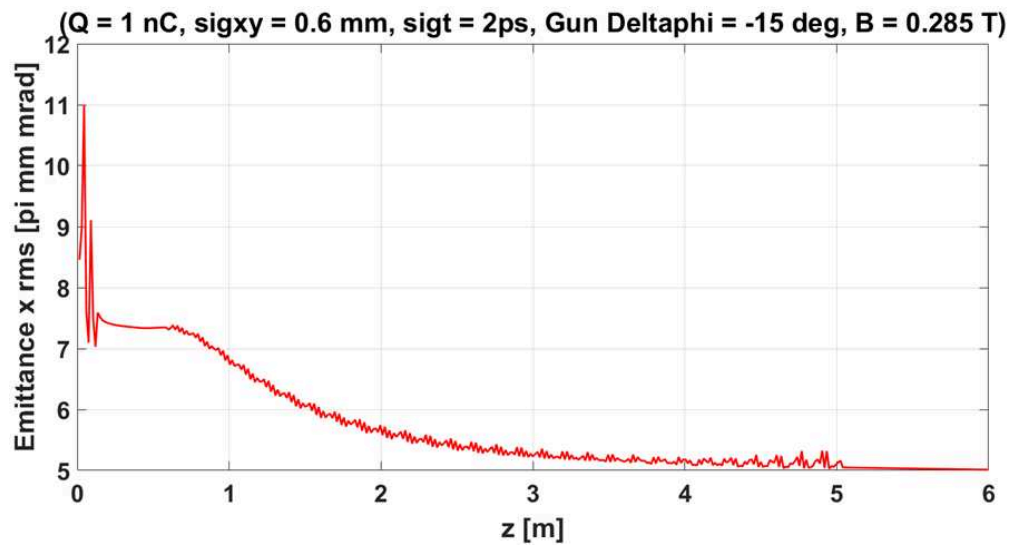
FIGURE 4.14:  $\epsilon_{xy}$  evolution along the RF gun and the drift space.

Figures 4.14 and 4.15 show the emittance and transverse size evolutions in the region downstream the gun as far as 6 meters in the drift space. The emittance oscillations are clearly visible as expected by the theory. The "invariant envelope" condition is achieved when a beam waist occurs together with a local maximum of the emittance. To fulfill this condition, the evolution of  $\epsilon_{x,y}$  and  $\sigma_{x,y}$  with respect to different magnetic field strength from the solenoids have been explored. For a fixed maximum magnetic field value, the condition is fulfilled at  $z = 0.57$  m. The TW accelerating section should be placed at that position corresponding to the local maximum between the so called

RF Gun (Q = 1 nC, sigxy = 0.6 mm, sigt = 2ps, B = 0.285 T, Gun Deltaphi = -15 deg)

FIGURE 4.15:  $\sigma_{xy}$  evolution along the RF gun and the drift space.

”double minimum” emittance oscillation (Ferrario working point [89]) at the minimum transverse size ( $\sigma'_{x,y} = 0$ , waist envelope).

FIGURE 4.16: Transverse emittance evolution for the TW section at  $z = 0.57$  m.

The resulting transverse emittance along the beam line is plotted in Fig. 4.16. The second emittance minimum, around 5 mm mrad occurs now downstream the TW structure at  $z = 6$  m. In this case, the emittance can be further improved with respect to that has been obtained in the TDR position of the LIL accelerating section. However, it is not possible to place the section at 0.57 m from the cathode because of mechanical constraints imposed by the beam diagnostic and vacuum element between the gun and section. As the beam waist is given by the focusing lens of the solenoid, a displacement of the solenoid can shift the beam waist closer to the entrance of the accelerating section. This will be the purpose of section 4.3.3.

### 4.3.2 Beam dynamics for the Linac energy upgrade

The standard TW accelerating section (LIL) will be replaced by a new high-gradient (HG) TW accelerating section whose characteristics are described in Chapter 2. This new section will have higher accelerating gradient that changes the transverse focusing force coming from the RF radial electric field component.

In order to analyse the effect of this high-gradient TW acceleration to the particle beam dynamics, the amplitude of the high-gradient on-axis electric field has been exported from HFSS and inserted in the ASTRA code. As in the case of the standard LIL accelerating structure, boundary conditions impose that the field profile in the input and output half cells of the RF period oscillates with standing wave pattern and is smoothly matched to the travelling wave profile of the inner cells. For sake of comparison between the standard LIL and high-gradient sections, we have set the ASTRA parameters for the HG section to achieve a final energy gain of 50 MeV. To do that, the ASTRA parameters are resumed in the Tab.4.8. The number of cells is reduced according to the gradient increase with respect to the LIL section.

TABLE 4.8: ASTRA parameters of the High-Gradient structure.

Parameters	values
Frequency	2998.5 MHz
Peak electric field	19 MV/m
Phase advance per cell	120 deg
Starting position	1.3782 m
Number of cells	96

The characteristics of the beam at  $z = 6$  m, for both standard LIL and HG structures are resumed in Tab.4.9. We can see that there is almost no modification in the longitudinal

TABLE 4.9: Linac beam parameters at  $z = 6$  m. Total bunch charge: 1 nC. Laser parameters: rms  $\sigma_{x,y} = 0.6$  mm, rms  $\sigma_t = 2$  ps, peak magnetic field = 0.28 T.

LIL section, $z = 1.3782$ m	
E [MeV]	50.4
$\epsilon_{x,y}$ [ $\pi$ mm mrad]	5.8
$\sigma_{x,y}$ [mm]	3.6
$\sigma_z$ [ps]	3.3
$\Delta E / E$ [%]	0.39
HG section, $z = 1.3782$ m	
E [MeV]	50.4
$\epsilon_{x,y}$ [ $\pi$ mm mrad]	5.6
$\sigma_{x,y}$ [mm]	2
$\sigma_z$ [ps]	3.2
$\Delta E / E$ [%]	0.38

bunch length. Also, there is no variation in the energy spread. The bunch length is determined by its value at the injector output while the energy spread, in the travelling wave structure, is dominated by the product of the gradient by the length of the structure if the bunch length is kept constant. As this product is similar to the LIL and the HG section, the energy spread is also similar. In addition, as the matching condition depends on the beam waist at the accelerating section entrance, the HG section is placed at the same position as the standard LIL section. Therefore, the improvement of the emittance is not significant (see Tab.4.10) as the normalised transverse emittance is driven by the input matching condition. The main difference occurs for the transverse size of the electron beam that is more focused for the upgrade section. This is again due to the slope of the RF radial field variation with respect to the position,  $z$ . This last aspect can rather be an important improvement for the beam propagation in the transfer line as it is presented below.

TABLE 4.10: Linac beam parameters at  $z = 6$  m. Total bunch charge: 1 nC. Laser parameters: rms  $\sigma_{x,y} = 0.6$  mm, rms  $\sigma_t = 2$  ps, peak magnetic field = 0.285 T.

LIL section, $z = 0.57$ m	
E [MeV]	50.5
$\epsilon_{x,y}$ [ $\pi$ mm mrad]	5
$\sigma_{x,y}$ [mm]	2.8
$\sigma_z$ [ps]	3.1
$\Delta E / E$ [%]	0.35
HG section, $z = 0.57$ m	
E [MeV]	50.5
$\epsilon_{x,y}$ [ $\pi$ mm mrad]	5.2
$\sigma_{x,y}$ [mm]	1.8
$\sigma_z$ [ps]	3.1
$\Delta E / E$ [%]	0.35

To conclude, the HG linac configuration will improve the focusing of the electron beam, which is better for the beam propagation in the transfer line. However, the beam matching condition can be improved only by moving the waist closer to the accelerating section. This is the next analysis we have performed and presented as follow.

### 4.3.3 Alternative solenoids configuration

As it has been previously pointed out, the beam enters the section far away from the beam waist. As the slope of the magnetic field profile is maximum at the early stage of the photoinjector (in the second cell) and its magnetic length is quite low, the beam waist is located near the photoinjector exit. A possible way to overcome this condition is to shift the focusing solenoid after the RF gun. A preliminary simulation shows that

the optimum position for the maximum value of the magnetic field profile can be located at 16 cm far from the cathode. But due to mechanical constraints, the only available position is at 23 cm, then just after the RF gun waveguide. Figure 4.17 shows the profile of the on-axis magnetic field for this new configuration (red curve) compared with the TDR configuration (blue line). The bucking coil current is set to cancel the field at the cathode.

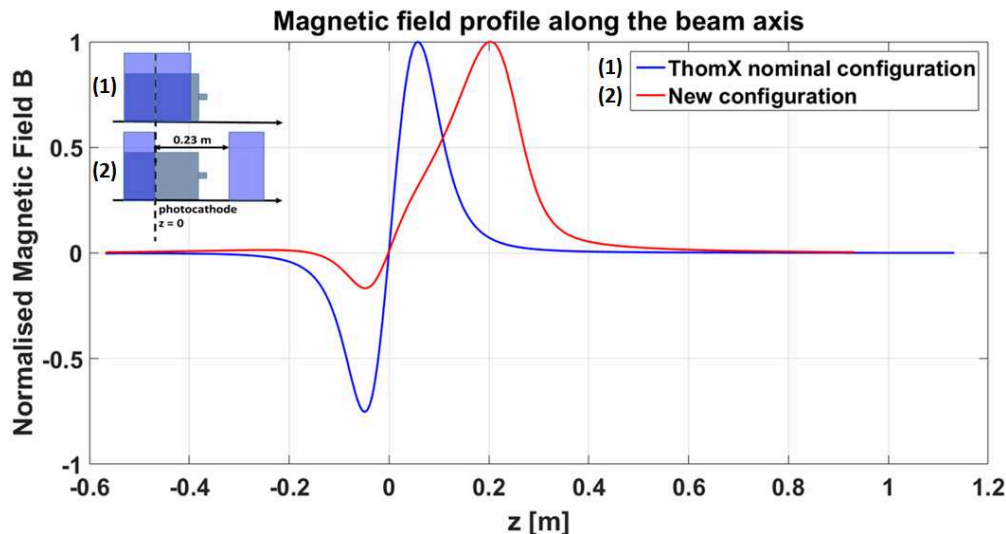


FIGURE 4.17: Magnetic field profile along the beam axis. Thomx nominal configuration, focusing solenoid 23 cm away.

#### 4.3.3.1 Beam matching to the TW LIL structure

A scan across several maximum magnetic field values has been performed with this new solenoids configuration and the evolution of the beam transverse size as well as the normalised transverse emittance in the region downstream the gun and the drift space have been investigated. We have explored two different couples of  $B_{z,max}$  and matching position. The results of the matching are resumed in Tab.4.12.

TABLE 4.11: Linac beam parameters at  $z = 6$  m. Total bunch charge: 1 nC. Laser parameters: rms  $\sigma_{x,y} = 0.6$  mm, rms  $\sigma_t = 2$  ps

B = 0.255 T, z = 1.32 m	
E [MeV]	50.5
$\epsilon_{x,y}$ [pi mm mrad]	5
$\sigma_{x,y}$ [mm]	1.8
$\sigma_z$ [ps]	3.2
$\Delta E / E$ [%]	0.38

We will first discuss the results concerning the LIL section at 1.32 m far from the cathode comparing with the ThomX TDR solenoids configuration. As we expected, the

longitudinal characteristics remain unchanged, but a normalised transverse emittance of  $5 \pi$  mm mrad is achieved after the section. In addition, the transverse dimension is 1 mm smaller than the previous configuration at the linac exit. This point is rather important for the conservation of the transverse emittance in the transfer line. In fact, high beam envelope transverse size (i.e. beta function) combined with high energy spread will induce a degradation of the emittance due to chromatic focusing in the first quadruple triplet. As a consequence, this new solenoid configuration not only enables better matching with the accelerating section, but also favours the emittance preservation at the ring entrance.

We explore this scheme also with a genetic algorithm optimisation with the GIOTTO software developed by A. Bacci [91]. A better solution was found with a small dephasing of the gun and the section at  $\Delta\phi = -5.1^\circ$ . This solution leads also to lower energy spread and better emittance. The solenoid is also finest tuned (0.254 T instead of 0.25 T) to have a maximum emittance at the linac entrance for matching condition. The laser spot size is also smaller (0.5 mm instead of 0.6 mm). The achieved emittance is  $4 \pi$  mm mrad, so 20% better. The energy spread falls down from 0.4% to 0.25%.

TABLE 4.12: Linac beam parameters at  $z = 6$  m. Total bunch charge: 1 nC. Laser parameters: rms  $\sigma_{x,y} = 0.5$  mm, rms  $\sigma_t = 2$  ps

LIL section	
B = 0.254 T, $z = 1.3782$ m	
E [MeV]	50
$\epsilon_{x,y}$ [ $\pi$ mm mrad]	4
$\sigma_{x,y}$ [mm]	1.2
$\sigma_z$ [ps]	3.8
$\Delta E / E$ [%]	0.25
HG section	
B = 0.258 T, $z = 1.3782$ m	
E [MeV]	50
$\epsilon_{x,y}$ [ $\pi$ mm mrad]	4
$\sigma_{x,y}$ [mm]	1.4
$\sigma_z$ [ps]	3.8
$\Delta E / E$ [%]	0.25

The optimisation with genetic algorithm led to good results for both standard LIL and HG section. In the case of HG section, a fine tuning of the solenoid field is necessary to control the higher focusing effect in the fringe field of the TW section.

## 4.4 Beam dynamics effects on X-rays spectral purity

The energy spread and the angular divergence of the electron beam affect the X-ray flux in a chosen kinematic region and, as mentioned in Chapter 1, the low electron bunch energy leads to gradually increase the emittance and the energy spread of the bunch because of intra-beam scattering (IBS) and Compton back-scattering (CBS) phenomena [92].

To see the effect of the electrons beam parameters on the X-ray spectrum, simulations have been performed with the CAIN Monte Carlo code generated with typical ThomX parameters, i.e. collisions between a 50 MeV electron beam and a laser of wavelength 1036 nm. Figure 4.18 shows the distribution of the X-rays energy as a function of the X-ray scattering angle in case where the generated values of the normalised electron emittance and the relative electron energy spread are very small (i.e.  $\epsilon_n = 1 \mu\text{m rad}$  and  $\sigma_e = 0.1\%$ ).

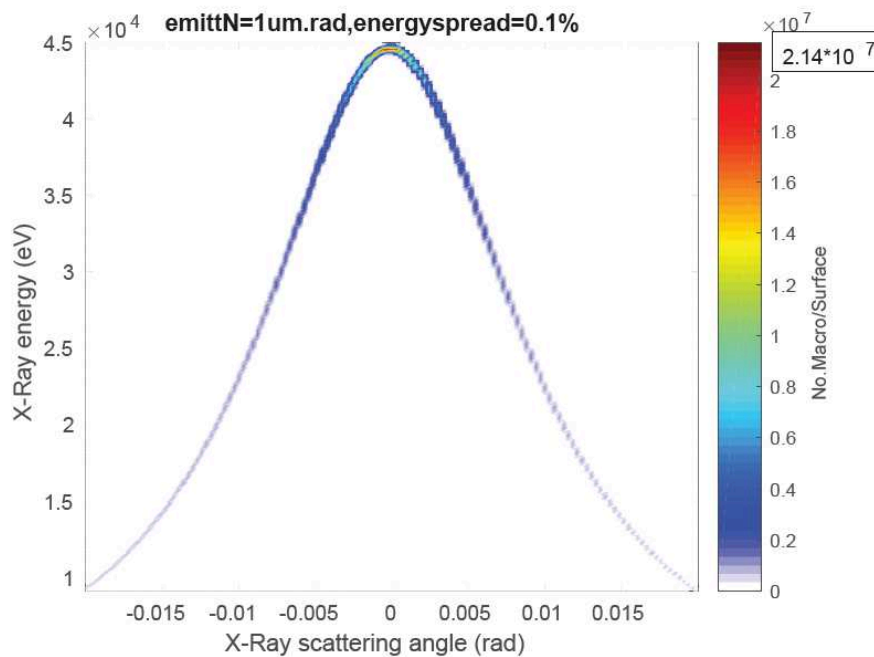


FIGURE 4.18: Distribution of energy of the scattering X-rays as a function of their scattering angle for an electron bunch normalized emittance of  $1 \mu\text{m}$  and an electron bunch relative energy spread of  $0.1\%$ .

In Figures 4.19 and 4.20, the same distributions are shown for the generated parameters  $\epsilon_n = 1 \mu\text{m}$ ,  $\sigma_e = 1\%$  and  $\epsilon_n = 10 \mu\text{m}$ ,  $\sigma_e = 0.1\%$  respectively. These plots show how, at given observation angle, the spectral purity is degraded according to the values of the electron emittance and energy spread: when the relative electron energy spread increases, the spectral purity at a given observation angle is degraded (Fig 4.19); when

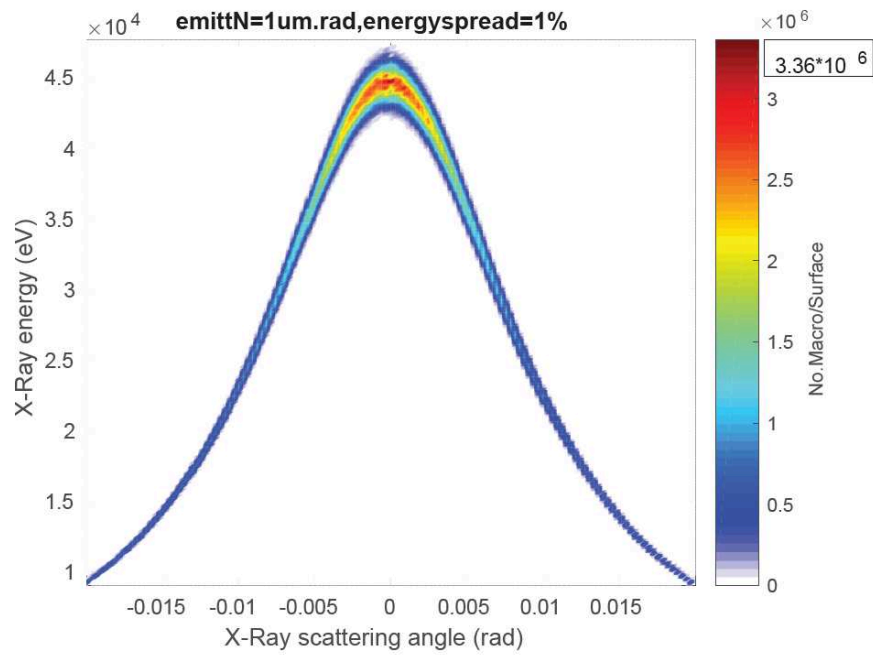


FIGURE 4.19: Distribution of energy of the scattering X-rays as a function of their scattering angle for an electron bunch normalized emittance of  $1 \mu\text{m}$  and an electron bunch relative energy spread of 1%.

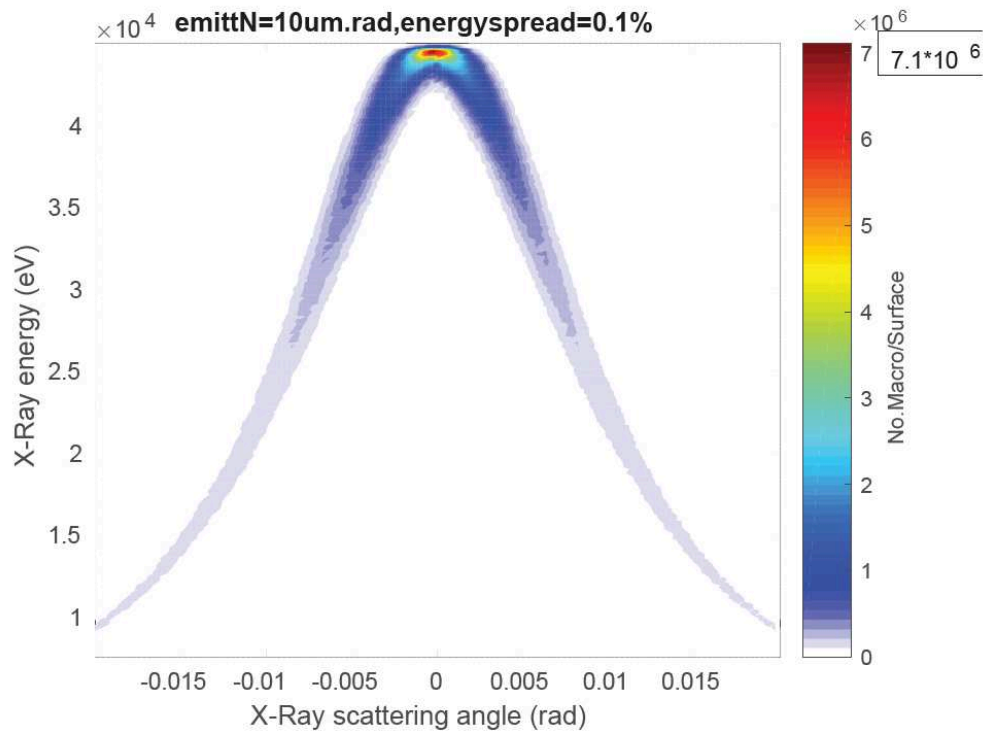


FIGURE 4.20: Distribution of energy of the scattering X-rays as a function of their scattering angle for an electron bunch normalized emittance of  $10 \mu\text{m}$  and an electron bunch relative energy spread of 0.1%.

the emittance increases, the distribution of the X-rays having a given energy spreads angularly.

Using an electron beam with a small emittance and a small energy spread is therefore an essential condition to increase the number of monochromatic photons scattered at a given direction.

## Chapter 5

# Conclusions

This dissertation is devoted to the design and technical aspects of the ThomX linear accelerator. Basically, ThomX linac is made up to two warm RF components: the RF gun and the accelerating section. A thermally stable operation is mandatory to prevent RF gun from parasitic field amplitude and phase jitters that lead to electron beam quality degradation. Since the gun is operating at high repetition rates, such a high-field level requires that cooling system guarantees an average power dissipation of several kW in the cavity walls. Therefore, the cooling system design has been performed to keep temperature variations as small as possible reducing structure deformations. A coupled electromagnetic to thermal and structural analysis by a unique simulation software (ANSYS) has been performed. This analysis has confirmed that the cooling system of the gun should be adequate for 1.5 kW power dissipation in the cavity walls, which corresponds to 50 Hz RF pulse repetition rate, 100 MV/m maximum accelerating gradient, 3  $\mu$ s RF pulse length, with 2.5 m/s water flow rate.

Another important aspect of this work is the ThomX linac energy upgrade. It implies a research and development activity at LAL in partnership with a French company (PMB-Alcen) aiming at the fabrication of a compact copper S-band constant-gradient accelerating section. The replacement of the standard LIL accelerating section with the new high-gradient structure should allow an electron energy boost up to 70 MeV corresponding to 90 keV X-rays energy fluxes, while maintaining compactness and beam characteristics at the ring injection. The fabrication of a high-gradient accelerating section requires a careful analysis and investigation on the main quantities that limit the achievement of a high-gradient accelerating fields in RF periodic structures. These main limitations are vacuum RF breakdown and pulsed heating fatigue.

The knowledge of the mechanisms that limit the achievement of high-gradient fields in RF accelerating structures relies on a wide experimental program of HG structure power

tests and breakdown phenomenology investigation that have been performed in several laboratories in the last years. A careful analysis of the large amount of experimental data has highlighted the dependence of the breakdown occurrence to certain parameters, such as RF pulse duration and power flow. A new local field quantity, the modified Poynting vector threshold, was then introduced as a new effective criterion to the design of high-gradient accelerating structures.

The electromagnetic design of regular cells has been performed taking into account the main quantities that drive the optimisation of the geometry parameters. The final cell shape has been defined on the basis of several criteria: maximum  $r_s/Q$ , minimisation of the ratio between the maximum surface electric field and on-axis accelerating gradient  $E_{s\ max}/E_a$ , minimisation of the modified Poynting vector. However, the cell geometry design is a difficult process because the improvement of certain RF parameters usually results in a degradation of other ones. Therefore, the optimum regular cell design is the consequence of the compromise between different cavity constraints aiming at the achievement of operational requirements. Final dimensions have been optimised to obtain a low maximum surface electric field using elliptical iris shape and minimum modified Poynting vector at the iris regions, and relatively high velocity group, with an accelerating gradient able to achieve the desired energy gain with respect to the available input power. The iris thickness has been chosen to get a compromise between high shunt impedance, acceptable filling time and mechanical rigidity. The cell edge has been rounded resulting in quality factor increase of 10% and reduction in power consumption. Moreover, a reasonable iris aperture range has been considered to guarantee a high acceleration efficiency with minimum breakdown risks, short filling time and good pumping speed.

Power coupler design has been performed in order to transmit maximum energy to the beam while protecting the power supply circuit. These conditions are fulfilled when there exists a good coupling between the waveguide and the accelerating periodic structure. Couplers have been designed to reduce as much as possible power reflections at the input/output coupling ports having a phase advance per cell equal to the nominal one ( $120^\circ$ ). Prototypes are equipped with quasi-symmetric single-feed couplers which have a waveguide (stub) of  $\lambda/4$  length at the coupling slot opposite site in order to compensate the asymmetry of the electromagnetic field in the coupling cell.

Coupler design techniques have been applied to CI TW prototype and final CG TW structure. The development of CI copper prototypes allows to verify the geometry, validate the fabrication procedure and check if the normal operation conditions are fulfilled. For couplers prototype and final accelerating section high-gradient limiting quantities point, i.e. RF breakdown probability (BDR) and pulsed heating have been analysed. Considering a peak power of 20 MW at the input of 16 cells CI copper prototype, the

maximum value of modified Poynting vector simulated is around  $0.19 \text{ MW/mm}^2$ , far below the limit of  $1.6 \text{ MW/mm}^2$  for a breakdown rate probability (BDR) of  $10^{-6}$  bp-p/m (medical applications). Also, the pulsed heating phenomenon has been carefully evaluated and monitored in each location of the designed structure where high surface currents density are significant. Taking into account an RF flat top pulse length of  $3 \mu\text{s}$  (20 MW input power) a maximum surface magnetic field equal to  $1.36 \times 10^5 \text{ A/m}$  has been obtained at the waveguide-to-coupling cell region. This value corresponds to a temperature rise on the metal less than  $8 \text{ }^\circ\text{C}$ , well below the “safe limit” of coupler damage risk. Moreover, the mechanical design of the regular cells and couplers have been performed. Each regular cell presents four holes on the external surface for frequency tuning. They present also eight cooling channels that are directly drilled in the copper body. The couplers are composed of separately machined parts: the body and cover. The body consists in the coupling cell with waveguides and one-half regular cell.

The electromagnetic design of a 3.2 m-long high-gradient compact S-band accelerating structure has also been carried out. This is a TW CG section type composed of 95 regular cells and 2 coupling cells resonating at a frequency of 2998.5 MHz at  $30 \text{ }^\circ\text{C}$  under vacuum, at  $TM_{010-2\pi/3}$ -mode. The constant accelerating gradient along the structure has been maintained by suitable shaping the iris aperture of each cell. The iris radius is then decreasing along the structure in order to have a flatness of the accelerating field amplitude through the whole section and to maintain a uniform cell-to-cell phase advance of  $120^\circ$  for the accelerating mode. The design of a linear tapered structure has been performed by simulating regular cells with different iris radius and calculating the main RF figure of merits every time. The iris radius variation range has been chosen as a compromise between maximum energy gain and minimum filling time. The accelerating structure is equipped with two quasi-symmetrical-type single feed couplers. For an maximum available input power of 24 MW, the remaining power is around 7 MW at the end of the section, corresponding to a dissipated power in the walls of the cavity of around 17 MW (2.55 kW average power). The effective accelerating field seen by the electron beam has an average value of  $20 \text{ MV/m}$ , whereas the maximum on-axis electric gradient shows an average value of  $24 \text{ MV/m}$ . Taking into account an energy of around 5 MeV provided by the RF gun, the energy gain of the accelerating section is around 65 MeV. It should be enough to accomplish the final goal of 70 MeV for the upgrade phase of the linac. The filling time is less than  $1 \mu\text{s}$ . This value should be reasonable to prevent breakdown phenomena in the structure during operation. The maximum surface electric field keeps constant to the value of  $34 \text{ MV/m}$  before decreasing along the structure. This value is well below the breakdown threshold of  $47 \text{ MV/m}$  according to the Kilpatrick’s criterion. The maximum simulated value of modified Poynting vector

along the structure is  $0.25 \text{ MW/mm}^2$  which is far below the limit of  $1.6 \text{ MW/mm}^2$  for a BDR of  $10^{-6}$  bpp/m.

A coupled thermo-mechanical study on 7-cells CI copper prototype has been performed. The water cooling system has been simulated to validate the capability to extract the heat generated by the dissipated power on the walls of the structure and guarantee that the temperature distribution is uniform along the accelerating section. The simulated dissipated power on the 7-cells prototype walls is around 333 W for an input peak power of 20 MW (RF pulse length of  $3 \mu\text{s}$  and repetition rate of 50 Hz). The temperature difference between the average copper structure and the inlet water circulating in the cooling system is  $0.7 \text{ }^\circ\text{C}$ . the increase of water temperature due to the RF power heat dissipation is  $0.08 \text{ }^\circ\text{C}$ , in good agreement with analytic estimations. Some initial parameters condition were fixed and applied to the Fluent structure model as thermal loads. Then, natural convection has been applied to the model. An uniform temperature throughout the whole structure body with an average value of about  $24.8 \text{ }^\circ\text{C}$  has been found, close to the analytic value. The temperature of the cells, which has the largest impact on the structure resonant frequency is about  $26 \text{ }^\circ\text{C}$ . Furthermore, the maximum pressure drop is around 0.17 bar showing the good agreement with analytic results. In addition, the temperature variation and the pressure drop for the cooling system have also been estimated for the 16-cells prototype and the final accelerating section. Starting from the thermal analysis, we are able to evaluate the deformation of the structure due to RF heating. The maximum deformation is around  $12 \mu\text{m}$ . The deformation calculated on the inner surfaces in the radial direction is below  $20 \mu\text{m}$ . The designed cooling system seems also adequate for the 16-cells CI prototype and for the final CG TW section. This cooling system allows to take under control the deformations of the structure while keeping temperature increase as small and uniform as possible.

The vacuum performances of the 16-cells CI copper prototype has been checked to prevent high probabilities of RF breakdowns, short beam lifetime and emittance blow-up. Four pumping configurations have been studied: pumping through one beam pipe of the prototype, pumping through one RF waveguide port, pumping through both beam pipes or pumping through both RF waveguide ports of the prototype. Pumping through two beam pipes allows to decrease by a factor of 2 the maximum and the average pressure values along the structure with respect to vacuum pump connected to one beam pipe. Pumping through one waveguide allows to decrease by a factor of 3 the maximum and the average pressure values along the structure in comparison with two beam pipes. Pumping through two waveguides allows to decrease by a factor of 3 the maximum and the average pressure values along the structure in comparison with the case of a single ionic pump connected to the waveguide port. When two vacuum pumps are connected to the two waveguides, the maximum pressure at the center of the structure is around

$4 \times 10^{-9}$  mbar without bake-out treatment. Also, the vacuum simulation of the 3.2-m long final accelerating section has been performed. The pressure is increasing along the section (because the iris diameters are progressively decreasing) up to the center and then decreasing at its minimum value equal of  $5.97 \times 10^{-9}$  mbar. The average pressure value is  $5.83 \times 10^{-8}$  mbar the maximum is  $8.78 \times 10^{-8}$  mbar. In the case of the final accelerating section configuration, the maximum vacuum pressure is  $8.78 \times 10^{-8}$  mbar without bake-out treatment. These values are below or comparable to  $8 \times 10^{-8}$  mbar that is enough for high-gradient operation. Moreover, with bake-out treatment the simulated vacuum pressure would be divided by a factor 10 - 100. The good news is that according to our conservative calculations, vacuum pumping for the prototype under present design should be adequate. For the final 3.2-m long high-gradient accelerating section we need to increase the vacuum inside the structure at least of factor 10 (better 100). We believe that pumping through the waveguides and performing back-out process to the section after installation will play a key role to the achievement of this goal.

The main steps performed during the ThomX RF gun fabrication at LAL have been also presented. In particular the machining, tuning, brazing and cleaning processes have been briefly reviewed. Moreover, the fabrication of 7-cells aluminium prototypes in collaboration with PMB-Alcen company has been described. After the machining procedure of regular cells, the tuning method under press have been presented. RF low power tests on the prototype has been performed in order to validate the 3D geometry design and the machining process. Those last steps are very important to tackle mechanical problems and technological constraints for the future copper prototype. The RF low power results before and after tuning procedure have been shown. Future work will focus on the fabrication of the 16-cells copper CI prototype for the validation of the manufacturing process, the RF conditioning and high power tests. After, a 3.2-m long high-gradient S-band accelerating section for the ThomX linac energy upgrade will be fabricated and brazed.

The optimisation of the beam energy spread and emittance is crucial for the spectral purity of the X-rays. Due to the relatively high charge required (1 nC), it is difficult to control the emittance at the linac output as it is dominated by space charge effect. However, some optimisation procedures have been already proposed in the literature. In this sense, complete simulations of the ThomX Linac have been carried out taking care to have a model close to the real electromagnetic components that compose the linear accelerator, such as RF gun, TW section and solenoids.

First we highlight that a laser spot size larger than 0.4 mm should be used to avoid charge losses by mirror effect at the cathode. In fact, this condition corresponds to a

space charge saturated emission regime and no more charge can be extracted even if the laser intensity is increased.

Second, by exploring the invariant envelop condition proposed by Serafini, Rosenzweig, and Ferrario, we found that a beam waist corresponding to a local maximum of emittance cannot happen for the nominal solenoid configuration chosen during the TDR phase of the project. As all the mechanical and magnetic component was already ordered, a solution has been found minimizing the impact of costs and delay on the project. Indeed, by moving the focusing solenoid after the gun, the invariant envelop condition can be achieved at a position of the TW section near TDR nominal one. Finally, the optimisation with the genetic algorithm software enables to achieve a normalised transverse emittance equal to  $4 \pi$  mm mrad with a relatively low energy spread. It has also been shown that the use of a 3 GHz high-gradient section can improve the focusing effect of the accelerating section leading to avoid emittance degradation in the first quadruple triplet at the linac exit.

The analysis, the optimisation of the solenoid position together with a genetic algorithm open the way for a full start to end optimisation of the ThomX beam dynamics from the electron emission to the interaction point. It constitutes also a strong basis for the future commissioning phase of the linac.

# Bibliography

- [1] Philippe Walter, Alessandro Variola, Fabian Zomer, Marie Jaquet, and Alexandre Loulergue. A new high quality x-ray source for cultural heritage. *Comptes Rendus Physique*, 10(7):676–690, 2009.
- [2] Frank E Carroll. Tunable monochromatic x rays: a new paradigm in medicine. *American Journal of Roentgenology*, 179(3):583–590, 2002.
- [3] Marie-Claude Biston, Aurélie Joubert, Jean-François Adam, Hélène Elleaume, Sylvain Bohic, Anne-Marie Charvet, François Estève, Nicolas Foray, and Jacques Balosso. Cure of fisher rats bearing radioresistant f98 glioma treated with cisplatin and irradiated with monochromatic synchrotron x-rays. *Cancer research*, 64(7):2317–2323, 2004.
- [4] Pekka Suortti and W Thomlinson. Medical applications of synchrotron radiation. *Physics in medicine and biology*, 48(13):R1, 2003.
- [5] Ryoichi Hajima, Takehito Hayakawa, Nobuhiro Kikuzawa, and Eisuke Minehara. Proposal of nondestructive radionuclide assay using a high-flux gamma-ray source and nuclear resonance fluorescence. *Journal of Nuclear Science and Technology*, 45(5):441–451, 2008.
- [6] Sakae Araki, Yasuo Higashi, Yousuke Honda, Yoshimasa Kurihara, et al. Conceptual design of a polarised positron source based on laser compton scattering (report submitted to snowmass05). *CARE/ELAN Document-2005-013*, *arXiv://physics/0509016*, *CLIC Note 639*, *KEK Preprint 2005-60*, *LAL 05-94 (2005)*, page 39, 2005.
- [7] G Moortgat-Pick et al. The role of polarized positrons and electrons in revealing fundamental interactions an the linear collider. report of the polarization working group ‘power’. *arXiv preprint hep-ph/0507011*, 2005.
- [8] G. Klemz, K. Moenig, and I. Will. Design study of an optical cavity for a future photon-collider at ilc. *Nucl.Instrum.Meth.A564:212-224*, 2006. doi: 10.1016/j.nima.2006.03.017.

- [9] M Jacquet. High intensity compact compton x-ray sources: Challenges and potential of applications. *Nuclear Instruments and Methods in Physics Research Section B: Beam Interactions with Materials and Atoms*, 331:1–5, 2014.
- [10] Changchun Sun and Ying K. Wu. Theoretical and simulation studies of characteristics of a compton light source. *Phys.Rev.ST Accel.Beams* 14:044701,2011, 2011. doi: 10.1103/PhysRevSTAB.14.044701.
- [11] Zhirong Huang and Ronald D Ruth. Laser-electron storage ring. *Physical review letters*, 80(5):976, 1998.
- [12] Jens Als-Nielsen and Des McMorrow. *Elements of modern X-ray physics*. John Wiley & Sons, 2011.
- [13] Roderick J Loewen. A compact light source: design and technical feasibility study of a laser-electron storage ring x-ray source. Technical report, Stanford University Stanford CA, 2003.
- [14] Michael Borland William Barletta. Report of the basic energy sciences workshop on compact light sources. Technical report, MIT, UCLA, ANL, 2010.
- [15] I Chaikovska, K Cassou, R Chiche, R Cizeron, P Cornebise, N Delerue, D Jehanno, F Labaye, R Marie, A Martens, et al. High flux circularly polarized gamma beam factory: coupling a fabry-perot optical cavity with an electron storage ring. *Scientific reports*, 6, 2016.
- [16] Günther Geschonke and A Ghigo. Ctf3 design report. Technical report, Cern, 2002.
- [17] A Variola, J Haissinski, A Loulergue, F Zomer, et al. Thomx technical design report. *LAL Internal Report RT14/21 and SOLEIL/SOU Internal Report RA*, 2014.
- [18] John David Jackson. *Classical electrodynamics*, 1999.
- [19] J Bonis, R Chiche, R Cizeron, M Cohen, E Cormier, P Cornebise, N Delerue, R Flaminio, D Jehanno, F Labaye, et al. Non-planar four-mirror optical cavity for high intensity gamma ray flux production by pulsed laser beam compton scattering off gev-electrons. *Journal of Instrumentation*, 7(01):P01017, 2012.
- [20] M Jacquet and C Bruni. Analytic expressions for the angular and the spectral fluxes at compton x-ray sources. *Journal of synchrotron radiation*, 24(1):312–322, 2017.
- [21] Marie Jacquet. Potential of compact Compton sources in the medical field. *Physica Medica*, 32(12):1790–1794, 2016. URL <http://www.sciencedirect.com/science/article/pii/S1120179716309784>.

- [22] Elena Eggl, Martin Dierolf, Klaus Achterhold, Christoph Jud, Benedikt Günther, Eva Braig, Bernhard Gleich, and Franz Pfeiffer. The munich compact light source: initial performance measures. *Journal of synchrotron radiation*, 23(5):1137–1142, 2016.
- [23] Ronald D Ruth and Zhirong Huang. Compton backscattered collimated x-ray source, March 7 2000. US Patent 6,035,015.
- [24] Thomas Vinatier. *Influence des paramètres du laser sur la dynamique des paquets courts d'électrons relativistes dans des accélérateurs linéaires basés sur des canons RF et développement de diagnostics associés*. PhD thesis, Paris 11, 2015.
- [25] Thomas P Wangler. *RF Linear accelerators*. John Wiley & Sons, 2008.
- [26] Silvia Verdú Andrés. High-gradient accelerating structure studies and their application in hadrontherapy. 2013.
- [27] Frank Gerigk. Cavity types. *arXiv preprint arXiv:1111.4897*, 2011.
- [28] Mario Weiss. Introduction to rf linear accelerators. 1994.
- [29] AL. Helm RH. Lisin AV. Loew GA Borghi, RP. Eldredge. Design, fabrication, installation, and performance of the accelerator structure. *The Stanford Two-Mile Accelerator*, page 95, 1968.
- [30] W Wuensch. Progress in understanding the high-gradient limitations of accelerating structures. Technical report, 2007.
- [31] Walter Wuensch. The scaling of the traveling-wave rf breakdown limit. Technical report, 2006.
- [32] NA Solyak. Gradient limitations in room temperature and superconducting acceleration structures. In *AIP Conference Proceedings*, volume 1086, pages 365–372. AIP, 2009.
- [33] Kyrre Ness Sjobak, Erik Adli, and Alexej Grudiev. New criterion for shape optimization of normal-conducting accelerator cells for high-gradient applications. 2014.
- [34] Alexej Grudiev, S Calatroni, and W Wuensch. New local field quantity describing the high gradient limit of accelerating structures. *Physical Review Special Topics-Accelerators and Beams*, 12(10):102001, 2009.
- [35] WD Kilpatrick. Criterion for vacuum sparking designed to include both rf and dc. *Review of Scientific Instruments*, 28(10):824–826, 1957.

- [36] Jorge Giner Navarro. Breakdown studies for high-gradient rf warm technology in: Clic and hadron therapy linacs. 2016.
- [37] Valery A Dolgashev and Sami G Tantawi. Effect of rf parameters on breakdown limits in high-vacuum x-band structures. In *AIP Conference Proceedings*, volume 691, pages 151–165. AIP, 2003.
- [38] Walter Wuensch, CE Adolphsen, Ian H Wilson, M Taborelli, Steffen Döbert, IV Syrathev, Samuli Tapio Heikkinen, and A Grudiev. A high-power test of an x-band molybdenum-iris structure. Technical report, 2004.
- [39] A Descoeudres, T Ramsvik, S Calatroni, M Taborelli, and W Wuensch. Dc breakdown conditioning and breakdown rate of metals and metallic alloys under ultra-high vacuum. *Physical Review Special Topics-Accelerators and Beams*, 12(3):032001, 2009.
- [40] XXX. www.ansys.com. Technical report, XXX.
- [41] XXX. www.cst.com. Technical report, XXX.
- [42] Mohamed El Khaldi, Julien Bonis, Abdoulaye Camara, Luca Garolfi, and Alexandre Gonnin. Electromagnetic, thermal, and structural analysis of a thomx rf gun using ansys. In *7th International Particle Accelerator Conference (IPAC'16), Busan, Korea, May 8-13, 2016*, pages 3925–3927. JACOW, Geneva, Switzerland, 2016.
- [43] Julien Brossard, M Desmons, B Mercier, Christophe Prevost, and Raphaël Roux. Construction of the probe beam photo-injector of ctf3. In *10th European Particle Accelerator Conference "EPAC'06"*, pages 828–830, 2006.
- [44] David P Pritzkau and Robert H Siemann. Experimental study of rf pulsed heating on oxygen free electronic copper. *Physical Review Special Topics-Accelerators and Beams*, 5(11):112002, 2002.
- [45] Gérard Bienvenu et al. *Mesure et etude de l'auto emission electronique et du champ électrique des sections acceleratrices d'électrons*. PhD thesis, 1993.
- [46] YW Kang, Paul J Matthews, and Robert L Kustom. A constant gradient planar accelerating structure for linac use. In *Particle Accelerator Conference, 1995., Proceedings of the 1995*, volume 1, pages 643–645. IEEE, 1995.
- [47] RH Helm and GA Loew. Linear accelerators, 1970.
- [48] G Bienvenu, JC Bourdon, P Brunet, and J Rodier. Accelerating structure developments for the lep injector linace (lil). Technical report, 1984.

- [49] D Alesini, R Boni, G Di Pirro, R Di Raddo, M Ferrario, A Gallo, V Lollo, F Marcellini, L Palumbo, V Spizzo, et al. The c-band accelerating structures for sparc photoinjector energy upgrade. *Journal of Instrumentation*, 8(05):P05004, 2013.
- [50] Luigi Faillace, RadiaBeam Tech, Ronald Agustsson, RadiaBeam Tech, Pedro Frigola, RadiaBeam Tech, Alex Murokh, RadiaBeam Tech, Valery Dolgashev, James Rosenzweig, et al. Ultra-high gradient compact s-band linac for laboratory and industrial applications. In *Conf. Proc. C100523: THPEA059, 2010*, number SLAC-PUB-15147. SLAC National Accelerator Laboratory (SLAC), 2012.
- [51] L Garolfi, M El Khaldi, and N Faure. 3 ghz single cell cavity optimization design. In *6th International Particle Accelerator Conference-IPAC'15*, 2015.
- [52] Jan Wilhelm Kovermann. *Comparative studies of high-gradient RF and DC breakdowns*. PhD thesis, CERN, 2010.
- [53] Stefano Benedetti, Ugo Amaldi, Alexej Grudiev, Alberto Degiovanni, and Walter Wuensch. Rf design of a novel s-band backward traveling wave linac for proton therapy. 2014.
- [54] Mohamed El Khaldi and Luca Garolfi. Rf design of a high gradient s-band travelling wave accelerating structure for thomx linac. In *IPAC'15, the sixth International Particle Accelerator Conference,, 2015*.
- [55] L. Faillace. *Innovative radio-frequency linear accelerating structure*. PhD thesis, 2008.
- [56] F. cardelli. *Design, realisation and commissioning of RF power system and accelerating structures for a Gamma Source*. PhD thesis, University of La Sapienza, Rome, 2016.
- [57] David Alesini, Alessandro Gallo, Bruno Spataro, Agostino Marinelli, and Luigi Palumbo. Design of couplers for traveling wave rf structures using 3d electromagnetic codes in the frequency domain. *Nuclear Instruments and Methods in Physics Research Section A: Accelerators, Spectrometers, Detectors and Associated Equipment*, 580(3):1176–1183, 2007.
- [58] Agostino Marinelli, Luigi Palumbo, and Dott David Alesini. Progetto di un accoppiatore in guida d'onda per una struttura accelerante ad onda viaggiante in banda x. *X-band coupler for RF gun master thesis (University of Rome "La Sapienza," 2004)*, 2004.
- [59] XXX. www.3ds.com. Technical report, XXX.

- 
- [60] Robert E Ellefson and JM Lafferty. *Foundations of vacuum science and technology*. John Wiley & Sons, Inc., New York, 1998.
- [61] J Howell, B Wehrle, and H Jostlein. Calculation of pressure distribution in vacuum systems using a commercial finite element program. Technical report, Argonne National Lab., 1991.
- [62] Scott R Wilson. Numerical modeling of vacuum systems using electronic circuit analysis tools. *Journal of Vacuum Science & Technology A: Vacuum, Surfaces, and Films*, 5(4):2479–2483, 1987.
- [63] DH Davis. Monte carlo calculation of molecular flow rates through a cylindrical elbow and pipes of other shapes. *Journal of Applied Physics*, 31(7):1169–1176, 1960.
- [64] R Kersevan and J-L Pons. Introduction to molflow+: New graphical processing unit-based monte carlo code for simulating molecular flows and for calculating angular coefficients in the compute unified device architecture environment. *Journal of Vacuum Science & Technology A: Vacuum, Surfaces, and Films*, 27(4):1017–1023, 2009.
- [65] R Kersevan. Molflow user’s guide. *available from one of the authors (RK)*, 1991.
- [66] Sanyi Zheng. Conductance calculation-molecular flow, long tube of circular cross section. Technical report, 1993.
- [67] MATTIA ORTINO. Sticking coefficients for technical materials in vacuum technology. 2016.
- [68] R Kersevan. Analytical and numerical tools for vacuum systems. 2007.
- [69] Chian Liu and John Noonan. Advanced photon source accelerator ultrahigh vacuum guide. Technical report, ANL/APS/TB-16, 1994.
- [70] D Alesini, S Bini, R Di Raddo, V Lollo, L Pellegrino, L Ficcadenti, V Pettinacci, L Palumbo, and L Serafini. Design and rf test of damped c-band accelerating structures for the eli-np linac. In *Proceedings of the International Particle Accelerator Conference IPAC2014*, page 3856, 2014.
- [71] Ian H Wilson. Cavity construction techniques. *xxx*, 1992.
- [72] Walter Wuensch. Improvements in cavity construction techniques. *xxx*, 2005.
- [73] Richard L Rhorer and Chris J Evans. Fabrication of optics by diamond turning. *Handbook of optics*, 1:41–1, 1995.

- [74] Y Tito Sasaki. A survey of vacuum material cleaning procedures: A subcommittee report of the american vacuum society recommended practices committee. *Journal of Vacuum Science & Technology A: Vacuum, Surfaces, and Films*, 9(3):2025–2035, 1991.
- [75] SI Kurokawa, M Month, and S Turner. *Frontiers of accelerator technology*. World Scientific, 1999.
- [76] E Westbrook. Microwave impedance matching of feed waveguides to the disk-loaded accelerator structure operating in the  $2\pi/3$  mode. *SLAC-TN-63-103*, 1963.
- [77] Yoichiro Nambu. Generalized hamiltonian dynamics. In *Broken Symmetry: Selected Papers of Y Nambu*, pages 302–309. World Scientific, 1995.
- [78] Klaus Halbach and RF Holsinger. Superfish-a computer program for evaluation of rf cavities with cylindrical symmetry. *Part. Accel.*, 7(LBL-5040):213–222, 1976.
- [79] Kwang-Je Kim. Rf and space-charge effects in laser-driven rf electron guns. *Nuclear Instruments and Methods in Physics Research Section A: Accelerators, Spectrometers, Detectors and Associated Equipment*, 275(2):201–218, 1989.
- [80] Ozgur Mete. *Study and Experimental Characterization of a Novel Photo Injector for the CLIC Drive Beam*. PhD thesis, CERN, 2011.
- [81] Luca Serafini and James B Rosenzweig. Envelope analysis of intense relativistic quasilaminar beams in rf photoinjectors: ma theory of emittance compensation. *Physical Review E*, 55(6):7565, 1997.
- [82] Bruce E Carlsten. New photoelectric injector design for the los alamos national laboratory xuv fel accelerator. *Nuclear Instruments and Methods in Physics Research Section A: Accelerators, Spectrometers, Detectors and Associated Equipment*, 285(1-2):313–319, 1989.
- [83] Fredericus Bernardus Kiewiet. Generation of ultra-short, high brightness relativistic electron bunches. 2003.
- [84] Vinit Kumar. Understanding the focusing of charged particle beams in a solenoid magnetic field. *American Journal of Physics*, 77(8):737–741, 2009.
- [85] Dennis Thomas Palmer et al. The next generation photoinjector. Technical report, Stanford Linear Accelerator Center (SLAC), 2005.
- [86] Rosenzweig. Space charge limited emission in photocathode gun. *XXX, XXX(XXX): XXX, XXX*.

- [87] SG Anderson, JB Rosenzweig, GP LeSage, and JK Crane. Space-charge effects in high brightness electron beam emittance measurements. *Physical Review Special Topics-Accelerators and Beams*, 5(1):014201, 2002.
- [88] Ji Li, Sakhorn Rimjaem, Matthias Groß, Andrey Shapovalov, Keerati Kusoljariyakul, Dieter Richter, Grygorii Vashchenko, Anne Oppelt, Guangyao Feng, Igor V Isaev, et al. Emission studies of photocathode rf gun at pitz. 2012.
- [89] M Ferrario, JE Clendenin, DT Palmer, JB Rosenzweig, and L Serafini. Homodyn study for the lcls rf photo-injector. In *The Physics of High Brightness Beams*, pages 534–563, 2000.
- [90] Concetta Ronsivalle and ENEA Frascati. Simulations of the emittance compensation in photoinjectors and comparison with sparc measurements. *EPAC2008*, 2008.
- [91] A Bacci, D Alesini, P Antici, M Bellaveglia, R Boni, E Chiadroni, A Cianchi, C Curatolo, G Di Pirro, A Esposito, et al. Electron linac design to drive bright compton back-scattering gamma-ray sources. *Journal of Applied Physics*, 113(19):194508, 2013.
- [92] C. Bruni, N. Artemiev, R. Roux, A. Variola, F. Zomer, and A. Loulergue. ThomX: A high flux compact X ray source. In *UVX 2010 - 10e Colloque sur les Sources Cohérentes et Incohérentes UV, VUV et X ; Applications et Développements Récents*, pages 49–55. EDP Sciences, 2011. ISBN 978-2-7598-0625-6 978-2-7598-0626-3. doi: 10.1051/uvx/2011007. URL <http://dx.doi.org/10.1051/uvx/2011007>.

# Resumé

Actuellement les sources de rayonnement par synchrotron et par électrons libres (FELs) sont les machines les plus performantes en termes de brillance et les seules disponibles pour réaliser des analyses et des recherches les plus ambitieuses que ce soit dans le domaine médical, nucléaire, de la physique de matériaux ou encore de l'histoire de l'art, dans un intervalle d'énergie comprise entre 10 et 100 keV. Mais les synchrotrons sont des grandes installations dont l'accès est limité, compte tenu du grand nombre d'utilisateurs potentiels, et qui présentent de fortes contraintes d'utilisation.

D'autre part, les plus performantes des sources conventionnelles et compactes (tubes à rayonnement X) ont un flux d'environ  $10^{10}$  ph/s, à une énergie fixe, limitée et ne pas tunable. Ces limitations ne permettent pas d'effectuer une large gamme d'applications lorsqu'il est demandé un haut flux de rayons X et/ou une largeur spectrale étroite.

Une autre façon de produire un haut flux de rayonnement X et gamma est par effet Compton Inverse (ICS) lorsque des paquets d'électrons interagissent avec des impulsions laser.

Les sources synchrotron de troisième génération sont généralement composées des aimants permanents, c'est à dire des onduleurs et des wigglers. Ces sources de lumière produisent le rayonnement X dépendant des caractéristiques de leurs éléments magnétiques. Les paramètres importants sont : le facteur de Lorentz ( $\gamma$ ) et la période spatiale de l'onduleur ( $\lambda_u$ ). La longueur d'onde de rayons X émis par l'onduleur est  $\lambda_u/2\gamma^2$ . Le paramètre  $\lambda_u$  est typiquement de quelque centimètre (soit 2 cm), tandis que  $\gamma$  doit être de l'ordre de  $10^4$  pour atteindre une longueur d'onde de l'Angstrom ( $10^{-10}$  m). Contrairement, la radiation qui est produit par le procès ICS a une longueur d'onde de  $\lambda_l/4\gamma^2$ . Etant donné que le laser a une longueur d'onde d'environ 1  $\mu\text{m}$ , c'est nécessaire un  $\gamma$  d'environ 50 (soit 25 MeV l'énergie de faisceaux d'électrons) pour obtenir une longueur d'onde à l'échelle de l'Angstrom. Pour cette raison pour produire des rayons X avec la même longueur d'onde l'énergie des électrons des machines ICS est d'environ de deux ordres de grandeurs plus faible par rapport à la grande échelle de synchrotrons. Cependant permet de réduire la taille de ces machines jusqu' à des dizaines des mètres carrés.

Ces sources compactes ICS peuvent aussi être installées dans des laboratoires de recherche grâce à une énergie des faisceaux d'électrons relativement faible par rapport aux machines synchrotrons. Les expériences avec des rayons X peuvent alors être faisables dans des emplacements où autrement ces applications seraient faites seulement dans les universités ou des centres de recherche. Par exemple, ces types de machines peuvent être installés dans des hôpitaux pour l'imagerie d'haute qualité, dans des laboratoires biomédicaux pour l'étude des protéines assez fragiles pour être transportées, ou dans des musées pour l'analyse des œuvres d'arts qu'ils ne peuvent pas être transportés. Dans ce sens, tels sources compactes seront plus accessibles et user-friendly que des larges machines.

Les avancées tant en technologie laser que de faisceaux d'électrons d'haute brillance ont récemment amené la communauté scientifique à considérer les sources ICS comme une des techniques les plus promettent pour la production de rayonnement X d'haute intensité. Bien évidemment ces sources de rayons X ne sont pas comparables avec les machines synchrotron et FELs actuelles en termes de flux de photons et de luminosité, mais autrement ils offrent quand même des capacités attractives et complémentaires en termes d'énergie de rayons X produits par rapport à la relativement faible énergie du faisceau d'électron qui est requise.

ThomX est une source compacte de rayons X et un démonstrateur de source de lumière par rétrodiffusion Compton, regroupant l'expertise de plusieurs laboratoires dans les domaines des accélérateurs (LAL, SOLEIL), des cavités optiques (LAL), des applicateurs laser (CELIA) et de l'utilisation des rayons X (Institut Neel, UMPC, INSERM, CHU Grenoble...). ThomX est en cours d'installation dans l'igloo du Laboratoire de l'Accélérateur Linéaire depuis février 2017.

Une source de lumière par rétrodiffusion Compton avec un anneau de stockage est composée par un canon HF, une section accélératrice, une ligne de transfert et un anneau de stockage où les paquets d'électrons interagissent avec les impulsions laser au point d'interaction (IP) pour produire des rayons X. Le schéma de ThomX et ses composants est basé sur l'expertise que le LAL a acquise dans le domaine de l'amplification des impulsions laser dans les cavités optiques (soit le projet MightyLaser). La cavité optique Fabry-Perrot est à l'état de l'art de la technologie pour ce type de dispositifs. De plus, le LAL a acquis une grande expérience pour la conception, la fabrication et les tests de canon haute fréquence (HF) pour la production de faisceaux d'électrons d'haute brillance (brillance crête de l'ordre de  $10^{12} A/m^2rad^2$ ). En particulier, le LAL a exploité l'expérience acquise pour la fabrication de photo-injecteurs, comme les canons « drive » et « sonde » qui a conçu, testé et fabriqué pour la Compact Linear Collider (CLIC) Test Facility 3 (CTF3) au CERN.

**But du manuscrit de thèse** Ce manuscrit de thèse est consacré à l'accélérateur linéaire (LINAC) de la source de rayonnement ThomX.

En effet, ThomX montre plusieurs enjeux dans le domaine d'accélérateurs, par exemple l'anneau de stockage n'est pas conventionnel en termes de dynamique des faisceaux. La faible énergie (quelques dizaines de MeV) des paquets d'électrons qui circulent dans l'anneau entraîne un court temps de stockage. Alors, le temps que le paquet d'électrons et stocké dans l'anneau le temps d'amortissement devient négligeable. Ces caractéristiques ne sont pas du tout typiques et rendent les propriétés du faisceau d'électrons cruciaux à la sortie de l'accélérateur linéaire pour déterminer les performances des rayons X produit au point d'interaction. Ce dernier détermine les propriétés finales des rayons X produites par la source ICS. Pour ces raisons, le schéma du photo-injecteur doit être analysé attentivement et plusieurs solutions techniques ont été considérés et proposés par rapport au schéma original pour la minimisation d'emittance et de la dispersion en énergie.

Une autre partie important est l'étude de la dynamique de faisceaux de particules qui se propagent le long du linac de ThomX. En particulier, des différentes caractéristiques de la dynamique des faisceaux ont été analysées, comme par exemple les propriétés de la forme du laser qui impact sur la cathode, les caractéristiques du paquet dans le photo-injecteur et son évolution le long de la section accélératrice à ondes progressives.

Une des parties plus importantes est l'upgrade de l'accélérateur linéaire pour l'augmentation de l'énergie des électrons en maintenant la compacité et les caractéristiques du faisceau à l'injection dans l'anneau. Cette partie implique une activité de recherche et développement (R&D) au LAL en partenariat avec une entreprise française (PMB-Alcen) dans le domaine de la technologie des structures accélératrices à fort-gradient (HG). La collaboration entre le LAL et PMB-Alcen a comme objectif la fabrication d'une structure en cuivre, à fort-gradient, en bande S (2998.55 MHz) en abordent les aspects technologiques que limitent l'obtention des champs accélérateurs très élevés en raison des claquages dans le vide et des stress thermiques dus aux champs magnétiques périodiques. Essentiellement, le LAL s'occupe de la conception électromagnétiques et thermique de la structure accélératrice en bande S à fort-gradient en utilisent des logiciels de simulation tels qu'ANSYS HFSS (High-Frequency Electromagnetic Solver), CST MWS (Computer Simulation Technology, Microwave Studio) et l'outil ANSYS Computational Fluid Dynamics (CFD, Fluent). D'autre coté, PMB-Alcen, d'après les simulations faites par le LAL, a été en charge des plans mécaniques de cellules standard ainsi que des coupleurs de puissance. L'étape suivante a été la fabrication des prototypes en bande S en aluminium avec un nombre réduit de cellules standard. Cette étape a prévu des tests HF bas puissance pour vérifier la géométrie et les tolérances mécaniques. Des prototypes en cuivre seront fabriquées de que le procès de fabrication sera validé. Après, ceux prototypes seront

testés à haute puissance pour vérifier la précision d'usinage en termes des tolérances et d'état de surface compte tenu de la fabrication de la section accélératrice finale en cuivre à fort-gradient (3.2 mètres de longueur). La durée de l'accord de collaboration de recherche est de quatre ans, du 1er octobre 2014 au 30 septembre 2018.

Ce manuscrit de thèse pose l'accent sur les aspects techniques des composants principaux de l'accélérateur linéaire de ThomX, tels que le canon HF, les solénoïdes et la section accélératrice. Ce mémoire est organisé en cinq chapitres.

Le premier chapitre est une introduction aux sources de lumière par rétrodiffusion Compton ou Thomson. Le chapitre décrit les facteurs principaux qui ont fait que la production de rayons X par l'interaction entre les paquets d'électrons et les impulsions laser soit efficace, ainsi que les avantages et désavantages de ce principe sont décrits. La source MuCLS est présentée, la seule machine dans le monde capable de produire un flux de rayons X comparable à ce qui est fourni par les sources synchrotron de première génération. Cette machine est en opération à l'institut Technique de Munich, et son schéma ainsi que celles des X produits sont reportés aux fins de comparaisons avec les propriétés attendues et potentielles de ThomX. Au final, le chapitre présente un aperçu du projet ThomX en incluant le schéma de l'accélérateur ainsi que ses possibles applications.

Le chapitre 2 détaille les principaux composants HF du linac. Dans un premier temps, les concepts basiques des ondes électromagnétiques à haute fréquence (HF) pour une cellule sont présentés avec les figures de mérite ainsi que le principe d'accélération dans des structures périodiques. Dans un deuxième temps, les quantités qui limitent l'accomplissement de forts gradients d'accélération dans les structures périodiques et la conception de parties HF du linac de ThomX sont décrites. En particulier, l'étude thermo-structurale du canon HF est détaillée. Ce canon a été développé au LAL pour le photo-injecteur de ThomX. De plus, la conception électromagnétique (EM) et mécanique des prototypes et la conception EM de la section accélératrice finale à fort-gradient sont décrites. Enfin, l'étude thermique du circuit de refroidissement de prototypes et une estimation de performances du vide, dans les prototypes et dans la section accélératrice finale ont été proposés, pour vérifier si la structure peut soutenir l'haute valeur de puissance dissipée ainsi que le régime d'ultravide (UHV) demandé pour ce type d'application.

Le chapitre 3 expose la procédure de fabrication du canon et des prototypes de la structure accélératrice de ThomX. En particulier, il décrit les solutions mécaniques qui ont été proposées pour la fabrication des composants. Après la fabrication, les composants doivent être réglés à la bonne fréquence ainsi qu'avancement de phase. Par conséquent, la procédure de réglage est présentée ainsi que l'appareil de mesures avec les résultats des tests HF bas niveau qui ont été effectués chez le LAL et PMB-Alcen. Enfin, les problèmes de fabrications sont mentionnés.

Le chapitre 4 décrit les simulations de la dynamique des faisceaux du paquet d'électrons le long de la ligne du faisceau du linac. Le paquet est généré de la cathode et fait l'objet de champs électriques et magnétiques qui doivent être matchés à la fin du linac, dans la ligne de transfert pour l'ultérieure injection dans l'anneau. A cette fin, on propose différents paramètres possibles d'opérations pour atteindre les spécifications du faisceau d'électrons qui sont demandés par le rapport technique de conception de l'accélérateur à la sortie du linac (TDR, Technical Design Report). L'impact des caractéristiques des paquets d'électrons sur la qualité de rayons X est en bref exposée à la fin du chapitre.

Le chapitre 5 résume les principaux résultats qu'ont été présentés au cours de ce manuscrit ainsi que les conclusions, les perspectives et les travaux futures concernant ces activités.

**Résumé des résultats** Ce manuscrit de thèse décrit la conception et les aspects techniques de l'accélérateur linéaire de ThomX. Essentiellement, ThomX est composé de deux composants HF normal-conducteurs : le canon HF et la section accélératrice. Pour prévenir des champs parasites et des jitters de phases, qui dégradent la qualité du faisceau d'électrons, il est demandé que la température du canon HF soit stable pendant l'opération. Le circuit de refroidissement doit garantir une dissipation de puissance moyenne de quelque kW dans les parois de la structure dus au haut niveau HF et haut taux de répétitions de fonctionnement du canon. Par conséquent, la conception du circuit de refroidissement a été faite pour maintenir les variations de température plus faibles possible en réduisant les déformations de la structure. Une analyse avec un seul logiciel de simulation (ANSYS) a été faite par une couplage électromagnétique, thermique et structurel. Cette analyse a confirmé que le circuit de refroidissement du canon devrait être appropriée pour une dissipation de puissance de 1.5 kW dans les parois de la structure, qui correspond à un taux de répétition des impulsions laser de 50 Hz, 100 MV/m du champs accélérateur maximum, 3  $\mu\text{m}$  de longueur d'impulsion, avec 2.5 m/s de débit d'eau.

Un autre aspect important de ce travail est la phase d'upgrade d'énergie du linac. Cette phase implique une activité des recherche et développement au LAL en partenariat avec une entreprise française (PMB-Alcen) ayant pour objective la fabrication d'une section accélératrice compacte, en cuivre, en bande S, à gradient constant. Le remplacement d'une section accélératrice LIL standard avec une nouvelle structure à fort-gradient doit permettre d'obtenir une énergie de paquets d'électrons jusqu'à 70 MeV qui corresponde à une énergie de flux de rayons X de 90 keV en maintenant la compacité et les caractéristiques du faisceau à l'injection dans l'anneau. La fabrication de la structure accélératrice à fort-gradient demande des analyses et investigations détaillées des principales quantités qui limitent la réussite d'un fort gradient d'accélération dans des structures périodiques

HF. Ces limitations sont principalement dues aux claquages du vide dans la structure et aux stress mécaniques dus aux stress thermiques.

La connaissance des mécanismes qui limitent la réussite des forts gradients accélérateurs dans les structures HF se base sur un vaste programme expérimental des tests de puissance et d'investigation des phénomènes de claquage qui a été faite dans plusieurs laboratoires au cours des années. Une analyse méticuleuse d'une large quantité des données expérimentaux a souligné la dépendance des claquages dus à certains paramètres, tels que la durée de l'impulsion HF et le flux de puissance circulant dans la structure. Un nouveau champ local, le seuil du vecteur de Poynting modifié, a été introduit comme un nouveau critère pour la conception des structures accélératrice à fort-gradient.

La conception électromagnétique des cellules standard a été faite en tenant en compte les principales quantités qui guident l'optimisation des paramètres géométriques. La forme finale de la cellule a été défini sur la base de différents critères : maximum  $r_s/Q$ , minimisation du rapport entre le champ électrique de surface crête et le gradient accélérateur sur l'axe  $E_{smax}/E_a$ , minimisation du vecteur de Poynting. Cependant, la conception de la géométrie est un procès difficile parce que l'amélioration des certaines paramètres HF normalement donne lieu à la dégradation d'autres quantités. Par conséquent, la géométrie optimale de cellules standards est une conséquence du compromis parmi différents contraintes de la cavité ayant pour objective l'accomplissement des spécifications demandés. Les dimensions finales ont été optimisées pour obtenir un champ électrique de surface crêt minimum en utilisant une forme d'iris elliptique et en considérant une valeur minimum du vecteur de Poynting modifié à ces régions, une vitesse de groupe relativement haute, un gradient accélérateur capable d'atteindre le gain d'énergie désirée par rapport à la puissance injecté disponible. L'épaisseur de l'iris a été choisi en tenant en compte du compromis parmi une haute impédance de shunt, un temps de remplissage acceptable et une bonne rigidité mécanique. Le bord de la cellule a été arrondi en permettant d'augmenter le facteur de qualité du 10% et réduisant la consommation de la puissance. De plus, une ouverture d'iris raisonnable a été considérée pour garantir une haute efficacité d'accélération avec le minimum des risques de claquages, temps de remplissage faible et bonne vitesse de pompage.

La conception de coupleurs de puissance a été faite pour transmettre le maximum d'énergie au faisceau et protéger l'alimentation électrique. Ces conditions sont satisfaites lorsqu'il est garanti un bon couplage entre la guide d'onde et la structure accélératrice périodique. Les coupleurs ont été conçu pour réduire le plus possible les réflexions de puissance aux ports de coupleur d'entrée et de sortie ayant une phase d'avancement pour cellule égal à la valeur nominale ( $120^\circ$ ). Les prototypes sont équipés de coupleurs quasi symétriques single-feed qu'ont une guide d'onde avec une longueur de  $\lambda/4$  (stub)

de l'autre côté de slot de couplage pour compenser les asymétries du champ électromagnétique dans la cellule de couplage.

Deux techniques pour la conception des coupleurs ont été utilisées sur le prototype à onde progressive (TW), à impédance constante (CI) et sur la structure finale TW, à gradient constant (CG). Le développement des prototypes CI en cuivre permettent la vérification de la géométrie, des conditions d'opération et la validation de la procédure de fabrication. Les quantités qui limitent la réussite des fort-gradient accélérateurs, tels que la probabilité du claquage HF (BRD) et le réchauffement thermique, ont été analysés pour la conception des coupleurs et de la structure accélératrice finale. En considérant une puissance crête de 20 MW à l'entrée du prototype 16-cellules CI en cuivre, la valeur maximum simulée du vecteur de Poynting modifié est d'environ  $0.19 \text{ MW/mm}^2$ , bien au-dessous de la limite de  $1.6 \text{ MW/mm}^2$ , pour une probabilité de claquage (BDR) de  $10^{-6}$  bpp/m (applications médicales). De plus, le phénomène de réchauffement du aux impulsions thermiques a été méticuleusement évalué et contrôlé à chaque position de la structure où les courants de surface deviennent importants. En considérant un plateau d'impulsion HF avec une longueur de  $3 \mu\text{s}$  (20 MW puissance d'entrée) on a obtenu un champ magnétique de surface crête de  $1.36 \times 10^5 \text{ A/m}$  à la région correspondent entre la guide d'onde et l'ouverture de couplage. Cette valeur correspond à une augmentation de température du métal inférieure à  $8 \text{ }^\circ\text{C}$ , bien au-dessous de la "seuil limite" de risque de dommage des coupleurs. En outre, il a été effectuée la conception mécanique des cellules standards et des coupleurs. Chaque cellule standard présente quatre trous sur la surface extérieure pour le réglage en fréquence. Ils présentent aussi huit tuyaux de refroidissement qui sont directement percés dans le corps en cuivre. Les coupleurs sont composés par des pièces usinées séparément : le corps et la couverture. Le corps est composé par la cellule de couplage qui est équipée des guides d'onde et une demi-cellule standard.

On a effectué la conception électromagnétique de la structure accélératrice compacte à fort-gradient en bande S de 3.2 mètre de longueur. Cette structure est une section à ondes progressives à gradient-constant, composée de 95 cellules standards et de 2 cellules de couplage qui résonnent à une fréquence de 2998.5 MHz à  $30 \text{ }^\circ\text{C}$  sous vide, en mode  $\text{TM}_{010-2\pi/3}$ . Un gradient accélérateur constant est maintenu le long de la structure grâce à un décroissement de l'ouverture des iris appropriée dans chaque cellule. Le rayon d'iris est alors réduit pour obtenir l'uniformité d'amplitude de champs accélérateur le long de la totalité de la structure et pour maintenir un avancement de phase constant entre chaque cellule de  $120^\circ$ , correspondent au mode accélérateur. On a effectué la conception d'une structure avec un décroissement linéaire des ouverture d'iris en simulant des cellules standards avec différentes valeurs de rayons d'iris et en calculant à chaque fois les principales figures de mérite HF. La variation du rayon d'iris a été choisi en tant que compromis entre le gain d'énergie maximum et le temps de remplissage minimum.

La structure accélératrice est équipée avec deux types de coupleurs quasi symétriques à “single-feed”. Pour une valeur maximum de puissance d’entrée de 24 MW, la puissance restant est d’environ 7 MW à la fin de la structure, correspondant à une puissance dissipée dans les parois de la cavité d’environ 17 MW (2.55 kW puissance moyenne). Le champ accélérateur effective vu par le faisceau d’électron a une valeur moyenne de 20 MV/m, alors que le gradient électrique crêt montré est de 24 MV/m. En tenant en compte une énergie d’environ 5 MeV à la sortie du canon HF, le gain d’énergie à la sortie de la section accélératrice est d’environ 65 MeV. Ce dernier devra être suffisant pour atteindre un’énergie finale de 70 MeV pour la phase d’upgrade du linac. Le temps de remplissage est inférieur à 1  $\mu$ s. Cette valeur est raisonnable pour prévenir les phénomènes de claquage dans la structure pendant l’opération. Le champ de surface crêt maintien une valeur constant de 34 MV/m et décroît le long de la structure. Cette valeur est bien au-dessous du seuil de claquage de 47 MV/m par rapport à la limite de Kilpatrick. La valeur maximum du vecteur de Poynting simulé le long de la structure est de 0.25 MW/mm<sup>2</sup> qui est bien au-dessous de la limite de 1.6 MW/mm<sup>2</sup> pour un BDR de 10<sup>-6</sup> bpp/m.

Une étude a été faite sur un couplage thermique - mécanique pour un prototype en cuivre 7 cellules à impédance constant. Le circuit de refroidissement a été simulée pour valider la capacité d’extraction de la chaleur qu’est générée par la dissipation de puissance dans les parois de la structure et pour garantir une distribution de température uniforme le long de la structure accélératrice. La dissipation de la puissance simulée sur les parois du prototype 7 cellules est d’environ 333 W pour une puissance d’entrée crêt de 20 MW (longueur d’impulsion HF de 3  $\mu$ s et taux de répétition de 50 Hz). La différence de température moyenne entre la structure en cuivre et l’eau qui circule dans le circuit de refroidissement est de 0.7 °C, l’incrément de température d’eau due à la chaleur de la puissance dissipée est de 0.08 °C, en accord avec les estimations analytiques. Quelque paramètre qui spécifiques des conditions initiales a été fixés et appliqué comme charge thermique au model Fluent de la structure. Puis, on a appliqué la convection naturelle au model. On a obtenu une température uniforme le long de la totalité de la structure avec une valeur moyen d’environ 24.8 °C qu’est proche à la valeur analytique. La température des cellules, qu’a l’impact majeur sur la fréquence de résonance des structures est d’environ 26 °C. De plus, la chute de pression maximum est d’environ 0.17 bar en montrant un bon accord avec les résultats analytiques. De plus, on a estimé la variation de température et la chute de pression pour le circuit de refroidissement du prototype 16 cellules et pour la section accélératrice finale. A partir de l’analyse thermique, nous sommes capables d’évaluer la déformation de la structure due au chauffage à haute fréquence. La déformation maximale est d’environ 12  $\mu$ m. La déformation calculée sur les surface internes en direction radiale est au-dessous de 20  $\mu$ m. On dirait que le circuit de refroidissement conçu est acceptable pour le prototype CI 16-cellules et pour

la structure finale CG TW. Ce circuit de refroidissement permet de tenir sous control les déformations de la structure en maintenant l'augmentation de température la plus faible et uniforme possible.

On a vérifié le niveau du vide d'une prototype 16-cellules à impédance constant en cuivre pour prévenir une haute probabilité des claquages HF, une durée du faisceau courte et une augmentation importante d'emittance. On a étudié quatre configurations de pompage du vide pour le prototype : pompage par un seul tube du faisceau, pompage par une seule guide d'onde HF, pompage par les deux tubes du faisceau ou par les deux guides d'onde HF. Le pompage par les deux tubes du faisceau a permis de diminuer d'un facteur 2 les valeurs maximum est moyen de pression le long de la structure par rapport au pompage connectée à un seul tube du faisceau. Le pompage par une seule guide d'onde HF permet de diminuer d'un facteur 3 les valeurs maximum et moyenne de pression le long de la structure par rapport au cas du pompage travers les deux tubes du faisceau. Le pompage par les deux guide d'ondes HF permet de diminuer d'un facteur 3 les valeurs maximum et moyen de pression le long de la structure par rapport au cas d'une seule pompe ionique connecté au guide d'onde HF. Lorsque deux pompes ioniques sont connectés aux deux guide d'onde HF, la pression maximum au centre de la structure est d'environ  $4 \times 10^{-9}$  mbar, sans procès d'étuvage. De plus, on a effectué la simulation du vide sur la structure accélératrice finale de 3.2 mètres de longueur. La pression augmente le long de la structure (parce que les diamètres décroissent progressivement) jusqu'à le centre et puis décroissent au valeur minimum égal à  $5.97 \times 10^{-9}$  mbar. La pression moyen est de  $5.83 \times 10^{-8}$  mbar et le maximum est  $8.78 \times 10^{-8}$  mbar. En cas de la configuration de la section finale, le maximum de pression est de  $8.78 \times 10^{-8}$  mbar sans étuvage. Ces valeurs sont au-dessous ou comparable à  $8 \times 10^{-8}$  mbar qu'est suffisant pour l'opération de structure à fort-gradient. De plus, avec le procès d'étuvage, la valeur simulée du vide devrait être divisée encore par un facteur 10 - 100. La bonne nouvelle est qu'en considérant nos calculs plutôt conservatifs, le pompage du prototype avec la conception actuelle devrait être raisonnable. Pour la structure accélératrice finale à fort-gradient, 3.2 mètres de longueur, on a besoin d'augmenter la valeur du vide dans la structure au moins d'une facteur 10 (100 au mieux). On croit que le pompage par les guides d'ondes HF et l'étuvage de la section après l'installation sera déterminante pour la réussite des spécifications.

De plus, une description des étapes principales concernant la fabrication du canon HF pour ThomX au LAL a été présentées : les procès d'usinage, réglage, brasage et nettoyage. En plus, la description des étapes de fabrication des prototypes 7-cellules en aluminium en collaboration avec l'entreprise PMB-Alcen a été détaillée. Après le procès d'usinage des cellules standards, on a présenté la méthode de réglage sous presse. Les

tests de puissance HF bas niveau sur le prototype ont été effectués pour valider la conception de la géométrie 3D et le procès s'usinage. Ces dernières étapes sont très importantes pour aborder les problèmes mécaniques et les contraintes technologiques pour le prochain prototype en cuivre. Les résultats des mesures HF à bas niveau, avant et après le procès de réglage ont été montrés. L'étape suivante sera consacrée à la fabrication du prototype en cuivre CI 16-cellules pour valider le procès de fabrication, du conditionnement HF et des tests haute puissance. Puis, une section accélératrice à fort-gradient en bande S, 3.2 mètres de longueur sera fabriquée et brasée pour l'upgrade d'énergie du linac de ThomX.

L'optimisation de la dispersion en énergie du faisceau et d'emittance est cruciale pour la pureté spectrale des rayons X produits. Dû à la charge d'électrons relativement haute qu'est demandée (1 nC), le control d'emittance à la sortie du linac est dominé par l'effet de charge espace. Cependant, des différents procédures d'optimisation ont été déjà proposées en littérature. Dans ce but, des simulations du linac complet de ThomX ont été faites en utilisant un modèle le plus proche possible aux composants électromagnétiques réels de l'accélérateur linéaire, tels que le canon HF, la section TW et les solénoïdes.

Dans un premier temps, nous remarquons que la taille transverse du laser doit être majeure à 0.4 mm pour éviter la perte de charge par effet de charge image à la cathode. En effet, cette valeur correspond à une régime d'émission saturée par l'effet de charge espace et pas plus de charge peut être extraite même si l'intensité du laser augmente.

Dans un deuxième temps, en examinant la condition d'enveloppe invariante qu'a été proposé par Serafini, Rosenzweig et Ferrario, on a trouvé que le waist du faisceau correspondant au maximum locale d'emittance ne peut pas se passer pour la configuration nominale des solénoïdes qu'a été choisi pendant la phase TDR (Technical Design Report) du projet. Puisque tous les composants mécaniques et magnétiques ont été déjà commandés, on a trouvé une autre solution en réduisant l'impact sur le budget et sur les retards du projet. En fait, en déplaçant le solénoïde de focalisation après le canon HF, la condition d'enveloppe invariante peut être accompli à la position d'entre de la section accélératrice TW avec une valeur proche de celle nominale du TDR. L'optimisation finale a été faite en utilisant un algorithme génétique qu'a permis d'atteindre une emittance transverse normalisée égal à  $4 \pi$  mm mrad avec une dispersion d'énergie relativement faible. On a aussi montré que l'utilisation d'une section fort-gradient à 3 GHz peut améliorer l'effet de focalisation de la section accélératrice en réduisant la dégradation d'emittance dans le premier triplet de quadripôles à la sortie du linac.

L'analyse et l'optimisation de la position des solénoïdes en utilisant un algorithme génétique constitue une méthode très robuste pour l'amélioration des caractéristiques du faisceau de ThomX de le début (émission d'électrons) jusqu'à le point d'interaction. Il

constitue aussi une base solide pour la prochaine phase de commissioning de l'accélérateur linéaire.

**Titre :** Accélérateur linéaire d'électrons à fort gradient en bande S pour ThomX

**Mots clés :** Accélérateur, Linac bande S, Electrons, Fort gradient, ThomX, Photo-injecteur

**Résumé :** ThomX, un démonstrateur de source Compton compacte de rayons X d'énergie réglable entre 45 et 90 keV, est en construction sur le campus de l'Université Paris-Saclay à Orsay. La thèse s'inscrit dans le cadre de l'upgrade du linac de ThomX qui consiste à réaliser une section accélératrice compacte à fort gradient en bande S (3 GHz) pour porter les faisceaux de ThomX de 50 MeV à 70 MeV. Un accord de collaboration R&D est signé entre LAL et PMB-Alcen pour développer une structure accélératrice en cuivre (OFHC) compacte en bande S à fort gradient. Une étude électromagnétique, thermique et dynamique de faisceau a été effectuée au LAL pour proposer une géométrie optimale de la section accélératrice pour atteindre des gradients accélérateurs très élevés. PMB est en charge d'améliorer les processus de fabrication en commençant par la réalisation des prototypes pour valider les choix technologiques et ensuite fabriquer la section finale pour répondre aux spécifications demandées. Dans un premier temps une étude couplée électromagnétique-thermique-structurelle du canon HF a été effectuée en utilisant le Logiciel d'analyse des éléments finis 3D (ANSYS). Ensuite l'étude électromagnétique et l'optimisation de la géométrie des cellules accélératrices ainsi que la conception des coupleurs de puissance pour constituer les prototypes à impédance constante avec un certain nombre de cellules réduit et la section accélératrice compacte à gradient constant ont été effectuées en utilisant les logiciels CST MWS et HFSS. Puis une étude thermomécanique de la structure accélératrice a été réalisée avec ANSYS pour concevoir et optimiser le circuit de refroidissement pour extraire la chaleur générée par la puissance HF dissipée dans les parois de la structure et garantir une répartition uniforme de la température au long de la structure. Les simulations du vide ont été également réalisées avec le code Monte Carlo pour envisager la meilleure solution de pompage pour le prototype de cuivre et la section finale. En outre, les principales étapes suivies dans la fabrication du Canon HF au LAL et le prototype en aluminium à 7 cellules chez PMB-Alcen ont été présentées. Des tests HF bas niveau du prototype ont été effectués afin de valider la géométrie « processus d'usinage ». Compte tenu des résultats expérimentaux, des problèmes techniques et des contraintes technologiques ont été abordés et certaines solutions ont été proposées pour la fabrication des prototypes en cuivre et de la section finale. Les simulations de la dynamique des faisceaux du linac de ThomX ont été effectuées en utilisant le code ASTRA. Le but est de réduire autant que possible la dispersion en énergie et l'emittance transverse du paquet d'électrons au point d'interaction avec les impulsions laser, pour préserver la pureté spectrale de rayons X produits. Un modèle aussi proche que possible des caractéristiques des composants réels, tels que le canon HF, la section accélératrice à onde progressive (OP) et les solénoïdes a été pris en compte dans les simulations. Des résultats importants ressortent de ces simulations concernant les paramètres du laser (taille et durée du spot), le champ magnétique maximal des solénoïdes pour la compensation de l'effet de charge espace, le déphasage entre l'onde RF et le laser et l'effet du champ électromagnétique sur la dynamique des électrons. Différentes options pour les paramètres de fonctionnement de la machine et une nouvelle configuration de la position des solénoïdes ont été proposées. L'optimisation des caractéristiques du paquet d'électrons a été obtenue en utilisant un algorithme génétique et les performances finales du faisceau d'électrons ont été mises en évidence.



**Title :** High-gradient S-band electron Linac for ThomX

**Keywords :** Accelerator, S-band Linac, Electrons, High gradient, ThomX, Photo-injector

**Abstract:** The ThomX source should provide quasi-monochromatic high-quality X-rays (range 45- 90 keV). The framework of the thesis is the electron beam linac energy upgrade from 50 MeV to 70 MeV necessary to achieve X-rays of 90 keV. For this purpose, the development of a compact high-gradient S-band electron accelerating structure is needed. It implies a research and development (R&D) activity at LAL in partnership with a French company (PMB-Alcen) in the High-Gradient (HG) technology of accelerating structures. The LAL-PMB-Alcen collaboration aims at the fabrication of a normal-conducting HG S-band structure by tackling the technological aspects that limit the achievement of high-gradient acceleration mostly due to vacuum RF breakdown and pulsed heating fatigue. Basically, the electromagnetic and thermal design of the HG S-band accelerating section has been performed at LAL. Meanwhile, PMB-Alcen was in charge to perform the fabrication, tuning and low power tests of prototypes and the final accelerating section. In this work, a fully coupled electromagnetic-thermal-structural finite element analysis on the THOMX RF gun has been performed with Ansys workbench. The HG accelerating section final regular cell dimensions and the power coupler design have been optimized. In particular, the electromagnetic simulation techniques and outcomes have been applied to constant impedance (CI) TW prototypes and also to a constant gradient (CG) final accelerating section. This allowed to verify the geometry choice, validate the fabrication procedure and check the fulfilment of the normal operating conditions. Moreover, a coupled thermo-mechanical study on a CI copper prototype has been performed. The water cooling system has been simulated to validate the capability to extract the heat generated by the dissipated power on the walls of the structure and guarantee a uniform temperature distribution along the section. Also, vacuum simulations have been performed on a 16-cells CI copper prototype and also on the final CG accelerating section. In addition, the main steps for the fabrication of the RF gun at LAL and a 7-cells aluminum prototype at PMB-Alcen have been presented. RF low power tests on the prototype have been performed in order to validate the 3D geometry design and the machining process. Taking into account the experimental results, mechanical problems and technological constraints have been tackled and some solutions have been proposed for the future copper prototype fabrication. Finally, beam dynamics simulations of the ThomX linac has been carried out by ASTRA code. The aim is to reduce as much as possible the energy spread and the transverse emittance to preserve the spectral purity of the produced X-rays, at the electron-photon interaction point. A model as close as possible to the characteristics of the real components, such as RF gun, TW section and solenoids has been considered. Important results came out from these simulations regarding laser parameters (spot size and duration), the maximum magnetic field of solenoids for high space charge effect compensation, dephasing between the RF and laser in the gun and effect of the travelling wave electromagnetic field on the particle dynamics. Different options for the parameter settings of machine operation and a new configuration of the solenoids position have been proposed. An optimization of the beam dynamics properties has been obtained by using a genetic algorithm and the ultimate performances of the electron beam have been highlighted.

